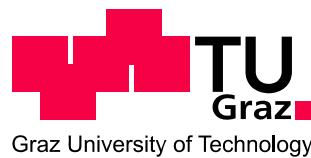# Modelling and Simulation of Strengthening in Complex Martensitic 9-12% Cr Steel and a Binary Fe-Cu Alloy

by

Dipl.-Ing. Ivan Holzer

Institute for Materials Science and Welding

Graz University of Technology

Submitted for the degree of

"Doktor der technischen Wissenschaften"

at the Faculty of Mechanical Engineering

GRAZ UNIVERSITY OF TECHNOLOGY

Graz, May 2010

por mi cari

Preface

This PhD is submitted for the Degree of "Doktor der Technischen Wissenschaften" at the Faculty of Mechanical Engineering at Graz University of Technology. The work was carried out between May 2005 and April 2010 under the supervision of Prof. Ernst Kozeschnik and Em. Prof. Horst Cerjak at the Institute for Materials Science and Welding. This work was funded by the Austrian Research Promotion Agency (FFG) and was part of the European research collaboration COST 536 "Alloy development for critical components of environmentally friendly power plants – ACCEPT".

I declare that I have authored this thesis independently, that I have not used other than the declared sources/resources, and that I have explicitly marked all material which has been quoted either literally or by content from the used sources.

<div align="right">
Ivan Holzer

Graz, May 2010
</div>

List of Publications

Parts of this work, as well as further research activities have been published by the author as corresponding or co-author elsewhere. The following list shows the references of these works which were published as journal papers, conference proceedings book chapters and posters during the time period 2005-2010.

[1] I. Holzer, E. Kozeschnik, *Computer simulation of the time-temperature-precipitation diagram of 1.4 wt.% Cu ferritic steel*, Philosophical Magazine, *submitted*.

[2] I. Holzer, E. Kozeschnik, *Computer simulation of the yield strength evolution in Cu-precipitation strengthened ferritic steel*, Materials Science and Engineering A 527 (2010) 3546-3551.

[3] I. Holzer, E. Kozeschnik, H. Cerjak, *New approach to predict the long-term creep behavior and evolution of precipitate back-stress of 9-12% chromium steels*, Transactions of the Indian Institute of Metals *in press*.

[4] B. Sonderegger, I. Holzer, E. Kozeschnik, *Calculation of energies of coherent interfaces and application to the nucleation, growth and coarsening of precipitates*, Materials Science Forum 638-642 (2010) 2730-2735.

[5] I. Holzer, E. Kozeschnik, *Simulation of Copper Precipitation in Fe-Cu*, Materials Science Forum 638-642 (2010) 2579-2584.

[6] I. Holzer, E. Kozeschnik, *The effect of quenched-in vacancies on the kinetics of coherent Cu-precipitation in Fe-Cu alloys*, 139th Annual Meeting & Exhibition TMS, Seattle, Washington (14.02.2010).

[7] F. Krumphals, T. Wlanis, Ch. Sommitsch, I. Holzer, B. Sonderegger, V. Wieser, *Modelling of Microstructure Evolution in Hot Work Tool Steels During Service*, Computer Methods in Materials Science 9 (2009) 228-233.

[8] P. Mayr, F. Mendez Martin, I. Holzer, A. Agüero, V. González, S. Baumgartner, H.H. Cerjak, *Experience with 9Cr3W3CoVNbBN base material and crosswelds at 650°C for implementation in USC power plants*, in: Proceedings of the 3rd Symposium on Heat Resistant Steels and Alloys for High Efficiency USC Power Plants 2009, http://www.nims.go.jp/hrdg/USC/Proceeding/Proceeding003Mayr.pdf (29.04.2010).

[9] I. Holzer, E. Kozeschnik, *Simulation of Copper Precipitation in Fe-Cu Alloys*, in: 6th International Conference on Processing and Manufacturing of Advanced Materials THERMEC 2009, Berlin (2010), 2579-2584.

[10] E. Kozeschnik, I. Holzer, in: F. Abe, T.U. Kern, R. Viswanathan (Eds.), *Creep resistant steels*, Woodhead Publishing, Cambridge (2008), 305-328.

[11] I. Holzer, E. Kozeschnik, *Predicted precipitate back-stress and creep rupture strength of the advanced 9-12% Cr steel COST E2*, International journal of materials research (Zeitschrift für Metallkunde) 99 (2008) 416-421.

[12] I. Holzer, E. Kozeschnik, H.H. Cerjak, *Computational Modeling of the Strength Evolution During Processing and Service of 9-12% CR Steels*, in: The Fifth International Conference on Mathematical Modeling and Computer Simulation of Materials Technologies, http://www.ariel.ac.il/management/research/pf/zinigrad/mmt/mmt-2008/Service_files/papers/Session_2/2_14-22.doc (29.04.2010).

[13] I. Holzer, E. Kozeschnik, H.H. Cerjak, *New Approach to Predict the Long-Term Creep Behaviour and Evolution of Precipitate Back-Stress of 9-12% Chromium Steels*, in: 5th International Conference on Creep, Fatigue and Creep-Fatigue Interaction - Technical Proceedings, (2008), *published on CD-ROM*.

[14] I. Holzer, E. Kozeschnik, H.H. Cerjak, *Prediction of the loss of precipitate back-stress in modern 9-12% Cr steels – a numerical approach.* in: Tagungsband zur 10. Werkstofftagung - Verarbeitungs- und Gebrauchseigenschaften von Werkstoffen - Heute und Morgen, Graz University of Technology, Graz (2008), 73-76.

[15] I. Holzer, E. Kozeschnik, H.H. Cerjak, *Prediction of the Loss of Precipitation Strengthening in Modern 9-12% Cr Steels – a Numerical Approach*, in: Advances in Materials Technology for Fossil Power Plants Proceedings of the Fifth International Conference, ASM International, Ohio (2008), 197-207.

[16] H.H. Cerjak, P. Mayr, I. Holzer, C. Pein, B. Sonderegger, E. Kozeschnik, *Application of a Comprehensive R&D Concept to Improve Long-Term Creep Behaviour of Martensitic 9-12% Cr Steels*, in: Advances in Materials Technology for Fossil Power Plants Proceedings of the Fifth International Conference, ASM International, Ohio (2008), 627-644.

[17] I. Holzer, P. Mayr, B. Sonderegger, E. Kozeschnik, H.H. Cerjak, *Simulation and Validation of the Evolution of Precipitates During Production and Fabrication of a Complex Martensitic 9 wt.% Cr Steel.* Proceedings of 17th International Conference Computer Technology in Welding and Manufacturing, (2008), *published on CD-ROM*.

[18] H.H. Cerjak, I. Holzer, P. Mayr, C. Pein, B. Sonderegger, E. Kozeschnik, *The relation between microstructure and creep properties of martensitic 9-12%Cr steels.* in: New Developments on Metallurgy and Applications of High Strength Steels: Buenos Aires 2008, The Minerals, Metals & Materials Society, Warrendale (2008), 247-265.

[19] B. Sonderegger, I. Holzer, P. Mayr, *Werkstoffmodellierung mit MatCalc und Anwendung für die Entwicklung eines neuen Stahls mit verbesserten kriech- und Schweißeigenschaften*, in: Langzeitverhalten warmfester Stähle und Hochtemperaturwerkstoffe: Beiträge zur 31. Vortragsveranstaltung der Arbeitsgemeinschaft für Warmfeste Stähle und der Arbeitsgemeinschaft für Hochtemperaturwerkstoffe, Düsseldorf (2008).

[20] P. Mayr, I. Holzer, B. Sonderegger, H.H. Cerjak, *Werkstoffentwicklung zur Effizienzsteigerung in der Energieerzeugung als aktiver Beitrag zur CO_2-Reduktion*, in: 6. Werkstoffkongress - Optionen für Energieeinsparung und Energieerzeugung, Leoben (2008).

[21] E. Kozeschnik, B. Sonderegger, I. Holzer, H.J. Rajek, H.H. Cerjak, *Computer Simulation of the Precipitate Evolution during Industrial Heat Treatment of Complex Alloys*, Materials Science Forum 539-543 (2007) 2431-2436.

[22] H.H. Cerjak, G. Dimmler, I. Holzer, E. Kozeschnik, P. Mayr, C. Pein, B. Sonderegger, *Development and Improvement of 9-12% Cr Steels by a Holistic R&D Concept*, Materials Science Forum 539-543 (2007) 2954-2959.

[23] E. Kozeschnik, I. Holzer, B. Sonderegger, *On the Potential for Improving Equilibrium Thermodynamic Databases with Kinetic Simulations*, Journal of Phase Equilibria 28 (2007) 64-71.

[24] I. Holzer, E. Kozeschnik, H.H. Cerjak, *Precipitation strengthening in modern 9-12% Cr steels - a numerical approach*. in: Proceedings of Symposium on Heat Resistant Steels and Alloys for USC Power Plants 2007, Korea Institute of Science and Technology, Seoul (2007), 105-113.

[25] P. Mayr, I. Holzer, F. Mendez Martin, E. Kozeschnik, H.H. Cerjak, *Weldability study of boron containing 9% chromium steels*, in: E. Strang, G.M. McColvin, W.M. Banks, R.W. Vanstone, J.E. Oakey (Eds.), Proceedings of the 7th International Charles Parsons Turbine Conference - Power Generation in an Era of Climate Change, IOM Communication Ltd., London (2007), 417-426.

[26] H.H. Cerjak, B. Sonderegger, E. Kozeschnik, H.J. Rajek, I. Holzer, P. Mayr, C. Pein, *Abfall der Zeitstandfestigkeit bei langen Zeiten*, in: Das 600-Grad-Kraftwerk: Die aktuellen Abwertungen bei hochwarmfesten Stählen und deren Konsequenzen für Auslegung und Bau hochmoderner Dampfkraftwerke, Gelsenkirchen (2006).

[27] H.H. Cerjak, B. Sonderegger, I. Holzer, E. Kozeschnik, C. Pein, G. Dimmler, G Kothleitner, S. Mitsche, *Einfluss langer Betriebszeiten auf die Mikrostruktur und das Zeitstandverhalten*, in: 32. MPA Seminar Werkstoff- & Bauteilverhalten in der Energie- & Anlagentechnik, Materialprüfungsanstalt Universität Stuttgart, Stuttgart (2006), 19.1-19.23.

[28] I. Holzer, J. Rajek, E. Kozeschnik, H.H. Cerjak, *Simulation of the Precipitation Kinetics During Heat Treatment and Service of Creep Resistant Martensitic 9-12% Cr Steel*, in: Materials for Advanced Power Engineering 2006, Forschungszentrum Jülich GmbH, Jülich (2006), 1191-1198.

[29] I. Holzer, J. Rajek, E. Kozeschnik, H.H. Cerjak, *Simulation of the precipitation kinetics during heat treatment and service of creep resistant martensitic 9-12% Cr steel*. Materials for Advanced Power Engineering 2006, Liege, Belgium (18.09.2006).

[30] H.H. Cerjak, N. Enzinger, E. Kozeschnik, I. Holzer, Y. Ghanimi, R. Vallant, S. Baumgartner, P. Mayr, *Activities in the field of joining at TU Graz*, in: Q. Chen, Y. Zhou D. Du, A. Wu, H. Zhao, B. Chang (Eds.), Frontiers of Welding and Joining ,Peking (2005), 37-58.

Acknowledgement

Abstract

Modern martensitic 9-12% Cr steels are alloys with excellent mechanical properties even at elevated temperatures. The high temperature strength of these materials is inevitably related to their complex microstructure in the 'as-received' condition. Due to diffusional processes however, this microstructure changes during high temperature service, which leads to a decrease in strength. To identify the impact of changing microstructure on the mechanical properties of an investigated material, a new methodology to model strengthening in steel is developed and presented in this dissertation. A microstructure-property link is formulated with focus on the precipitate and solid solution hardening effect. Also, additional strengthening effects, i.e. from the grain and subgrain structure, as well as dislocation strengthening are critically assessed. The developed strength module is applied on a two-component Fe-Cu alloy with 1.4at.% Cu and a complex 11% Cr steel (COST E2) to determine the evolution of the lower yield stress or rather 0.2% proof stress of these alloys. For different heat treatments, the numerical results are compared with experimental results. The numerical simulation shows excellent agreement in the case when all operative strengthening mechanisms are duly considered. Furthermore, the role of precipitates on the creep rupture strength evolution in martensitic steels is critically discussed based on two numerical studies on the potential of heat treatment optimization to increase creep strength and precipitation reactions during service. It is shown that the evolution of precipitation parameters, i.e. size and number density of the second phase particles, significantly influences the evolution of the overall creep strength. For this, the calculated precipitate back-stress is compared to the creep rupture strength of the investigated alloys. The experimental results can be reproduced in a comprehensive and consistent manner by the numerical simulations using the software MatCalc.

Contents

1 Introduction

Martensitic 9-12% Cr steels are mainly used for large scale components in modern thermal power plants. This type of steel is characterized by a low price by still acceptable oxidation resistance and good mechanical properties at elevated temperatures compared to Ni- or Co-based Super alloys or austenitic steels. The high strength of these steels originates from their complex ferritic/martensitic microstructure with high dislocation density, fine subgrain structure and dense distribution of different types of precipitates.

Although these materials show excellent mechanical properties in the initial stage of service, after long term application at elevated temperatures, a change of these properties can be observed. Due to the ongoing diffusion processes, substructure coarsening with simultaneously growth, coarsening and sometimes dissolution of precipitate populations can be observed. This leads to a remarkable change in the mechanical properties, which represents the main limiting factor in the temperature applicability of the material and, thus, in the efficiency increase of the whole thermal power plant. This topic is schematically illustrated in Figure 1.1.
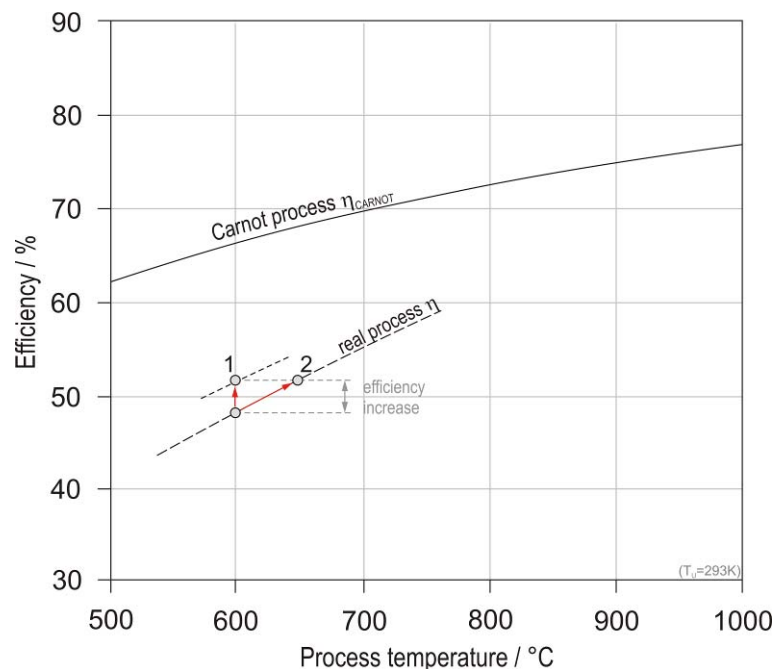
Figure 1.1. Schematic illustration of possibilities of efficiency increase of thermal power generation compared to the Carnot efficiency as ideal process. The first possibility (1) represents an improved thermodynamic design. The second possibility (2) shows the potential of improved heat resistant materials.

The figure shows the possibilities of efficiency increase of a defined thermal cycle compared to the efficiency of the ideal Carnot cycle, which is only influenced by the process inlet and outlet temperatures. Generally, the efficiency of a thermal cycle can be increased in two ways[1]. First is an improvement in the thermodynamic design, e.g. reduction of losses within the process or optimized flow-geometry in the turbine. The second possibility is the application of improved heat resistant materials for the power plant components to increase service temperature. Since the efficiency of thermal turbomachinery is almost maximized, development of improved heat resistant materials appears as practicable way to assure a continuous efficiency increase. Thus, a huge effort towards material development has been undertaken in the past 25 years, carried out in several international research projects, such as e.g., the activities within the European COST Group[*]. A detailed overview of the different international research activities on the topic of material development for thermal power plant application is given in ref.[2].

Within this European cooperation during the last decades, many experimental as well as numerical investigations were carried out at the Institute for Materials Science and Welding (IWS) to identify the key mechanisms operating in these materials and to finally optimize the processability and mechanical properties of the alloys. In this context, especially, numerical modelling of microstructural evolution and long term creep behaviour became an important working field at the IWS. Also this work can be seen as part of these simulation efforts.

The present work applies a new methodology to model strengthening in steel on the basis of the microstructural parameters, e.g. precipitate radius and number density, as well as the chemical composition of the considered phases. To determine these magnitudes of influence as well as their evolution during different heat treatment patterns, the software MatCalc is used. The applicability of this numerical model to simulate precipitation kinetics in complex alloys was already shown by several researchers[3-5].

The present thesis is structured in a first part, where application of modern martensitic 9-12% Cr steels is outlined, focusing on the microstructural characteristics and evolution during long term service. The basic strengthening mechanisms in these steels are discussed and a short introduction to thermodynamic modelling and simulation is given in this section.

---

[*] European Cooperation in Science and Technology

In the second part of the work, the developed approach to model strengthening in steel is documented focusing on the influence of the precipitate and solid solution hardening effect, considering the conditions in multi-component, multi-phase, multi-particle alloys. Several applications of different alloying systems are shown and critically discussed in the third part of the work.

2 Objectives

Objective of the present thesis is the development of a new methodology to model strengthening in steel, taking into account the microstructural evolution during heat treatment and service. In the present work, a microstructure-property link is formulated with focus on the precipitate and solid solution strengthening effect to evaluate the effect of an evolving microstructure on mechanical properties. Thus, the introduced model is implemented in the software MatCalc, which was further utilized to calculate the microstructural evolution as a function of chemical composition and heat treatment pattern of the investigated alloys.

The strengthening model is formulated and verified, in a first step, for a two-component Fe-Cu alloy with 1.4at.% Cu. For isothermal ageing at 500°C, the evolution of the lower yield stress was determined and compared to experimental data from literature.

In a second step, the model is applied on complex ferritic/martensitic 9-12% Cr steels. Based on the results of the kinetic simulations, the evolution of the total precipitate back-stress as well as the precipitate back-stress of each single phase is evaluated and correlated with the overall creep strength of the investigated 11% Cr steel CB8. Furthermore, the influence of varying heat treatment parameters (austenitising as well as tempering time and temperature) on the creep strength of the 10% Cr steel E2 is studied. It is shown that the creep strength degradation of the investigated alloys can be consistently represented by the calculated precipitate back-stress evolution.

Finally, based on the present strengthening model, a simulation approach to calculate the 0.2% proof stress ($\sigma_{0.2}$) of martensitic steels is outlined. For the 11% Cr steel D1, $\sigma_{0.2}$ is determined and compared to the experimentally determined values.

With the introduced strengthening model, a step forward is aspired to the long-run aim of a materials development approach mainly based on numerical simulation methods, saving time as well as costs for further efforts in material development and optimisation of production and fabrication procedures.

3   Literature Review

3.1   Martensitic 9-12% Cr steels for power plant application

Fossil fired thermal power plants supply, and further will supply in the next decades, the major part of total world's electricity needs[6,7]. The expected growing demand and the inevitable requirement in reduction of environmental emissions, thus makes high efficiency low emission coal fired power plants to a main-pillar in electric energy supply.

   The most direct and economic way to increase the efficiency of a coal fired steam power plant is to increase steam temperatures and pressures. Therefore, power plant technology was developed during the last decades shifting live steam conditions from the 'sub-critical' state beyond the critical point of water (374.4°C, 221.2 bar) to the so-called 'supercritical' (SC) and 'ultra-supercritical' (USC) state. This led to higher requirements for the used materials due to increasing steam temperature and pressure, as shown in Figure 3.1. The relation between evolution of unit parameters and net plant efficiency is illustrated in Figure 3.2.
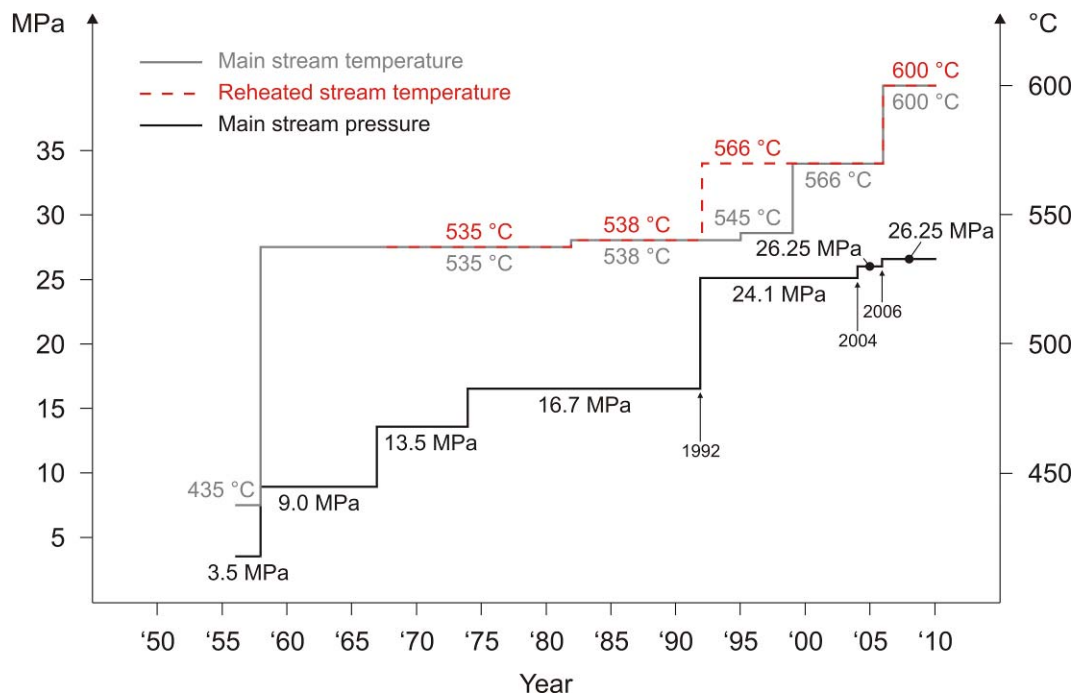
Figure 3.1. Evolution of unit parameters (temperature and pressure) during the last decades.[8]
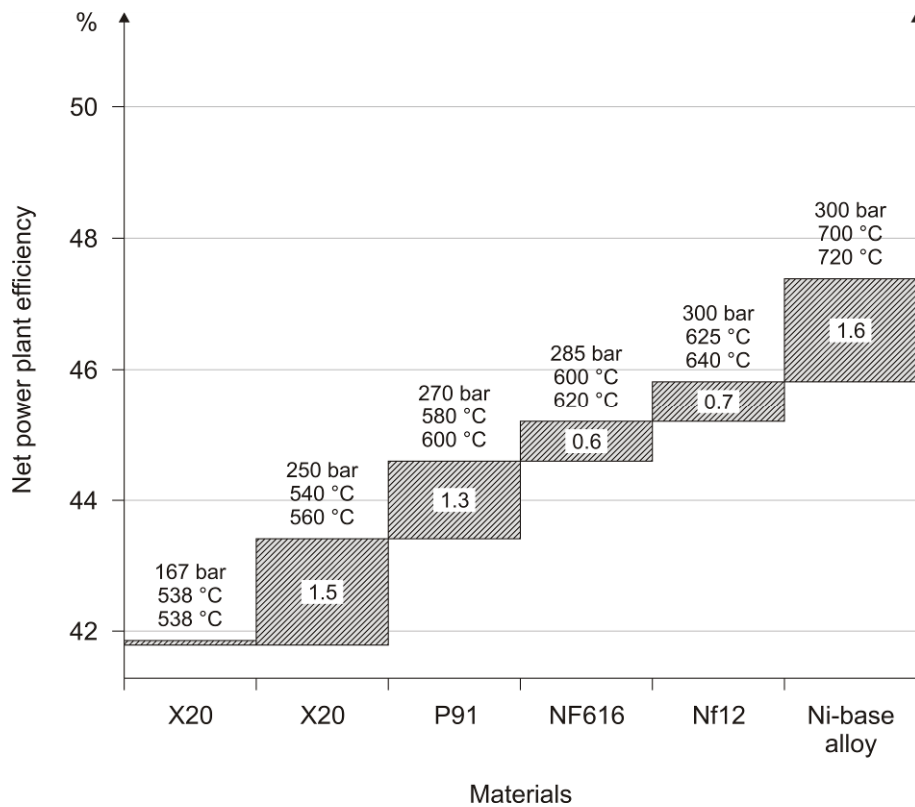
Figure 3.2. Connection between unit parameters (temperature and pressure)
and net power plant efficiency.[7]

The requirements for heat resistant materials used in thermal power plants are primarily geared to dependable and economic power plant operation. Thus, materials development and testing must be aligned to the following conditions[13]:

- operational capability in the medium and peak load ranges of power generation,
- high cost effectiveness during production and service of the power plant components,
- short manufacturing and maintenance periods,
- operating times of at least $2 \cdot 10^5$ hours.

Therefore, for high temperature materials applied in thermal power plants, it is required that following properties are implied[13]:

- high ductility under creep conditions,
- high fracture toughness,
- satisfactory properties in terms of casting, forging, hot forming and welding,

- high oxidation resistance at elevated service temperatures,
- superior long term creep rupture strength exceeding creep rupture times of 10^5 hours, characterized by the creep rupture strength of 100MPa after 10^5 hours.

Basically, four groups of materials are currently used for high temperature components in thermal power plants[2]. Dependent on application conditions, low alloyed steels, martensitic 9-12% Cr steels, austenitic steels and Ni- or Co-based superalloys are applied. Low alloyed steel grades are used in sub-critical units with relatively low steam temperatures and pressures for e.g. heat exchangers and piping systems[9], plates for boilers and pressure vessels[10] or small forgings for steam turbines. The most known representatives of this steel group are the 0.13C-1%Cr-0.5%Mo and the 0.1%C-2.25%Cr-1%Mo steels characterized by a ferritic/bainitic microstructure typically observed in low chromium steels[11-13].During the last 15-20 years, new low-alloyed heat resistant steels have been developed for lower stressed components (e.g. water walls) in SC and USC plant components. One representative is the low C-2.25%Cr-1.6%W-V-Nb grade. The increase in creep strength is mainly achieved by the combination of solid solution hardening with W and (V,Nb)C dispersion hardening in a fully bainitic matrix[14]. The typical temperature range up to where low-alloyed steels are used is about 550°C, as schematically illustrated in Figure 3.3.
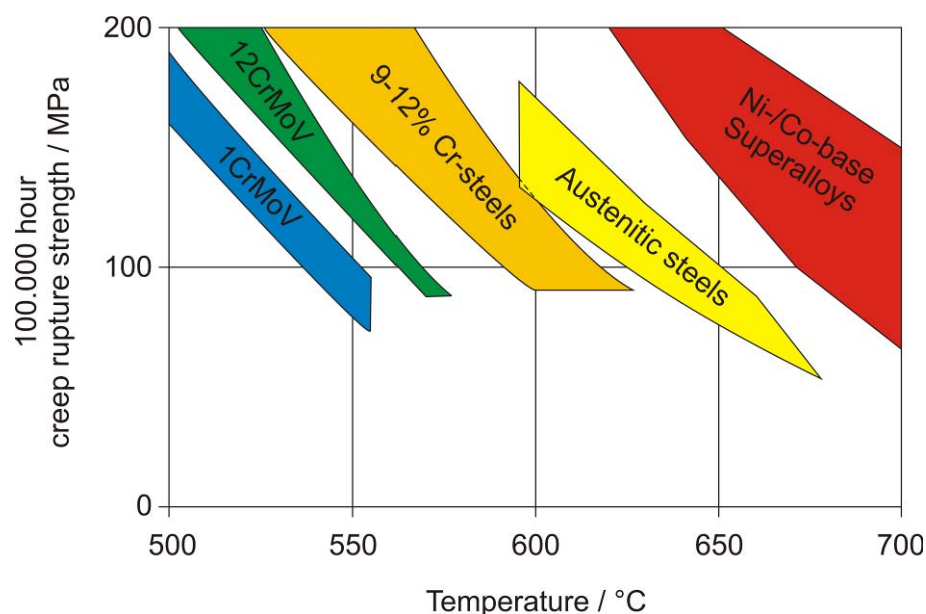
Figure 3.3. Schematic illustration of application range of power plant materials against process temperature.

For power plant components exposed to the maximum thermal load, austenitic steels and Ni-based Superalloys are used. These materials show superior creep properties and oxidation resistance even at the highest temperatures reached in thermal power plants. Different research projects (e.g. THERMIE AD700[15] and DOE Vision 21[16]) were carried out in the past to study the application potential of these material groups for the utilization in high temperature components of new power plants operating at steam temperatures of 700°C and higher[16,17]. Typical representatives investigated in these projects are the austenitic steels HR 6W and SUPER 304H as well as the Ni-based alloy INCONEL 740 and INCONEL 617. Despite their high creep strength and oxidation resistance, the application range of these materials is limited to highly mechanically and thermally loaded components due to the high material costs as well as the disadvantageous physical properties regarding thermal conductivity and expansion.

Compared to austenitic steels and Ni-based alloys, martensitic 9-12% Cr steels show favourable properties concerning cost effectiveness as well as thermal expansion and conductivity, resulting, on one hand, in lower investment costs for power plant components and, on the other hand, in reduced thermal stresses of cyclic loaded components, compared to austenitic steels. Thus, these steel grades have been identified as a favoured group of materials for thick walled components in thermal steam power plants[18].
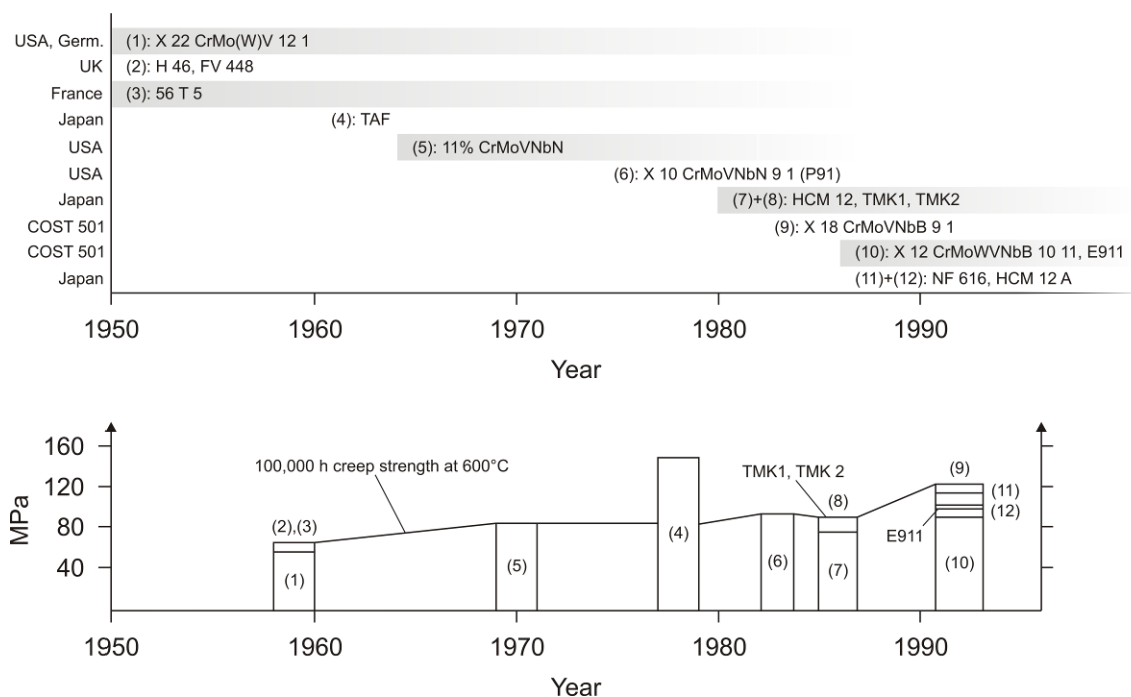
Figure 3.4. Overview of the historical development of heat resistant 9-12% Cr steels within the time range 1950-1995 and the 100,000 h creep rupture strength of these steels at 600°C.[13]

In the following, a short overview of the most important historical development steps of martensitic 9-12% Cr steels is given. A much more comprehensive overview of the historical development of 9-12% Cr steels is given by Mayer and Masuyama[13], where also Figure 3.4 is taken from.

The development of martensitic 9-12% Cr steels for power plant components started in the 1950s[18]. First alloying concepts, such as the X22CrMoV 12 1, were developed for thin-walled and thick-walled power station components. The creep strength of this material was mainly based on solid solution strengthening and precipitation strengthening by chromium carbides[13]. This steel has been applied successfully in power stations over several decades. Further developments in the optimization of the alloying concept led to the development of the TAF steel[19,20] for small components and later to the advanced pipe steel P91[13,21,22] in the 1970s. Compared to the early 12% Cr grades, the latter is mainly characterized by a lower C content of 0.10%, a reduced Cr content of 9% and additional alloying elements, such as Nb and V[13,23] leading to increased creep strength up to about 580°C[24,25] by precipitation of fine dispersed MX secondary phases[26]. This steel has meanwhile found wide application in all newer Japanese and European power stations as material for pipes and forgings. A further representative of the group of 9-12% Cr steels is the Japanese steel HCM 12, a 12% Cr steel, were high creep strength is mainly related to the duplex structure of delta-ferrite and tempered martensite and finely dispersed VN precipitates[27]. The European efforts in the field of materials development led in the 1980s to the introduction of the new steel grade X18CrMoVNbB 9 1[28]. This steel is an onward development of the TAF steel for large components with reduced contents of Cr, Nb and B and with an increase in V. A further steel grade based on the TAF steel was developed in the 1980s. The Japanese NF616 (P92) is a pipe steel with 9% Cr with creep rupture strength above 100MPa at 600°C[13,29,30]. A similar pipe steel (P122) with increased Cr content of 11% in order to improve oxidation resistance was also developed in Japan[13].

Martensitic 9-12% Cr steels are currently used up to steam parameters of 620°C and 300 bar[13,31], whereas, most estimates of upper temperature limit are about 650°C, identifying creep strength as the limiting factor[32].

Current alloying concepts in the field of 9-12% Cr steels are focused on the systematic addition of B and N to stabilize microstructure and, thus, improve creep strength at higher temperatures[2,33-35]. These steels further show an interesting welding behaviour, suppressing the formation of a fine grained zone in the heat affected zone (HAZ). Thus, this steels represent also a promising alloying concept to overcome type IV cracking, which

represents the main cause of failure of welded structures in modern thermal power plants[36,37]. For further details about this alloying concept, the interested reader is referred to Mayr[2].

A further, very new approach to increase creep strength of martensitic heat resistant steels is the development of a Z-phase strengthened steel type[38]. The basic idea of the alloying concept is the acceleration of Z-phase precipitation by a suitable chemical composition to assure fine dispersion of small stable Z-phase precipitates. It is expected that these small precipitates have the same beneficial effect on creep strength as it is usually known from the MN nitrides precipitating in these types of steel. However, experimental validation of this concept has not been achieved yet due to the short runtime of the creep tested specimens.

3.2   Strength and structure of martensitic 9-12% Cr steels

3.2.1   Microstructural characteristics during heat treatment and service

The microstructure of martensitic 9-12% Cr steels is a consequence of the complex chemical composition as well as the large-scale processing of this steel group. The chemical composition of these steels is first and foremost characterized by a relatively low amount of C and a Cr content, which ranges from 9 to 12 wt.%. Further important alloying elements are the solid solution strengtheners Mo and W, as well as V, Nb and N, which form small densely distributed second phase particles. A much more detailed discussion of alloying elements and their effect on macroscopic properties of 9-12% Cr steels is given by Hofer[39] and Schaffernak[40]. The heat treatment of martensitic Cr steels is basically characterized by a normalizing treatment in the austenite regime (usually between 1040°C and 1100°C) and several tempering cycles between 650°C and 780°C, depending on the kind of component (e.g. rotors, boiler tubes or pipes)[23]. After austenitising, during air cooling, due to the high Cr concentration, the material transforms entirely into martensite[41]. The prior austenite grains are divided into packets and further into blocks, as shown schematically in Figure 3.5 (a). The microstructure in this state is characterized by the martensitic lath structure and a high density of dislocations[42].

During the tempering treatment, the dislocation density reduces and a dislocation substructure is introduced. This subgrain structure is composed of small angle grain boundaries due to the reconfiguration of dislocations during annealing. These small angle boundaries must not be confused with martensitic lath boundaries, still present in the material, as shown by Sonderegger[43]. This author showed by EBSD measurements that there is a definite difference in misorientations between subgrains and martensite lath boundaries. Whereas misorientations of small angle grain boundaries are completely random, martensite lath boundaries show preferential axes-angle combinations. However, it is often reported in literature that martensitic lath and block boundaries are regarded as elongated subgrains[23,44].

Depending on the effective chemical composition of the material, different secondary phases precipitate during tempering, whereas $M_{23}C_6$ and/or MX carbo-nitrides are considered as main strength determining precipitate phases present in the material[13,22,23,26,33,45-51]. The Cr carbides $M_{23}C_6$ are generally located at grain and subgrain boundaries[21,22,46,52,53]. After tempering, in the so-called 'as-received' condition, $M_{23}C_6$ can

reach sizes of about 50-100 nm[21,42,44,52]. During further service at elevated temperatures, these precipitates generally show a clear tendency for precipitate coarsening[42,52]. Exceptions are the boron-alloyed steels TAF[19,20] and the COST alloy B2[28], were pronounced precipitate coarsening has not been observed even after long service times[54].
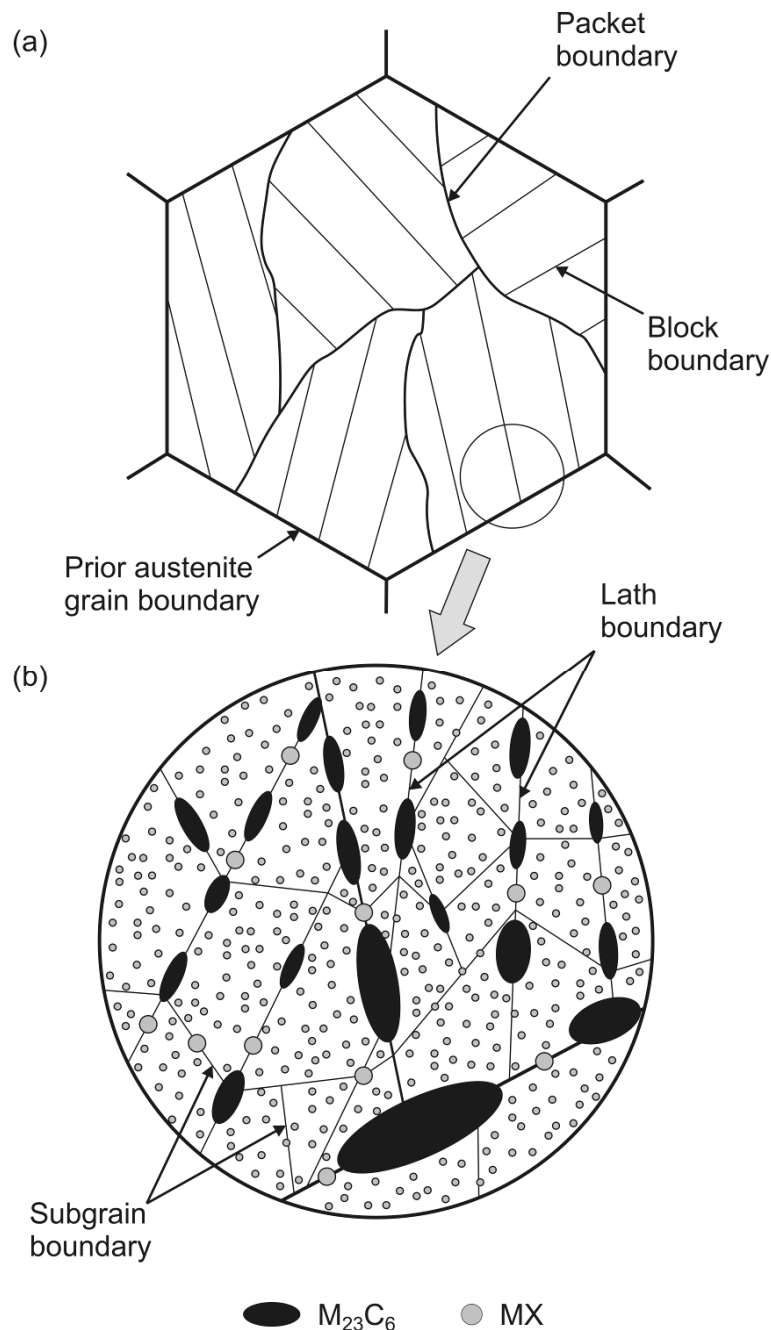
Figure 3.5. Schematic illustration of tempered martensitic microstructure of 9-12% Cr steels.

The smaller MX carbo-nitrides are commonly classified into VN and NbC[19]. However, parts of the N in VN and C in NbC can be substituted with C and N, respectively[42,55]. The

MX precipitates typically range from 20 to 50nm[42,44,52] size in the 'as-received' condition and show a much smaller tendency for coarsening as compared to the $M_{23}C_6$ precipitates[23]. Thus, the effect of these precipitates on creep strength of 9-12% Cr steels must be considered as superior over the $M_{23}C_6$ precipitates. The precipitates are located within the subgrains as well as on sub-boundaries[22,44,52]. Thus, in the 'as-received' condition, the microstructure of 9-12% Cr steels is characterized by prior austenite grains, which imply martensite lath and subgrain boundaries together with small finely distributed precipitates, as shown schematically in Figure 3.5 (b).

This microstructure state corresponds to the 'ideal' microstructure for martensitic steels with high creep strength at elevated temperatures. However, during service, this microstructure changes again. On one hand, a further decrease in dislocation density as well as martensite lath and subgrain coarsening can be observed[42,44,56]. On the other hand, a change in the precipitate microstructure can be identified. After several hundreds of hours, precipitation of Laves-phase ($Fe_2(W,Mo)$) takes place[42,57,58]. The effect of this phase on the creep strength of 9-12% Cr steels is still not completely clear. Due to the high coarsening rate of this phase and the decreasing solid solution strengthening effect by depletion of W and Mo in the matrix, precipitation of Laves-Phase was identified by several researchers as an important impact factor leading to creep strength degradation[26,42,44]. This effect however, could not be proved by a recent work of Dimmler[47,57,59], who studied in detail the precipitation kinetics of Laves-Phase in 9-12% Cr steels.
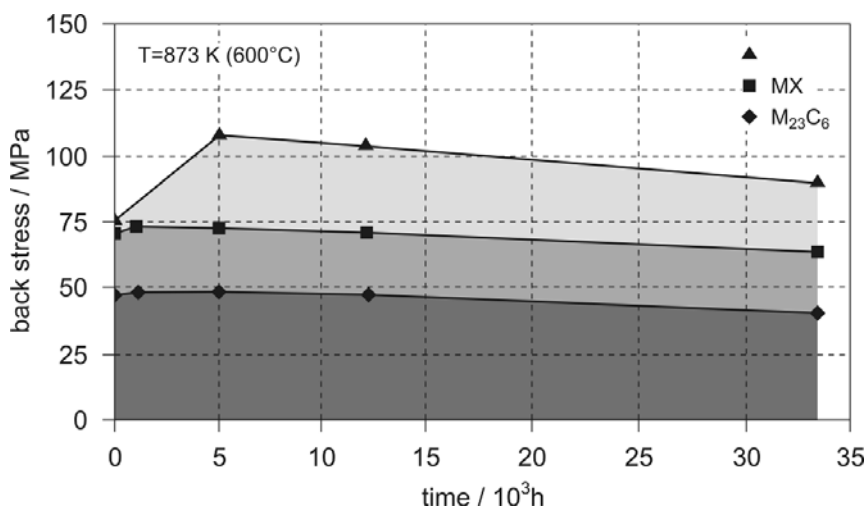
Figure 3.6. Calculated precipitate back-stress of an 11Cr-1Mo-1W steel (GX12) against creep exposure time at 600°C according to ref.[59].

Instead of a negative impact of Laves-phase on creep strength, the author showed by application of the so called 'back-stress' concept (see section 3.2.4) that Laves-phase, especially in the initial stages of service, contributes remarkably to the creep strength of the material (Figure 3.6).

With ongoing service times, after several thousand hours, an additional precipitate phase can appear in 9-12% Cr steels, the so-called modified Z-phase, a complex Cr(V,Nb)N[44,60,61,62]. The time of precipitation of this phase is mainly dependent on the service temperature and the chromium content of the material, as shown by Sawada et al.[63].
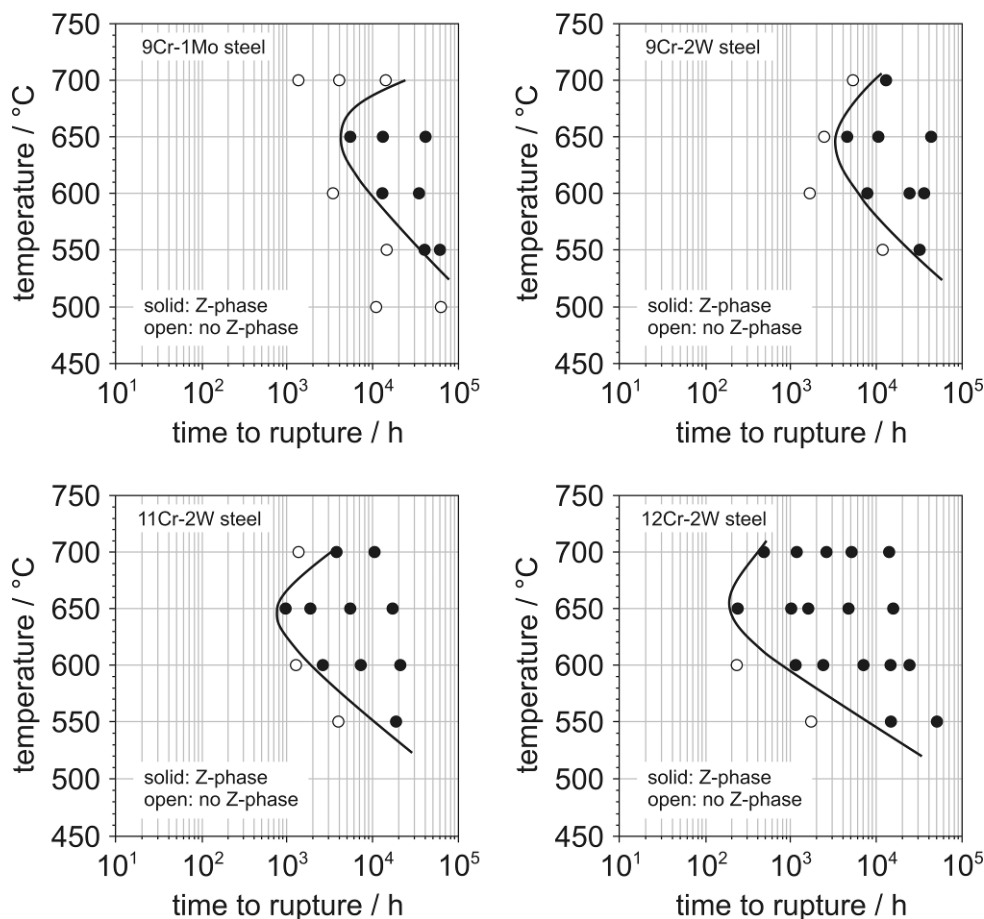
Figure 3.7. TTP diagrams of Z-phase precipitation in different 9-12% Cr steels (redrawn from ref.[63]).

From Figure 3.7, it can be seen that, the higher the chromium content of the steel, the faster precipitation occurs, which was already shown previously by Danielsen and Hald[64] by thermodynamic equilibrium considerations. Z-phase typically forms only few, large particles, which do not contribute to the overall creep strength of the material. Instead,

during nucleation, other beneficial nitrides, mainly VN, are consumed by the Z-phase precipitates, finally resulting in an observable drop of creep rupture strength[42,63] as shown in Figure 3.8. Therefore, the modified Z-phase was identified by many researchers as the main impact factor for the often observed drop of creep strength of numerous 9-12% Cr steels[23,44,63,65-67].
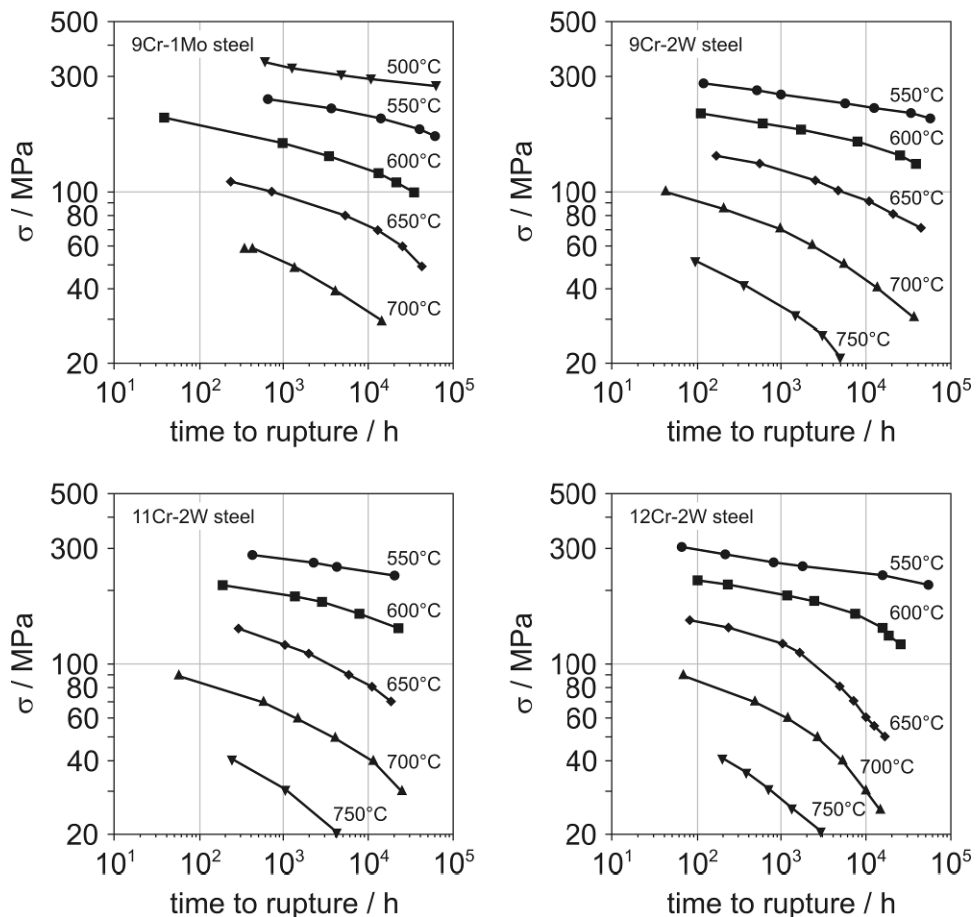
Figure 3.8. Experimentally determined creep rupture strength
in different 9-12% Cr steels (redrawn from ref.[63]).

The present section gives only a short overview about microstructural characteristics and development during heat treatment and service. The above excursions should impart a basic understanding about microstructural characteristics in 9-12% Cr steels necessary for the following chapters. For a more detailed discussion of these topics, the interested reader is referred to the works of Sonderegger[42], Danielsen[60] and Mendez-Martin[68], who studied in detail the microstructure of these alloys.

3.2.2   Strengthening mechanism

As mentioned in the previous section, martensitic Cr steel contains a multitude of different obstacles to dislocation motion. There are sub-boundaries, free dislocations within the subgrains as well as different kinds of second phase precipitates located within the subgrains and on grain and subgrain boundaries. Furthermore, solute atoms, such as Mo or W, can also effectively hinder dislocation motion and, thus, contribute to the material strength. All these structural features influence the mechanical properties of the material and can be related to the following strengthening mechanisms operative in 9-12% Cr steels[23,44,69,70]:

- Solid solution hardening
- Precipitate or dispersion hardening
- Boundary or sub-boundary hardening
- Dislocation hardening

In the following, the different strengthening mechanism are shortly discussed on the basis of 9-12% Cr steels, whereas it is assumed that the structural features determining the athermal yield stress at intermediate temperatures also control creep deformation and thus, rupture life[23].

3.2.2.1 Solid solution hardening

The strength increase by solid solution hardening (SSH) is commonly explained by atomic size and shear modulus variations due to differences between solute and solvent atoms[71,72,73].

Due to the differing sizes of the solute atoms, local strain fields are introduced, which can effectively increase the lattice resistance to deformation. The effect of atomic size differences, commonly expressed by an atomic misfit parameter δ, is defined as

$$\delta = \frac{1}{a}\frac{da}{dc},$$

(3.1)

where a is the lattice constant and c is the concentration of the solute atom in the matrix. Analogously, the shear modulus effect can be expressed as

$$\eta = \frac{1}{G}\frac{dG}{dc}, \tag{3.2}$$

where G is the shear modulus. To determine the strength increase by solid solution hardening the general formulation

$$\Delta\tau_{ssh} \sim \left(\sqrt{\delta^2 + \eta^2}\right)^m \cdot c^n \tag{3.3}$$

can be used[72]. In this equation, m is an interaction exponent between 1 and 2[71,72] and n a concentration exponent, generally between 1/2 and 1[71-78] depending on solute concentration and temperature[75].

In literature[79-85], it is also found that the first term in eq. (3.3) containing the atomic misfit parameter δ as well as the modulus mismatch parameter η and the exponent m is replaced by a constant strengthening coefficient k. Thus, eq. (3.3) reduces to

$$\Delta\tau_{ssh} = k \cdot c^n. \tag{3.3}$$

Table 3.1. Summary of different strengthening coefficients k_i in b.c.c. iron for several substitutional as well as interstitial solute elements reported in literature.

Element	Solute type*	k_i, MPa/wt.%	Ref.
Al	*sub.*	27.5	[81]
C	*int.*	1722.5	[21] in ref. [82]
		1171.3	[22] in ref. [82]
Cr	*sub.*	9.5	[81]
Co	*sub.*	12.5	[81]
Cu	*sub.*	40	[83]
Mn	*sub.*	48	[81]
Mo	*sub.*	66	[81]
N	*int.*	1722.5	[84]
Ni	*sub.*	42	[81]
Si	*sub.*	76	[81]
V	*sub.*	27.5	[81]
W	*sub.*	76	[81]
Ti	*sub.*	96.5	[81]

* *sub.* … substitutional solute element, *int.* … interstitial solute element
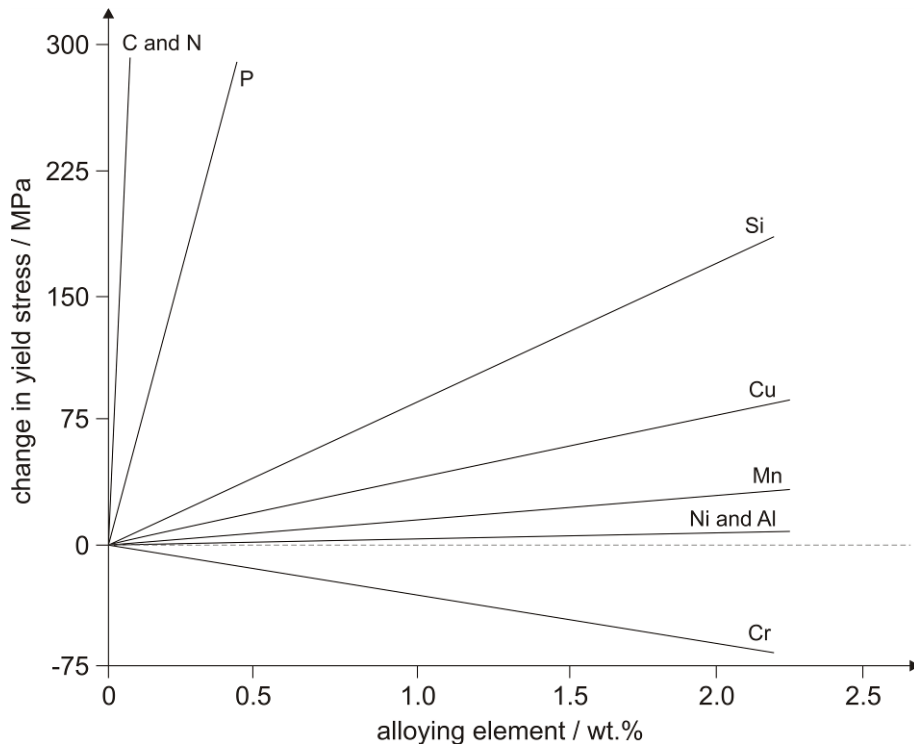
Figure 3.9. Solid solution hardening effects in b.c.c. iron of different
substitutional and interstitial solute elements in wt.%[86].

Values for the experimentally determined strengthening coefficient *k* for different alloying elements in ferrite, as well as the effect of different alloying elements on the change in yield stress in ferrite and austenite are shown in Table 3.1, Figure 3.9 and Figure 3.10.
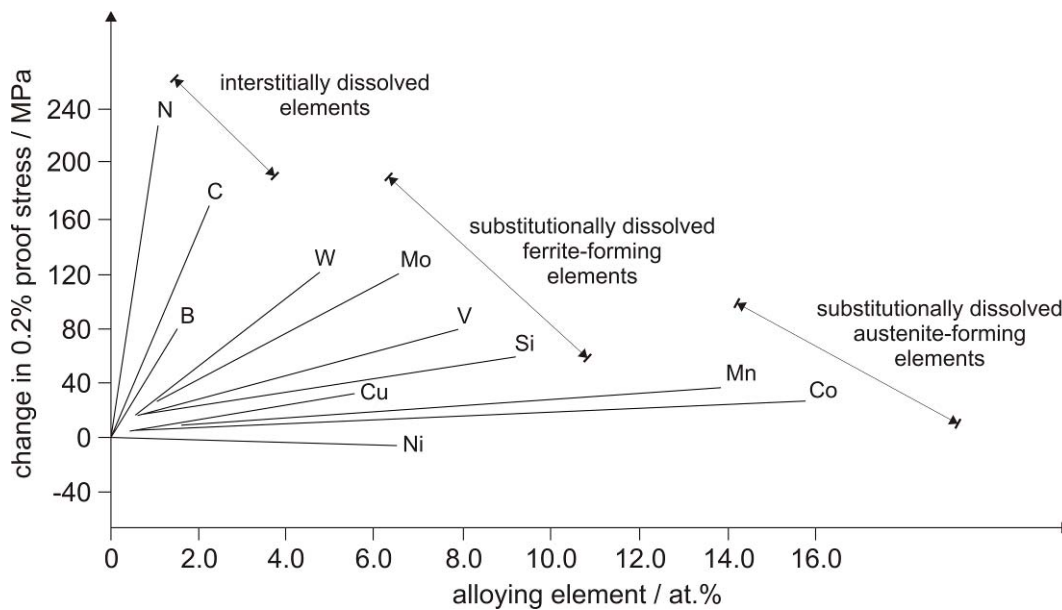
Figure 3.10. Solid solution hardening effects in austenitic stainless steel[86].

From Figure 3.9 and Figure 3.10 it can be seen that, especially the solute atoms dissolved interstitially, have a huge strengthening effect.

In the case of 9-12% Cr steels, Mo and W have been identified as most effective solid solution strengtheners due to their much larger atomic sizes compared to the size of solvent iron. In Figure 3.11, the minimum creep rate of α-Fe and solid-solution α-Fe-Mo-W alloys (FE, MH, MWH and WH) at 600°C are compared[69]. It can be seen that the minimum creep rate of the α-Fe-Mo-W alloy is three orders of magnitude lower than that of α-Fe, indicating an effective solid solution hardening effect by Mo and W.
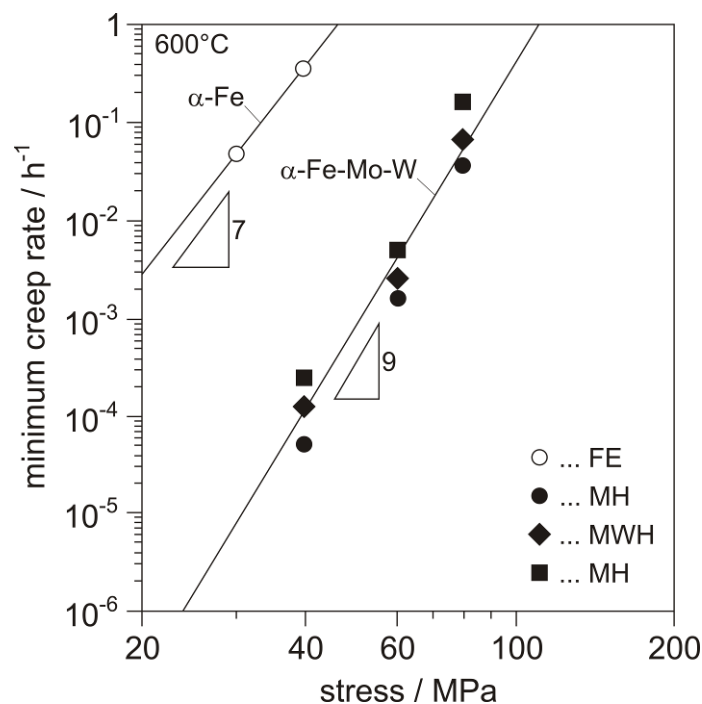
Figure 3.11. Minimum creep rate of α-Fe and solid-solution α-Fe-Mo-W alloys with a ferrite matrix[69].

Thus, it is generally accepted, that addition of Mo and W improve creep strength of ferritic/martensitic steels[19]. However, it has to be pointed out that, the strengthening effect by Mo and W due to solid solution strengthening can be reduced by precipitation of Laves-phase (Fe$_2$(W,Mo)), decreasing the solute content of Mo and W in the matrix. Such effects due to precipitation of second phase particles must be taken into account when discussing solid solution hardening in 9-12% Cr steels.

3.2.2.2 Precipitate or dispersion hardening

Precipitate or dispersion hardening is one of the most effective strengthening mechanisms in 9-12% Cr steels. To achieve sufficient strengthening by this mechanism, creep resistant steels usually contain several types of carbonitrides and intermetallic compounds such as $M_{23}C_6$, M_6C, M_7C_3, MX, M_2X and $Fe_2(Mo,W)$ Laves Phase, where M denotes a metallic element and X is carbon and/or nitrogen[44].

Second phase particles can nucleate at different locations, e.g. grain boundaries, subgrain boundaries and within subgrains. Depending on the nucleation site, two explanations on the effect of particle hardening can be given[23]:

1. Increase of creep strength by direct interaction of particles with mobile dislocations acting themselves as obstacle for dislocation motion.
2. Increase of creep strength indirectly by pinning of grain and subgrain boundaries. Thus, the initially 'ideal' microstructure state (see Figure 3.5) is retained for longer duration and microstructure coarsening is slowed down.

If the precipitates interact directly with the dislocation, several mechanism have been proposed to determine the threshold stress required for the dislocation to bypass the obstacles present in the glide plane. Due to the character of the second phase particles in 9-12% Cr steels, it was assumed by Polcik[87] that precipitates are not being cut by dislocations. Thus, depending on temperature, a dislocation can overcome a particle only by general or local climb[88] or by the so called Orowan mechanism[89]. The additional case of particle dragging at higher temperatures is not considered here, due to the apparently small contribution to creep deformation[90]. The Orowan mechanism depends only little on temperature and becomes operative at higher loads, whereas the climb mechanism determines the strain rate at higher temperatures and lower stresses.

If a dispersion of particles is intercepting the glide plane of a dislocation, a threshold stress is introduced for dislocation glide. If these particles of planar spacing λ are sufficiently strong, such that they are not cut by the dislocation, the threshold stress required to cause plastic flow is known as the Orowan stress σ_{Or}, which can be approximated as

$$\tau_{Or} = C \cdot \frac{Gb}{\lambda}. \tag{3.4}$$

In eq. (3.4), *C* is a constant, *G* is the shear modulus, *b* the Burgers vector and λ the mean spacing of precipitates in the glide plane. It can be seen that the Orowan stress is mainly determined by the inter-particle spacing λ. In Figure 3.12, the different stages of precipitate bypassing according to Orowan is shown. In a first step, when the moving dislocation encounters the obstacles, the dislocation segments between the particles start to bow out due to the acting shear stress in the glide plane (Figure 3.12 (a)). If the acting shear stress, representing the driving force for dislocation movement, is large enough to bow out the dislocation segments in a way that the segments contact themselves behind the precipitate, the dislocation segments annihilate in the contact point (Figure 3.12 (b)) and can thus move on, leaving a dislocation loop around the precipitate (Figure 3.12 (c)).
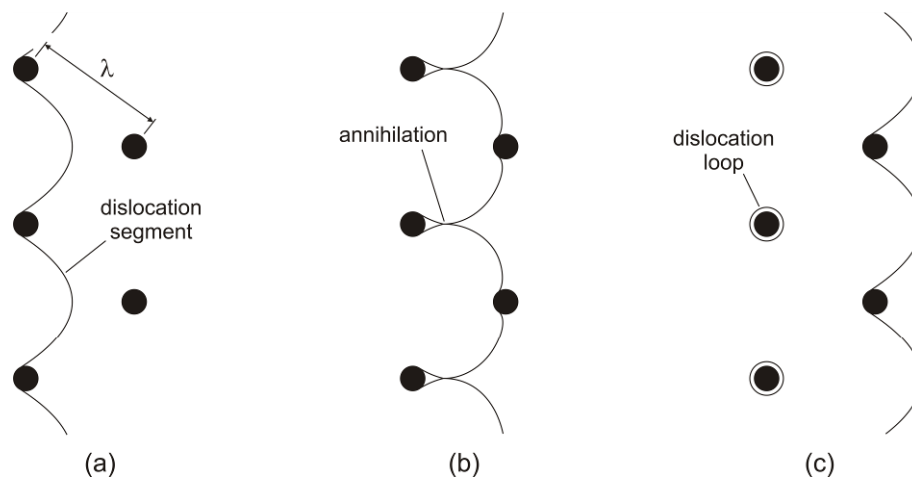
Figure 3.12. Bypassing of strong obstacles by a dislocation according to Orowan. λ denotes the mean planar spacing of precipitates[91].

At higher temperatures when diffusional mass transport is accelerated and the threshold stress σ_{Or} is not exceeded, dislocations can surmount obstacles by climb, partially extending normal to the glide plane in order to avoid the particles. Two limiting cases can be defined when discussing the dislocation climb mechanism.

On one hand, the dislocation can overcome the obstacle by local climb (Figure 3.13 (a)). In this case, the dislocation segment between the particles remains in the glide plane and the remainder profiles the particle surface as it climbs[90]. The threshold stress for local climb is determined by the stress necessary to create the new length of dislocation generated during climb and is mainly determined by the precipitate parameters[57]. The critical stress for local

climb was defined by Arzt and Ashby[88] with $0.35 \cdot \sigma_{Or}$. McLean[90] stated a value of $0.7 \cdot \sigma_{Or}$ and Dimmler[57] referred to a threshold stress in the range of $0.2...0.6 \cdot \sigma_{Or}$.

On the other hand, when general climb occurs, all of the dislocation climbs out of the glide plane as shown in Figure 3.13 (b). This climb process occurs with a smaller increase in dislocation length and leading thus to lower threshold stresses ($0.01 ... 0.1 \cdot \sigma_{Or}$[57]). However, due to the increased diffusional mass transport, general climb is intrinsically slower than the local climb mechanism[57].

<div align="center">(a)   (b)</div>
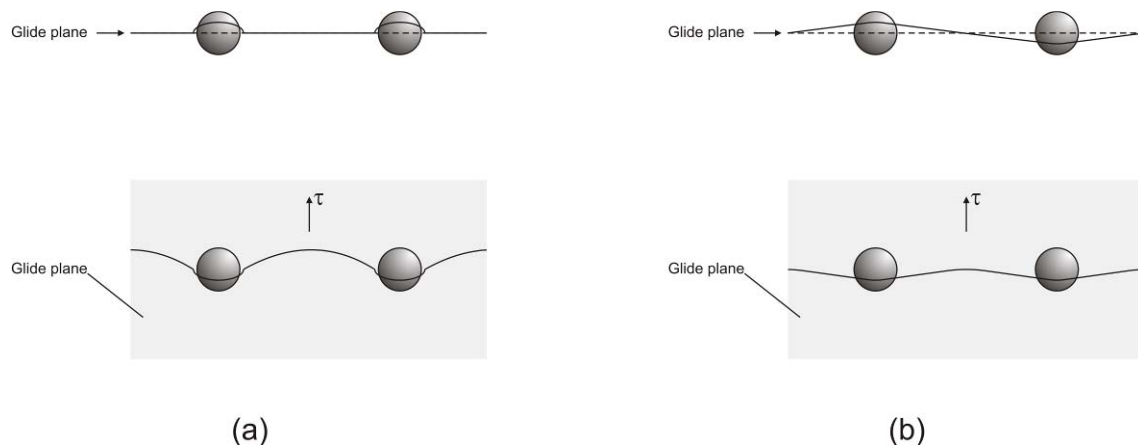
Figure 3.13. Schematic illustration of dislocation configurations perpendicular to and in the glide plane for (a) local and (b) general climb around particles.

Beside these precipitate-dislocation interactions, precipitates can further increase material strength and thus lower creep strain by effectively hinder the movement of grain and subgrain boundaries, which leads to a carbide stabilised substructure hardening[48,92-94].

This is shown in Figure 3.14, where the effect of particle pinning on subgrain boundaries is illustrated. The figure shows creep curves of 9Cr-0.1C steel having $M_{23}C_6$ particles on sub-boundaries and 9Cr-2Ni steel without particles. Both steels have the dislocation substructure typical for tempered martensite. The $M_{23}C_6$ particles obviously improve creep resistance, since they slow down the recovery of the dislocation substructure[23]. This boundary pinning effect can be explained by the model introduced by Zener and described by Smith in ref.[95]. The basic idea is that a precipitate located on a grain boundary reduces the effective grain boundary area. Thus, on leaving this particle behind, this area must be re-established. This process requires energy and thus acts against boundary migration. For a given precipitate fraction distributed on a grain boundary area, the highest pinning effect is obtained by a dense distribution of small precipitates. It was

pointed out by McLean[96] and Weinert[94] that Zener's idea of grain boundary pinning can likewise be applied also to subgrains. A numerical model for this case was derived by Sandström[97].
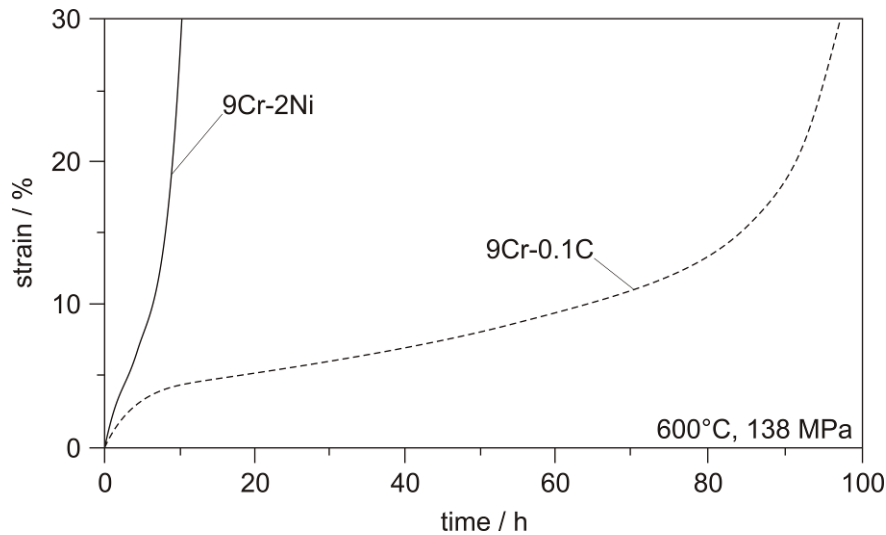
Figure 3.14. Creep curves of tempered martensitic steels with (Fe-9Cr-0.1C) and without (Fe-9Cr-2Ni) $M_{23}C_6$ particles.

The effect of precipitate hardening on the creep rates of 9-12% Cr steels is shown in Figure 3.15. The figure presents a comparison of the minimum creep rates at 600°C of an α-Fe solid solution as well as a precipitation strengthened α-Fe-V-Nb (PO) and α-Fe-Mo-W-V-Nb alloy (PSM, PSW)[69]. Compared to the α-Fe solid solution the precipitation strengthened alloys show a remarkably smaller minimum creep rate. The additional solid solution hardening effect by adding Mo and W to the PSM and PSMW alloy lowers the minimum creep rate only by about 50%, suggesting that the strengthening effect by solid solution hardening is not predominant if second phase particles are present in the material.
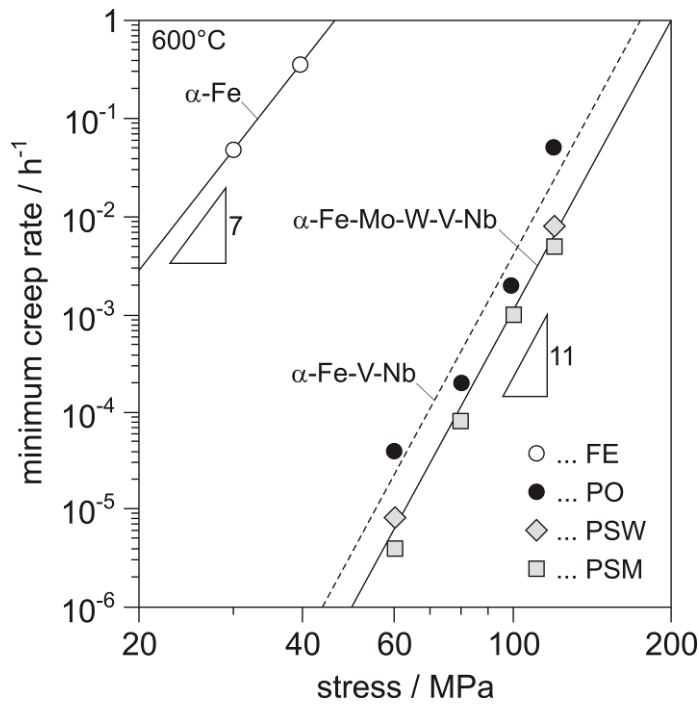
Figure 3.15. Comparison of minimum creep rate of α-Fe
and precipitation strengthened alloys[69].

3.2.2.3 Boundary or sub-boundary hardening

The strengthening effect of grain and subgrain boundaries can be explained by their obstacle effect on dislocation movement. A mobile dislocation cannot penetrate these interfaces and is thus hindered in its further movement. Thus, the smaller the grain or subgrain sizes the higher the obstacle density, the higher is the strength contribution. According to the classical Hall-Petch equation[85] the strength contribution by grain refinement can be determined according to

$$\tau_{gr} = k_{gr} \cdot d_{gr}^{-\frac{1}{2}},\tag{3.5}$$

where k_{gr} is the strengthening coefficient and d_{gr} is the grain size. In the case of 9-12% Cr steels the fraction of grain boundaries is very small compared to subgrain boundaries due to the large grain size in these materials. Thus, the contribution of strengthening by grain refinement in these steels is rather small and not further considered here.

However, the grain size-dependent strength contribution in eq. (3.5) can be also applied to determine the subgrain contribution according to Gladman[85] and McElroy and Szkopiak[98] with

$$\tau_{sgb} = k_{sgb} \cdot d_{sgb}^{-\frac{1}{2}}.$$
(3.6)

In this equation k_{sgb} is the strengthening coefficient for subgrains and d_{sgb} is the subgrain size. According to Gladman[85] k_{sgb} is usually much smaller than the coefficient for grains. Maruyama et al.[23] gives another correlation between subgrain size and strength increase. According to these authors the lath and block boundaries (in this context regarded as elongated subgrains) proved the sub-boundary hardening given by

$$\sigma_{sgb} = 10 \cdot \frac{Gb}{\lambda_{sgb}},$$
(3.7)

where G is the shear modulus, b the Burgers vector and λ_{sgb} is the short width of elongated subgrains[23,69]. After tempering, the subgrain width is in the range between 0.3-0.7 µm in martensitic high Cr steels after tempering[43,69]. This leads to a remarkable strength and led Maruyama et al.[23] to the conclusion that subgrain strengthening is the predominant effect determining the creep strength of tempered martensitic 9-12% Cr steels.

3.2.2.4 Dislocation hardening

The strength increase by dislocation hardening can be determined according to the formulation of Taylor (see e.g. ref.[23,44,84]).

$$\tau_{disl} = \alpha \cdot G \cdot b \cdot \sqrt{\rho}$$
(3.8)

The strength contribution in eq. (3.8) is a function of shear modulus G, Burgers vector b and free dislocation density in the matrix (ρ). α is a constant. Weinert[94] discussed in detail this pre-factor and showed that α can vary between 0.25 and 1 depending on the respective assumptions.

Dislocation hardening is an important means of strengthening at ambient temperatures due to the high dislocation density in 9-12% Cr steels after tempering of about $1 \cdot 10^{14} \mathrm{m}^{-2}$[69]. However, at elevated temperatures a high dislocation density enhances softening by promoting the recovery of excess dislocations and the recrystallization of deformed microstructure. Thus the dislocation density has therefore only a temporary benefit on long term creep rupture strength as it was pointed out by e.g. Abe[69].

3.2.3   Influence of microstructural changes on strengthening mechanism

Many efforts have been made to clarify the creep strength loss mechanisms in martensitic 9-12% Cr steels by characterization of the microstructural evolution[49,52,59,99-103]. It was shown that the proposed mechanism mainly relates to the impact of precipitate evolution, leading to a loss of precipitation hardening and to an accelerated coarsening of the dislocation substructure. The latter effect leads to a decrease of subgrain boundary hardening, which can be explained by precipitate coarsening on subgrain boundaries leading to a general increase of particle size and decrease of number density with service time. Therefore, the obstacle effect for sub-boundary movement, and thus substructure coarsening, can be remarkably reduced (see also section 3.2.2.2).

The loss of precipitation hardening is caused on one hand by coarsening of $M_{23}C_6$ and MX particles[69]. Thus, the strength determining inter-particle spacing λ increases (see eq. (3.4)). On the other hand, it was found that the contribution by precipitation hardening can be detrimentally influenced by dynamic precipitation of additional second phase particles during service. In this context, the effect of the Laves-phase and modified Z-phase must not be neglected. According to Abe[69], precipitation of these phases during creep exposure cause a loss of creep strength over long periods of time.

The negative effect of the Laves-phase for long term creep strength can be explained by the effect of Laves-phase precipitation on solid solution strengthening[26,42,44]. As already pointed out, W and Mo are the most effective solid solution strengtheners in martensitic 9-12% Cr steels. The solute content of these elements however, is remarkably reduced by precipitation of Laves-phase, which cannot be compensated over long time by the precipitation strengthening effect of this phase due to the relative large precipitate sizes and the relatively strong coarsening tendency[42].

Furthermore, it was reported by Lee et al.[49] that coarsening of Laves-phase particles over a critical size triggers cavity formation and the consequent brittle intergranular fracture. Figure 3.16 shows such a cavity in the vicinity of a Laves-phase particle.

After several thousand hours of creep exposure, precipitation of the modified Z-phase is often observed in martensitic 9-12% Cr steels. As reported, e.g. by Sonderegger[42], the time of nucleation correlates with an observed drop in creep rupture strength. This creep strength degradation was explained by several researches with the dissolution of the finely dispersed VN within the subgrains due to the formation of modified Z-phase[44,61]. Because

modified Z-phase forms only few large particles compared to VN, this has a detrimental effect on precipitation hardening.
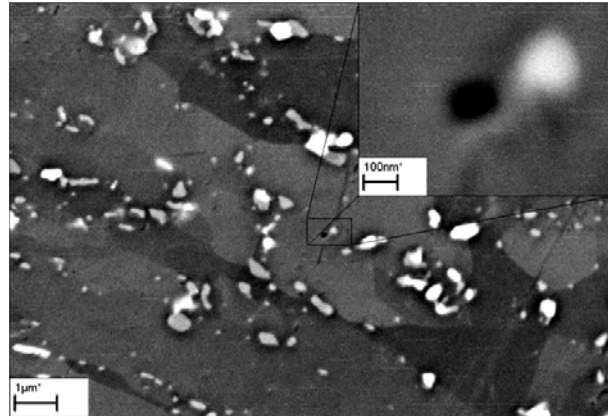
Figure 3.16. Creep cavity in the vicinity of a Laves-phase particle[57].

3.2.4 The back-stress concept

If an external force is acting on a microstructure, it is frequently assumed that the external force acts on each representative volume of the microstructure simultaneously. If the external force is high enough, plastic deformation of the material occurs via movement of dislocations and grain (subgrain) boundaries. At elevated temperatures, and if only a small external load is applied, which are conditions that are typical for creep deformation, the situation is different. In this case, part of the external driving pressure σ_e is counteracted by heterogeneous internal microstructural constituents, such as precipitates and interfaces. Consequently, not the entire external load can be assumed to represent the driving force for the creep process; only this part of the external stress σ_{ex}, which exceeds the amount of inner stress σ_i from the counteracting microstructure, effectively contributes to the creep process. Since the inner stress reduces the effect of the external stress, this approach is commonly denoted as back-stress concept. The effective creep stress σ_{eff} can be expressed as

$$\sigma_{eff} = \sigma_{ex} - \sigma_i \tag{3.9}$$

In a recent treatment by Dimmler[57], the inner stress σ_i has been expressed as a superposition of individual contributions from dislocations and precipitates. When also taking into account the contribution from subgrain boundaries, the inner stress is

$$\sigma_i = M \cdot \tau_i = M \cdot \left(\tau_{disl} + \tau_{prec} + \tau_{sgb} \right) \tag{3.10}$$

where M is the Taylor factor (usually between 2 and 3, see ref.[57]) and τ is the shear stress. The subscripts in the bracket term denote contributions from dislocations, precipitates and subgrain boundaries, respectively. When taking into account the inner stress, the general Norton creep law (see, e.g., ref.[104]) can be rewritten as

$$\dot{\varepsilon} = A \cdot \left(\sigma_{ex} - \sigma_i \right)^n = A \cdot \sigma_{eff}^n \tag{3.11}$$

where A and n are constants. When examining the individual contributions of the different mechanisms to the back-stress based on eq. (3.9), according to Taylor (see e.g. ref.[23,44,84]), the part stemming from dislocations can be expressed according to eq. (3.8).

The contribution of precipitates to the total back-stress has already been discussed in section 3.2.2.2 and it is described by the critical Orowan stress τ_{Or} (eq. (3.4)). This quantity denotes the maximum back-stress caused by a random distribution of precipitates with a mean distance λ between the precipitates. The latter can be estimated e.g. with the assumption that the mean particle distance λ commensurates indirectly with the square root of the number density of precipitates intersecting the glide plane ($\lambda \sim N^{-0.5}$[105]).

The quantity τ_{prec} represents the maximum back-stress caused by precipitates. If the external load reduced by the back-stress contribution of the other strengthening mechanisms is below this threshold, the dislocations are effectively pinned and can only pass the precipitates by the climb mechanism. Since dislocation climb is a diffusional process, the effective creep rates are usually low. If the threshold stress is exceeded, the dislocations can bypass the precipitates by the Orowan mechanism, which is a much faster process compared to climb. When this change in mechanism occurs, the exponent in the Norton creep law increases significantly and creep deformation is strongly enhanced.

Figure 3.17. Schematic illustration of the interrelationship between inner stress σ_i (substructure and particle contribution), applied stress σ and threshold stress for climb (σ_{cl}) and particle looping (σ_{Or}) according to refs.[57,106].

The selection of operative creep mechanism is mainly determined by the height of the external load, as shown in Figure 3.17. However, a transition from dislocation climb to the

Orowan mechanism can also be caused by a decrease of back-stress during service. If this transition occurs, for instance, due to coarsening of precipitates or thermodynamic instability of a precipitation strengthening phase, extrapolation of the creep strength from short term experiments to long term service behaviour can result in fatal overestimation of the residual life time of components. This aspect has been discussed in detail in refs.[57,59].

3.3   Theoretical treatment of precipitation kinetics in multi-component alloys

3.3.1   Theory of precipitation kinetics

Precipitation is a type of phase transformation where atoms agglomerate to form clusters of a new phase. The spatial extension of the new phase is usually small (few nanometres or micrometres) compared to the parent phase (micrometres or millimetres)[107].

Precipitation occurs when the solute content of alloying elements at a certain temperature exceed the solubility limit in the matrix. Then, second phase particles are formed. The life time cycle of the particles can be divided into three different stages, see e.g. ref.[107]:

(i)   Nucleation stage: The initial stages in precipitate life. Stochastic process driven by microscopic thermal and compositional fluctuations.

(ii)   Growth stage: Controlled attachment of atoms to the precipitate. Deterministic process driven by chemical and/or mechanical driving forces.

(iii) Coarsening stage: Dissolution of small precipitates in favour of larger ones. Driven by curvature-induced pressure (Gibbs-Thomson effect[108]).
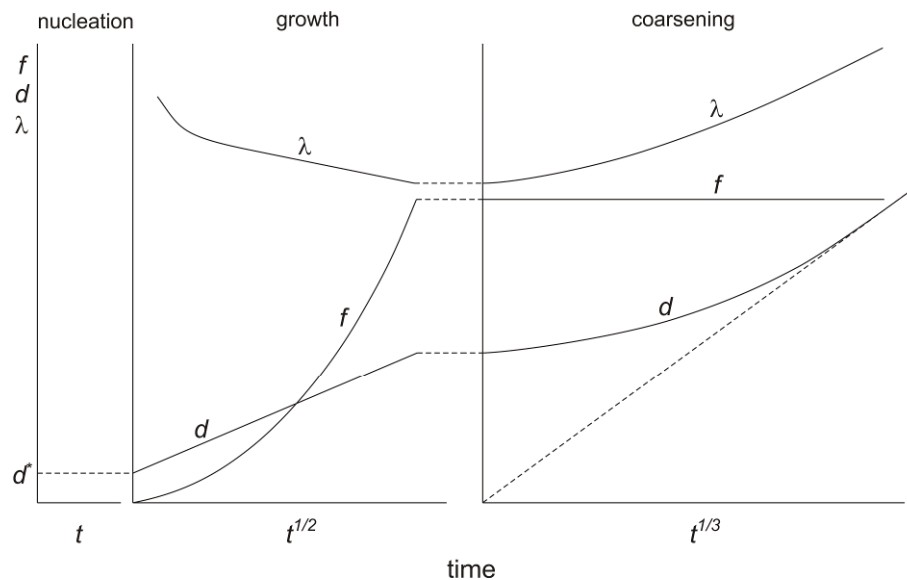
Figure 3.18. Evolution of precipitate phase fraction f, diameter d and inter-particle spacing λ against time at a temperature T[109].

The chronological sequence of the evolution of precipitate volume fraction f, diameter d and inter-particle spacing λ for isothermal annealing at a constant temperature T during the nucleation, growth and coarsening stage is shown schematically in Figure 3.18.

In the nucleation stage with an incubation time τ, nuclei of critical size with a critical size d^* are formed. After the nucleation process, the particles start to growth. This process usually follows a $t^{1/2}$ dependency. In the growth stage, the phase fraction increases until the equilibrium phase fraction at the respective temperature T is reached. When the equilibrium phase fraction is reached, precipitation coarsening follows. This stage is characterized by a further growth of large precipitates at the expense of smaller ones by nearly constant phase fraction f. The precipitate size evolution usually follows a $t^{1/3}$ dependency (Ostwald ripening).

3.3.2 Modelling multi-particle precipitation kinetics with the software MatCalc

Since the interaction of various different precipitates in different stages of thermal treatment of multi-component, multi-phase materials is rather complex, a theoretical approach has recently been developed by Svoboda, Fischer, Fratzl and Kozeschnik (SFFK model) for simulation of precipitation kinetics in these advanced alloy systems[110,111,112]. The numerical implementation of this approach in the software MatCalc is described in detail in ref.[111]. The numerical model takes into account all thermodynamic and kinetic interactions of the different alloying elements and is briefly reviewed here.

3.3.2.1 The precipitation kinetics model

Consider unit volume of a multi-component alloy. Allow an arbitrary number of spherical precipitates to nucleate and grow on random locations in this volume. The corresponding situation is sketched in Figure 3.19. The total Gibbs energy of this thermodynamic system can be written as[110]

$$G = \sum_{i=1}^{n} N_{0i}\mu_{0i} + \sum_{k=1}^{m} \frac{4\pi\rho_k^3}{3}\left(\lambda_k + \sum_{i=1}^{n} c_{ki}\mu_{ki}\right) + \sum_{k=1}^{m} 4\pi\rho_k^2\gamma_k \qquad (3.12)$$

where N_{0i} is the number of moles of component i in the matrix phase, μ_{0i} is the corresponding chemical potential, λ_k is the energy contribution due to volumetric misfit, ρ_k is the radius of the precipitate with index k, c_{ki} is the concentration of component i, μ_{ki} the corresponding chemical potential and γ_k is the precipitate/matrix interfacial energy.

In the formulation of the total Gibbs energy in eq. (3.12), each of the three terms can be related to a particular energy contribution[107]:

(i) The first term describes the Gibbs energy of the matrix by summing up the product of all moles of components N_{0i} with the corresponding chemical potentials μ_{0i}.

(ii) The second term is related to the sum of the bulk free energies of all m precipitates, where the specific quantities for the mechanical free energy contribution λ_k and the chemical free energy $\Sigma_{i=1}^{n} c_{ki}\mu_{ki}$ are multiplied with the precipitate volume $4/3\pi\rho_k^3$. The summation over k in the second term is performed over all m precipitates.
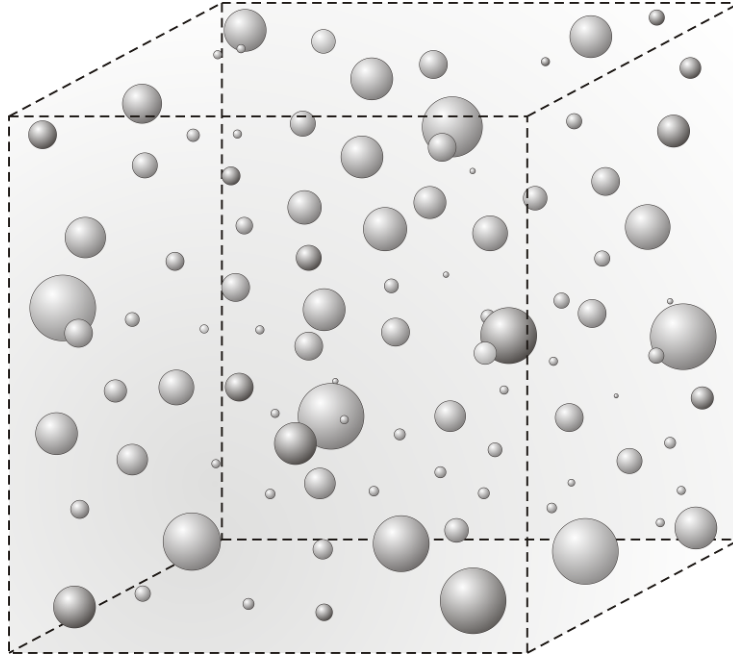
Figure 3.19. Spherical precipitates distributed randomly in a multi-component matrix.

(iii) The third term takes into account the energy contribution of the precipitate/matrix interfaces. The specific interfacial energy γ_k is multiplied by the precipitate surface $4\pi\rho_k^2$ and summation is performed over all precipitates k.

In thermodynamic equilibrium, the Gibbs free energy is a minimum. Since real systems during heat treatments are in a highly non-equilibrated state, driving forces exist for an evolution of the precipitate microstructure such that G is minimized. With each microstructural process that occurs in the system, part of the free energy is dissipated. In the SFFK model, three dissipative processes have been considered[107]:

(i) Migration of interfaces with a mobility M_k. The Gibbs energy dissipation due to interface movement can be related to the resistance against the driving pressure for interface migration which is comparable in its character to a friction force. The dissipation by interface movement can be written as

$$Q_1 = \sum_{k=1}^{m} \frac{4\pi\rho_k^2}{M_k} \dot{\rho}_k^2,$$ (3.13)

where $\dot{\rho} = \partial\rho / \partial t$ is the interface velocity, namely the growth rate of the precipitate.

(ii)   Diffusion of atoms inside the precipitates which is given by the expression

$$Q_2 = \sum_{k=1}^{m} \sum_{i=1}^{n} \int_{0}^{\rho_k} \frac{RT}{c_{ki} D_{ki}} 4\pi r^2 j_{ki}^2 dr,$$ (3.14)

where R is the universal gas constant and c_{ki}, j_{ki} and D_{ki} are the concentration, flux and diffusion coefficient of component i in the precipitate k, respectively. r denotes the particle radius $0 < r < \rho_k$.

(iii)   Diffusion of atoms in the matrix, which can be obtained assuming that the distance between the individual precipitates is sufficiently large such that the diffusion profiles of the individual precipitates do not overlap. Then, the diffusive flux inside the matrix can be expressed as

$$Q_3 = \sum_{k=1}^{m} \sum_{i=1}^{n} \int_{\rho_k}^{Z} \frac{RT}{c_{0i} D_{0i}} 4\pi r^2 J_{ki}^2 dr.$$ (3.15)

In eq. (3.15), Z is a characteristic length given by the mean distance between two precipitates and c_{0i} and D_{0i} are the concentration and diffusivity of element i in the matrix, respectively. The flux J_{ki} can be obtained applying the mass conservation law across the interface.

Thus, the total rate of dissipation is finally given as the sum of the individual contributions with $Q = Q_1 + Q_2 + Q_3$.

With the total Gibbs free energy and the corresponding dissipation terms, the thermodynamic extremal principle[113,114] can be applied and a linear system of rate equations for the change of radius and chemical composition of each individual precipitate is obtained. To determine the evolution of the entire precipitate population, the rate equations are integrated numerically under the constraint of mass conservation.

Time integration of the evolution equations is carried out based on to the numerical Kampmann-Wagner approach[115], as shown in Figure 3.20. For every time step Δt and for each precipitate phase, the growth kinetics and the change in composition are evaluated based on the evolution equations[111]. Further details about the model and the numerical treatment of the evolution equations are given by Kozeschnik[107,111].
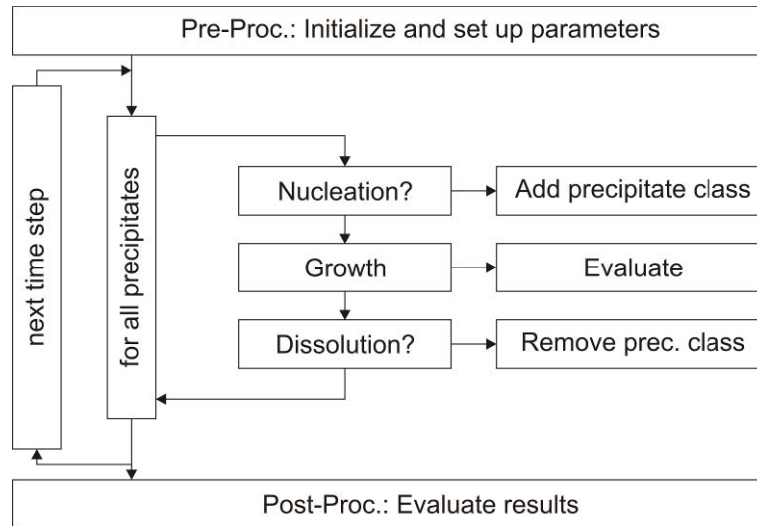
Figure 3.20. Flow chart for kinetic simulation[111].

3.3.2.2 Treatment of multi-component nucleation

The correct treatment of the nucleation stage is an essential step in modelling precipitation kinetics. In the software MatCalc, nucleation of precipitates is dealt with in the framework of an extension of classical nucleation theory (CNT). According to this theory, the nucleation rate J, which describes the frequency of creation of new precipitates in unit time and unit volume, is given as

$$J = Z\beta^* N_0 \exp\left(-\frac{G^*}{kT}\right)\exp\left(-\frac{\tau}{t}\right) \qquad (3.16)$$

where Z is the Zeldovich factor, N_0 is the number of potential nucleation sites, β^* is the atomic attachment rate, G^* is the energy barrier to form a critical nucleus, k is the Boltzmann constant, T is the absolute temperature, τ is the incubation time and t is time. Details about the different terms in eq. (3.16) are given in ref.[107].

The term 'extended' CNT emphasizes that, in multi-component systems, some quantities in eq. (3.16) must be reformulated to apply to multi-component situations. These expressions have been summarized and discussed recently by Kozeschnik et al.[116].

3.3.2.3 Linking microstructure and precipitate nucleation

Most quantities in eq. (3.16) are either thermodynamic quantities or kinetic quantities related to the diffusivity of the atoms. They are global parameters and can be obtained

from independent thermodynamic and kinetic databases. In contrast, the number of potential nucleation sites, N_C, strongly depends on the microstructure of the material and the type of heterogeneous nucleation sites, which is preferred by the particular precipitate. This feature allows for a straightforward consideration of the material microstructure, i.e. grain and subgrain size and dislocation density, in the nucleation stage of the precipitation simulation.

In order to obtain the correct number of available nucleation sites, a simple but yet realistic representation of the real microstructure is necessary. In the software MatCalc, the grain and subgrain structure of the matrix is approximated by an arrangement of tetrakaidecahedrons, which are space-filling objects with 14 surface elements, as shown in Figure 3.21. In the symmetric geometry, these objects resemble globular grains (Figure 3.21 (a)). If this structure is elongated, a good representation of martensite laths can be given (Figure 3.21 (b) and (c)).
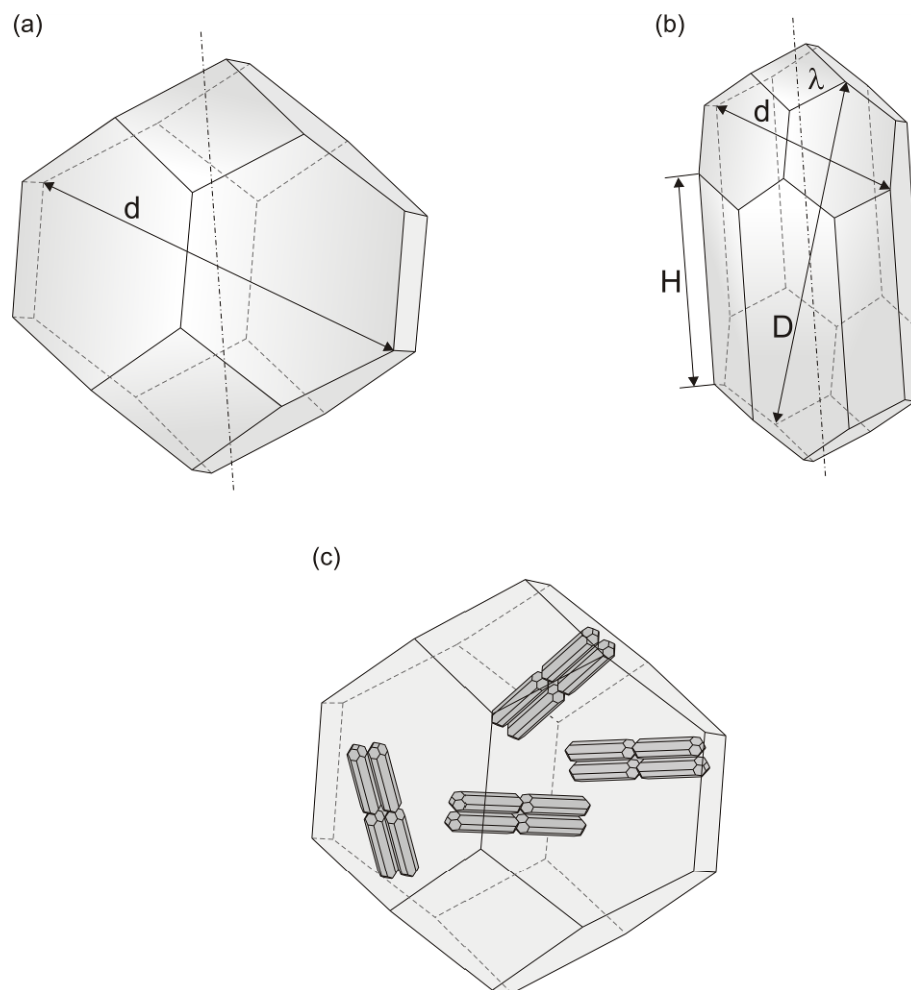
Figure 3.21. Tetrakaidechahedrons representing the matrix microstructure and determining the number of potential nucleation sites in the precipitation simulation.

Table 3.2. Number of nucleation sites per m^{-3} in a stretched tetrakaidecahedron with subgrain structure. Dislocation density in austenite is assumed to be $\rho = 10^{11}$m^{-2}, the dislocation density in ferrite $\rho = 10^{14}$ m^{-2}, the austenite and ferrite grain sizes are 100 µm and the ferrite subgrain size is 0,1 µm with an elongation factor s = D/d= 100.

Nucleation sites, m^{-3}	Ferrite (bcc) a_0=2.87 10^{-10} m a_{bcc}=2.27 10^{-10} m	Austenite (fcc) a_0=3.515 10^{-10} m a_{fcc}=2.214 10^{-10} m
Bulk (B)	8.27 10^{28}	8.37 10^{28}
Dislocations (D)	4.36 10^{23}	4.37 10^{20}
Grain boundary (GB)	7.63 10^{23}	7.70 10^{23}
Grain boundary edge (E)	5.13 10^{18}	5.15 10^{18}
Grain boundary corner (C)	1.68 10^{13}	1.68 10^{13}
Subgrain boundary (SGB)	2.00 10^{26}	/
bcc= body centred cubic, fcc= face centred cubic		

On basis of the real, experimentally observed microstructure, the number of potential nucleation sites on, e.g., prior austenite grain boundaries or subgrain boundaries, can be evaluated. The mathematical expressions for these quantities are described by Rajek[3]. Table 3.2 presents an overview of the number of potential nucleation sites at different heterogeneous lattice positions, if each atomic position is considered to represent a potential nucleation site.

3.3.3 Calculation of interfacial energy γ in complex systems

The interfacial energy γ is a most essential input parameter for precipitation simulation due to the huge impact of γ on the critical nucleation energy G^* ($G^* \sim \gamma^3$), and thus, on the predicted nucleation rate J (compare eq. (3.16)). Furthermore, the interfacial energy plays also an important role in the coarsening stage of a precipitate life.

Small variations in the interfacial energy can lead to large variations in the predicted precipitation behaviour of an alloying system, so that interfacial energy γ is often used to fit experimental results to the corresponding kinetic models[117]. In MatCalc, this quantity is estimated from thermodynamic data, which is briefly reviewed below.

The classical concept to calculate the interfacial energy of a precipitate / matrix phase boundary is the nearest-neighbour-broken-bond (NNBB) concept. This concept is based on a work of Bragg and Williams[118] who assumed that the binding energy of a crystal can be expressed as the sum of the binding energies of the neighbouring atoms. This concept was applied by Becker[119] to determine the interfacial energy of an interface. In his treatment of interfacial energies, this author assumed that the interfacial energy of a planar sharp interface (infinitely small interface thickness) can be determined as the difference of the total energy (enthalpy) of two homogeneous and two heterogeneous blocks of material of phase α and β, as shown schematically in Figure 3.22. The total energy of the respective systems is equivalent to the sum of all binding energies between neighbouring atoms.

$$\Delta H = \Delta H_\alpha + \Delta H_\beta \qquad\qquad \Delta H = \Delta H_\alpha + \Delta H_\beta + \Delta H_{\alpha\beta}$$
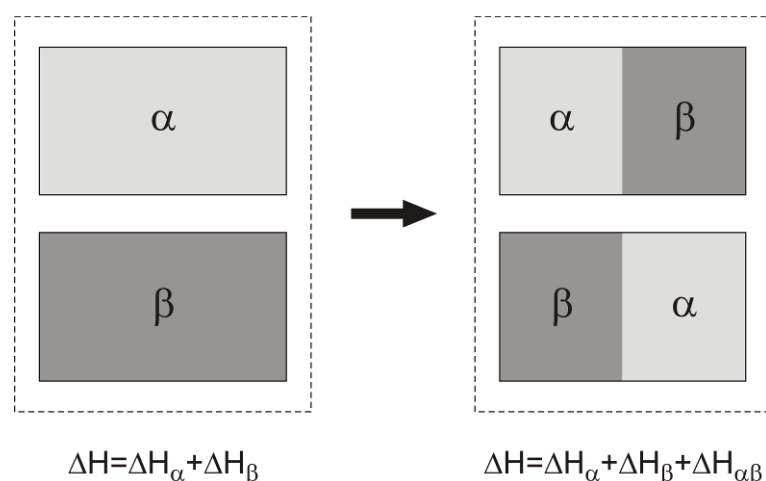
Figure 3.22. Thought experiment of Becker[119] to determine the interfacial energy γ.

Later, Turnbull[120] suggested that the sum of all individual nearest-neighbour atomic binding energies can be replaced by the enthalpy of solution ΔE_{sol}. Thus, in the NNBB concept the interfacial energy of a planar sharp interface γ_0 takes the form

$$\gamma_0 = \frac{n_S \cdot z_S}{N \cdot z_L} \cdot \Delta E_{sol} \qquad (3.17)$$

where n_S is the number of atoms per unit interface area, z_S is the number of bonds per interface atom across the interface and z_L is the coordination number of one atom.

This treatment of the interfacial has originally been derived for 2-component systems. Recently, Sonderegger and Kozeschnik[117] showed that this expression is also valid for multi-component systems without any change in the formalism. Furthermore, these authors extended the classical approach, where only interactions between first nearest neighbours have been considered, to a generalized broken-bond (GBB) approach for n-next nearest neighbours. In order to incorporate these longer distance interactions, the structural quantities z_S and z_L have been replaced by $z_{S,eff}$ and $z_{L,eff}$ to take into account also the effect of the second, third, ... to the n-nearest neighbour. In ref.[117], the structural factor $z_{S,eff}/z_{L,eff}$ is derived for up to 100 nearest-neighbour shells in fcc ($z_{S,eff}/z_{L,eff} \approx 0.329$) and bcc ($z_{S,eff}/z_{L,eff} \approx 0.328$) systems.

In the case of a large precipitate, the above formalism gives good estimates for the interfacial energy γ. However, as shown by Sonderegger and Kozeschnik[121], due to the strong precipitate size dependency of z_S, for very small precipitates, e.g. in the nucleation stage, the interfacial energy is considerably overestimated by the NNBB as well as the GBB concept. Thus, these authors introduced a size correction factor $\alpha(\rho)$ to take into account the effect of interface curvature, which reads*

$$\alpha(\rho) = 1 - \frac{6}{11} \cdot \frac{r_1}{\rho} + 0.08921 \frac{r_1^2}{\rho^2} + 0.045 \cdot \ln\left(\frac{10}{3} \frac{\rho}{r_1}\right) \cdot \frac{r_1^2}{\rho^2}. \qquad (3.18)$$

In this expression, r_1 is the nearest neighbour distance and ρ is the precipitate radius. A graphic illustration of the effect of interface curvature on the interfacial energy γ is shown in Figure 3.23. With increasing precipitate size ρ, the ratio of γ/γ_0 approximates the value

---

* Please note that the original publication [121] contains a typing error in equation (27) in the coefficient of the second term, which is supposed to read 0.08921.

of 1, resulting in no size effect for large precipitates. The grey shaded area in the figure indicates the range of typical nucleation radii with a size of 1.5 to 3 times r_1. The size correction factor α for such cluster radii varies in the range between 0.7 to about 0.85, thus strongly affecting the nucleation rate J.
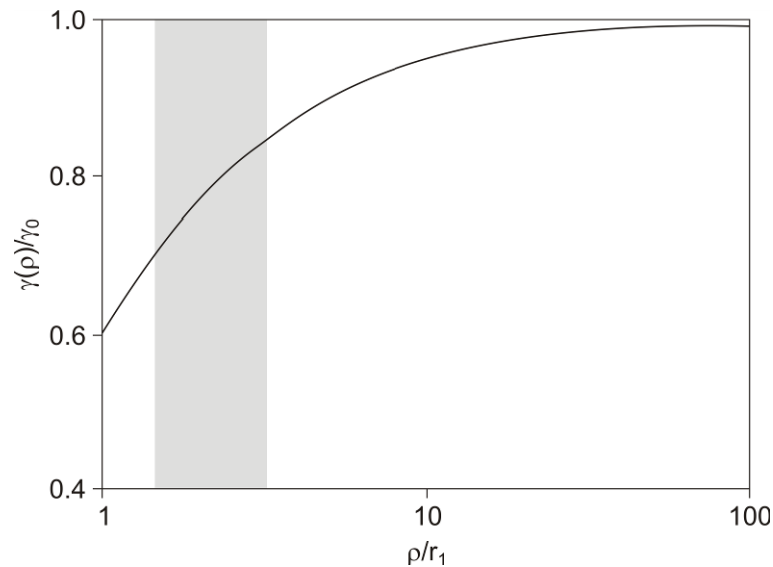
Figure 3.23. Size correction $\alpha(\rho)$ as function of precipitate size (redrawn from ref.[121]).

A further impact on interfacial energy which must not be neglected in the case of coherent precipitates is the effect of entropic contributions from finite interface thickness[122]. This effect becomes particularly prominent close to the solution temperature of the respective precipitate phases and can be considered by an additional correction factor $\beta < 1$. Thus, the interfacial energy γ can finally be written as

$$\gamma = \alpha(\rho) \cdot \beta \cdot \gamma_0 ,\qquad\qquad(3.19)$$

where γ_0 is the interfacial energy of the planar sharp interface and $\alpha(\rho)$ and β are the respective correction factors to consider the interface curvature dependency and entropic contributions from finite interface thickness.

4   Modelling of Strengthening in Steel

In the present section, the strengthening model, which has been developed and implemented in the software MatCalc is introduced and basic formulations to determine the strengthening contribution of precipitates as well as the solid solution hardening effect in multi-component alloys are developed. The most essential input parameters on the strengthening models, which is the inter-particle distance λ, are discussed and a general superposition rule for different strengthening mechanism is stated.

(a)   (b)
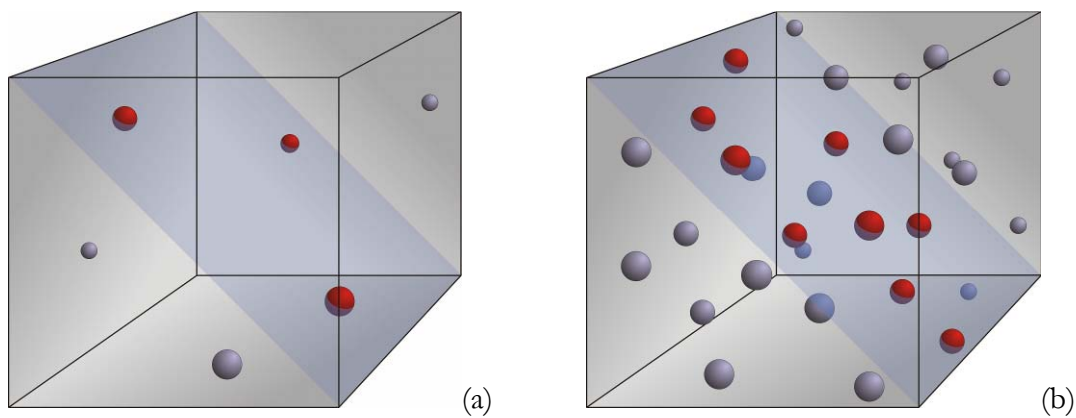
Figure 4.1 (a)-(b). Schematic illustrations of an intersected dislocation glide plane by second phase particles.

4.1   Precipitation strengthening

As already pointed out in section 3, the strengthening effect of densely distributed precipitates in a material is basically related to the obstacle effect of the precipitates intersecting the glide plane of a dislocation. This context is shown schematically in Figure 4.1 (a) and (b).

The amount of strengthening due to second phase particles generally depends on the effective number of particles intersecting the glide plane of the dislocation and, thus, on the effective inter-particle spacing. The higher the number of particles in the glide plane (Figure 4.1 (b)), the higher is the strengthening effect of the precipitates due to an increased hindering effect on dislocation movement. Independent of the nature of the dislocation-particle interaction, a higher strengthening effect in Figure 4.1 (b) compared to Figure 4.1 (a) can be expected, provided that the same dislocation-particle interaction is considered.
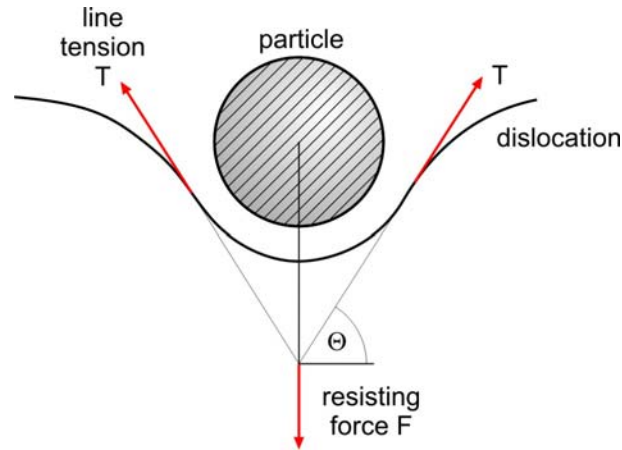
Figure 4.2. General illustration of the particle-dislocation interaction. Balance of forces acting during particle resistance to dislocation movement.

To determine the absolute value of precipitation strengthening in a solid state material, the nature of the dislocation-particle interaction must be taken into account. Basically, when a single dislocation encounters a second phase particle when moving through the glide plane of a stressed metal, the precipitate-dislocation interaction can be described in the most general form as

$$F = 2T \sin \Theta, \tag{4.1}$$

where T is the line tension of the dislocation segment and F is the resistance force of the second phase particle[123] (Figure 4.2). With increasing resistance force F, the bowing of the dislocation increases, i.e. Θ increases. Depending on the strength of the second phase particles characterized by the resistance force F, two major cases of particle-dislocation interaction can be determined for hard and weak particles.

1. <u>Hard particles:</u> If the strength (i.e. the resistance force F) of the second phase particle exceeds twice the line tension of the dislocation ($F \geq 2T$, $\Theta = 90°$), the particle will not be cut through or sheared by the dislocation. Thus, the obstacle is denoted as strong obstacle. In this case, the dislocation can bypass the precipitate either by the Orowan mechanism or cross slip. At elevated temperatures, the dislocation segment can surmount the particle also by climb, as reported in section 3.2.2.2. The particle will remain unchanged, i.e. non-deformed (Figure 4.3). The properties of the second phase particles will not affect the amount of precipitation strengthening.
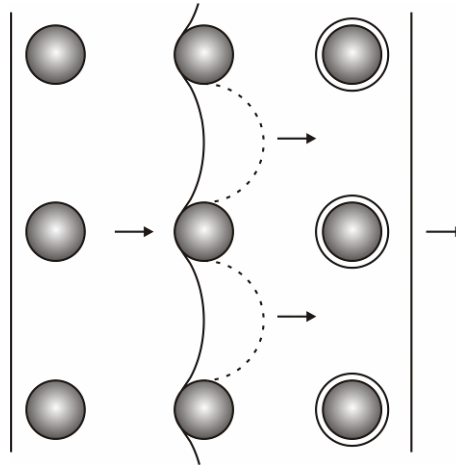
Figure 4.3. Particle-dislocation interaction for hard particles (Orowan mechanism[105]).

2. <u>Weak particles:</u> If the second phase particles are weak ($F<2T$, $\Theta<90°$), i.e. sheared by the dislocation, the particle will deform as shown schematically in Figure 4.4. The properties of the second phase particles will strongly affect the amount of precipitation strengthening and several effects may be involved in raising the stress level required for yielding related to, e.g. chemical strengthening, coherency strengthening or modulus mismatch hardening.
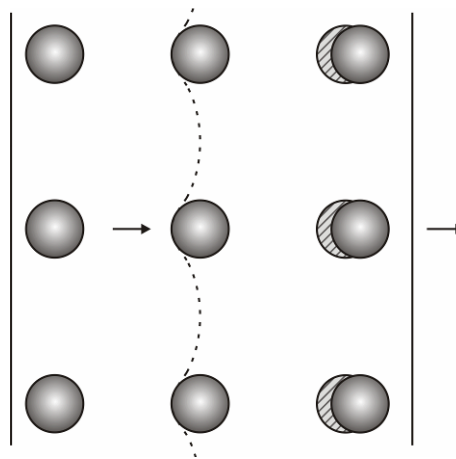
Figure 4.4. Particle-dislocation interaction for weak particles.

From this general distinction between hard and weak obstacles follows that, for a given phase fraction and particle distribution, hard particles will always give the maximum precipitation strengthening attainable. In the following, the amount of precipitation strengthening is quantified in terms of the dislocation-particle interaction for hard and weak particles.

4.1.1 Strengthening effect of hard particles

As already pointed out, in the case of hard particles, a distinct bowing of the dislocation segments between the particles can be observed due to the acting shear stress τ, operative in the slip plane.
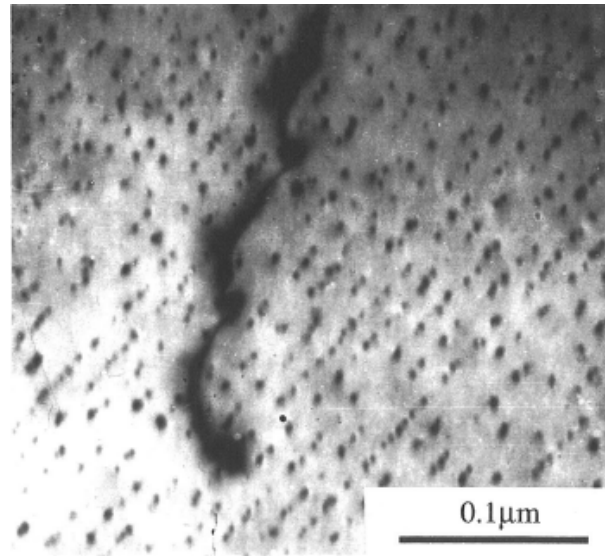
Figure 4.5. Transmission electron micrograph showing the interaction of a dislocation with the particulate array of Nb(CN).[85]

The relation between the acting shear stress τ and the radius of curvature R of the bowed dislocation segment can be determined according to Figure 4.6. The force equilibrium between acting shear stress τ and line tension of the dislocation T leads to

$$\tau = \frac{T}{b \cdot R} \, .$$

(4.2)

b is the Burgers vector, usually taken as $b \sim 0.25$nm. The line tension of the dislocation can be described by

$$T = \frac{Gb^2}{4\pi K} \ln\left(\frac{r_\mathrm{a}}{r_\mathrm{i}}\right),$$

(4.3)

where G is the shear modulus, b the Burgers vector, K is a constant and r_i and r_a are the inner and outer cutoff radius of the dislocation, respectively[124].The inner and outer cutoff radius can be interpreted as adjustable parameters, but must be in the ranges of the

dislocation core radius and the distance l between dislocations, respectively[125]. The latter can be evaluated according to $l=\rho^{-0.5}$ [124], where ρ is the dislocation density, usually in the range of $1\cdot10^{11}$ to $1\cdot10^{16}$ m^{-2} depending on the microstructure state. The constant K takes values between $K=1$ for a screw dislocation and $K=1-\nu$ for an edge dislocation, where ν is the Poisson ratio ($\nu\sim 1/3$ for metallic materials).
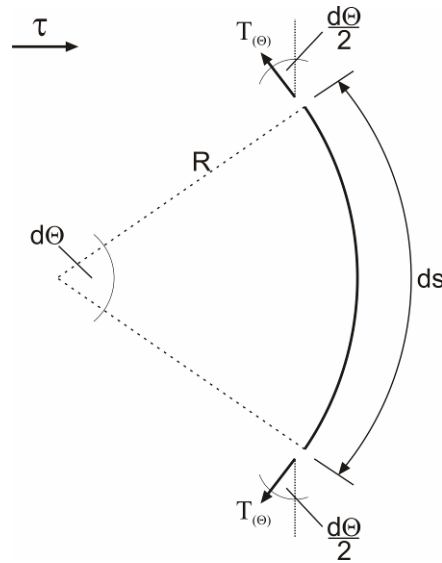
Figure 4.6. Forces on a curved dislocation line due to an acting shear stress τ.

To determine the Orowan threshold stress in a stressed metal strengthened by second phase particles, Orowan[89] assumed that the radius of curvature of the dislocation segments between the obstacles is almost equal to the half of the mean particle distance of precipitates. Orowan further assumed in his work a uniform distribution of precipitates intersecting the glide plane of the dislocation. It was shown by Kocks[126] and Foreman and Makin[127], however, that this assumption leads to an overestimation of the threshold stress in the case of randomly distributed particles. Thus, Ashby[105] reformulated the classical Orowan relationship introducing a correction factor to account for the impact of random particle distribution (Ashby-Orowan relationship). Combining eq. (4.2) and eq. (4.3), the Ashby-Orowan relationship can be expressed as

$$\tau_O = C \cdot \frac{Gb}{\lambda} \ln\left(\frac{r_a}{r_i}\right), \tag{4.4}$$

where C is a constant (C=0.051...0.073), G, b, r_i and r_a have their common meanings and λ is the mean particle distance in the slip plane.

Table 4.1. Shear moduli G and Burgers vectors b in metal matrices[123]

Matrix	G, MPa	b, nm	Slip system
Al	26200	0.286	(111)<110>
Cu	48300	0.255	(111)<110>
Fe	92600	0.248	(110)<111>
Mg	17300	0.321	(0001)<1120>
Ni	76500	0.249	(111)<110>
Ti	45600	0.295	(0001)<1120>

Table 4.2. Assumptions for the inner cutoff radius r_i reported in literature.

Autor	inner cutoff radius r_i	Ref.
Ashby	$2b$	[105]
Vollertsen	$< 3b$	[128]
Hull & Bacon	b - $4b$	[124]
Dieter	0.5-1 nm	[129]
Ardell	$b - 4b$	[130]
Arzt	$b - 10b$	[131]

G and b are characteristic values for each material and the mean particle distance λ will be discussed in section 4.1.4. A listing of shear moduli and Burgers vectors for different metallic materials is given in Table 4.1. The inner cutoff radius of the dislocation can be defined according to references in the literature (Table 4.2) and is generally assumed to be several times the Burgers vector b (r_i=1..4b).

To define the outer cutoff radius, the argumentation in ref.[105] is followed. Ashby pointed out that the critical stage of bypassing of a particle by the Orowan mechanism involves the linking up of two or more dislocation segments more or less bowed-out. Thus, attractive interactions between the segments will tend to make bypassing easier. The resulting reduction in by-passing stress can be obtained by noting that, at the critical stress, segments form a dipole with a width equal to the particle diameter. Thus, according to Ashby, the outer cutoff radius is assumed to be two times the mean particle radius. However, in the present work, this assumption is extended by the important note that, to consider the dipole width consistently, the effective mean particle radius in the slip plane must be used to determine the outer cutoff radius. According to Sonderegger[132], this radius deviates

from the mean particle radius r, because the precipitates are not generally intersected in their equatorial plane, as shown in Figure 4.7. The effective mean particle radius in the slip plane can be calculated as
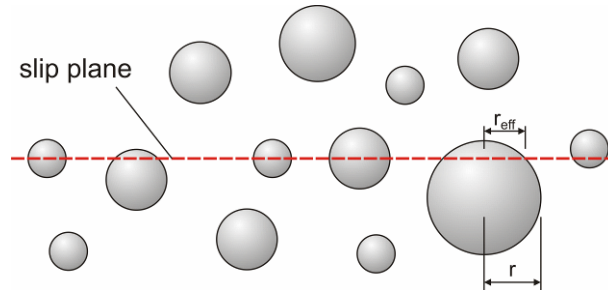
Figure 4.7. Difference between the particle radius r and the effective particle radius r_{eff} of precipitates intersecting a slip plane.

$$r_{eff} = \sqrt{\frac{2}{3}} \cdot r \,, \qquad (4.5)$$

where r is the mean particle radius of the precipitates intersecting the glide plane. Thus, the final expression to determine the strengthening effect of hard particles (Orowan threshold stress) can be rewritten as

$$\tau_O = C \cdot \frac{Gb}{\lambda} \ln\left(\frac{2 \cdot r_{eff}}{(1...4) \cdot b} \right). \qquad (4.6)$$

4.1.2 Strengthening effect of weak particles

In contrast to the strengthening effect of hard particles, where the properties of the precipitates have no influence on the strengthening contribution, for weak obstacles, the precipitate properties must not be ignored. In this case, i.e. when the particle is sheared by the dislocation, different mechanism can affect the amount of precipitation strengthening related to the respective nature of the dislocation-particle interaction. Strengthening can occur e.g. by the deformation of the particle or an increase of the particle matrix interfacial energy by production of new interface area. Further,more the passage of the dislocation through a particle can produce an antiphase boundary in the case of ordered particles, or can produce a stacking fault with its associated stacking fault energy. Another important

effect, which can be observed in precipitation hardened alloys, is the strengthening related to the strain fields around coherent precipitates, particularly in the early stages of precipitation[123].

In the present work, the strengthening effect of weak obstacles is taken into account by the following dislocation-particle interactions:

1. Interaction of the dislocation with coherent precipitates, when the precipitate is sheared and new interface area is produced (Section 4.1.2.1 Chemical hardening),
2. Interaction of the dislocation with the coherency strain field around coherent precipitates (Section 4.1.2.2 Coherency strengthening) and
3. Interaction of the dislocation with coherent precipitates with lower/higher shear modulus (Section 4.1.2.3 Modulus strengthening effect).

For a clear layout of the formulas used to determine the strengthening effect, a formulation is chosen based on the general formulation for strong obstacles according to eq. (4.4).

$$\tau_C = C \cdot \frac{Gb}{\lambda} \ln\left(\frac{r_a}{r_i}\right) \cdot f(\Theta_{crit}),$$

(4.7)

In eq. (4.7), τ_C is the critical shear stress to move the dislocation through the glide plane. The equation is, compared to eq. (4.4), extended by a term $f(\Theta_{crit})$, which accounts for the nature of the different strengthening mechanism, taking into account the reducing effect of the lower particle strength of weak obstacles compared to strong obstacles as a function of the critical angle Θ_{crit}. The critical angle Θ_{crit} defines the angle of dislocation bowing to the point where the dislocation can overcome the particle due to the acting shear stress in the slip plane ($\Theta_{crit} = 0° \dots 180°$).
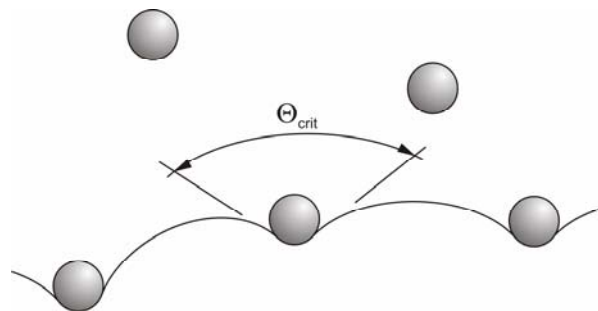
Figure 4.8. Critical angle Θ_{crit} between dislocation segments.

Thus, $f(\Theta_{crit})$ can be interpreted as the *relative* obstacle strength and it can take values between 0 and 1 (limit case of strong obstacles)[133]. The general form of eq. (4.7) can be also deduced from the classical Friedel-Brown-Ham equation[134]

$$\tau_C = \frac{2T}{b\lambda}\left(\frac{F_C}{2T}\right)^{\frac{3}{2}}.$$ (4.8)

In this equation, τ_C again is the critical shear stress, T, b and λ have their common meanings and F_C represents the obstacle strength, i.e. the strength of the precipitate. The latter term in eq. (4.8), i.e. $\left(\frac{F_C}{2T}\right)^{\frac{3}{2}}$, is equivalent to the expression $f(\Theta_{crit})$ in eq. (4.7).
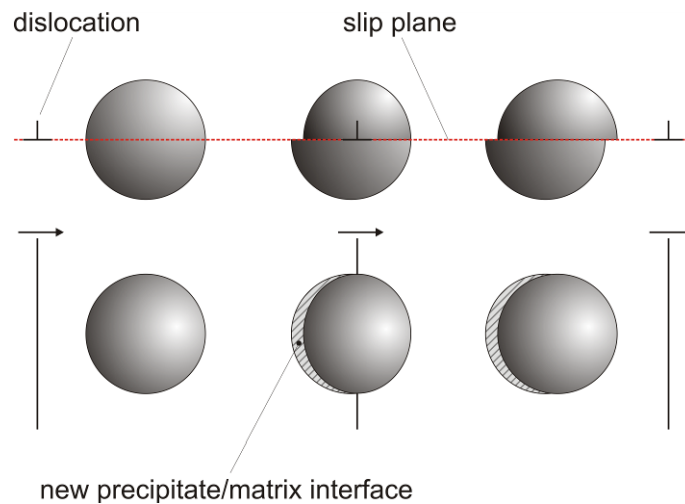
Figure 4.9. Schematic illustration of the shear process. After the precipitate is sheared by the dislocation, new precipitate/matrix interface has been created.

4.1.2.1 Chemical hardening

When a precipitate is sheared by a dislocation, precipitation strengthening occurs based on the chemical hardening mechanism. The hardening effect is caused by the production of new particle/matrix interfacial area as a result of the shearing process, as shown in Figure 4.9. Accordingly, the maximum interaction force F_C between particle and dislocation is given, according to ref.[134,135], as ($2\gamma b$), where γ is the effective interfacial energy of the precipitate – matrix phase boundary and b is the Burgers vector. If this interaction force is inserted into the general Friedel-Brown-Ham equation (eq. (4.8)), the critical shear stress τ_C can be calculated as

$$\tau_{\text{C}} = C' \cdot \frac{Gb}{\lambda} \ln\left(\frac{r_{\text{a}}}{r_i}\right) \cdot \left(\frac{\gamma b}{T}\right)^{\frac{3}{2}}.$$ (4.9)

C' is a constant (C'=0.064 ... 0.091) and G, b and λ have their common meanings. r_i and r_a are the inner and outer cutoff radius. The inner cutoff radius is defined in Table 4.2, whereas, the outer cutoff radius in eq. (4.7) is assumed to be identical to the mean particle distance λ, according to ref.[105] for low dislocation bending.

4.1.2.2 Coherency strengthening

As described by Gladman[123], in the case of coherency strain hardening, the dislocation segment interacts with the coherency strain field in the matrix around the precipitate as shown schematically in Figure 4.10. Because of different molar volumes of precipitates and matrix, a strain field around the particles is produced, resulting in an internal stress, which acts against dislocation movement.
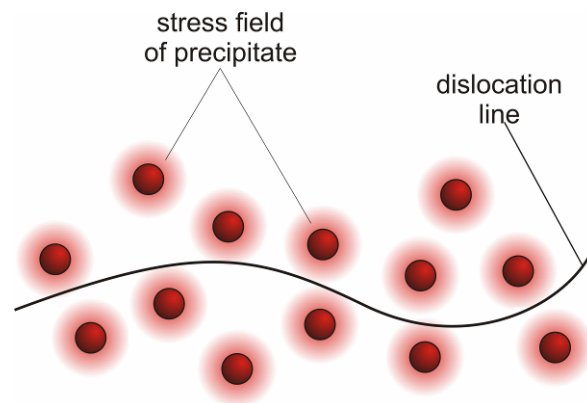
Figure 4.10. Schematic illustration of the effect of a stress field around precipitates due to volumetric misfit.

In the case of a very limited dislocation bending for small obstacles, according to Gerold and Haberkorn[136], a maximum dislocation-particle interaction force F_C=$4Gb|\varepsilon|r$ can be assumed. In this case eq. (4.7) finally takes the form

$$\tau_{\text{C}} = C' \cdot \frac{Gb}{\lambda} \ln\left(\frac{r_{\text{a}}}{r_i}\right) \cdot \left(\frac{2Gb|\varepsilon|r_{\text{eff}}}{T}\right)^{\frac{3}{2}}.$$ (4.10)

C again is a constant (C'=0.064 ... 0.091) and G, b, λ and r_i and r_a have the same meaning as in eq. (4.9). ε in this equation is the linear misfit strain, which is calculated according to

$$\varepsilon = \frac{1}{3} \frac{\Delta V}{V} , \tag{4.11}$$

where $\Delta V / V$ is the volumetric misfit between matrix phase and precipitate.

4.1.2.3 Modulus strengthening effect

If a dislocation intersects a spherical precipitate with a shear modulus G_p embedded in a matrix of shear modulus G_m, a strengthening effect occurs due to the differences in the dislocation line energies within the precipitate and the matrix. This item was first treated by Russell and Brown[137], based on the argumentation of Brown and Ham[134] and according to Foreman and Makin's[127] numerical solution for the critical stress, when a dislocation moves large distances through an array of obstacles.

$$\tau_C = 0.8 \frac{Gb}{\lambda} \left[\cos \frac{\Theta}{2} \right], \qquad \Theta \leq 100° \tag{4.12}$$

$$\tau_C = \frac{Gb}{\lambda} \left[\cos \frac{\Theta}{2} \right]^{\frac{3}{2}}, \qquad \Theta \geq 100° \tag{4.13}$$

To calculate the angle, which controls the strength (Θ_{crit}), Russell and Brown introduced a kind of Snell's Law for dislocations, equating the line energy of the dislocation in the precipitate (U_p) and the matrix (U_m) according to

$$U_p \sin \Theta_p = U_m \sin \Theta_m . \tag{4.14}$$

Θ_p and Θ_m in eq. (4.14) are the angles between the dislocation and the normal to the interface in the precipitate and the matrix, respectively, as shown in Figure 4.11.
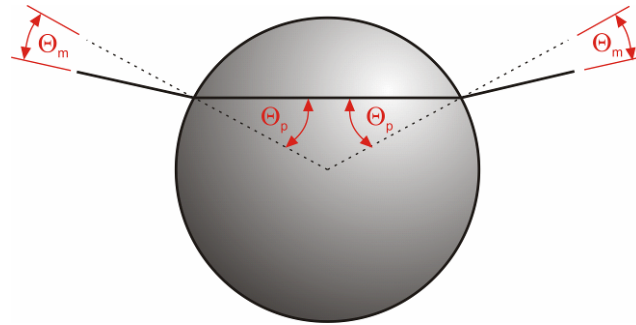
Figure 4.11. Dislocation cutting a spherical precipitate
with an elastic modulus lower than the matrix.

When the line energy of the dislocation in the precipitate is lower than in the matrix ($U_p < U_m$), τ_C becomes a maximum ($\Theta_{crit} \Rightarrow$ min.) when the dislocation is about to break away from the precipitate, as shown schematically in Figure 4.12.
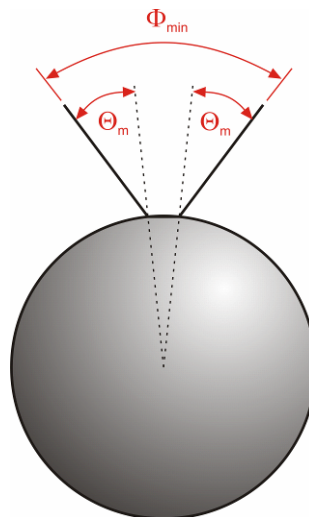
Figure 4.12. Position of dislocation arms when τ_C reaches a maximum (i.e. $\Theta_{crit} \Rightarrow$ min.) in the case when the precipitate has a lower elastic modulus than the matrix.

In this case, Θ_{crit} becomes about $2\Theta_{\text{m}}$, which is equal to the expression $2\sin^{-1}(U_{\text{p}}/U_{\text{m}})$. Thus, combined with the previous formulation for dislocation bow-out (eq (4.4)), eq. (4.12) and (4.13) can be rewritten as

$$\tau_{\text{C}} = C \frac{Gb}{\lambda} \cdot \ln\left(\frac{r_{\text{a}}}{r_{\text{i}}}\right) \cdot \left[1 - \left(\frac{U_{\text{p}}}{U_{\text{m}}}\right)^2\right]^{\frac{1}{2}}, \quad \sin^{-1}\left(\frac{U_{\text{p}}}{U_{\text{m}}}\right) \leq 50° \tag{4.15}$$

$$\tau_{\text{C}} = C' \frac{Gb}{\lambda} \cdot \ln\left(\frac{r_{\text{a}}}{r_{\text{i}}}\right) \cdot \left[1 - \left(\frac{U_{\text{p}}}{U_{\text{m}}}\right)^2\right]^{\frac{3}{4}}. \quad \sin^{-1}\left(\frac{U_{\text{p}}}{U_{\text{m}}}\right) \geq 50° \tag{4.16}$$

The variables in eq. (4.15) and eq. (4.16) are the same as defined in the previous sections. To calculate the size-dependent ratio $U_{\text{p}}/U_{\text{m}}$, Russell and Brown have suggested the following expression

$$\frac{U_{\text{p}}}{U_{\text{m}}} = \frac{U_{\text{p}}^{\infty} \log \frac{r_{\text{eff}}}{r_{\text{i}}}}{U_{\text{m}}^{\infty} \log \frac{r_{\text{a}}}{r_{\text{i}}}} + \frac{\log \frac{r_{\text{a}}}{r_{\text{eff}}}}{\log \frac{r_{\text{a}}}{r_{\text{i}}}}, \tag{4.17}$$

where r_{eff} is the effective mean particle radius in the slip plane, r_{i} is the inner cutoff radius (see Table 4.2) of the dislocation stress field and $r_{\text{a}} (=\lambda)$ is the outer cutoff radius of the dislocation stress field.

U_{p}^{∞} and U_{m}^{∞} refer to the energy per unit length of a dislocation in infinite media. The ratio $U_{\text{p}}^{\infty}/U_{\text{m}}^{\infty}$ can be determined as the ratio of the products of shear modulus and Burgers vector squared of the precipitate and the matrix, when the line energies of the dislocation in the matrix and the precipitate are given as $\frac{1}{2}Gb^2$, respectively.

Although it was previously assumed that line energy of the dislocation in the precipitate is lower than in the matrix ($U_{\text{p}} < U_{\text{m}}$), the outlined method to calculate precipitation strengthening by modulus mismatch in principle also applies to the opposite case ($U_{\text{p}} > U_{\text{m}}$)[137]. In this case, one simply inverts the ratio $U_{\text{p}}/U_{\text{m}}$ and uses eq. (4.15) and (4.16).

Table 4.3 gives an overview of the introduced formulas to determine the precipitation strengthening effect for hard and weak obstacles, as developed here and implemented in the software package MatCalc.

Table 4.3. Overview of the formulas utilized to determine the strength contribution of the different strengthening mechanism considered in the software package MatCalc. For details about the different mechanism the reader is requested to refer to the sections 4.1.1 and 4.1.2.

Strengthening mechanism	Formula	$f(\Theta_{crit})$	Comment
(General formulation)	$\tau_C = C \cdot \dfrac{Gb}{\lambda} \ln\left(\dfrac{r_a}{r_i}\right) \cdot f(\Theta_{crit})$	—	C ...constant (0.051 ... 0.073) C' ...constant (0.064 ... 0091) G ...shear module b ...Burgers vector λ ...mean particle distance (section 4.1.4) r_i ...inner cutoff radius (Table 4.2)* r_a ...outer cutoff radius* γ ...precipitate/matrix interfacial energy T ...line tension of a dislocation ε ...linear misfit strain, $\varepsilon = \dfrac{1}{3}\dfrac{\Delta V}{V}$ r_{eff} ...effective mean particle radius in the slip plane U_p ...line energy of dislocation in precipitate U_m ...line energy of dislocation in matrix
Orowan threshold stress	$\tau_O = C \cdot \dfrac{Gb}{\lambda} \ln\left(\dfrac{r_a}{r_i}\right)$	1	
Chemical strengthening	$\tau_C = C' \cdot \dfrac{Gb}{\lambda} \ln\left(\dfrac{r_a}{r_i}\right) \cdot \left(\dfrac{\gamma b}{T}\right)^{\frac{3}{2}}$	$\left(\dfrac{\gamma b}{T}\right)^{\frac{3}{2}}$	
Coherency strengthening	$\tau_C = C' \cdot \dfrac{Gb}{\lambda} \ln\left(\dfrac{r_a}{r_i}\right) \cdot \left(\dfrac{2Gb|\varepsilon| r_{eff}}{T}\right)^{\frac{3}{2}}$	$\left(\dfrac{2Gb|\varepsilon| r_{eff}}{T}\right)^{\frac{3}{2}}$	$r_{eff} = \sqrt{\dfrac{2}{3}} r$
Modulus strengthening	$\tau_C = C \dfrac{Gb}{\lambda} \cdot \ln\left(\dfrac{r_a}{r_i}\right) \cdot \left[1-\left(\dfrac{U_p}{U_m}\right)^2\right]^{\frac{1}{2}}, \quad \sin^{-1}\left(\dfrac{U_p}{U_m}\right) \leq 50°$ $\tau_C = C' \dfrac{Gb}{\lambda} \cdot \ln\left(\dfrac{r_a}{r_i}\right) \cdot \left[1-\left(\dfrac{U_p}{U_m}\right)^2\right]^{\frac{3}{4}}, \quad \sin^{-1}\left(\dfrac{U_p}{U_m}\right) \geq 50°$	$\left[1-\left(\dfrac{U_p}{U_m}\right)^2\right]^{\frac{1}{2}}$ $\left[1-\left(\dfrac{U_p}{U_m}\right)^2\right]^{\frac{3}{4}}$	$\dfrac{U_p}{U_m} = \dfrac{U_p^\infty \log\dfrac{r_{eff}}{r_i} + U_m^\infty \log\dfrac{r_a}{r_{eff}}}{U_m^\infty \log\dfrac{r_a}{r_i}}$ with $U_p^\infty = \dfrac{1}{2} G_p b_p^2$, $U_m^\infty = \dfrac{1}{2} G_m b_m^2$

* The inner and outer cutoff radius correspond to the lower and upper integration limit, when the line energy of a dislocation is calculated (see also Hull and Bacon[124]). In the case of strong obstalces (determination of the Orowan threshold stress) the outer cutoff radius is assumed as the dislocation dipole width according to Ashby[105] as $r_a = 2r_{eff}$. In the case of weak obstacles the outer cutoff radius is assumed as $r_a = \lambda$, due to the lower dislocation bowing, where λ is the mean particle distance in the slip plane.

4.1.3   The critical radius for particle looping r^*_{loop}

As generally discussed in section 4.1, depending on the obstacle strength, a dislocation can bypass second phase particles either by the Orowan mechanism (strong obstacles) or by shearing in the case of coherent precipitates (weak obstacles).

Nevertheless, also for coherent precipitates it is possible that the particle is circumvented by the Orowan mechanism. This is the case when the particles become too large and the critical stress to shear the particle exceeds the Orowan threshold stress. In this case, although the obstacle is susceptible to shear, the Orowan mechanism becomes operative. Which mechanism prevails (shearing or looping) basically depends on the particle size, characterized by the critical radius for particle looping r^*_{loop}, as shown schematically in Figure 4.13.
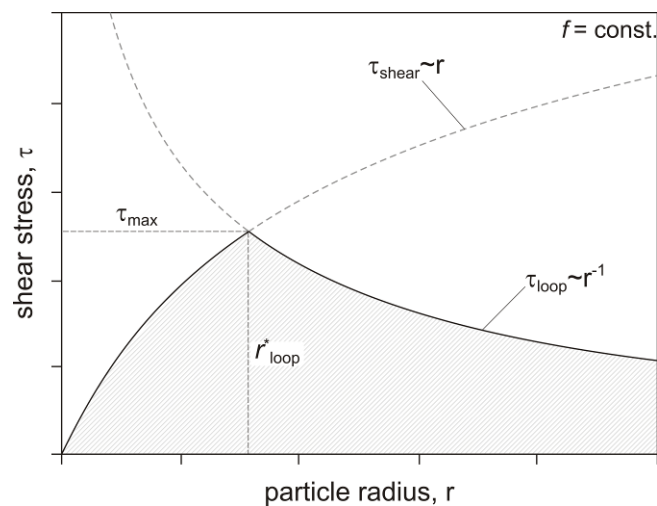
Figure 4.13. Transition from particle shearing to particle looping of weak obstacles as a function of particle radius r (f=const.). The critical radius for particle looping r^*_{loop} denotes the point where $\tau_{shear} = \tau_{loop} = \tau_{max}$.

According to Figure 4.13, the critical radius for particle looping r^*_{loop} can be determined as the particle radius, where the required stress to shear the precipitate is equal to the stress necessary to circumvent the particle by the Orowan mechanism ($\tau_{shear} = \tau_{loop}$). This radius defines the optimum particle size for a given particle distribution of phase fraction f, leading to the maximum strengthening effect τ_{max}.

Moreover, the figure shows that particles with a size smaller than r^*_{loop} are sheared by the dislocation ($\tau_{shear} < \tau_{loop}$), whereas particles with a size larger than r^*_{loop} are bypassed by the dislocation according to the Orowan mechanism ($\tau_{shear} > \tau_{loop}$).

From this basic consideration, it follows that, for a given precipitate size distribution present in a material, not all precipitates of the same precipitate population are overcome by the same mechanism. Instead, only a certain portion of the precipitates is bypassed by shearing or looping, depending on the precipitate size. This item has to be taken into account, when the strength contribution of weak obstacles is determined and it is considered in the software implementation in MatCalc as shown in Figure 4.14. For the determination of the strength contribution τ_{shear}, only the precipitate parameters of the particle classes with a size smaller than r^*_{loop} are utilized. Accordingly, for the determination of τ_{loop}, only the precipitate parameters of the particle classes with a particle size larger than r^*_{loop} are used.
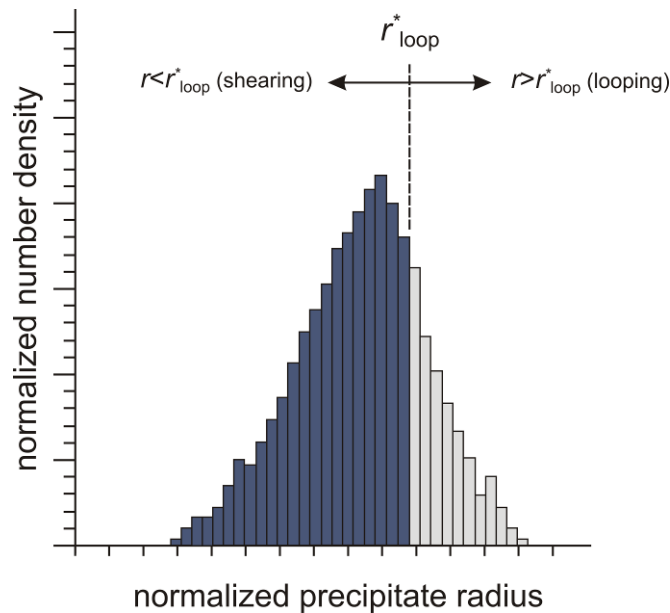
Figure 4.14. Application of the critical radius for particle looping r^*_{loop} to determine the respective number of particle classes (precipitate parameters) to evaluate τ_{shear} and τ_{loop} for a given precipitate distribution of coherent obstacles.

An example for this 'particle class splitting' is shown in Figure 4.15 for Cementite precipitation in an Fe-C model alloy with 0.4 wt.% C aged at 600°C. The figure shows the evolution of the total number density N and the total mean particle radius r (*solid lines*), as well as the evolution of the number density and mean radius of the particle classes below (*dashed-dotted lines*) and above (*dashed lines*) the limit of the critical radius for particle looping r^*_{loop} =10nm. The reappearance of the line r< r^*_{loop} in Figure 4.15 after longer times can be explained by the dissolution of the smaller particle classes during coarsening.
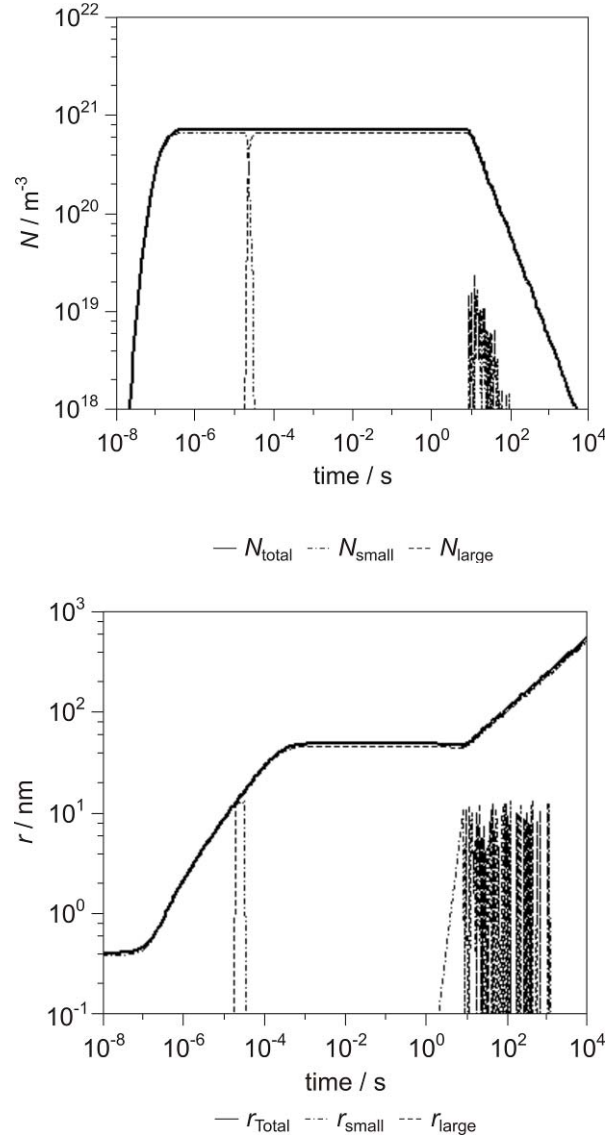
Figure 4.15. Evolution of total number density N and mean particle radius r, as well as the evolution of the number density and mean radius of the particle classes below and above the critical radius for particle loop r^*_{loop}.

Thus, for a physically based evaluation of precipitation strengthening in the case of weak obstacles, the critical radius for shearing r^*_{loop} is a crucial factor. As already pointed out, the determination of r^*_{loop} can be performed from a comparison of τ_{shear} and τ_{loop}. From the generalized form of eq. (4.7) introduced in the previous sections, determination of r^*_{loop} reduces to the evaluation of the relative obstacle strength as $\sum_{i=1}^{n} \sqrt{f(\Theta_{crit})_i} = 1$, according to the superposition rules defined in section 0. Thus, a general formulation to determine the critical radius for particle looping r^*_{loop} can be stated, assuming a distinct dislocation bending ($\Theta \leq 100°$), according to

$$
1 = \left(\overbrace{\left(\frac{\gamma b}{T}\right)^{\frac{3}{2}}}^{A} + \overbrace{\left(\frac{3Gb|\varepsilon|r_{\text{eff}}}{2T}\right)^{\frac{3}{2}}}^{B} + \overbrace{\left(1 - \left(\frac{U_p^{\infty}\log\dfrac{r_{\text{eff}}}{r_i}}{U_m^{\infty}\log\dfrac{r_o}{r_i}} + \frac{\log\dfrac{r_o}{r_{\text{eff}}}}{\log\dfrac{r_o}{r_i}}\right)^2\right)^{\frac{1}{2}}}^{C} \right)^{\frac{1}{2}}.
\tag{4.18}
$$

In the basic form of eq. (4.18), it is assumed that all strengthening mechanisms introduced in the previous section can contribute to precipitation strengthening (terms A, B and C), whereas the equation can by simplified by taking into account only selective mechanisms. This leads to an equation, which can be solved for the effective particle radius r_{eff} and further for the particle radius r.

Assuming a case, where only the coherency strengthening effect is considered, the critical radius for particle looping r^*_{loop} can be determined as

$$
r^*_{\text{loop}} = \sqrt{\frac{3}{2}} \cdot \left(\frac{2T}{3Gb|\varepsilon|}\right),
\tag{4.19}
$$

after combining eqs. (4.5) and (4.18). It is interesting to note that the critical radius can be determined irrespective of the volume fraction of the second phase particles.

According to eq. (4.19), the critical radius can be plotted as a function of the linear misfit strain ε, as shown in Figure 4.16. The figure clearly shows the decrease of the critical radius for particle looping r^*_{loop} with increasing misfit strain ε.
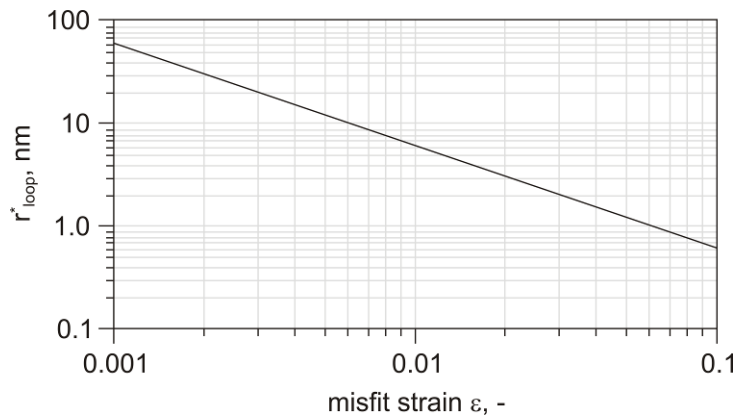
Figure 4.16. Dependence of the critical radius for particle looping r^*_{loop} on the linear misfit strain ε.
(G=83 GPa, b=0.248 nm, T= ½ Gb²)

4.1.4 The particle distance λ

As already pointed out in section 4.1, the strengthening effect of precipitates strongly depends on the number of precipitates intersecting the slip plane of a dislocation, i.e. on the mean distance between the precipitates. Thus, the particle distance λ is a most essential input parameter to determine the strengthening effect of precipitates distributed in a material. The smaller the effective inter-particle spacing, i.e. the higher the number of precipitates in the slip plane, the higher is the strengthening effect due to dislocation-particle interaction.

In early works[89,105], the mean particle distance λ was often assumed to be given by $\lambda \sim N^{-1/2}$, given a uniform distribution of precipitates. *N*, in this case, is the number density of precipitates in the slip plane. However, it should be pointed out that this formulation leads to an overestimation of the evaluated strengthening contribution caused by a given precipitate distribution[105]. Since then, various experimental and numerical works were carried out to determine the effective particle distance[126,138-145].

In the following, formulations for the 3D and 2D particle distances for equally sized precipitates are developed on the base of the nearest neighbour distance (*NND*), following the approach of Sonderegger[146] for randomly distributed precipitates.
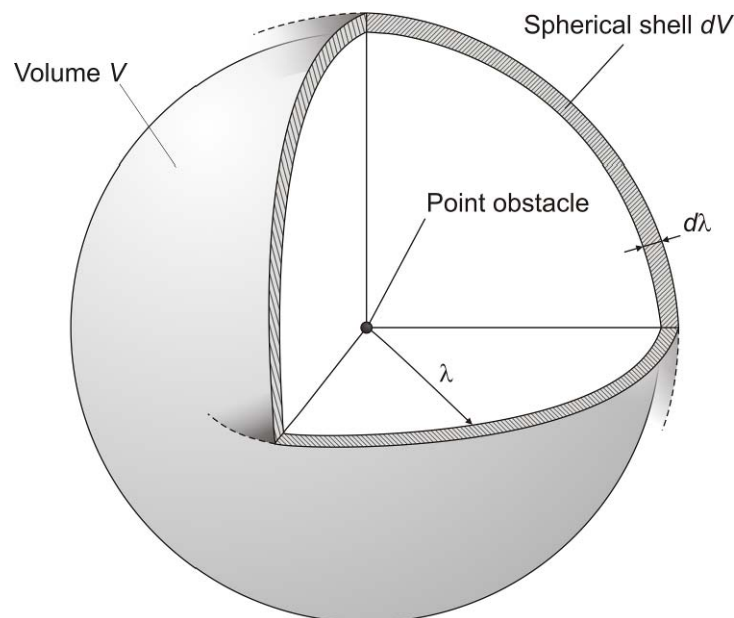
Figure 4.17. Considered spherical volume V with sphere radius λ and shell volume dV with shell thickness $d\lambda$ to determine the 3D nearest neighbour distance according to ref.[146].

4.1.4.1 3D particle distance of point obstacles

In the simplest case of uniformly distributed point obstacles, the distance between point obstacles can be calculated assuming that each obstacle consumes approximately the same bulk volume. In this case, the 3D distance of point obstacles is given by

$$\lambda_{3Dc-c} = \sqrt[3]{\frac{6}{\pi \cdot N}} \quad , \tag{4.20}$$

where N represents the number density of precipitates in units of (m^{-3}). However, the assumption of a uniform distribution is not generally applicable. Thus, the determination of the mean particle distance λ for randomly distributed precipitates in a complex multi component, multi phase and multi particle alloy must be modified, as outlined below.

Assume a point obstacle located in the centre of a volume V, surrounded by a shell of infinitesimal volume dV (Figure 4.17). Assumed further that, in the considered volume, additional point obstacles are distributed with a certain number density (frequency) n_V. Thus, the question arises about the probability that the nearest neighbour is located in the spherical shell dV and about the distance λ between that nearest neighbours. To be able to solve this problem, two general conditions have to be fulfilled:

1. The potential nearest neighbour obstacle must be located in the spherical shell dV.
2. In the considered volume V, no other point obstacle is located. Otherwise the point obstacle in the shell would not be the nearest neighbour.

Due to the small size of dV, it is useful to express the probability of obstacle location 'P' by the probability density 'p' because a decreasing shell volume ($dV \rightarrow 0$) always results in a probability $P_{(dV \rightarrow 0)} = 0$.

The probability density of an obstacle being located in the spherical shell is denoted as d$p(\lambda)$, where λ is the radius of the considered sphere volume V, equivalent in the present case to the inter-particle spacing. The probability density for another particle being located within the volume V is expressed as p_V. Thus, the above stated conditions for the nearest neighbour can be written as

$$\mathrm{d}p(\lambda) = (1 - p_V) \cdot (n_V dV) \quad . \tag{4.21}$$

To determine $(1-p_V)$, the considered volume V is divided into small partial volumes $(V_1 \ldots V_N)$, where $V_1 = V_2 = \ldots = V_N = V/N$. Thus, the probability that no particle is located in the volume V is equal to the probability that no particle is located in one of the partial volumes.

$$(1 - p_V) = (1 - p_{V_1}) \cdot (1 - p_{V_2}) \cdot \ldots \cdot (1 - p_{V_N}) = (1 - p_{V_1})^N . \tag{4.22}$$

If it is further assumed that the probability density of the partial volume p_{V_1} can be determined as $p_{V_1} = n_V \cdot V_1$ (only for small partial volumes), eq. (4.22) becomes

$$(1 - p_V) = \left(1 - n_V \frac{V}{N}\right)^N . \tag{4.23}$$

For $V_N \to 0$, i.e. $N \to \infty$, the probability that no obstacle is located in the volume V can be expressed as

$$(1 - p_V) = \lim_{N \to \infty} \left(1 - n_V \frac{V}{N}\right)^N = \exp(-n_V \cdot V) . \tag{4.24}$$

If eqs. (4.21) and (4.24) are combined, the probability that a point obstacle is located in a spherical shell of volume dV around the considered Volume of the size V can be expressed as

$$P(V) = 1 - \exp(-n_V \cdot V) . \tag{4.25}$$

In the case of the considered spherical volume, where $V_0 = 4/3 \pi \lambda_0^3$ and $dV = 4\pi \lambda^2 d\lambda$, the equation takes the final form

$$P(V) = 1 - \exp\left(-n_V \cdot \frac{4\pi}{3} \lambda^3\right) . \tag{4.26}$$

To calculate the mean 3D center to center distance of randomly distributed precipitates, the median of the mean particle distance has to be determined. For this, a probability of $P(V) = \frac{1}{2}$ is assumed. This means that half of the particle distances are smaller and half of the particle distances are larger than the calculated value $\lambda_{3D\ c-c}$. Thus, from eq. (4.26), one obtains

$$\lambda_{3D\,c\text{-}c} = \sqrt[3]{\dfrac{3 \cdot \ln(2)}{4\pi \cdot n_{\mathrm{V}}}} \quad .$$

(4.27)

The center to center distance only depends on the number density n_{V} of the precipitates. It is interesting to note that eq. (4.27) is close to the expression for the mean particle distance reported by Underwood[147].
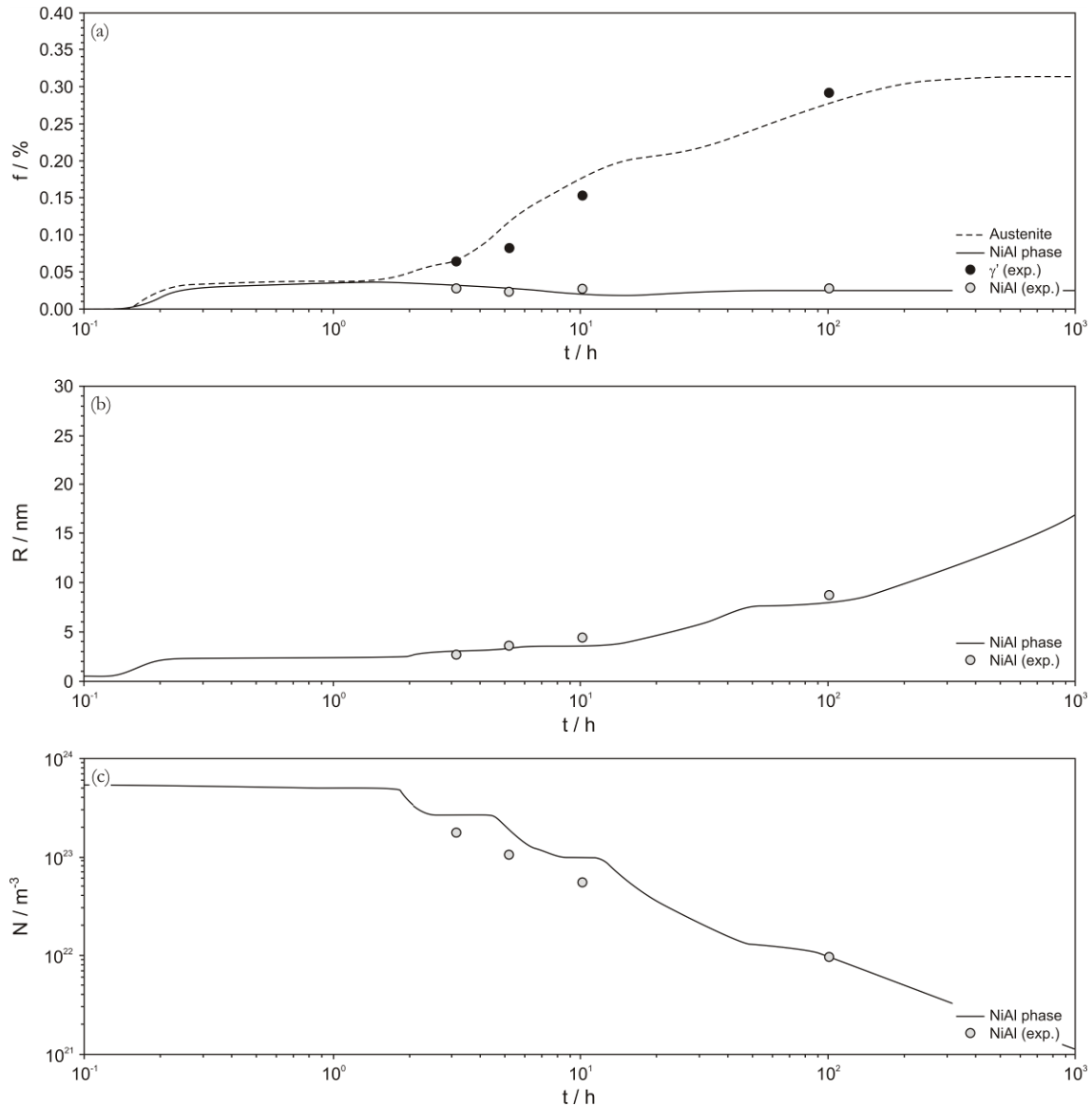
Figure 4.18. Comparison of calculated phase fraction (f), mean particle radius (R) and number density (N) with experimental data from Schnitzer et al.[148] and Radis et al.[149].

In Figure 4.18, the simulation results reported by Schnitzer et al.[148] and Radis et al.[149] for the evolution of reverted Austenite and NiAl-precipitates are shown for the maraging steel

PH 13-8 Mo during ageing at 575°C. The figure shows the evolution of the phase fraction *f*, mean particle radius *r* and number density *N* compared with the experimentally determined values. A good agreement between simulation results and experiment can be observed.

Based on these simulation results, the mean particle distance ($\lambda_{\text{3D c-c}}$) is calculated according to eq. (4.27). The result is shown in Figure 4.19. Comparison with the experimentally determined values by Schnitzer[150] shows encouraging agreement. The evolution of the mean particle distance can be described over the whole investigated time scale.
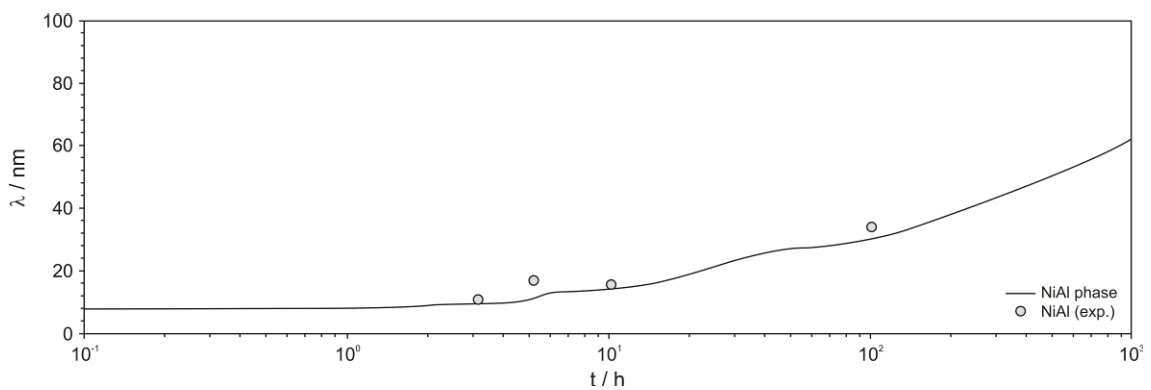
Figure 4.19. Calculated mean center to center particle distance (λ) compared with the experimental data reported by Schnitzer[150].

4.1.4.2 The effective 3D particle distance

If - instead of point obstacles - precipitates with a certain spatial extension are considered, the precipitate size must be taken into account when the effective mean particle distance (surface distance) is calculated.

To calculate the effective mean particle distance $\lambda_{\text{3D s-s}}$, the same assumptions as in section 4.1.4.1 are made. Consequently, the effective 3D particle distance $\lambda_{\text{3D s-s}}$ can be calculated according to

$$\lambda_{\text{3D s-s}} = \sqrt[3]{\frac{3 \cdot \ln(2)}{4\pi \cdot n_V} + 8r^3} - 2r \ . \tag{4.28}$$

In this equation, n_V again is the number density and *r* is the mean particle radius of the precipitates. The last term in eq. (4.28) accounts for the precipitate extension and the term

$8r^3$ results from the boundary condition that the effective mean particle distance cannot be negative (λ<0).

4.1.4.3 The effective 2D particle distance

Although, the 3D particle distance is an important microstructural parameter, it is necessary to know the mean particle distance in the slip plane of the dislocation for the evaluation of the strengthening contribution of precipitates. Thus, it is rather useful to calculate the effective 2D particle distance of precipitates within a plane. For this case, the calculation of the mean particle distance λ is based on the same assumptions as in the previous sections and can be carried out analogously. However, in the present case, a circular area and a ring segment are considered, instead of a spherical and shell volume (compare Figure 4.17). This is shown schematically in Figure 4.20.
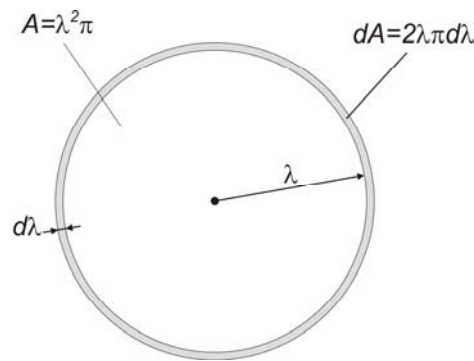
Figure 4.20. Considered circular area A with radius λ and ring segment dA with thickness $d\lambda$ to determine the 2D nearest neighbour distance according to ref.[146].

Further, instead of a probability of $P(V)$=1/2 to calculate the 3D mean particle distance, a probability $P(V)$=2/3 is assumed, following the argumentation of Ashby[105] on the effect of a random particle distribution. Ashby pointed out that every spacing between a pair of particles has its own passing stress. It was shown by Kocks[151,152] that extensive slip can first occur at the critical value of the applied stress, such that about one third of the spacings between the particles are "transparent".

Thus, the effective 2D particle distance $\lambda_{2D\ s\text{-}s}$ is calculated according to eq. (4.29), taking into account the effective precipitate size (r_{eff}) in the slip plane of the dislocation, finally reading

$$\lambda_{2D\,s\text{-}s} = \sqrt{\frac{\ln(3)}{2\pi \cdot n_V \cdot r} + 4r^2} - 1.63r \ .$$

(4.29)

n_V is the number density and r is the mean particle radius of precipitates. The last term in eq. (4.29) accounts for the influence of the precipitate size on the mean particle distance. The term corresponds to the effective particle diameter in the slip plane (=1.63r, see ref.[132]). The term $4r^2$ results from the boundary condition that the effective mean particle distance cannot be negative (λ<0). A summary of all formulations for the mean particle distances utilized in the software MatCalc is given in Table 4.4.

Table 4.4. Overview of the different formulations for the particle distance λ for randomly distributed precipitates. The table contains the formulation for the 3D centre to centre distance $\lambda_{3D\,c\text{-}c}$ and the effective 3D and 2D particle distances considering the influence of precipitate size.

mean particle distance λ	Formula	Comment
general formulation (3D)	$\lambda_{3D\,c\text{-}c} = \sqrt[3]{\dfrac{3\cdot\ln((1-P(V))^{-1})}{4\pi\cdot n_V}}$	$P(V)$ ...Probability of obstacle location [-]
	$\lambda_{3D\,s\text{-}s} = \sqrt[3]{\dfrac{3\cdot\ln((1-P(V))^{-1})}{4\pi\cdot n_V}+8r^3} - 2r$	n_V ...Number density [m^{-3}] r ...Mean particle radius [m]
general formulation (2D)	$\lambda_{2D\,s\text{-}s} = \sqrt{\dfrac{\ln((1-P(V))^{-1})}{2\pi\cdot n_V\cdot r}+4r^2} - 1.63r$	
3D 'center-center' distance	$\lambda_{3D\,c\text{-}c} = \sqrt[3]{\dfrac{3\cdot\ln(2)}{4\pi\cdot n_V}}$	$P(V) = 1/2$
3D 'surface' distance	$\lambda_{3D\,s\text{-}s} = \sqrt[3]{\dfrac{3\cdot\ln(2)}{4\pi\cdot n_V}+8r^3} - 2r$	$P(V) = 1/2$
2D 'surface' distance	$\lambda_{2D\,s\text{-}s} = \sqrt{\dfrac{\ln(3)}{2\pi\cdot n_V\cdot r}+4r^2} - 1.63r$	$P(V) = 2/3$

By definition of the probability of obstalce location P(V) the particle distance λ can be calculated. A probability P(V)=1/2 defines the mean particle distance (median). a probability P(V)=2/3 defines the particle distance where 1/3 of the particle spacings are larger than the calculated value, assuming a random particle distribution.

4.2   Solid solution strengthening

Apart from the possibility of strengthening a material by densely distributed precipitates, a distinct increase in materials strength can also be achieved by addition of alloying elements due to the interaction of the stress field around a size mismatched solute atom and the dislocation. The main strength determining parameters, on which the hardening of the material by a solute element i depends, are the interaction between solute atom and dislocation segment expressed in the present work by the strengthening coefficient k_i, the concentration of solute atoms c_i and the concentration exponent n[74-76,153-155].

$$\Delta\tau_{SSi} = k_i \cdot c_i^{\;n} \tag{4.30}$$

In the following, the model of Gypen and Deruyttere[79,80], utilized to account for the solid solution hardening effect in a multi-component alloy, is briefly outlined and the basic formalism to determine the solid solution strengthening effect is summarized.

4.2.1   Solid solution strengthening in a multi-component alloy

If solid solution strengthening in a multi-component alloy with ζ alloying elements is considered, the contribution of each alloying element must be taken into account separately. To calculate the hardening effect when different solutes are present in the material simultaneously, Gypen and Deruyttere [79,80] introduced a fictitious solute j with respective strengthening coefficients k_j and a concentration exponent n. Thus, an equivalent concentration c_{eqji} of solute atoms j can be calculated for each solute element i ($i=1\ldots\zeta$) according to

$$c_{eqji} = \left(\frac{k_i}{k_j}\right)^{\frac{1}{n}} c_i \tag{4.31}$$

To calculate the equivalent solute concentration, in a first approximation, it is assumed that the concentration exponent n is equal for all solute elements i and the fictitious solute j. If it is assumed that all solute elements present in the material produce the same strengthening effect as the solute atoms of type j with a concentration c_{eqj} equal to the sum of the equivalent concentrations c_{eqji}, the total hardening effect can be calculated according to

$$\Delta\tau_{SS} = k_j \left(\sum_{i=1}^{\zeta} c_{eqji} \right)^n \tag{4.32}$$

The graphical interpretation of eq. (4.32) is given in Figure 4.21 for a ternary solid solution (ζ=2).

Combining eq. (4.31) and eq. (4.32) leads to an expression to calculate the total solid solution hardening effect in a multi-component alloy according to

$$\Delta\tau_{SS} = \left(\sum_{i=1}^{\zeta} k_i^{\frac{1}{n}} c_i \right)^n \tag{4.33}$$

It is interesting to note that the strengthening factor k_j does not appear in the equation. Thus, the final result is independent of the fictitious reference distribution.
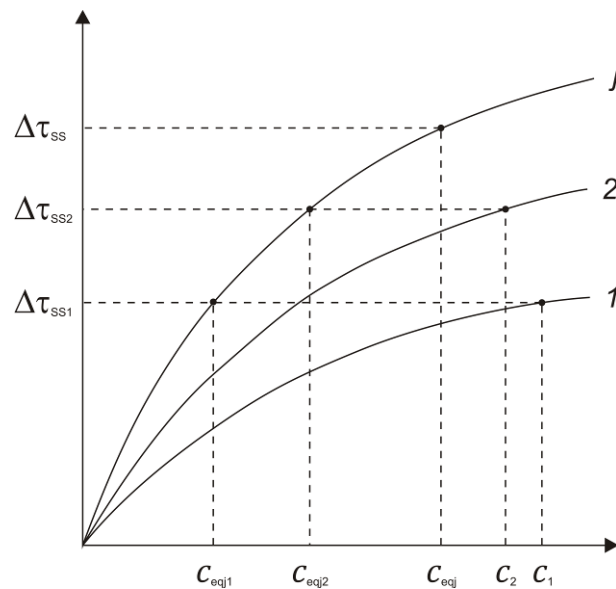
Figure 4.21. Solid solution strengthening in a multi-component alloy, where two solute elements (ζ=2) are present simultaneously with concentrations c_1 and c_2. The respective strengthening effect of each solute is given by $\Delta\tau_{SS1}$ and $\Delta\tau_{SS2}$, whereas the total hardening effect produced is represented by $\Delta\tau_{SS}$ for an equivalent solute concentration $c_{eqj} = c_{eqj1} + c_{eqj2}$.

As it was already pointed out, eq. (4.33) was derived assuming a constant concentration exponent n. However, as often reported in literature, the concentration exponent n can easily vary in the range between 0.5 and 1[75,80], depending on the solute concentration as pointed out by Feltham[156]. This is taken into account by the extension of eq. (4.33) according to

$$\Delta\tau_{SS} = \left(\sum_{i=1}^{\zeta} k_i^{\frac{1}{n_j}} c_i^{\frac{n_i}{n_j}} \right)^{n_j}, \tag{4.34}$$

where k_i, c_i and n_i are the strengthening coefficient, the solute concentration and the concentration exponent of each solute element i. n_j is the concentration exponent of the reference solute j. To determine the concentration exponent n_j, a weighted average of the concentration exponents n_i is proposed in ref.[79]:

$$n_j = \frac{\sum_{i=1}^{\zeta} n_i \Delta\tau_{SSi}}{\sum_{i=1}^{\zeta} \Delta\tau_{SSi}}. \tag{4.35}$$

In eq. (4.35), the hardening effect of each solute element $\Delta\tau_{SSi}$ is calculated according to eq. (4.30). A summary of different strengthening coefficients in α-iron for different substitutional and interstitial solute elements is given in Table 3.1.

4.3 Superposition of strengthening effects

If more than one strengthening mechanism resulting from the interaction of mobile dislocations with the lattice potential, solute atoms, forest dislocations, precipitates, etc. is operative, a linear superposition of the mechanism, as one might intuitively assume, is not always observed. The nature of superposition is rather dependent on the strength and distribution of individual obstacle types present in the material. In the present work, a general formulation based on the common superposition law[157-162]

$$\tau_{res}^{\alpha} = \sum_i \tau_i^{\alpha} \tag{4.36}$$

is utilized to determine the resulting strengthening effect τ_{res} for different strengthening mechanisms τ_i. The exponent α is supposed to range between 1 and 2.

Table 4.5. Different strength mechanisms contributing
to the total strength of a material.

Strength contribution	Comment
τ_d	*work hardening*
τ_i	*intrinsic lattice strength*
τ_{ss}	*solid solution strengthening*
τ_p	*particle strengthening*
τ_{gb}	*grain size strengthening*
τ_{sgb}	*subgrain size strengthening*
τ_A	$= \tau_d$
τ_B	$= \tau_i + \tau_{ss} + \tau_p + \tau_{gb} + \tau_{sgb}$

As often referred in literature[84,163,164], the strength contributions from different effects can be generally related to two groups of obstacle types, τ_A and τ_B. Kocks et al. identified τ_A as strength contributions related to forest dislocations ($= \tau_d$) and τ_B as contribution from particles, whereas, in this term, further strengthening contributions such as, e.g., the intrinsic lattice strength, solid solution strengthening, or the work hardening effect are considered[84,163,164] (compare Table 4.5). Thus, a formulation for the superposition law for different operative strengthening effects can be given according to

$$\tau_{res} = \sqrt[\alpha]{\tau_A^\alpha + \tau_B^\alpha} \quad . \tag{4.37}$$

4.3.1 Superposition of precipitate strengthening effects

In many cases, several types of precipitates of varying strength (see also section 4.1.1 and 4.1.2) are distributed in a material, leading to a superposition of different strengthening effects. Additionally, the precipitate distributions are not always monodisperse. Even if there is only a single particle size, there would still be a size distribution in the slip plane of a dislocation, since the slip plane intersects not all precipitates at the same position. Also, this effect results in a distribution of obstacle strengths (see section 4.1.3). Thus, the question arises, as to how a *distribution* of obstacle strengths affects the total strength of a material?

To calculate the overall precipitation strengthening effect for weak and strong obstacles of varying size (τ_p), the different mechanisms are superimposed according to the general formulation of Ardell[130,157] as

$$\tau_p^\alpha = n_{\text{weak}}^{\frac{\alpha}{2}} \tau_{p,\text{weak}}^\alpha + n_{\text{strong}}^{\frac{\alpha}{2}} \tau_{p,\text{strong}}^\alpha \,, \tag{4.38}$$

where α is a constant, n_{weak} and n_{strong} are the density fractions and $\tau_{p,\text{weak}}$ and $\tau_{p,\text{strong}}$ are the strengthening contributions from weak and strong obstacles, respectively. The density fractions n are determined as the ratios between the number density of weak (N_{weak}) and strong (N_{strong}) obstacles and the total number density (N_{total})[130].

$$n_{\text{weak}} = \frac{N_{\text{weak}}}{N_{\text{total}}} \tag{4.39a}$$

$$n_{\text{strong}} = \frac{N_{\text{strong}}}{N_{\text{total}}} \tag{4.39b}$$

In the case when different weak precipitate populations are present in the material and/or different "weak" strengthening mechanism, e.g. modulus mismatch hardening or coherency strain hardening, are operative simultaneously, the strength increase of weak particles is calculated according to the formulation of Koppenaal and Kuhlmann-Wilsdorf[165]. These authors defined a superposition law for obstacles with similar strength according to

$$\tau_{p,\text{weak}} = \sqrt[\beta]{\sum_i \tau_{pi,\text{weak}}^\beta} \,. \tag{4.40}$$

β in this equation is a constant with a value around $\beta=2$. Thus, the total amount of precipitation strengthening of strong and weak obstacles can be calculated according to

$$\tau_p^\alpha = \left(\frac{N_{\text{weak}}}{N_{\text{total}}}\right)^{\frac{\alpha}{2}} \left(\sqrt[\beta]{\sum_i \tau_{i,\text{weak}}^\beta}\right)^\alpha + \left(\frac{N_{\text{strong}}}{N_{\text{total}}}\right)^{\frac{\alpha}{2}} \tau_{p,\text{strong}}^\alpha \,, \tag{4.41}$$

A final schematic illustration of the precipitation strength module described in the present section is shown in Figure 4.22. For given matrix composition and precipitation parameters (e.g. phase fraction, particle size, number density), the strengthening effect by solid solution hardening and precipitation strengthening can be calculated.

To determine the precipitation strengthening effect, it must be decided whether the precipitate is susceptible to shear or not, i.e. if the particle is weak or strong. In the case of strong obstacles, the operative mechanism is the Orowan mechanism. The strength contribution, thus, can be calculated from eq (4.6). In the case of weak obstacles, the critical radius for particle looping is evaluated to determine whether a particle of a certain size is circumvented by the dislocation according to the Orowan mechanism or if the particle is cut through by the dislocation. Thus, the effective precipitation parameters of weak and strong obstacles can be determined according to the formalism in section 4.1.3. The operative mechanism for the precipitates of a size larger than the critical radius for particle looping r^*_{loop} is again the Orowan mechanism (eq. (4.6)). For precipitates smaller than r^*_{loop}, the strengthening effect is evaluated according to eq. (4.7). The total precipitation strengthening effect, finally, is determined according to the superposition law introduced in section 0 and superimposed with other strengthening effects, among others the solid solution hardening effect according to eq. (4.36), as pointed out in section 4.3.

Figure 4.22. Schematic illustration of the strength module implemented in the software MatCalc.

5 Application

In the following sections 5.1 to 5.4, the previously introduced strength module is applied on different Fe-base alloys to determine the evolution of different strengthening mechanisms as a function of time and temperature history.

In the first application example (section 5.1), precipitation strengthening in an Fe-1.4at.% Cu alloy aged at 500°C is critically discussed. Thereto, a novel simulation method to simulate the precipitation kinetics in Fe-Cu alloys is introduced to describe the evolution of the precipitation parameters in an appropriate manner. Based on these simulation results, the evolution of the lower yield stress (LYS) is determined as a function of aging time and compared to experimental data reported in literature. The results presented in this section were recently published in ref.[166].

In section 5.2, the back-stress concept is applied on an 11Cr-1Mo-3Co steel to investigate the influence of the precipitate evolution on the creep strength of the material. The study shows the detrimental impact of the appearing modified Z-phase on the creep strength evolution, based on the calculated development of the total precipitation strengthening effect in this complex alloy. This section is a continuation of a previous work carried out by Dimmler[57,59], who already applied this concept on an experimental base on several 9-12% Cr steels to establish a connection between microstructure evolution and mechanical properties. Basis for this numerical investigation are the simulation results carried out with the software MatCalc. The simulation results are compared to the experimental data reported in refs.[42,57]. The results of this section were already published in ref.[167].

Section 5.3 deals with the effect of different heat treatment parameters (austenitising time and temperature as well as tempering time and temperature) on the long term creep strength of a 10Cr-1Mo-1W steel. It is often believed that an optimization of the precipitate morphology in the initial 'as-received' condition by heat treatment variation leads to a superior long term creep strength. Based on numerical simulations, however, in the present section, the experimental observation is confirmed that microstructure optimization by variation of the heat treatment parameters gives only a temporary benefit. The numerical simulations as well as the experimental observations show that, after longer service times, the creep strength of the distinctly heat treated materials approach the same level. Also, the results of this section were published previously[168,169].

In the last section of the application examples (section 5.4), the strength module introduced in section 4 is utilized to calculate the 0.2% yield stress of an 11Cr-0.5Mo-0.5Mn steel. The microstructural evolution during different heat treatments is simulated and, based on these results, the total strength of the material is determined. For that, beside the precipitation and solid solution strengthening effect, the strength contributions by dislocations and subgrains are further considered.

All simulations carried out in the following were performed with the software MatCalc[110-112,170].*

---

* http://www.matcalc.at

5.1   Simulation of precipitation kinetics and strength evolution in an Fe-1.4at.% Cu alloy

5.1.1   Cu precipitation in steel – precipitation kinetics and influence on mechanical properties

The kinetics of Cu-precipitation in steel was subject to several experimental as well as numerical analyses[171-176]. Therefore, morphology, crystallography and kinetics of Cu precipitation in α-iron are well documented. It is generally accepted that, in the early stages of ageing, Cu precipitates undergo a multi-stage transformation from coherent body centred cubic (bcc) to incoherent face centred cubic (fcc) structure. During this transition, a change in the chemical composition of the Cu precipitates with respect to the Fe content can be observed. The exact amount of Fe in the early bcc Cu precipitates is still a topic under discussion, as concluded by Fine et al.[176]. These authors point out that, considering experimental results obtained by atom probe analysis, a significant amount of Fe can be detected in the Cu precipitates. In contrast, positron annihilation and neutron scattering studies suggest compositions close to pure Cu. Also, numerical analyses are inconclusive with conflicting results[177,178]. In a recent theoretical study[179], evidence is provided towards the assumption that finely dispersed Cu precipitates in the very early stages of ageing contain a significant amount of Fe.
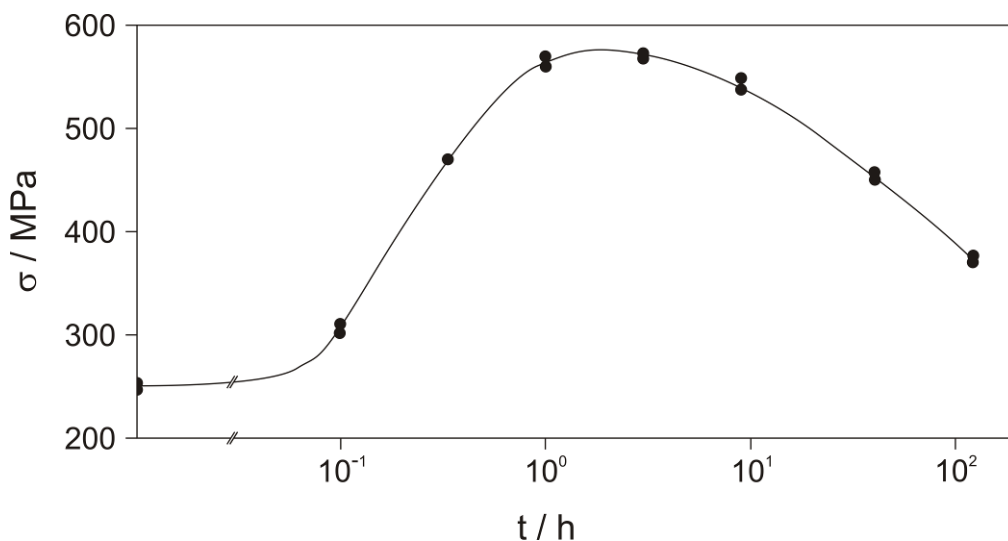
Figure 5.1. Evolution of lower yield stress (LYS) of an Fe-1.4at.% Cu alloy
as a function of ageing time at 500°C (re-plotted from ref.[171]).

The dense distribution of coherent bcc Cu precipitates leads to a distinct increase in strength and hardness (Figure 5.1), where the peak strength condition coincides with the maximum precipitate number density. At this point, the mean diameter of the precipitates is approximately 2-3 nm. Depending on the ageing conditions, this maximum is often observed after several hours[83,137], followed by a pronounced decrease in number density during overageing with a simultaneous decrease in strength. Interestingly, this drop in number density cannot be described by classical Ostwald ripening theory alone, as shown in the following, due to the fact that the reduction in number density predicted by this theory would be several orders of magnitude too low.

This discrepancy has stimulated detailed numerical investigations and the development of a new simulation methodology, which differs from conventional approaches reported in literature[83,180,181] by taking into account compositional variations of the critical nucleus. In the present approach, the actual composition of the nuclei is evaluated based on the concept of a minimum nucleation barrier[172,179]. It is demonstrated that these initial variations of nucleus composition have a huge impact also on the further precipitate evolution and must be duly considered to reproduce the precipitation kinetics in Fe-Cu alloys.

Finally, on the example of an Fe 1.4 at.% Cu alloy, which was investigated experimentally by Goodman et al.[171] during ageing at 500 °C using field ion microscopy (FIM) and transmission electron microscopy (TEM), the theoretical precipitation strengthening potential is evaluated based on different strengthening models. Together with the inherent strength of the alloy and the solid-solution strengthening effect by Cu, the lower yield stress (LYS) evolution during a precipitation hardening treatment is evaluated.

5.1.2   Numerical simulation of Cu-precipitation in α-iron

As already pointed out, the simulations carried out are performed with the software MatCalc (version 5.30.1096). The thermodynamic and diffusion data are compiled from the assessments of Turchanin[182] and Fridberg et al.[183], respectively. The data are implemented in the thermodynamic database 'mc_steel'[184] and the mobility database 'mc_sample_fe'[185]. The energy of the precipitate/matrix interface γ_0 is calculated from the generalized broken-bond (GBB) approach. The precipitate size effect is taken into account by a radius-dependent correction factor, which considers the impact of surface curvature of the precipitate nucleus on the interfacial energy. Moreover, the impact of atomic mixing at the precipitate/matrix interface (entropic effects, see e.g. ref.[122]) is taken into account with a constant correction factor of 0.9. A more detailed discussion on calculation of interfacial energy γ is given in section 3.3.3. Kinetic effects of, e.g., quenched-in vacancies, are taken into account in the diffusion coefficient by a constant factor of 150. No other fitting parameters are used in the simulations.

In the present simulation, it is assumed that precipitates can nucleate in the bulk. For further details on the methodology of kinetic simulations, the interested reader is referred to previous applications of the MatCalc model, e.g. Rajek[3], Sonderegger et al.[4] and Radis et al.[5]. These papers contain supplementary details on the simulation procedure[111].

5.1.2.1 Simulations with constant nucleus composition – the conventional approach

In a first step, the precipitation kinetics of the investigated Fe-Cu alloy was simulated considering a constant nucleus composition. The simulation results are compared to the experimental data in ref.[171] to generate a reference base for a comparison with the novel simulation method. The time dependent nucleation rate J is calculated according to classical nucleation theory (see therefore section 3.3.2.2) with

$$J = N_0 Z \beta^* \exp\left(\frac{-G^*}{k \cdot T}\right) \cdot \exp\left(\frac{-\tau}{t}\right). \tag{5.1}$$

J describes the rate at which new nuclei are created per unit volume and unit time. N_0 represents the total number of potential nucleation sites, Z is the Zeldovich factor, β^* is the

atomic attachment rate, k is the Boltzmann constant, T is temperature, G^* is the critical nucleation energy, τ is the incubation time and t is time.

In multi-component alloys, it is generally assumed that supercritical precipitate nuclei adopt the particular chemical composition, which yields the maximum driving force (ortho-equilibrium composition) for precipitation. With this criterion, the otherwise undetermined Fe and Cu-content of the nucleus can be fixed and the individual terms in equation (5.1) can be evaluated. In the present case, the ortho-equilibrium criterion implies that the nuclei consist of practically pure Cu. With equation (5.1) and application of a suitable growth law, see e.g. refs.[107,110,186], the further evolution of the supercritical nuclei is fully determined. Time integration of the evolution equations is performed in the framework of the numerical Kampmann-Wagner approach as described in section 3.3.2.1. Similar approaches have been reported by e.g. Hutchinson et al.[83] and M. Perez et al.[181] for Cu precipitation in α-iron, or by Myhr et al.[187,188] and Nicolas and Deschamps[189] in Al-alloys.

In order to reproduce the experimental results of Goodman et al.[171], numerous simulations have been carried out in the MatCalc software with parameter variations in the interfacial energy and diffusional mobility. Exemplary results of such variations are shown in Figure 5.2 (a)-(c), where the calculated sharp interface energy γ_0 is varied with multiplicative pre-factors. Interestingly, no combination of simulation input parameters could be found, which leads to a consistent representation of the experimentally measured precipitation kinetics. With any variation of parameters (interfacial energy and diffusional mobility) and assuming that the critical bcc-Cu nucleus has ortho-equilibrium chemical composition, it has only been possible to capture either the increase of phase fraction (see curve for $1.0 \cdot \gamma_0$), the evolution of the mean radius ($1.1 \cdot \gamma_0$) or the maximum number density ($0.9 \cdot \gamma_0$). A consistent description of all precipitation parameters with a single set of simulation parameters could not be achieved.
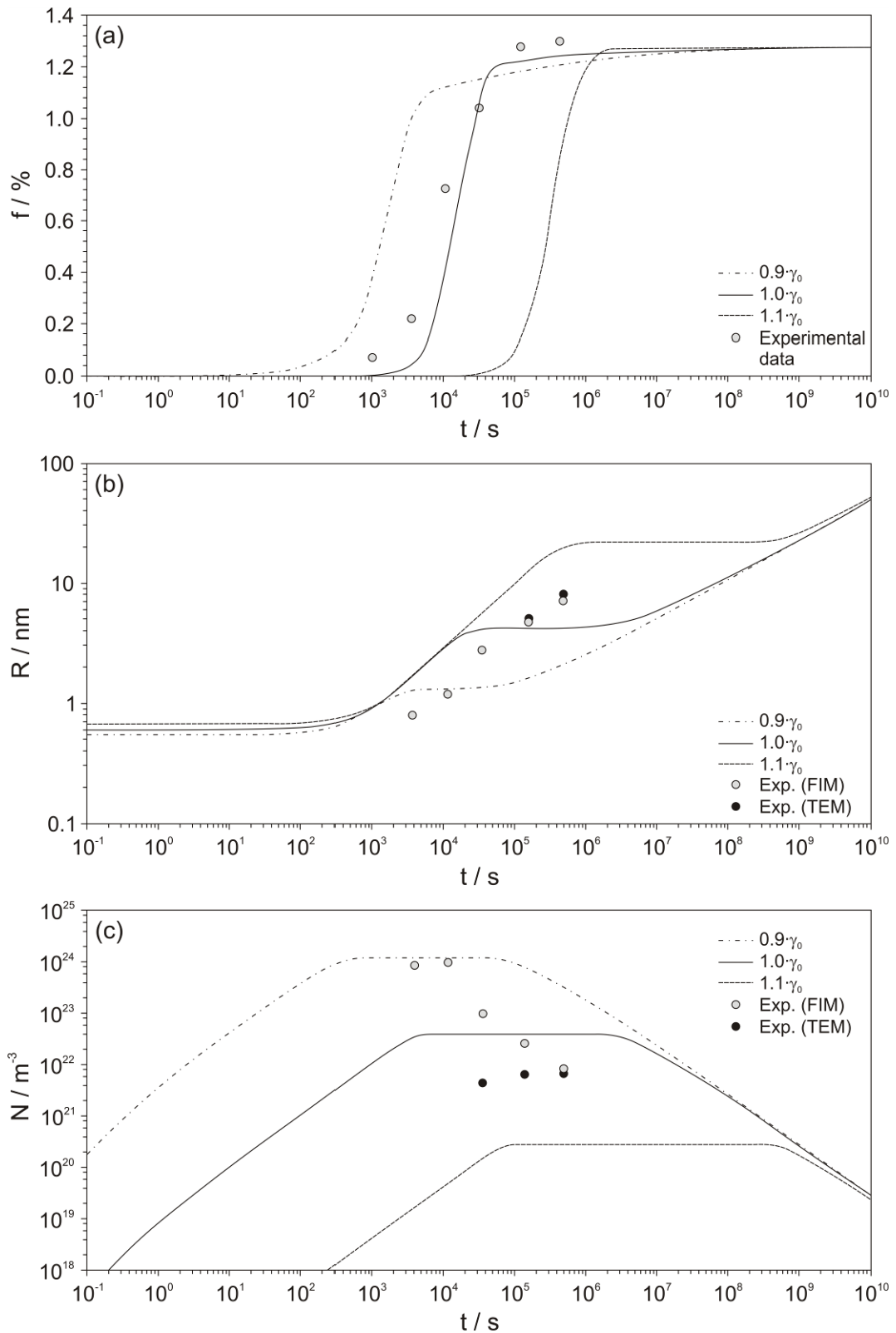
Figure 5.2 (a)-(c). Calculated evolution of phase fraction (*f*), mean particle radius (*R*) and number density (*N*) for bcc Cu-precipitates with ortho-equilibrium nucleus composition. The different lines in each plot show the result of a parameter variation of the interfacial energy (γ_0).

5.1.2.2 Simulations with variable nucleus composition – the novel approach

Motivated by these observations, simulations have been performed next, which account for the predicted variations in chemical composition of the bcc Cu precipitates in the nucleation stage[172,178,179]. In addition, stable fcc-Cu precipitates are also included in the simulations as described below. In all other aspects, the simulations in this section are identical to the simulations with ortho-equilibrium nucleus composition presented in the previous section.

To determine the actual nucleus composition of the coherent bcc Cu precipitates the calculation concept of the 'most likely' nucleus composition introduced by Kozeschnik[179] is applied. Kozeschnik showed that the critical nucleation energy G^*_{krit} varies with the Cu content of the precipitate for a given matrix composition and temperature, as shown in Figure 5.3 (a). Thus, it is possible do determine a minimum G^*_{krit}, which leads to a maximum nucleation probability, as illustrated in Figure 5.3 (b), where the normalized nucleation probability P^* is plotted as a function of precipitate composition.
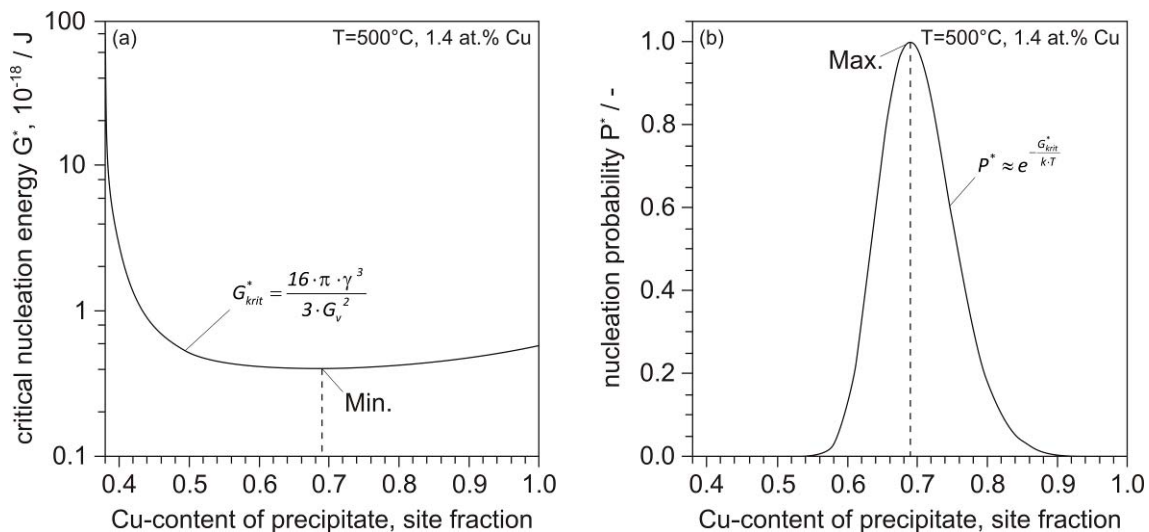
Figure 5.3 (a)-(b). Critical nucleation energy C^*_{krit} and normalized nucleation probability P* as a function of Cu-content of precipitate according to ref.[179] for a Fe-1.4at.% Cu alloy at 500°C.

According to this concept of a 'most likely' nucleus composition, the Cu to Fe ratio in the critical nucleus can be made a function of supersaturation of the matrix, where the composition of the critical nucleus can be calculated as a function of temperature and matrix composition (Figure 5.4). For a nominal Cu content of 1.4 at.% at 500°C, the equilibrium Fe content in the nucleus is evaluated with 31 at.%, corresponding to 69 at.% Cu. This agrees well with an estimated value reported by Goodman et al.[172], who predicted

a minimum nucleation barrier at about 70 at.% Cu. Since this value increases to approximately 98 at.% Cu with decreasing supersaturation, a variation in the Cu concentration of the critical nucleus between 69 and 98 at.% Cu is expected in the present case.
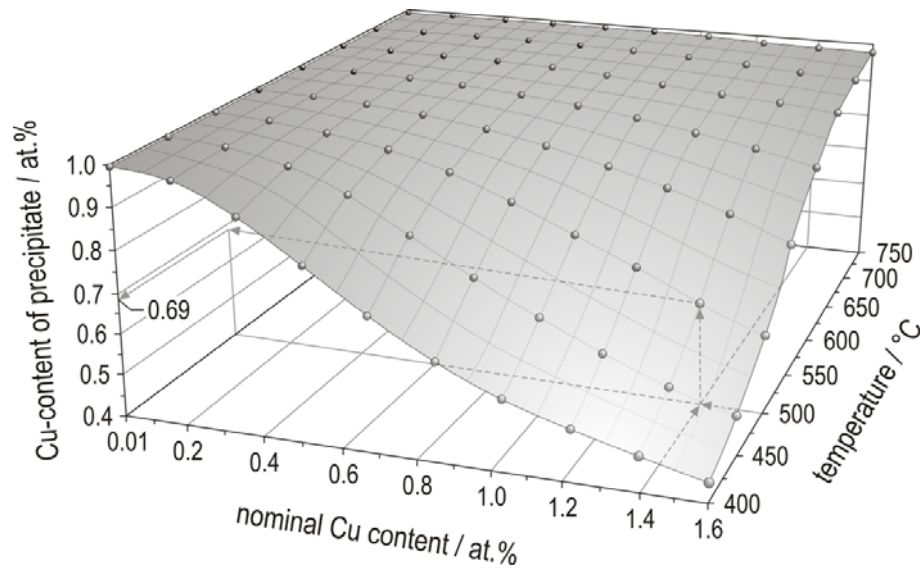
Figure 5.4. Calculated equilibrium Cu-content of the critical nucleus as function of nominal Cu-content and temperature according to ref.[179].

The experimentally observed loss of coherency of the Cu precipitates, when changing from bcc to fcc crystal structure, is taken into account in the simulations indirectly by an additional population of precipitates with equilibrium fcc structure. When both precipitate types (bcc and fcc) are treated simultaneously and in competition, initially, faster precipitation of the coherent metastable bcc phase with lower Cu content and, thus, lower interfacial energy is observed. With increasing annealing time, the incoherent, but thermodynamically stable, fcc precipitates become favourable. Finally, the bcc precipitates disappear, consistent with experimental observations[171,173].

The results of the simulations with variable nucleus composition are summarized in Figure 5.5 (a)-(c) and Figure 5.6. The graphs show the evolution of the individual and accumulated phase fractions, mean particle radii and number densities for the bcc and the fcc precipitates, as well as the evolution of precipitate and matrix composition. Phase fraction and number density are evaluated as the sum of the calculated values for bcc and fcc precipitates. The accumulated mean radius is evaluated as the volume-weighted mean radius of the two precipitate populations.
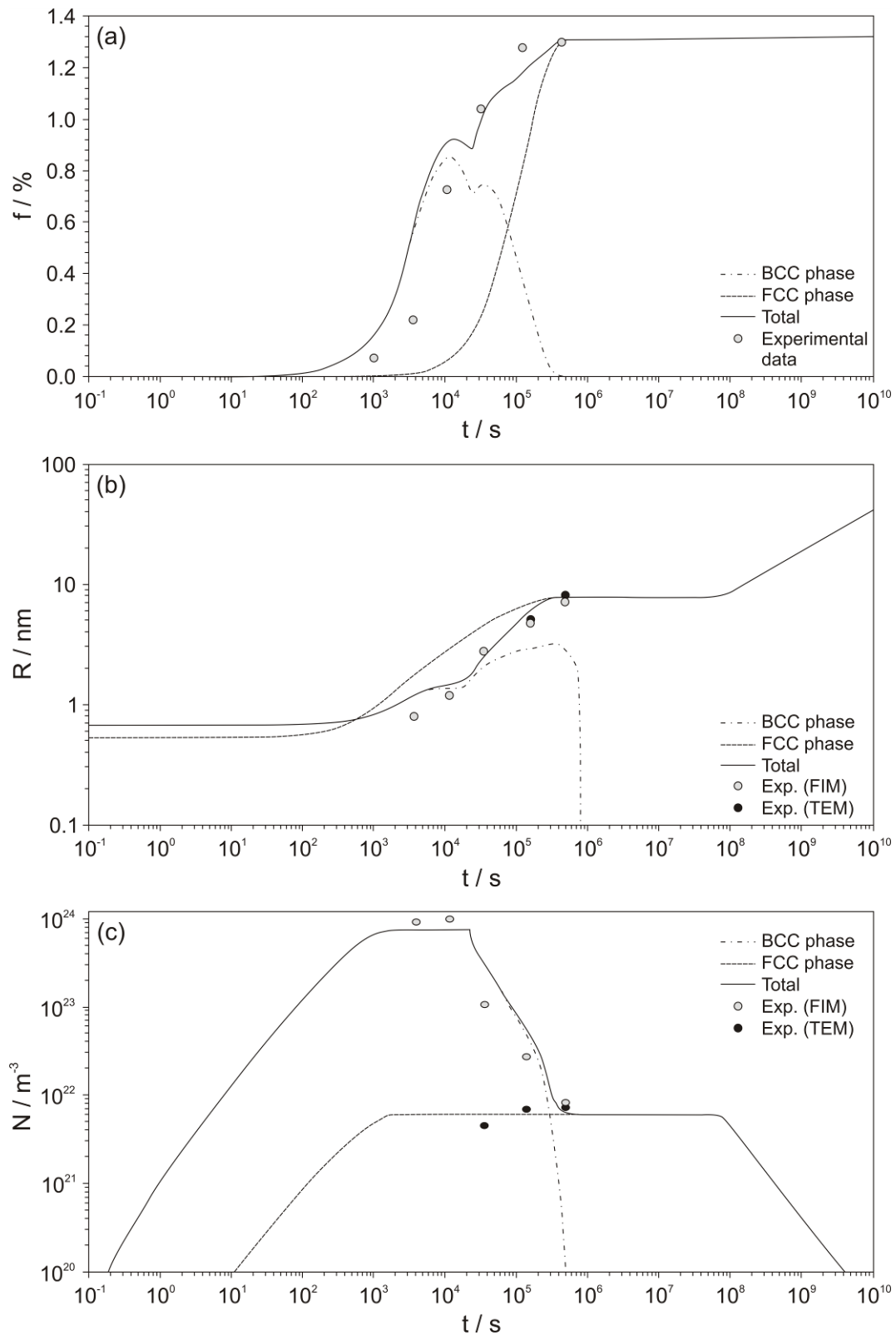
Figure 5.5 (a)-(c). Calculated evolution of phase fraction (*f*), mean particle radius (*R*)

and number density (*N*).
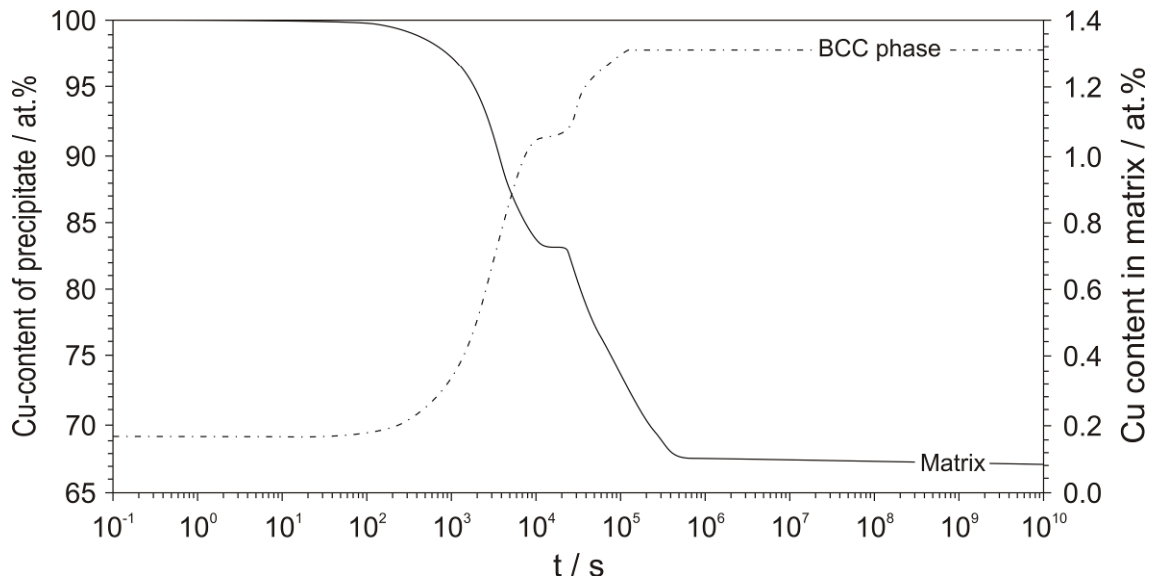
Figure 5.6. Calculated evolution of matrix and nucleus composition.

When comparing the results of the numerical simulation with variable nucleus composition with experiment, good agreement is observed. In contrast to the conventional approach, the evolution of all precipitate parameters, i.e. phase fraction, mean radius and number density, can be consistently reproduced.

Closer inspection of the results reveals that the evolution of the mean precipitate radius (Figure 5.5 (b)) in the early stages is mainly determined by the size evolution of the bcc precipitates. With ongoing ageing, a remarkable increase of the mean particle radius is observed, triggered by the dissolution of small precipitates with higher Fe-content. After about $5 \cdot 10^5$ s, the total mean radius evolution is governed by the fcc precipitates only.

The evolution of the number density is strongly affected by the rapid dissolution of the less stable bcc Cu-precipitates (Figure 5.5 (c)). The calculated total number density increases rapidly up to the experimental values. After about 10^4 s, a pronounced decrease in number density is predicted, consistent with experimental observations.

Figure 5.6 shows the evolution of the Cu content of the α-iron matrix together with the predicted nucleus composition of the bcc precipitates. It is interesting to see that the major variations in nucleus composition are present in the early stages of precipitation up to 10^4 s, where the precipitate radius does not exceed values of 1.5 nm. At about 10^4 s, the predicted nucleus composition has changed from 69 at.% to 91 at.%, while the matrix Cu content decreased to 0.75 at.%, which is about half the initial value. With further decreasing Cu content in the matrix, the calculated amount of Cu in the nuclei increases until the equilibrium value of 98 at.% is reached after 10^5 s.
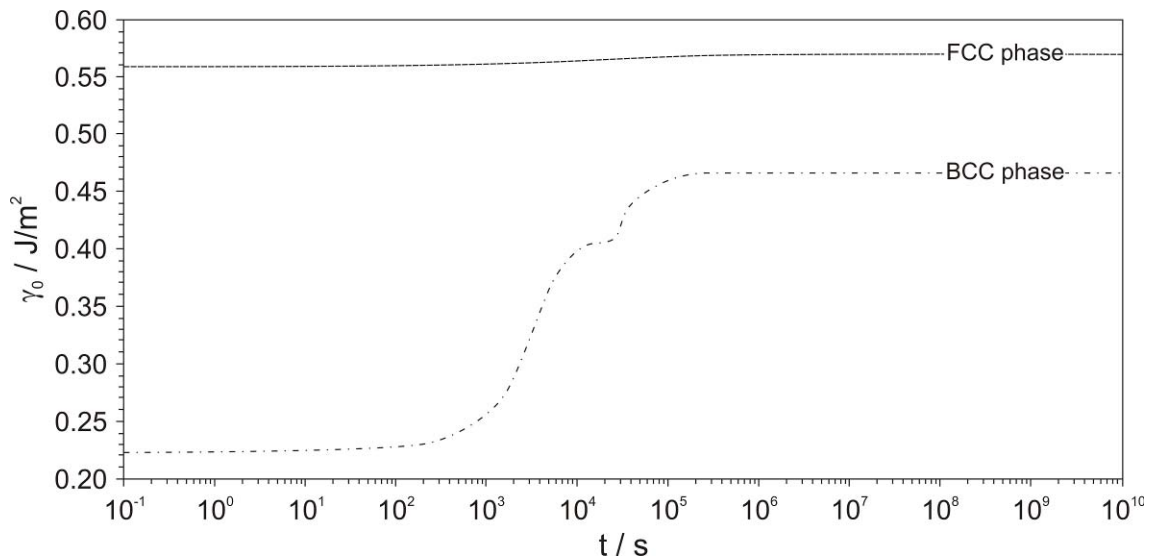
Figure 5.7. Calculated evolution of the planar, sharp interface energy γ_0 of fcc and bcc Cu nuclei.

Because of variations in the Cu content of the bcc precipitates, a remarkable variation of the calculated composition-dependent planar, sharp interface energy γ_0 is observed (Figure 5.7). Compared to the almost constant value for the fcc precipitates (0.56...0.57 J/m^2), an increase of the bcc interfacial energy from 0.22 J/m^2 to 0.47 J/m^2 is observed. This effect has been postulated before by Perez et al.[181], although as a function of precipitate radius. Please note that, in the present simulations, the calculated effective interfacial energy in the nucleation stage is approximately 20% less than the value of the planar, sharp interface due to the effect of interfacial curvature (see section 3.3.3).

5.1.3 Simulation of precipitation strengthening in Fe-Cu alloys

The remarkable strength increase in Cu-containing steel already pointed out in section 5.1.1 can be attributed to a high number density of small coherent bcc Cu precipitates with a mean diameter of about 2-3 nm[83,137,171,172,176,190-194]. For an Fe 1.4 at.% Cu alloy aged at 500°C, Goodman et al.[171] reported a maximum increase of the lower yield stress (LYS) at room temperature of about 355 MPa. At peak hardness, the Cu precipitate volume fraction for this alloy is found to be 0.73% with a mean diameter of 2.4 nm and a number density of 10^{24}m^{-3}. The simulation results in section 5.1.2.2 are in good agreement with these values.

In terms of the prevailing precipitation strengthening mechanism, however, as pointed out by Fine and Isheim[195], it is still not completely clear which mechanism is mainly responsible for the pronounced strength increase in Fe-Cu alloys. In the present work it is assumed that, for the coherent bcc Cu precipitates susceptible to shear, the potential operative strengthening mechanisms are the

a.   chemical hardening effect,
b.   the coherency strain effect and
c.   the modulus strengthening effect[83,137,195-197].

These effects will be investigated in the following sections together with the classical Orowan mechanism for impenetrable particles. The latter mechanism is assumed to be operative after transformation of the precipitates to fcc structure with incoherent precipitate/matrix interfaces.

In a recent treatment by Harry and Bacon[198,], an additional strengthening mechanism was proposed as being operative in Fe-Cu alloys. When a precipitate is sheared by a dislocation, a strengthening contribution from the transformation of the unstable bcc Cu lattice to a close-packed structure was proposed by these authors based on first-principle atomic-scale computer simulations. Basic considerations revealed[195] that this mechanism can lead to a notable strength increase, however, due to the 'preliminary nature' of this theory[125197], and due to the fact that this strengthening contribution is only operative for the first dislocation shearing the particle, this mechanism is not considered further in this section.

To determine the respective strengthening potential of the chemical hardening, the coherency strain and the modulus hardening effect, in the following, the basic formulations introduced in section 4.1.2 are utilized. To determine the mean particle distance λ, eq. (4.29) is applied. Based on these formulations, the strengthening effects are evaluated in the peak strength condition ($t_{peak} \sim$3h) and compared with the experimentally determined strength increase in ref.[171]. Thus, the calculated critical shear stress τ_i is multiplied with a Taylor factor $M=$ 2.5 to convert the critical shear stress in the macroscopic yield strength σ_i of the polycrystalline material. Table 5.1 summarizes the utilized parameters and the results for the different mechanism.

Table 5.1. Evaluated strengthening potential of the different strengthening mechanisms in the peak strength condition after ~3h of ageing at 500°C. The values for σ_i are calculated based on the simulation results in section 5.1.2.2. The input parameters for the different equations are stated in the table, too.

Strengthening mechanism	σ_i, MPa ($\sigma_i = M \cdot \tau_i$)	σ_i / σ_{max}, % (σ_{max}=355 MPa)	Comments
Chemical hardening (according eq. (4.9))	9.5	2.7	b=0.25 nm[125,197] C=0.06
Coherency strain hardening (according eq. (4.10))	70	19.7	C'=0.07 ε_{coh}=0.0057[195] G_{Fe}=81 GPa[125,197]
Modulus mismatch hardening (according eq. (4.16))	283	77.6	G_{Cu}=50 GPa[125,197] M=2.5 λ=eq. (4.29)

Table 5.1 shows that, depending on the considered strengthening mechanisms, different values can be determined varying by about an order of magnitude.

The chemical hardening effect in the peak strength condition reaches values of 9.5 MPa, which are distinctly smaller than the experimentally observed value of 355 MPa. In accordance with Fine and Isheim[195], it can be concluded that chemical hardening makes only a small contribution to the overall strength in Fe-Cu alloys. Considering the effect of a strain field around the coherent bcc precipitates, the maximum strength increase in the peak strength condition amounts to about 70 MPa. In contrast to chemical strengthening, this effect represents a partial strengthening contribution that must not be neglected in this type of alloy. The modulus mismatch hardening amounts to a value of 283 MPa. This is about 80% of the experimentally determined strength increase of 355 MPa, thus making the modulus strengthening effect the major source of precipitation strengthening in the investigated alloy. However, also the chemical hardening effect and the coherency strain effect contribute to the overall strength of the considered Fe-Cu alloy to a greater or lesser extent.

When discussing precipitation strengthening in Fe-Cu alloys, the impact of the structural change of the Cu-precipitates from the coherent bcc to the incoherent fcc structure must not be ignored. Due to the loss of interface coherency, the nature of the precipitate-dislocation interaction changes from shearing of soft precipitates to bypassing of hard particles by looping. In the presence of impenetrable particles, the dislocation interaction with precipitates is described by the Orowan mechanism[89,105]. The strength increase in this

case can be determined according to eqs. (4.4) and (4.29) multiplied with the Taylor factor *M*.

Based on the results of the evaluation of the potential strengthening effects in the peak strength condition and taking into account the structural transformation of the Cu-precipitates during ageing, the precipitation strengthening can be evaluated as a superposition of the chemical hardening effect, the coherency strain effect, the modulus hardening effect and the Orowan mechanism for impenetrable particles. For determination of the first three effects, only the coherent bcc Cu-precipitates are taken into account. For the evaluation of the Orowan threshold stress, only the number density and mean particle radius of the fcc Cu-precipitates are considered.

To calculate the overall precipitation strengthening effect (σ_p), the different mechanisms are superimposed according to the general formulation in section 4.3.1. In the present case, for an assumed value of $\alpha=1$ and $\beta=2$, this superposition rule takes the form

$$\sigma_p = \left(\frac{N_{bcc}}{N_{total}}\right)^{\frac{1}{2}} \sqrt{\sigma_{chem}^2 + \sigma_{coh}^2 + \sigma_{mod}^2} + \left(\frac{N_{fcc}}{N_{total}}\right)^{\frac{1}{2}} \sigma_O . \tag{5.2}$$

In eq. (5.2) N_{bcc}, N_{fcc} and N_{total} are the number densities of the coherent bcc, the incoherent fcc and the sum of the number densities of bcc and fcc precipitates, respectively. The three terms within the square root are the strength contributions of the weak bcc precipitates, caused by the chemical hardening effect (σ_{chem}), the coherency strain effect (σ_{coh}) and the modulus hardening effect (σ_{mod}). The final term in eq (5.2), σ_O, represents the strength contribution of the impenetrable fcc precipitates.

This formulation for precipitation strengthening in the following is utilized, together with the evolution of the solid solution strength module (section 4.2.1), to calculate the evolution of the lower yield stress.

5.1.3.1 Calculation of the LYS

In the present work, the LYS is treated as a superposition of the inherent lattice strength (σ_i), the grain size strengthening (σ_{gr}), solid solution strengthening (σ_{ss}) and precipitation strengthening (σ_p). The strengthening effect from dislocations is expected to be negligible in the present case. For superposition of strengthening mechanisms, eq. (4.37) is used. Thus, the LYS can be calculated as

$$LYS = \sigma_i + \sigma_{gr} + \sigma_{ss} + \sigma_p \,. \qquad\qquad (5.3)$$

According to Hutchinson et al.[83], the inherent lattice strength is σ_i=140 MPa. The effective grain size strengthening contribution of σ_{gr}=40 MPa is determined at time t=0 after reducing the measured LYS in the solution treated state by the intrinsic lattice strength and the solid solution strengthening contribution. The latter can be written as a function of Cu concentration according to eq. (4.30) with a concentration exponent n= 2/3 and a strengthening factor k_{Cu}=40 MPa/(wt.% Cu)[83].

Figure 5.8 shows the calculated LYS evolution together with the individual strengthening contributions. According to the experiment, peak strength is observed after about 1-3 hours ($\sim 10^4$s) of ageing. At this time, a LYS of about 580 MPa is calculated, which corresponds well with the data reported in ref.[171]. After exceeding the point of peak strength, the observed strong decrease of the LYS is well reproduced by the simulation as a consequence of the dissolution of the less stable Fe-rich bcc Cu-precipitates.
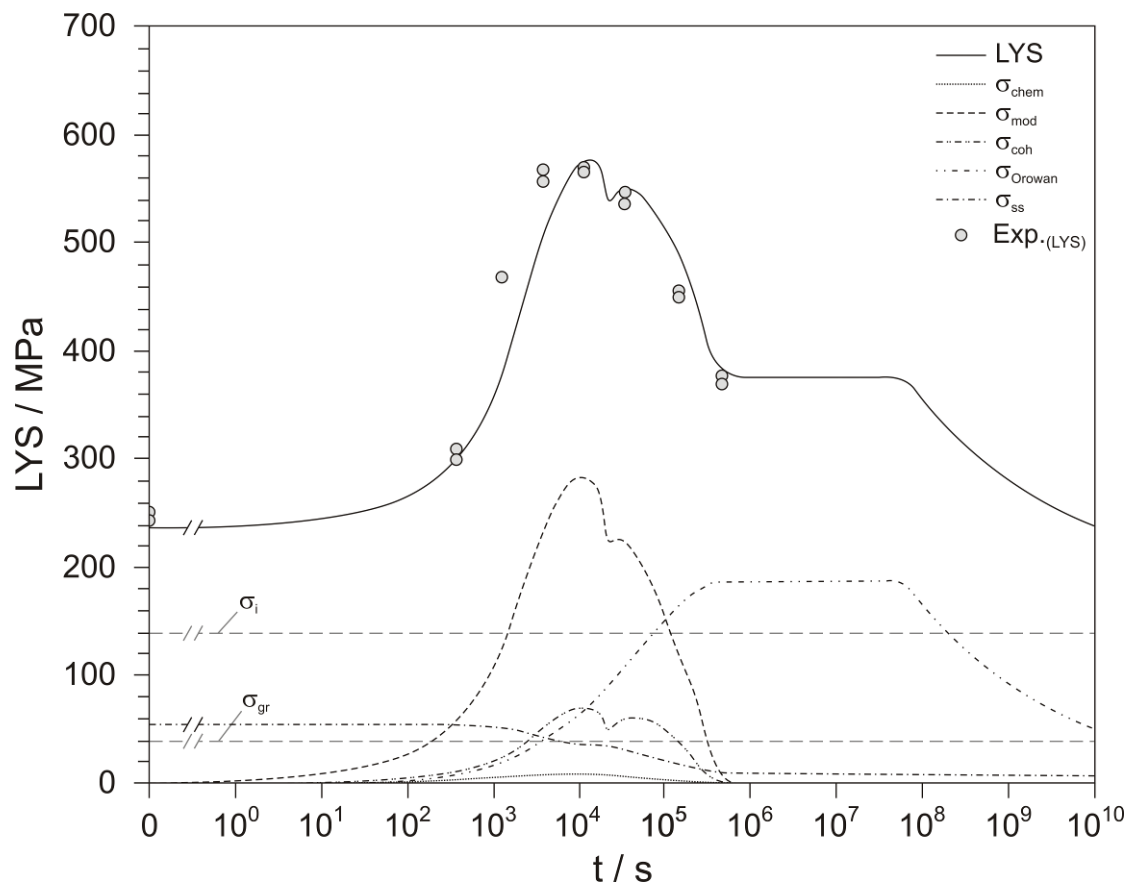
Figure 5.8. Calculated and experimental evolution of the lower yield stress (LYS) as a function of inherent lattice strength (σ_i), grain size strength contribution (σ_{gr}), chemical strengthening (σ_{chem}), coherency strengthening (σ_{coh}) modulus mismatch hardening (σ_{mod}) and solid solution hardening (σ_{ss}).

5.1.4 Summary and Discussion

An extended continuum simulation approach is utilized for the numerical simulation of Cu precipitation in α-iron. The main feature of the simulation model is that the dependence of the chemical composition of the critical nucleus on supersaturation is fully taken into account. The rapid precipitation kinetics in the nucleation and early growth stages are found to be a direct consequence of the significantly decreased interfacial energy of precipitates with lower Cu-content. The rapid dissolution of precipitates after reaching peak density is due to the lower thermodynamic stability of the same precipitates as compared to the higher-Cu containing bcc and stable fcc-precipitates. When taking into account the variable nucleus composition, the evolution of the precipitation parameters, phase fraction, mean radius and number density, can be consistently described.

The precipitation parameters obtained from the computer simulation are utilized in an assessment of precipitation strengthening mechanisms. It is shown that the overall precipitation strengthening effect can be quantitatively described by superposition of the effects of coherent (weak) and incoherent (impenetrable) precipitates. The former effect mainly comprises the coherency strain effect and the modulus hardening effect as well as a small contribution of the chemical strengthening effect. The strengthening contribution from impenetrable particles is calculated from the Ashby-Orowan relationship. Together with the intrinsic strength of the matrix and the solid solution strengthening contribution, good qualitative and quantitative agreement between the calculated and experimental lower yield strength is achieved.

5.2 Application of the back-stress concept on the complex 11% Cr steel COST CB8

5.2.1 The effect of precipitates on the high temperature strength

Precipitation hardening is one of the most prominent ways of strengthening materials. Precipitates can effectively hinder dislocation and subgrain movement and, thus, increase the resistance of the material microstructure against plastic deformation. In industrial processes, size and number density of precipitates are controlled by the chemical composition of the alloy as well as the thermo-mechanical processing route. Due to the significant influence of precipitates on the mechanical properties of the material, efficient characterization, modelling and simulation of precipitation processes in multi-component alloys is of considerable relevance for industry as well as academics. The goal of these activities is to be able to produce materials with an optimized spectrum of mechanical properties based on a fundamental understanding of the complex interactions between precipitates and microstructure.

Materials with superior creep properties are characterized by a microstructure, which exhibits a superior long-term resistance against plastic deformation. This can be achieved by strong pinning forces upon dislocations and subgrain boundaries. The two major effects of precipitates on the creep properties of a material are:

a. Increase of the creep strength by direct interaction between precipitates and dislocations. Precipitates effectively hinder dislocations in their ability to move through the material as a consequence of an external load. Thus, the creep process is considerably slowed down and the creep rate is minimized.

b. Stabilisation of the initial microstructure by pinning of grain and subgrain boundaries. The high strength of the materials in the 'as-received' condition, i.e. the conditions in the delivery state before service, is conserved, because grain and subgrain coarsening is hindered.

The interactions between microstructure and creep properties have been investigated in detail in numerous experimental and theoretical studies. Thus, the interested reader is referred, at this point, to further literature[23,48,50,67,69,200-204].
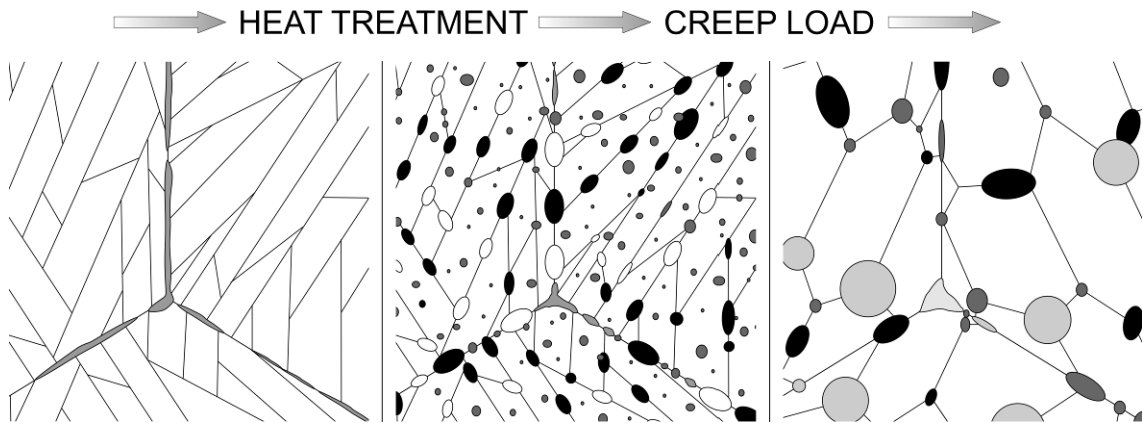
Figure 5.9. Schematic evolution of the microstructure during heat treatment and service. Note that all images relate to the same length scale.

Figure 5.9 shows a schematic picture of the evolution of a typical microstructure as observed in ferritic/martensitic 9-12% Cr-steels. The schematics emphasize the role of precipitates in conserving the favourable fine-grained microstructure. After solidification and cooling to room temperature, the microstructure of typical 9-12% Cr-steels consists of primarily martensite, with, usually, coarse and elongated precipitates along the prior austenite grain boundaries (see Figure 5.9, left). In the course of the austenitising and quality heat treatments, a dense distribution of fine precipitates is produced (see Figure 5.9, centre). If the material is exposed to long-term thermal and mechanical loading during service, coarsening of the precipitate microstructure occurs (see Figure 5.9, right). Simultaneously, the material softens because the mean distance between individual precipitates increases, which leads to a decrease of the effective pinning force.

In the following sections, the evolution of precipitates throughout the entire manufacturing process is investigated. First, the results of a comprehensive experimental characterisation of the precipitate microstructure at several stages of the casting, austenitising and quality heat treatment processes are briefly reviewed based on the experimental work reported in refs.[42,205]. Then, the interaction of precipitates with dislocations and subgrains and the consequences for the strength of the material are discussed. The chapter is concluded by a quantitative analysis of the loss of precipitation strengthening during service on the example of the 11% Cr-steel CB8.

5.2.2 Microstructure analysis of the COST alloy CB8

The experimental test alloy CB8, which is exemplarily used in the following analyses, has been designed in the COST programme 522[*]. It is a typical 11% Cr steel for cast application, which showed excellent creep properties in short-term tests. For this reason, the variant CB8 has been extensively investigated also at longer times. However, a significant drop in creep strength has been observed after approximately 10,000 hours of service exposure. The most important results of the experimental characterization are summarized subsequently. The chemical analysis of the steel CB8 is given in Table 5.2.

5.2.2.1 Precipitate evolution during manufacturing

In extensive work of Sonderegger[42] and Plimon[205], the evolution of precipitates has been investigated for the first time at different positions (Pos. 1-4) of the heat treatment

Table 5.2. Chemical composition of steel CB8 steel - heat 173 (in wt.%)

C	Si	Mn	Cr	Ni	Mo	W	V	Nb	Co	Al	B	N
0.17	0.27	0.2	10.72	0.16	1.40	-	0.21	0.060	2.92	0.028	0.0112	0.0319
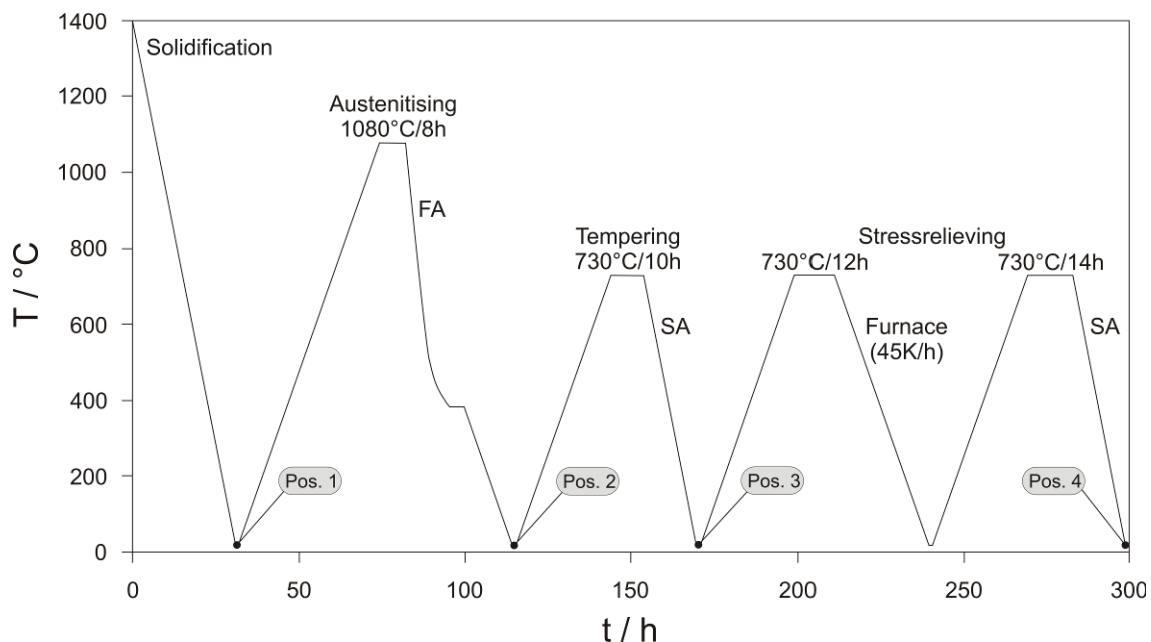
Figure 5.10. Heat treatment of COST alloy CB8 with specimen positions for experimental characterization.

[*] The COST variant CB8 has been selected because the most complete experimental picture of the precipitate evolution is available for this melt. These data are finally used for verification of the computer simulations.

process. The thermal profile of this treatment is shown in Figure 5.10. It is typical for industrial components and already applied for other 9-12% Cr cast steels.

In the 'as-cast' condition (Pos. 1), the specimen microstructure consists of mostly martensite. Only small amounts of retained austenite could be detected by X-ray diffraction (0.8%). The size of the primary austenite grains is between 0.5 and 2.0 mm. The martensite lath width as well as the subgrain size is approximately 1 μm. These parameters remain almost constant throughout the entire heat treatment. Figure 5.11 shows an optical micrograph of the 'as-cast' microstructure, with prior austenite grain boundaries clearly visible as thin white lines.
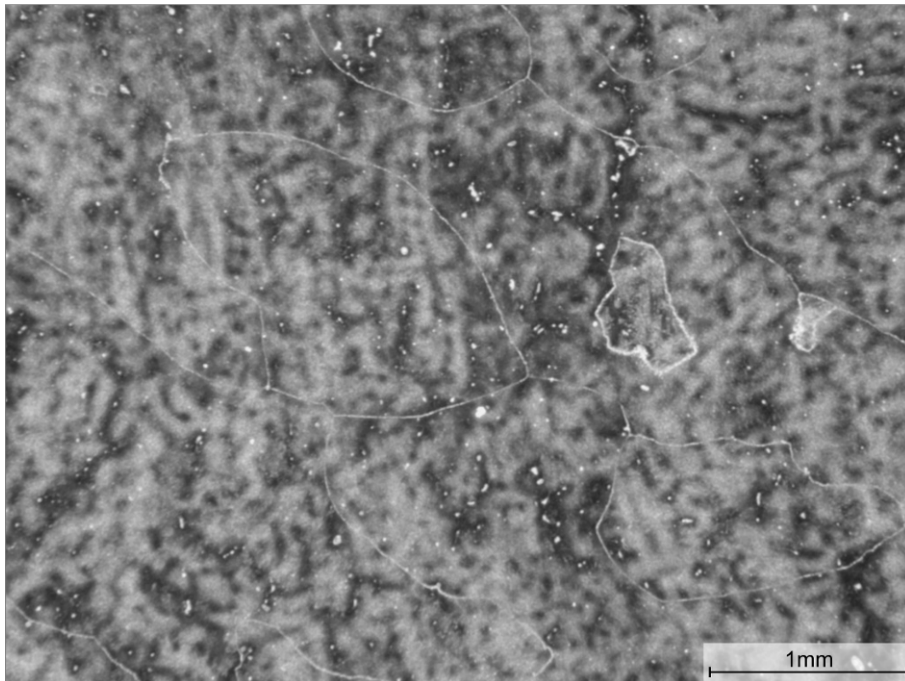
Figure 5.11. Optical micrograph of microstructure in the 'as-cast' condition. Segregated regions from solidification are clearly observed as well as prior austenite grain boundaries.

On detailed investigation of the prior austenite grain boundaries (PAGB), elongated precipitates have been detected (see Figure 5.12). The chemistry and crystal structure of the precipitates indicates that these are large Mo-rich precipitates (probably Mo_3B_2) and Cr-rich precipitates (probably M_7C_3 and $M_{23}C_6$) with diameters of approximately 200 nm. Precipitates of similar type also occur in the strongly segregated interdendritic regions (dark regions in Figure 5.11). The interior of the prior austenite grains is otherwise more or less free from precipitates (see Fe-jump ratio TEM image in Figure 5.13).
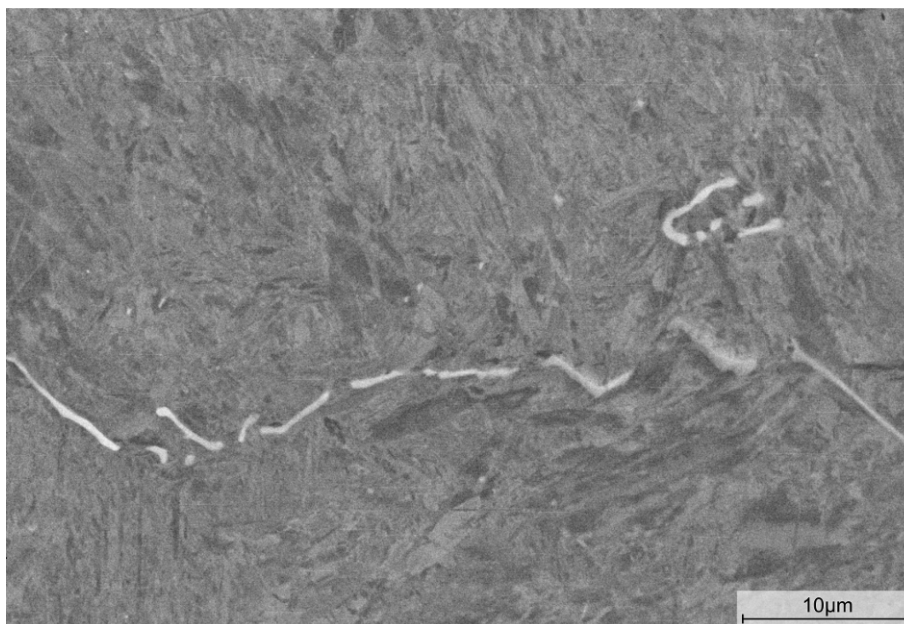
Figure 5.12. Elongated precipitates along the PAGB (scanning electron micrograph, SEM).
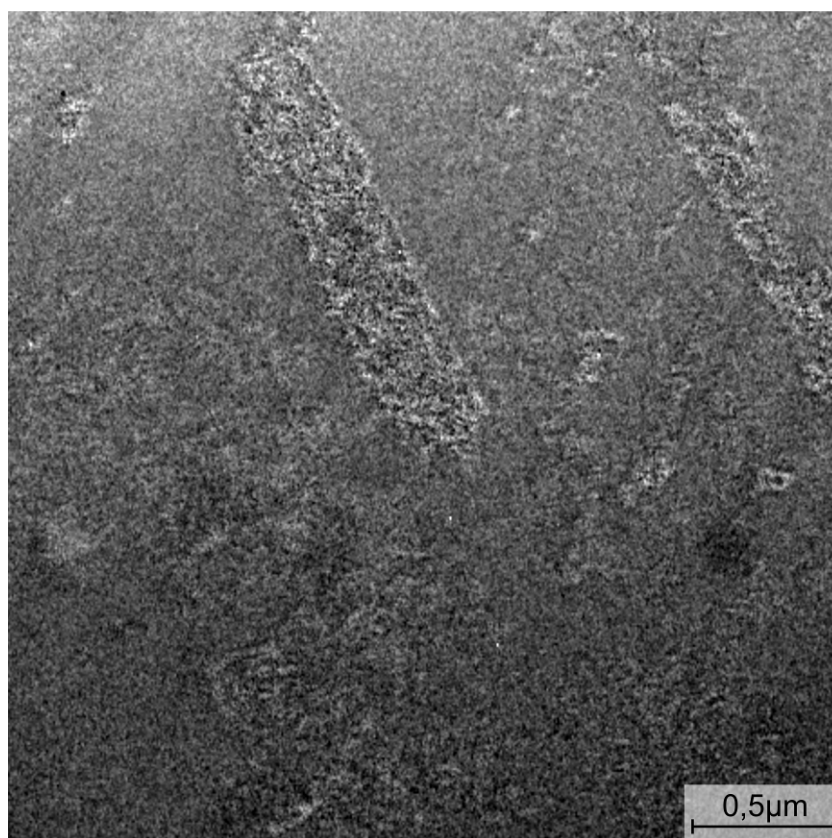
Figure 5.13. CB8 in 'as-cast' condition. Fe jump-ratio image

(transmission electron micrograph, TEM).
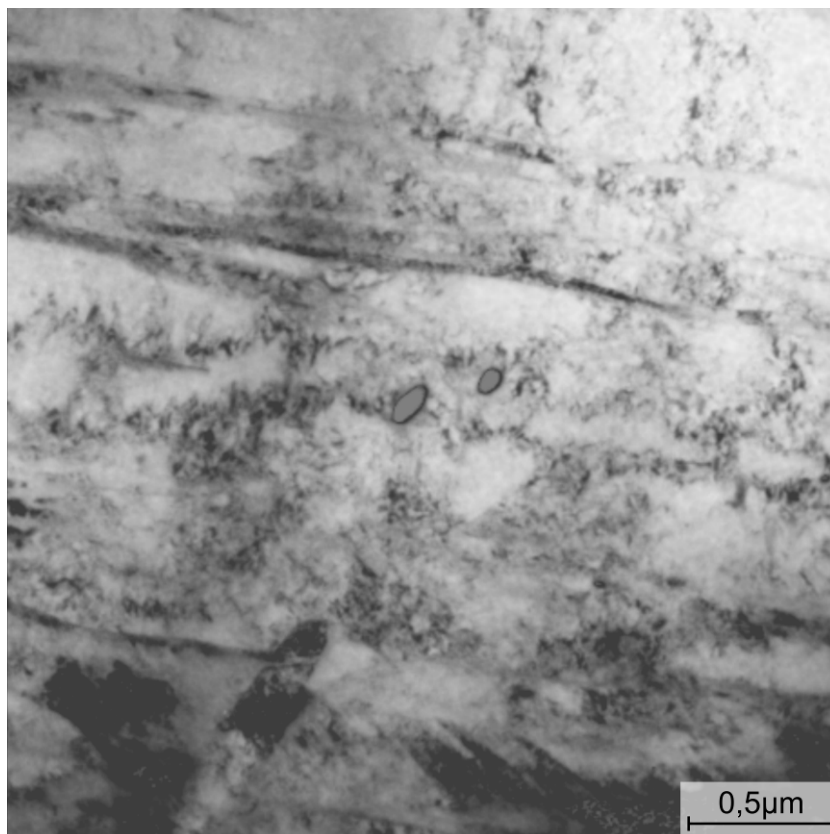
Figure 5.14. CB8 after austenitising (TEM bright field).
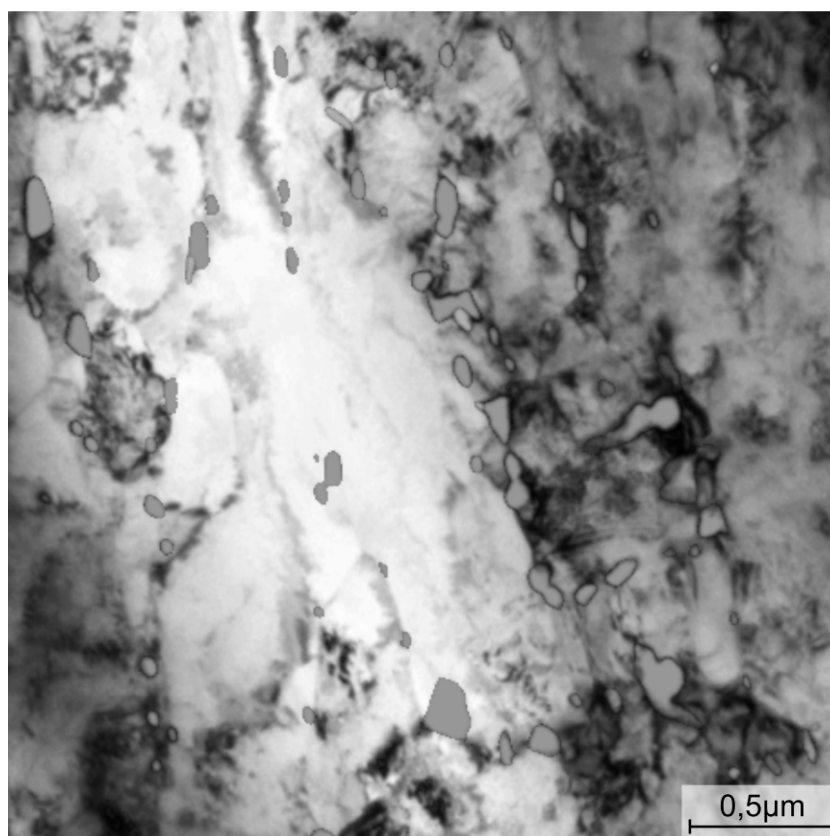
Figure 5.15. CB8 after first heat treatment (TEM bright field).

After austenitising (Figure 5.14), a certain degree of homogenization of the segregated concentration peaks is observed. The Mo_3B_2 precipitates at the PAGB have more or less disappeared. Moreover, NbC precipitates are identified, which are randomly distributed in the matrix, and small, needle-shaped Mo-rich precipitates. The latter disappear again during further heat treatment.

After the first quality heat treatment (Pos. 3), a significant increase in the number of precipitates is observed (Figure 5.15). $M_{23}C_6$ precipitates are found in high number as well as VN particles. Both types of precipitates appear preferentially at the martensite lath and subgrain boundaries.

In the sample, corresponding to the 'as-received' condition (Pos. 4), first indications of slight coarsening of $M_{23}C_6$ precipitates are observed (Figure 5.16). The volume fraction of VN and the mean precipitate radius have significantly increased. NbC is still present also in this heat treatment condition. According to Dimmler et al.[58], first sparse Laves phase precipitation is observed in the 'as-received' condition.
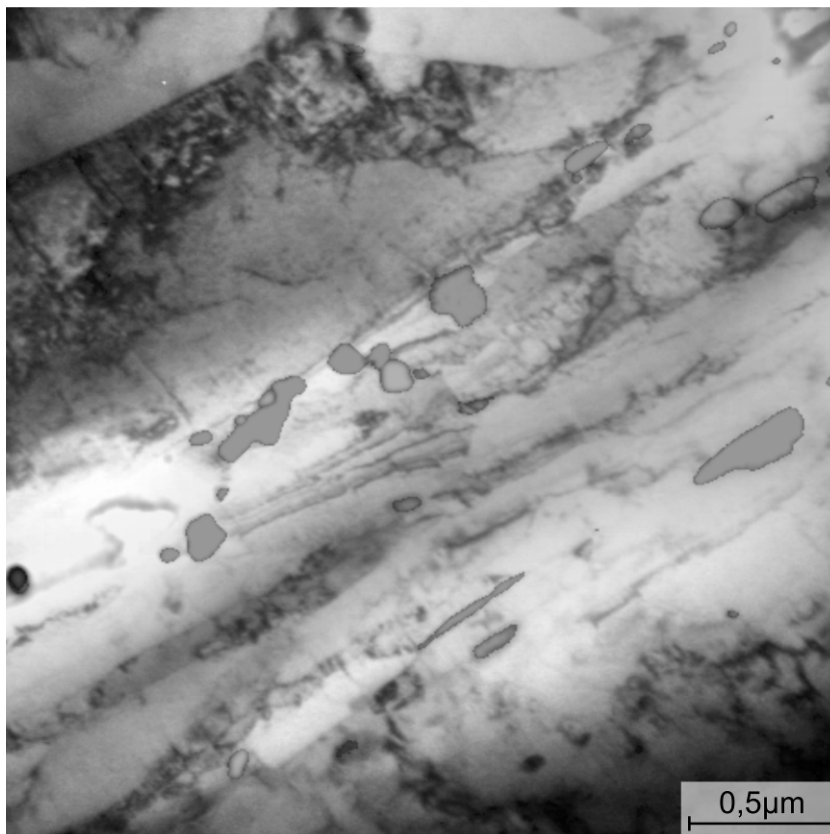
Figure 5.16. CB8 in the 'as-received' condition (TEM bright field).

5.2.2.2 Precipitate evolution during service

In the analysis of the development of the microstructural parameters in the course of long-term service of CB8 at 650°C for 2,000 und 7,000 hours, Sonderegger[42] found that the martensite lath width and the subgrain size remain almost constant in samples without mechanical loading. In the samples, which have been exposed to creep loading, the subgrain size slightly increases from 0.7 μm to 1.0 μm. Moreover, clear indications for coarsening of $M_{23}C_6$ precipitates are observed in the heat-treated and creep-loaded samples. In contrast, the mean precipitate radius of VN remains almost constant in both samples, while the number density increases visibly.

The phase fraction of Laves phase increases significantly during service. Dimmler[58] found that the phase fraction increases from 0.4 to 0.8% for samples analysed after 50 and 16,000 hours, respectively. Simultaneously, the mean radius also increases. In the first 1,000 hours, an increase of the number density of Laves phase precipitates is observed, indicating significant nucleation of new precipitates of this phase. After 1,000 hours, the number density remains constant.

After 16,000 hours of service, the number density of the VN precipitates suddenly reduces drastically. This tendency is stronger in the creep-loaded samples, which indicates that the external load enhances the microstructure evolution. The reason for the VN dissolution is found in the appearance of the modified Z-phase, which has first been detected in the sample with 16,000 hours service time. Z-phase has a higher thermodynamic stability compared to VN, however, nucleation of this phase is very difficult, which is the reason that Z-phase is not observed earlier. The role of Z-phase in the drop of creep resistance in many 9-12% Cr steels is discussed in ref.[69].
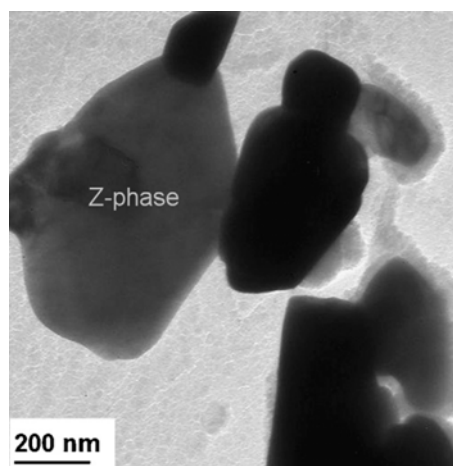
Figure 5.17. Z-phase particle after heat treatment (ref.[62]).

5.2.3   Computer simulation of the precipitate evolution in CB8

In the following, the MatCalc model outlined in section 3.3.2 is applied to the simulation of the precipitate evolution during the entire heat treatment and service of the steel CB8.

First, a thermodynamic equilibrium analysis of this steel is performed, which provides an overview of the type and amount of different phases that can be expected to occur at given chemical composition and temperature. Then, the results of the kinetic simulation are discussed. For details about the simulation settings utilized for the following calculations, the reader is referred to Rajek[3] who discussed in detail the simulation input parameters for the kinetic simulations of complex 9-12% Cr steels.

5.2.3.1 Thermodynamic equilibrium analysis

The thermodynamic equilibrium analysis is an important step in a comprehensive material characterization. By this method, information can be obtained about:

a.   The type and amount of phases, which occur in this material under equilibrium conditions.

b.   Chemical composition of the equilibrium phases.

c.   Equilibrium solution temperatures of the individual phases, giving indications on temperatures for optimum heat treatment conditions.

d.   Equilibrium transformation temperatures at which allotropic transformations (e.g., fcc-bcc/bct transition) occur.

Figure 5.18 and Figure 5.19 show the calculated phase diagrams for the steel CB8 as a function of carbon and nitrogen content. All simulations are based on the thermodynamic database TCFE3 and the diffusion database Mobility_v21 from ThermoCalc AB, Stockholm, Sweden. To account for the stabilizing effect of silicon on Laves phase, the corresponding parameters have been modified as suggested by Dimmler[58]. Moreover, although not considered in the phase diagrams of Figure 5.18, a revised thermodynamic description for the modified Z-phase[206] has been added to this database, which is a further development of the initial assessment of Danielsson and Hald[207]. These values have been used in the kinetic simulations presented in the following section.
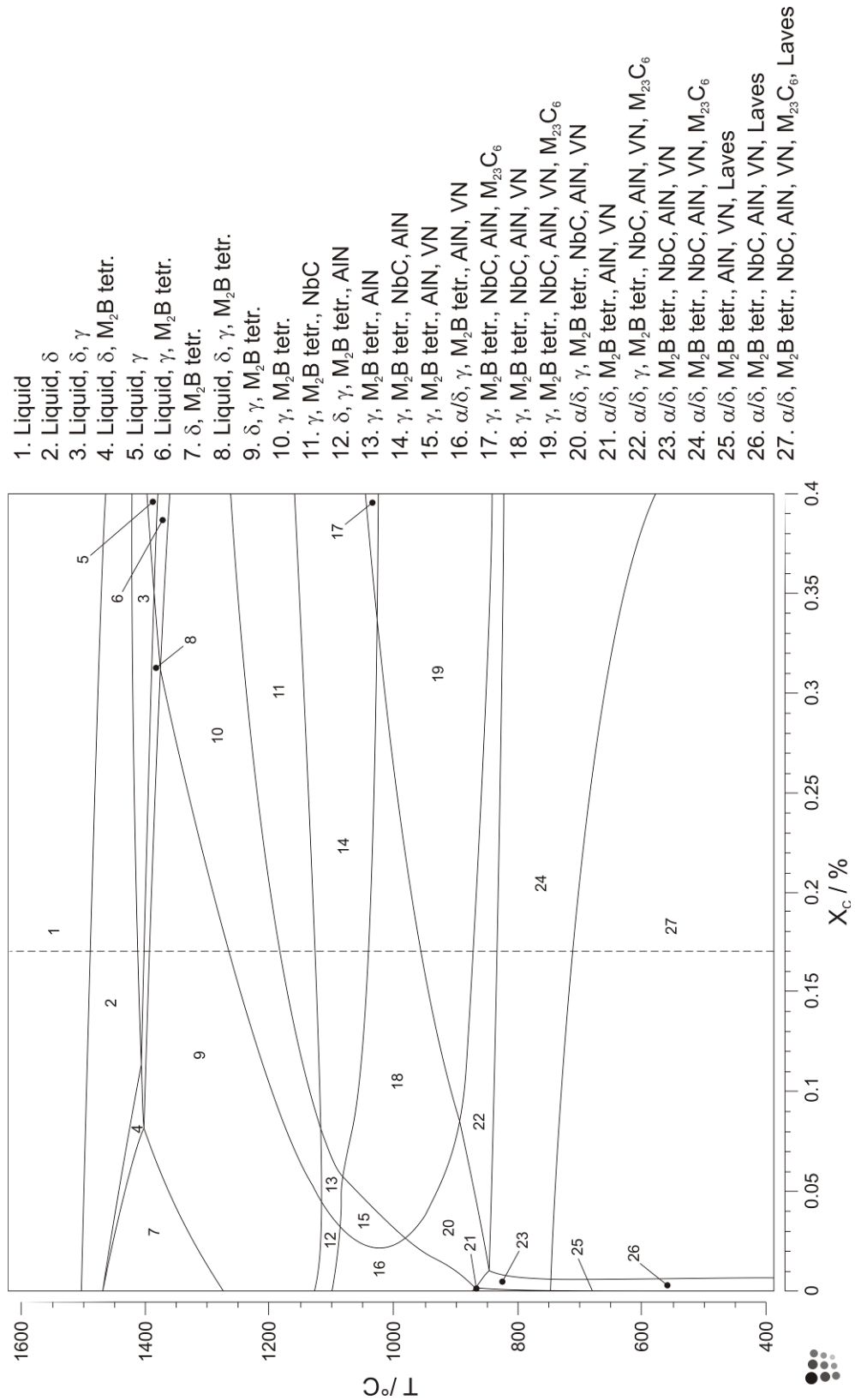
Figure 5.18. Phase diagrams for steel CB8 obtained from computational thermodynamics as function of carbon. The modified Z-phase, which replaces VN and, eventually, NbC precipitates at long times, has been neglected,; the boride phases are included.
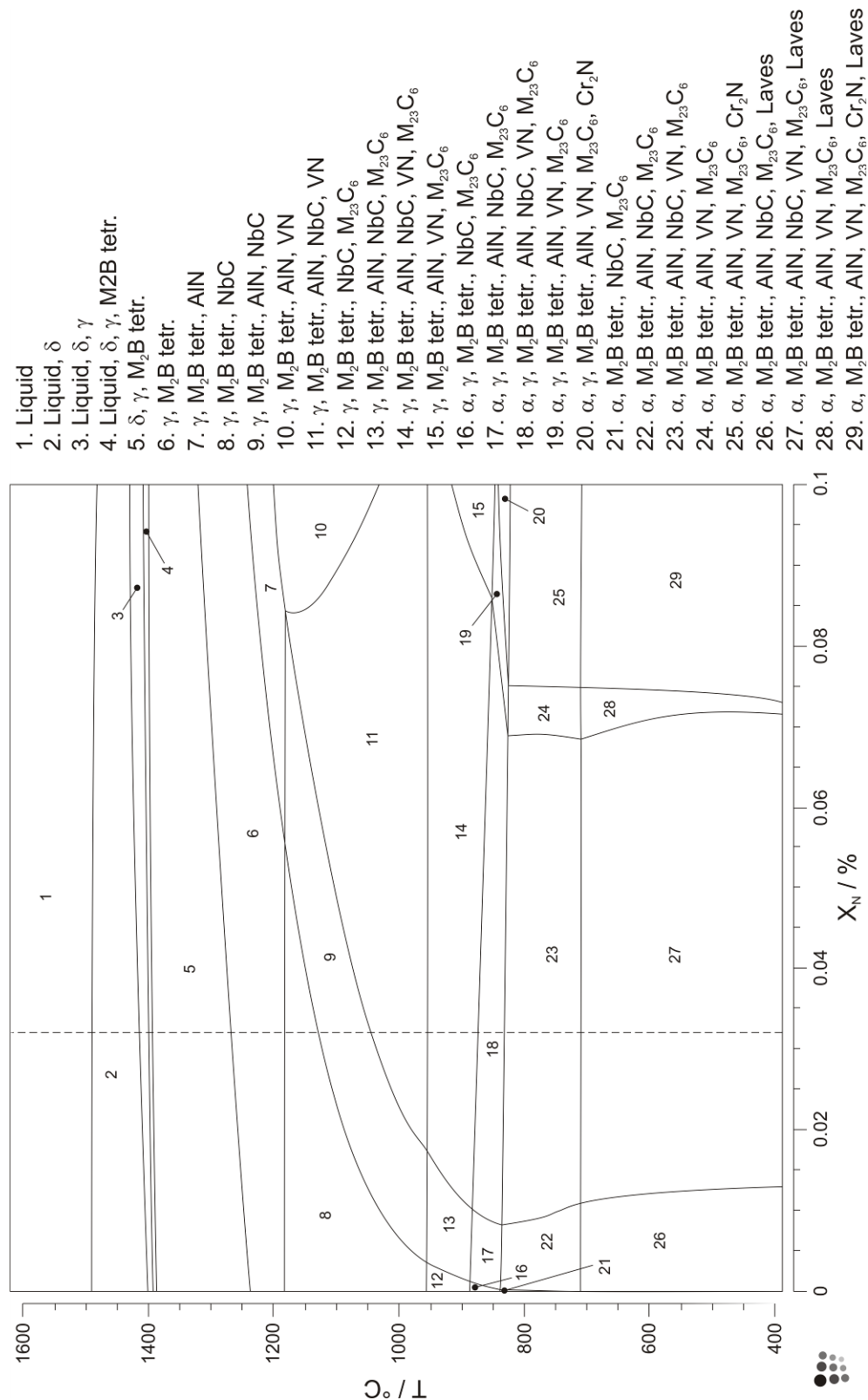
Figure 5.19. Phase diagrams for steel CB8 obtained from computational thermodynamics as function of nitrogen. The modified Z-phase, which replaces VN and, eventually, NbC precipitates at long times, has been neglected,; the boride phases are included.

5.2.3.2 Simulation of the precipitation kinetics in the COST alloy CB8

With the theoretical model for multi-component precipitation kinetics implemented in the software MatCalc and the thermodynamic and kinetic data described in the previous section, the entire heat treatment of the COST alloy CB8 has been studied. Figure 5.20 summarizes the results of the simulation.

When looking at the temperature profile of the heat treatment (top image in Figure 5.20), several individual steps can be distinguished. The simulation starts at 1400°C, which is closely below the solidus temperature of this alloy. It is assumed that all elements are homogeneously distributed in the matrix at this time and no precipitates exist. The material then cools linearly to a temperature of 350 °C. This temperature corresponds to the observed austenite to martensite start temperature. In the simulation, it is assumed that this transformation occurs instantaneously and the parent and target phases have identical chemical composition. It is further assumed that no diffusive processes and, consequently, no precipitation occur below this temperature. At this point, the matrix phase is changed from face centered cubic (fcc) austenite to body centered cubic (bcc) ferrite structure.[*]

In the next step, the material is reheated for austenitising. At the experimentally observed transformation temperature of 847°C, the ferrite matrix is changed to austenite again. After austenitising, the transformation to martensite/ferrite is performed again at 350°C. After three quality heat treatments, service at 650°C for 100,000 hours is simulated.

The three other plots in Figure 5.20 display the evolution of the phase fraction f, the mean precipitate radius R and the number density N of each precipitate type. The phase fractions of $M_{23}C_6$ and Laves-phase are multiplied by a factor of 0.1 to give a better visual representation of the results.

During cooling from 1400°C, various precipitate phases nucleate at the austenite grain boundaries. At room temperature, NbC, VN, $M_{23}C_6$, M_7C and Laves-phase precipitates are observed. After changing the matrix phase from austenite to ferrite and reheating, severe precipitation of all phases sets in again. Most phases, except NbC, dissolve again during further heating to and holding at austenitising temperature of 1080°C. During subsequent cooling and the first of the three quality heat treatments, nucleation of various precipitates continues. Slight coarsening of some precipitates, particularly $M_{23}C_6$ is already observed.

---

[*] Since no separate thermodynamic description is available for the bct martensite phase, the bct phase is substituted by the bcc phase in the simulations.

During service, the simulation predicts significant precipitation of Laves-phase, which is in accordance with the observations of Dimmler[57]. After several thousand hours of service, the phase fraction of the modified Z-phase gradually increases and, simultaneously, the thermodynamically less stable VN precipitates start to dissolve. Again, this is consistent with experimental observation[42]. It should be noted that, due to the different possibilities of Z-phase nucleation (Z-phase can be formed by heterogeneous nucleation in the matrix as well as by direct transformation of VN into Z-phase[208]), two Z-phase populations are introduced in the simulation.

Generally, the simulation results are in reasonable agreement with the experimental data for CB8. In view of the complexity of the problem and the high degree of abstraction of the theoretical model, the overall performance of the simulation is excellent. It is particularly important to emphasize that the simulations have been performed on basis of independent thermodynamic and diffusion databases and no general fit parameters have been used. The very few necessary modifications of the original thermodynamic database and the correction of the estimated interfacial energy for the Laves-phase are well founded and described in detail in ref.[3].

In the next section, the interaction between precipitates and microstructure is analyzed, until in section 5.2.5, a prediction of the loss of precipitation strengthening over the lifetime of a component made from CB8 is attempted.
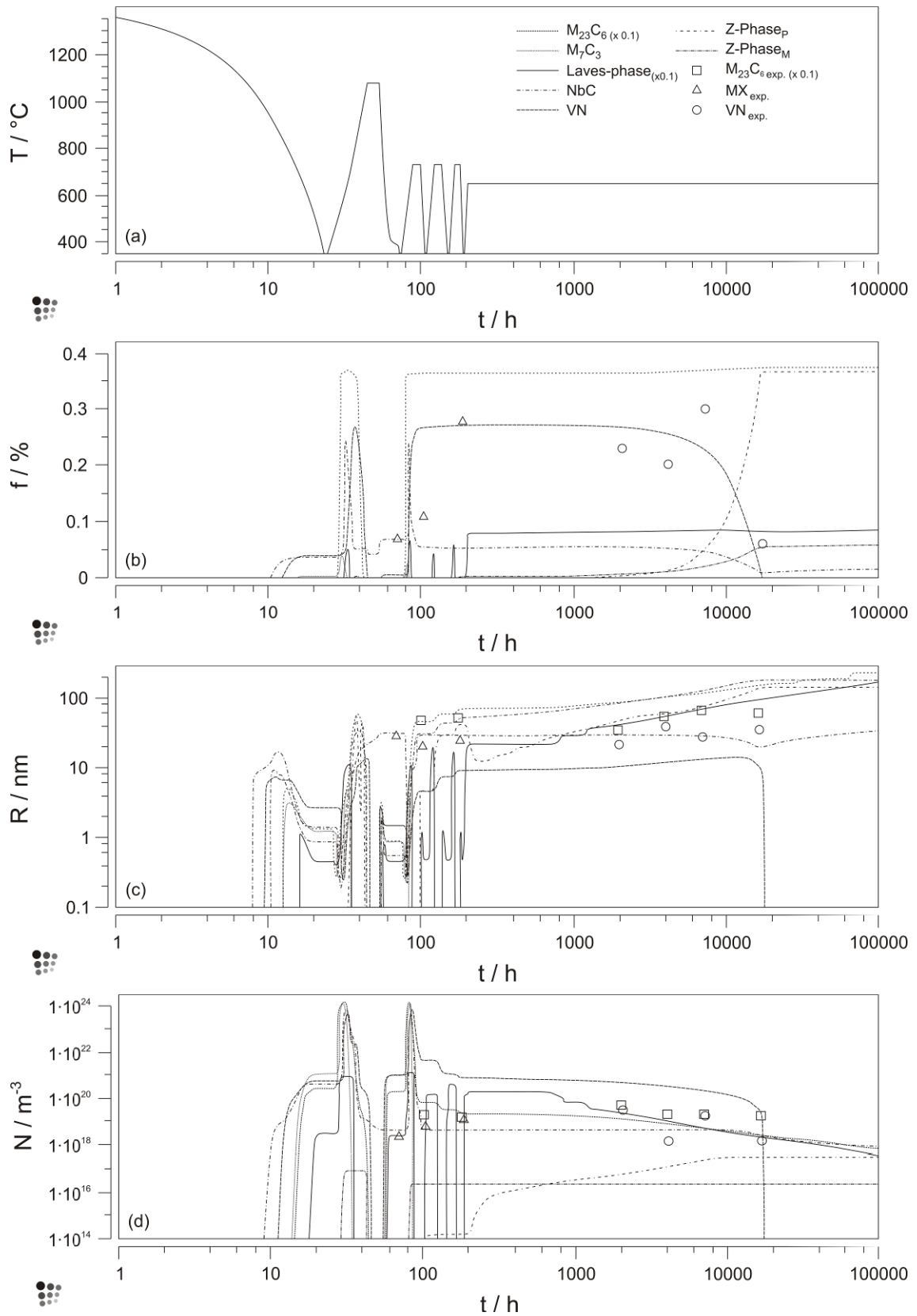
Figure 5.20. Kinetic simulation of the precipitate evolution in CB8 during (a) heat treatment and service; (b) *f*, phase fraction, (c) *R*, mean precipitation radius, (d) *N*, number density. The phase fractions of $M_{23}C_6$ and Laves-phase are multiplied by a factor of 0.1 to give a better visual representation of the results.

5.2.4 Microstructure – property relationships

As already pointed out in section 5.2.1, precipitates act as microstructure-stabilizing components and as efficient obstacles for dislocation movement. In this section, the interaction forces between precipitates and dislocations as well as grain and subgrain boundaries are analyzed on a quantitative basis according to the remarks given in chapter 3.2.2. Based on this discussion, the application of the back-stress concept to evaluate the impact of precipitates on the overall creep strength evolution is briefly outlined.

5.2.4.1 Precipitate - dislocation interaction

Precipitates and mobile dislocations can interact in one of the following ways (see e.g. reference[209]):

a. A dislocation can pass coherent precipitates by cutting the precipitate*[210]. A stacking fault is left in the precipitate.
b. A dislocation can pass precipitates by bending between them and closing the bent lines to loops. A dislocation loop is left around the bypassed precipitate (Orowan mechanism[89]).
c. A dislocation can pass the precipitate by climbing (general or local climb[88]).
d. A dislocation can drag the precipitates with it. This mechanism is possible only for very small precipitates. The velocity-determining factor in this case is the mobility of the dragged precipitates.

The operating precipitate-dislocation interaction mechanism is depending on a number of factors, among which the availability of glide planes, the height of the local forces and the hardness of the precipitates are most important. Due to the physical nature of the four processes, mechanisms 1 and 2 are considerably faster than mechanisms 3 and 4. If the latter are the operating creep mechanisms, the creep rate is significantly lower than the creep rate based on mechanisms 1 and 2. For details, the interested reader is referred to references[88,90,134211,212].

---

* Even in the case of a precipitate, which is not susceptible to shear, irrespective of the hardness of a hard particle, there will be a transition to particle cutting at very small particle sizes.

In the case of 9-12% Cr steels, the precipitates are sufficiently hard and large, such that dislocations cannot bypass them by cutting[87]. Thus, the upper limit of the pinning force of precipitates on dislocations is determined by the Orowan threshold stress according to eq. (4.4).

5.2.4.2 Precipitate - subgrain boundary interaction

The pinning force of precipitates upon subgrain boundaries can be described based on a suggestion of C. Zener (reference [3] (private communication) in C.S. Smith[95]), which originally describes the drag force on grain boundaries during grain growth in the presence of precipitates. The basic idea is that a precipitate, which is located on a grain boundary, reduces the effective grain boundary area. On leaving the particle behind, this area must be re-established. This process requires energy and, thus, acts against boundary migration. A number of modifications of the original theory have been developed since, which have been reviewed by Manohar et al.[213].

McLean[96] has pointed out that Zeners's ideas can likewise be applied to subgrain pinning. Accordingly, the mobility of subgrain boundaries is strongly reduced in the presence of precipitates, which has been observed experimentally, for instance, in TEM investigations of Eggeler[100]. The critical subgrain radius R_{crit} during subgrain coarsening, above which the coarsening process comes to a stop, is given by

$$R_{\text{crit}} = 0.846 \sqrt{\frac{1}{N \cdot r}}, \tag{5.4}$$

where N is the number density of the precipitates and r is the mean precipitate radius. The effective retarding force of subgrains upon dislocation movement can be estimated according to Gladman[85] and Mc Elroy and Szkopiak[98] based on the grain size dependent contribution to the Hall-Petch relation. Taking into account eq. (5.4), the strength contribution from subgrains (τ_{sgb}) can be determined as

$$\tau_{\text{sgb}} = \frac{k_{\text{d}}}{d_{\text{s}}^{m}}, \tag{5.5}$$

where k_{d} represents the subgrain strengthening coefficient[85], d_{s} is the subgrain size and m is an exponent, which is typically in the order of $m=1/2$. According to Gladman[85], k_{d} is

usually much smaller than the coefficient for grains. Kosik et al.[214] have considered the effect of subgrains as being comparable to cold-working. However, it has been found that the subgrain size changes only slightly during heat treatment and service[42]. Consequently, the stress contribution of subgrains remains more or less constant during service and it is therefore not further considered when determining the possible reasons for the strong change in creep strength with ongoing service time.

5.2.4.3 Precipitate - grain boundary interaction

Precipitates similarly affect the mobility of grain boundaries; however, the mechanism of pinning is different to that for subgrain boundaries. The latter are small angle boundaries and, thus, represent an array of dislocations, which accommodate the small lattice misfit between the two subgrains. A grain boundary is a randomly oriented high-angle boundary. In the case of 9-12% Cr steels, the fraction of grain boundaries is very small compared to subgrain boundaries because typical grain sizes are on the order of several hundred micrometers for forged materials or even millimetres in the case of cast materials, whereas subgrain sizes are typically on the order of few micrometers or less. The influence of grain boundaries is therefore also neglected in the further analysis due to the small strengthening contribution.

5.2.4.4 Application of the back-stress concept

As already pointed out in section 3.2.4, at elevated temperatures, and if only a small external load is applied, which are conditions that are typical for creep deformation, part of the external driving pressure σ_e is counteracted by heterogeneous internal microstructural constituents, such as precipitates and interfaces. Consequently, not the entire external load can be assumed to represent the driving force for the creep process; only this part of the external stress σ_{ex}, which exceeds the amount of *inner stress* σ_i from the counteracting microstructure, effectively contributes to the creep process. Since the inner stress reduces the effect of the external stress, this approach is commonly denoted as *back-stress concept*. The impact of the consideration of an internal stress or back-stress σ_i on the creep rate, as a superposition of individual contributions from dislocations, subgrains and precipitates, was already explained, but is briefly recapitulated in the following. When taking into account the inner stress, the general Norton creep law (see, e.g., ref.[104]) can be rewritten as

$$\dot{\varepsilon} = A \cdot (\sigma_{ex} - \sigma_i)^n = A \cdot (\sigma_{eff})^n, \tag{5.6}$$

where A and n are constants. Thus, a microstructure property link is stated, which directly allows an inference on the change of creep properties based on the microstructural evolution expressed by the different strength contributions of the respective microstructural quantities.

As stated previously, due to the important role of precipitates as microstructure stabilizing element and the small grain boundary and the almost constant subgrain boundary contribution to the overall creep strength, it is assumed that the change in creep strain rate of the alloy[91] and, thus, the evolution of the creep properties of the material is primarily determined by the evolution of the precipitate microstructure.

The contribution of precipitates to the total back-stress has already been discussed in section 5.2.4.1 and is described by the critical Orowan stress τ_{Orowan}. This quantity denotes the maximum back-stress caused by a random distribution of precipitates with a mean distance λ between the precipitates. The latter is estimated for the present investigations according to eq. (4.20). When combining eqs. (4.4) and (4.20), the total back-stress contribution from a bulk distribution of precipitates reads

$$\tau_{prec} = CGb\sqrt[3]{\frac{\pi N_i}{6}} \ln\left(\frac{r_a}{r_i}\right). \tag{5.7}$$

The quantity τ_{prec} represents the maximum back-stress caused by precipitates. If the external load reduced by the back-stress contribution of the other strengthening mechanisms is below this threshold, the dislocations are effectively pinned and can only pass the precipitates by the climb mechanism. Since dislocation climb is a diffusional process, the effective creep rates are usually low. If the threshold stress is exceeded, the dislocations can bypass the precipitates by the Orowan mechanism, which is a much faster process compared to climb. When this change in mechanism occurs, the exponent in the Norton creep law increases significantly and creep deformation is strongly enhanced.

The selection of operative creep mechanism is mainly determined by the height of the external load. However, a transition from dislocation climb to the Orowan mechanism can also be caused by a decrease of back-stress during service. If this transition occurs, for instance, due to coarsening of precipitates or thermodynamic instability of a precipitation strengthening phase, extrapolation of the creep strength from short term experiments to

long term service behaviour can result in fatal over-estimation of the residual life time of components. This aspect has been discussed in detail by Dimmler et al.[57,59].

5.2.5 Loss of precipitation strengthening during service of COST alloy CB8

In this section, the theory and methodology described previously is applied to a prediction of the evolution of the strength contribution of precipitates during service of the steel CB8. The simulation results shown previously in section 5.2.3.2 are used as a basis and evaluated in terms of the maximum Orowan stress, i.e. the back-stress contribution from precipitates.

For the evaluation of the back-stress during service at 650°C, the constants in equation (5.7) are assumed to be C=0.19 and G=62.3 GPa (converted from the data in ref.[215]). The outer cutoff radius r_a is assumed to have a value of two times the mean precipitate radius r_a=$2r_{prec}$[105] and the inner cutoff radius is taken as two times the Burger's vector with r_i~$2b$ (~0,5 nm). Figure 5.21 shows the predicted evolution of the back-stress during service as calculated with the model described in this chapter. The graphs show the predicted contributions for each phase separately as well as the total back-stress including the combined effect of all precipitates with and without the effect of Z-phase.
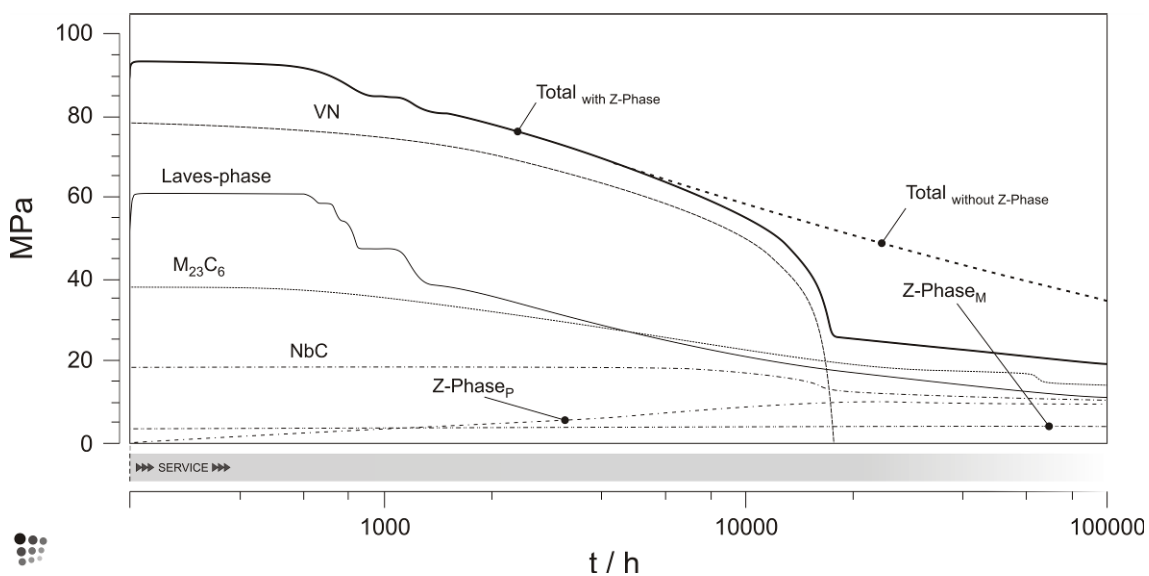
Figure 5.21. Predicted degradation of the precipitate back stress (Orowan threshold stress) during service of the COST alloy CB8 including the modified Z-phase contribution (solid bold line) and artificially suppressing this phase (dashed bold line). The subscript P denotes precipitates of Z-phase nucleated on existing VN particles, the subscript M denotes Z-phase precipitates nucleated in the matrix.

In the 'as-received' condition, after all heat treatments, the total strength contribution from precipitation hardening is estimated to be in the order of 90 MPa[*]. Due to the inevitable effect of Ostwald ripening (coarsening), the density of precipitates is reduced, which is reflected in the gradual decrease of the total back-stress up to times of approximately 10,000 hours. When the modified Z-phase is included, the total back-stress shows a drastic depression between 10,000 and 20,000 hours. This effect is due to the enhanced nucleation and subsequent growth of the Z-phase, which causes dissolution of the VN precipitates. In the later stages, the decrease of back-stress continues in a steady manner again, however, on a much lower level than before. Comparison of the curves for the integrated back-stress in Figure 5.21 indicates that Z-phase formation causes an additional back-stress reduction at 100,000 hours of approximately 20 MPa. This effect is assumed to be responsible for the drop in creep strength of various of the different ferritic/martensitic creep resistant 9-12% Cr-steels during long-term creep exposure accordingly to ref.[69].
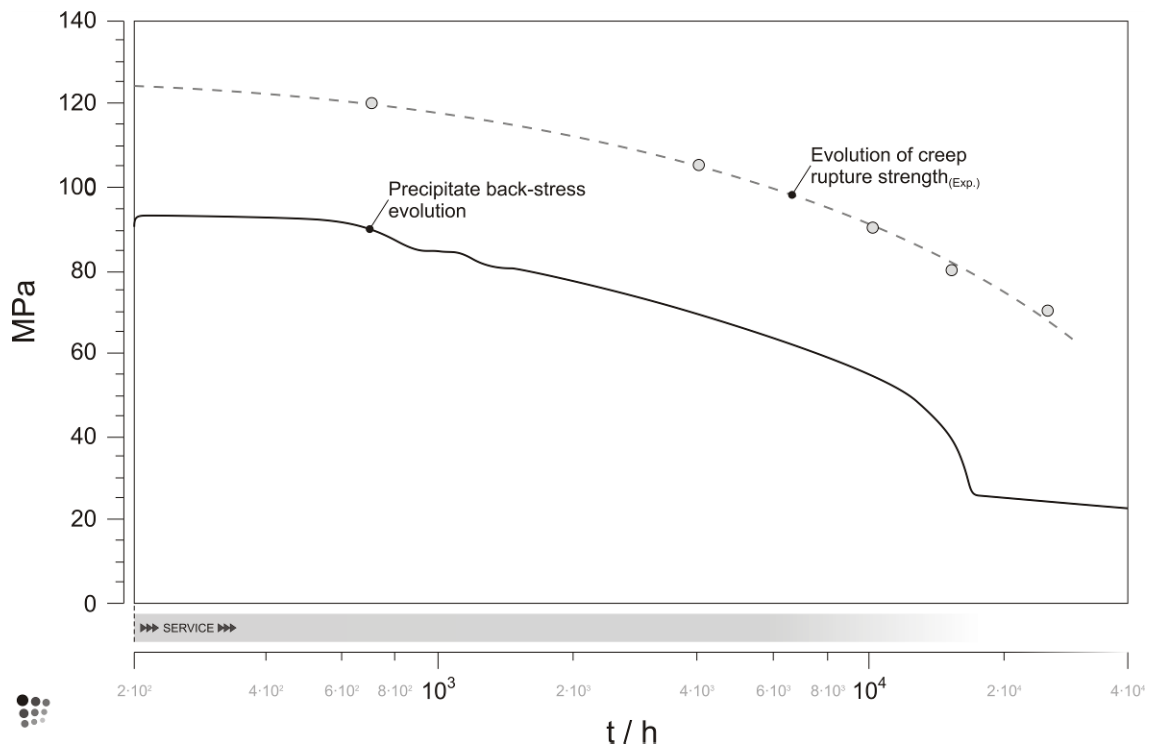
Figure 5.22. Comparison of the calculated precipitate back-stress τ_{prec} with the experimentally determined evolution of the creep rupture strength of the CB8 steel. Time scale starts with starting service according to Figure 5.21.

---

[*] This quantity varies strongly with selection of input values and should therefore not be considered in terms of absolute values.

Further comparison of the calculated precipitate back-stress and the experimentally determined evolution of the creep rupture strength clearly shows the effect of precipitates on the evolution of creep strength. The decrease in precipitate back-stress observed in Figure 5.22 is attended by an equivalent depression of creep rupture strength. Thus, it is assumed that the evolution of second phase particles during service is a main determining impact factor on creep rupture strength evolution.

5.2.6   Summary and Discussion

Precipitation strengthening is a key mechanism for improving mechanical properties of creep resistant materials. To capture the evolution of the precipitate microstructure during heat treatment and service in these complex materials, experimental characterization must be performed with state-of-the-art techniques and methodologies. If these are complemented with suitable modelling and simulation approaches, profound understanding of the interactions of all microstructural constituents can be achieved and predictions of the influence of variations of chemical composition and process parameters can be attempted.

A corresponding methodology is introduced in this chapter. With the simulation software MatCalc, which is based on independent thermodynamic and kinetic databases and on a novel theoretical approach to model multi-component multi-phase precipitation kinetics, the strengthening contribution from precipitates is predicted for the entire life time of a sample on the example of the 11% Cr steel COST CB8. The influence of Z-phase precipitation on the degradation of the creep strength is quantified and a significant drop of the creep strength is confirmed at the time when the VN precipitates dissolve.

5.3 Influence of heat treatment variation on predicted precipitate back-stress and creep rupture strength of a 9% Cr steel

As already pointed out, the superior creep resistance of the modern 9-12% Cr steels originates from their complex microstructure with a high density of different types of precipitates in combination with a ferritic/martensitic microstructure. While the fine subgrain structure and the dense distribution of small precipitates provide high strength and good toughness, simultaneously, the precipitates conserve the excellent mechanical properties efficiently over long time. The precipitates exert strong pinning forces on dislocations, grain and subgrain boundaries[23,48,50,200-203] and, thus, act against the inevitable effect of microstructure coarsening[42,67].

The starting point of the present study is a series of experiments on the influence of austenitising and tempering temperatures and times on the short-term and long-time creep rupture strength of the COST alloy E2[216] carried out in the European COST program 501 Round 3. Despite the observation that significant improvement in the short-term creep rupture strength can be achieved with optimized heat treatment parameters, it was also observed that the various strength levels after different heat treatments converge after long-term creep loading. The advantage of high strength in the 'as-received' material condition, i.e. the condition after quality heat treatment, diminishes with increasing service times.

In the following, computer simulations of the microstructure development using the software MatCalc are carried out to predict the evolution of precipitates during processing and service of the COST alloy E2. Based on these results, the strength contribution from each precipitate population as well as the integral precipitation strengthening potential is evaluated and the evolution of precipitate back-stress is followed over the lifetime of the material based on the methodology introduced in the previous chapters. The influence of different heat treatments on the precipitate microstructure on creep strength is investigated theoretically and compared to the experimental results.

5.3.1 Heat treatments of COST alloy E2

The alloying concept of steel E2 was developed in the mid eighties in the COST program 501 round 3. It is a typical 9–12 % Cr forging steel[217]. The chemical composition of the steel[218] is shown in Table 5.3. To examine the influence of heat treatment parameters on

creep strength (i.e. austenitising temperature and time and tempering treatment parameters), different heat treatments were performed on the same melt[218]. The parameters used in the experiments as well as the measured prior austenite grain sizes are summarized in Table 5.4. For heat treatment variant A, no prior austenite grain size was recorded. After heat treatment, the specimens were creep tested at 600°C.

Table 5.3. Chemical composition of steel E2 in wt.%[218] considered in the present simulations.

C	Cr	Fe	Mn	Mo	N	Nb	Ni	Si	V	W
0.13	10.20	bal.	0.48	1.10	0.05	0.03	0.77	0.04	0.02	0.90

The creep rupture strength for heat treatment variants A–D[218] is shown in Figure 5.23. Depending on the heat treatment parameters, the 100 h creep rupture strength varies from 204 to 274 MPa. At longer testing times, the creep strength decreases in all cases and reaches similar values between 102 and 109 MPa at the design lifetime of 100,000 h.

Table 5.4. Heat treatment parameters and prior austenite grain size[218].

Heat Treatment Variant	Solution treatment		Tempering						Grain size
			1		2		3		
	(°C)	(h)	(°C)	(h)	(°C)	(h)	(°C)	(h)	(μm)
A	1020	2	570	8	700	16	710	17	-
B	1070	2	570	8	720	16	-	-	205
C	1070	2	570	8	700	16	-	-	280
D	1120	2	570	8	700	16	700	16	430
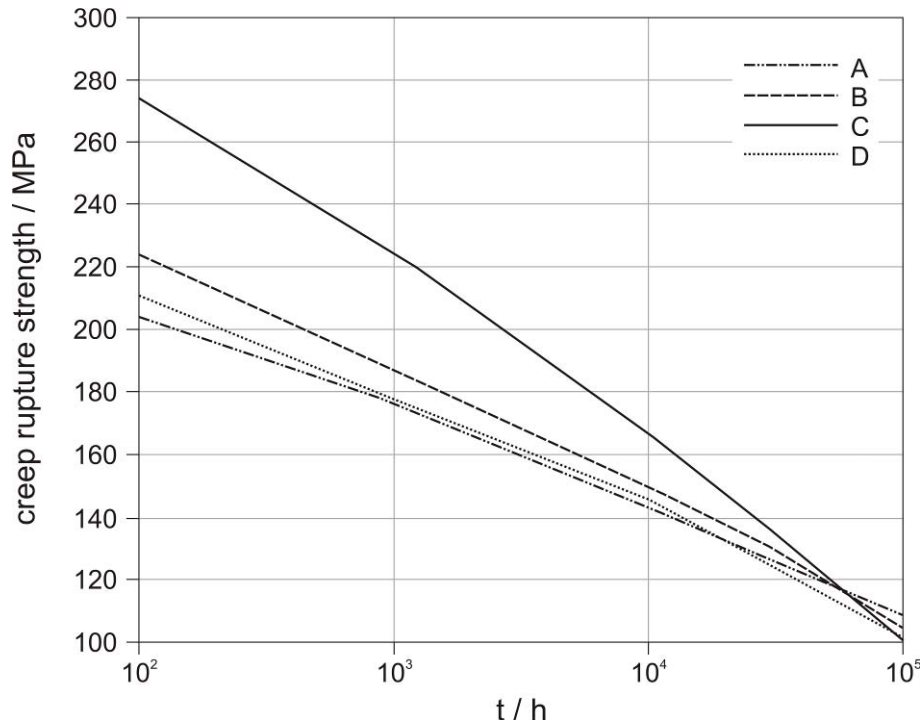
Figure 5.23. Creep rupture strength degradation of COST alloy E2
with heat treatment variants A–D according to ref.[218].

5.3.2   Numerical simulation setup

In the present simulations, the precipitate phases $M_{23}C_6$, M_7C_3, M_3C, MX, M_2X, Laves and
the so-called modified Z-phase[219] are taken into account in accordance with experimental
findings in this type of steel[42,218]. Experiment[42] also showed that two types of MX
precipitates are present in these steels, i.e. a vanadium and nitrogen-rich phase and a
niobium and carbon-rich phase. These are taken into account by definition of a miscibility
gap for the FCC_A1 phase and an additional MX precipitate.

Figure 5.24 shows the calculated equilibrium phase fraction diagram based on the
thermodynamic database TCFE3[220] with slight modification of the original data for better
representation of the observed phase equilibria, as described in ref.[3]. The mobility data
used in the simulations are taken from the diffusion database of MatCalc 5.21.
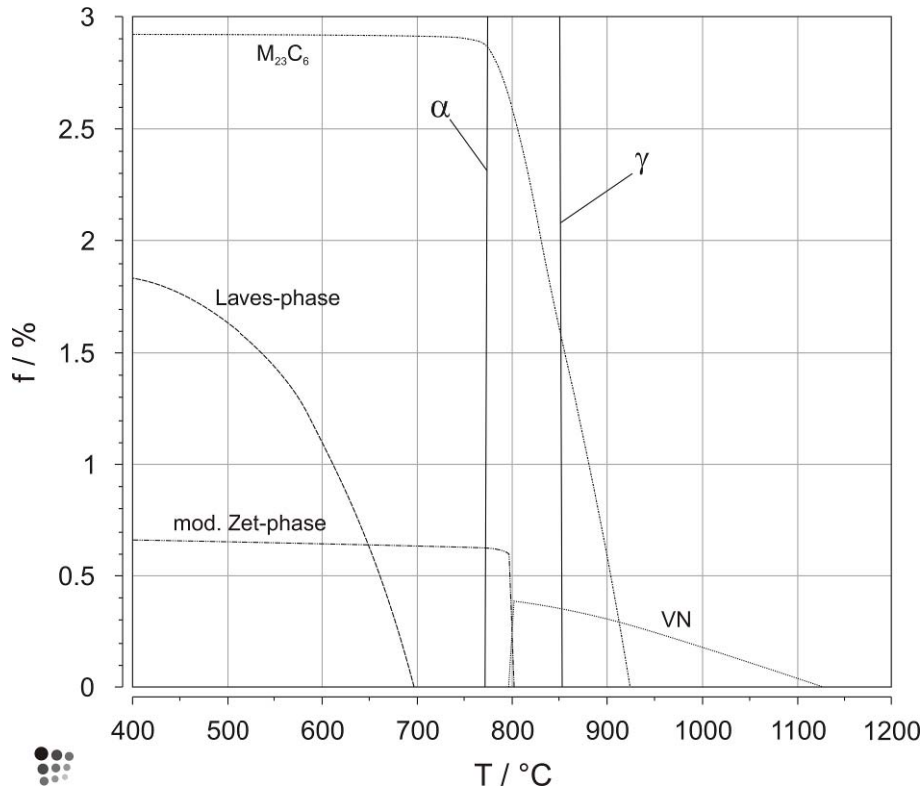
Figure 5.24. Calculated phase fraction diagram of COST alloy E2.

For the heat treatment simulations, the time–temperature history summarized in Table 5.4 is applied. The entire time–temperature sequences, including service at 600°C, are shown in Figure 5.25. It is important to emphasize that, in the course of the production process, the material undergoes several austenite/ferrite phase transformations. These are fully taken into account in the present simulation (see also ref.[3]).

For all heat treatments, the numerical simulation starts with a cooling segment in an austenitic matrix starting at 1400°C. According to Figure 5.24, precipitation of VN does not start until a temperature of approximately 1125°C is reached. At this temperature, the matrix is fully austenitic. Cooling down slowly to the calculated M_S temperature of 390°C is carried out within 2.5 h. At this temperature, the austenite matrix (thermodynamic phase FCC_A1) is assumed to fully transform into martensite. It is further assumed that no precipitation reactions occur below this temperature due to sluggish substitutional diffusion. In the next simulation step, the temperature is increased again. The simulation is now performed in a ferritic matrix (thermodynamic phase BCC_A2) up to the calculated transformation temperature of 812°C. Then, the matrix is switched to austenite again. Austenitising is simulated for temperatures between 1020 and 1120°C, depending on the

heat treatment variant, with subsequent cooling to M_S at 390°C. The following quality heat treatments and service exposure at 600°C take place in ferrite again.
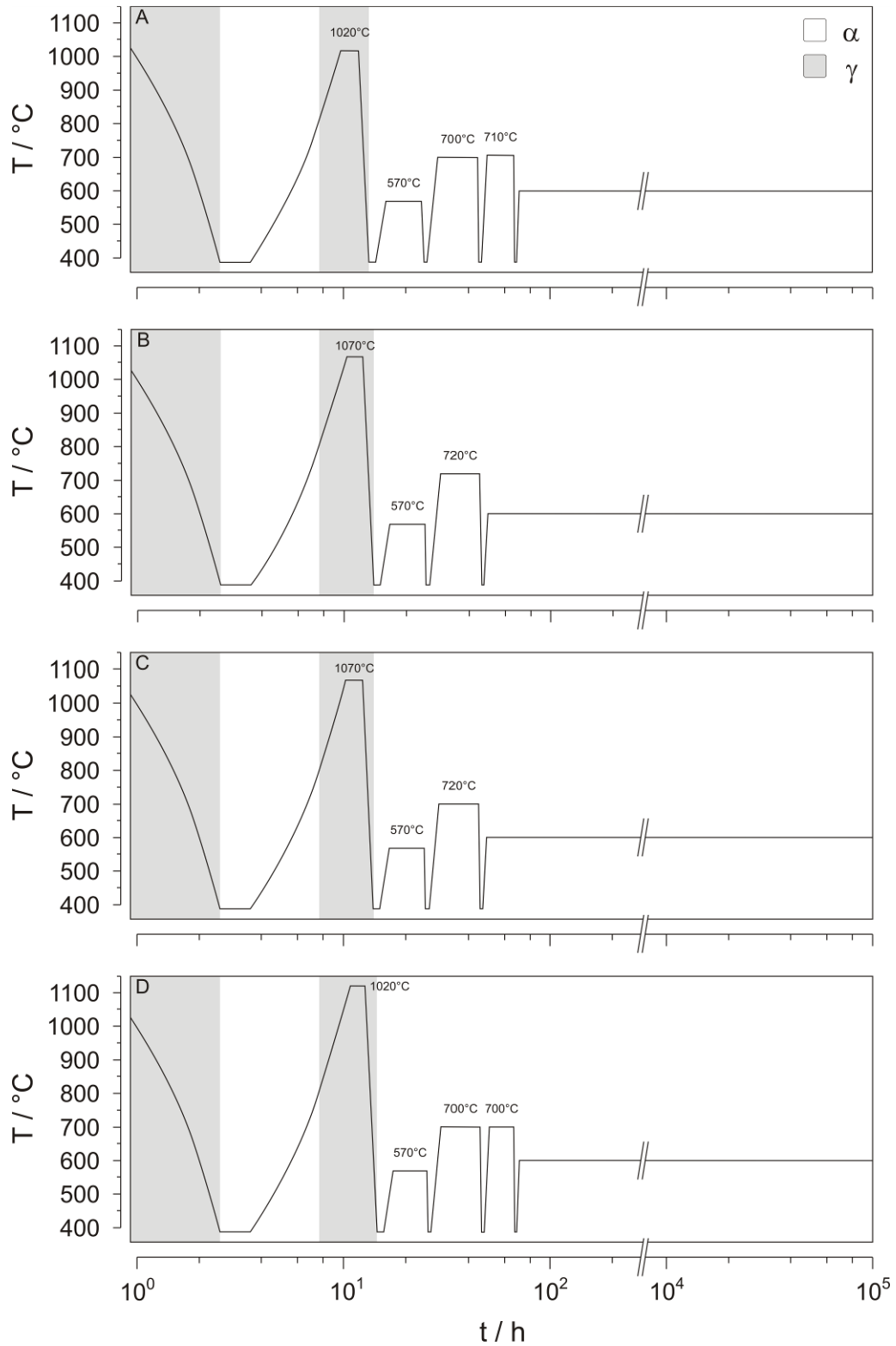
Figure 5.25. Simulated time–temperature history of cooling after casting, austenitising, heat treatment variants A–D (see also Table 2) and service at 600°C.

In addition to the thermodynamic and kinetic data as well as the time-temperature sequence, another important input parameter for the simulation is the type of heterogeneous nucleation sites for each of the precipitate phases. For the present simulation, the type of nucleation sites for each precipitate is defined according to experimental observations[39,42,67]. This was already discussed in section 3.3.2.3 and section 5.2.3.2.
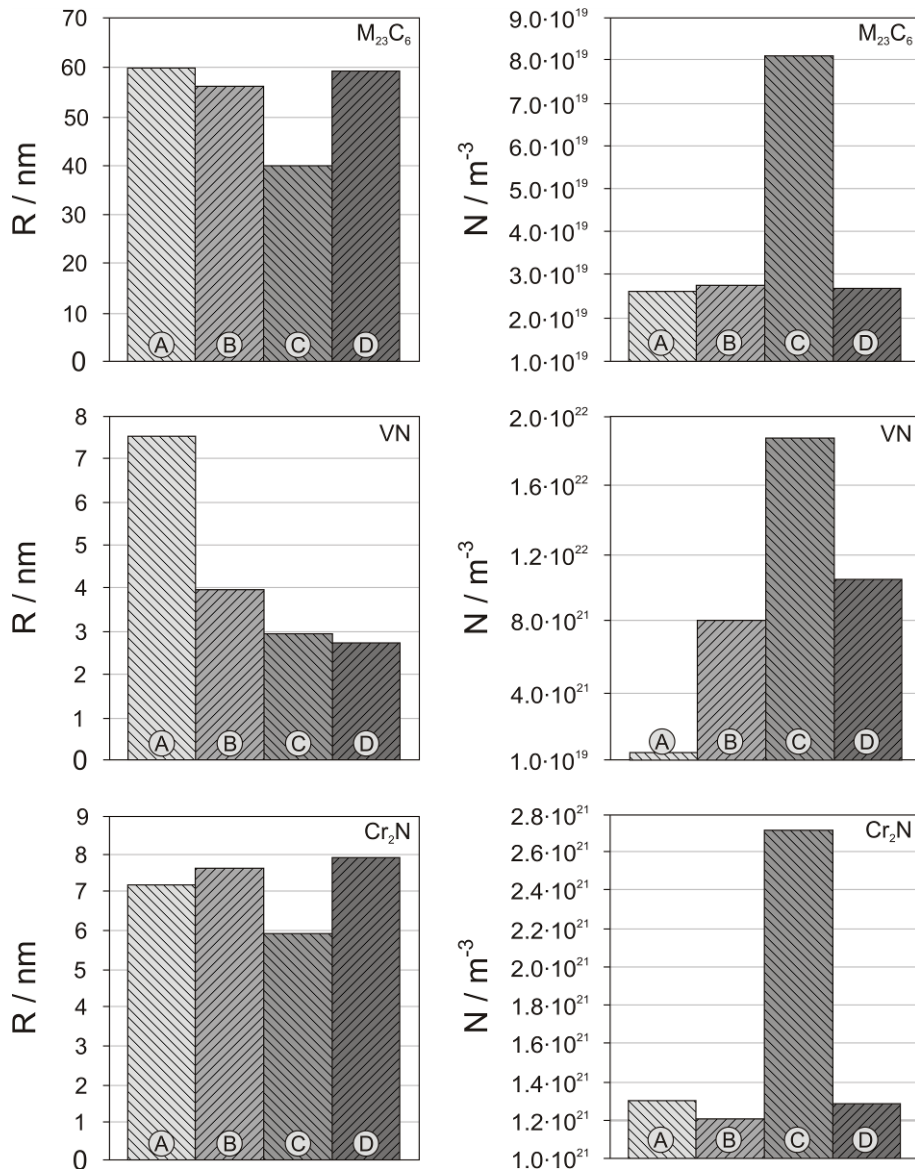
Figure 5.26. Mean precipitate radius R and total number density N of $M_{23}C_6$, VN and Cr_2N for heat treatment variants A–D in the 'as-received' condition.

In the simulations, it is assumed that the transformation from austenite to martensite and back occurs instantaneously and that the parent and product phase have identical chemical

composition. The precipitate populations are assumed to remain unchanged during this transformation. When the simulation starts at 1400°C, all elements are initially assumed to be in solid solution. Furthermore, no restrictions regarding the nucleation and growth of the several precipitate phases were made. Nucleation of any precipitate phase at any time is possible. In Figure 5.26, the precipitate radius and number density for the $M_{23}C_6$, VN and Cr_2N in the 'as-received' condition are shown for heat treatment A–D. Different mean particle radii and number densities for each precipitate phase are observed. The consequences for the predicted mechanical properties are outlined in the following.

5.3.3   Calculation of the back-stress evolution

The plots in Figure 5.27 show representative examples of the simulated evolution of mean precipitate radius, number density and obstacle effect of each precipitate phase as well as the total back-stress for the heat treatment variant D during service.
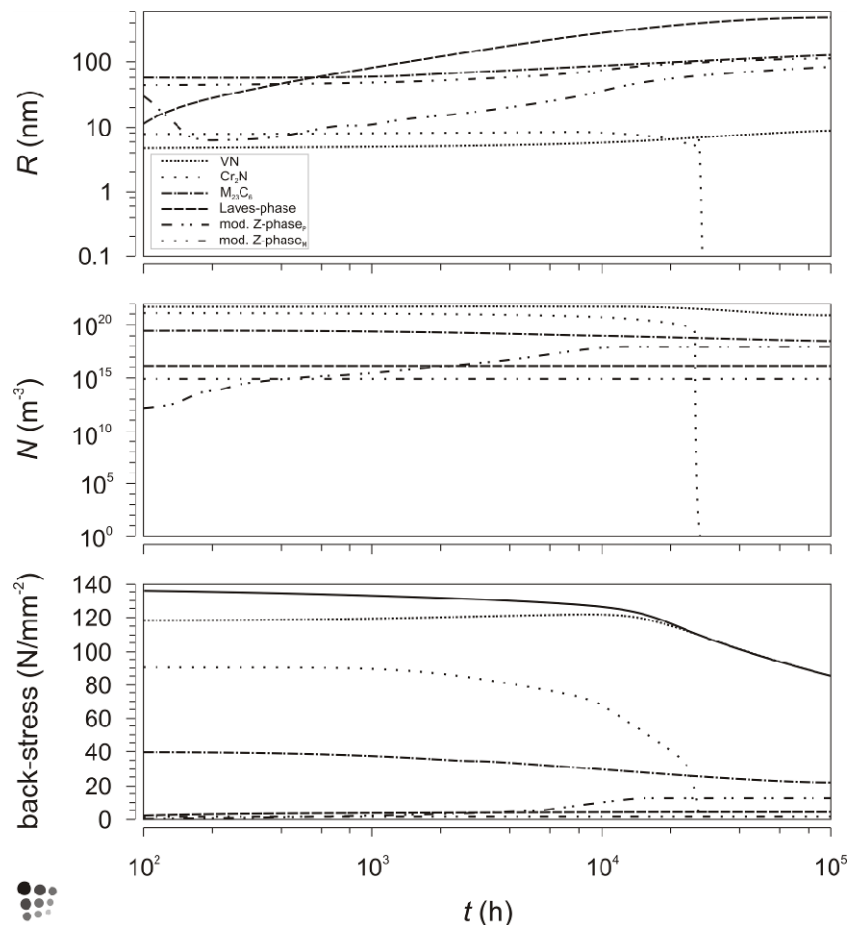
Figure 5.27. Evolution of mean precipitate radius R, number density N and precipitate back-stress during service in COST alloy E2 with heat treatment variant D.

It must be emphasized that the back-stress contribution from *individual* precipitates has only limited physical relevance, since these contributions cannot be separated from the total back-stress. The major quantity determining the back-stress is the mean precipitate distance, and this quantity is only defined in meaningful way in terms of the entity of all precipitates. Thus, the individual back-stress contributions should only be considered in terms of relative stress contributions from individual precipitate types. To calculate the precipitate back-stress, eq. (5.7) was applied. The constants are assumed to be C=0.19 and G=64.6 GPa (converted from ref.[215]). r_a is assumed to have a value of two times the mean precipitate radius $r_a=2r_{prec}$[105] and the inner cutoff radius is taken as r_i~$2b$ (~0,5 nm).

The starting point in Figure 5.27 corresponds to the 'as-received' condition at the end of the quality heat treatments. With the constants C and G as defined before, the total strength contribution from precipitates is evaluated as 135 MPa (solid line in the bottom graph of Figure 5.27). During service, the density of precipitates reduces due to Ostwald ripening. This effect, together with the predicted dissolution of Cr_2N and VN, the latter at times exceeding 10^5 hours, and the appearance of coarse, modified Z-Phase precipitates leads to a constant loss of precipitation strengthening. After 100,000 h, the calculated obstacle effect has declined to a value of 85 MPa.

5.3.4 Comparison of the experimental creep rupture strength with the predicted precipitate back-stress

The variation in precipitate back-stress after quality heat treatment shown in Figure 5.28 differs strongly between 175 MPa for variant C and 100 MPa for variant A. Simulation of the back-stress evolution of E2 for the different heat treatment variants A to D clearly reflects the observed differences in short-term creep strength. At the end of the simulated service, the precipitate back-stress contributions lie between 60 and 97 MPa.
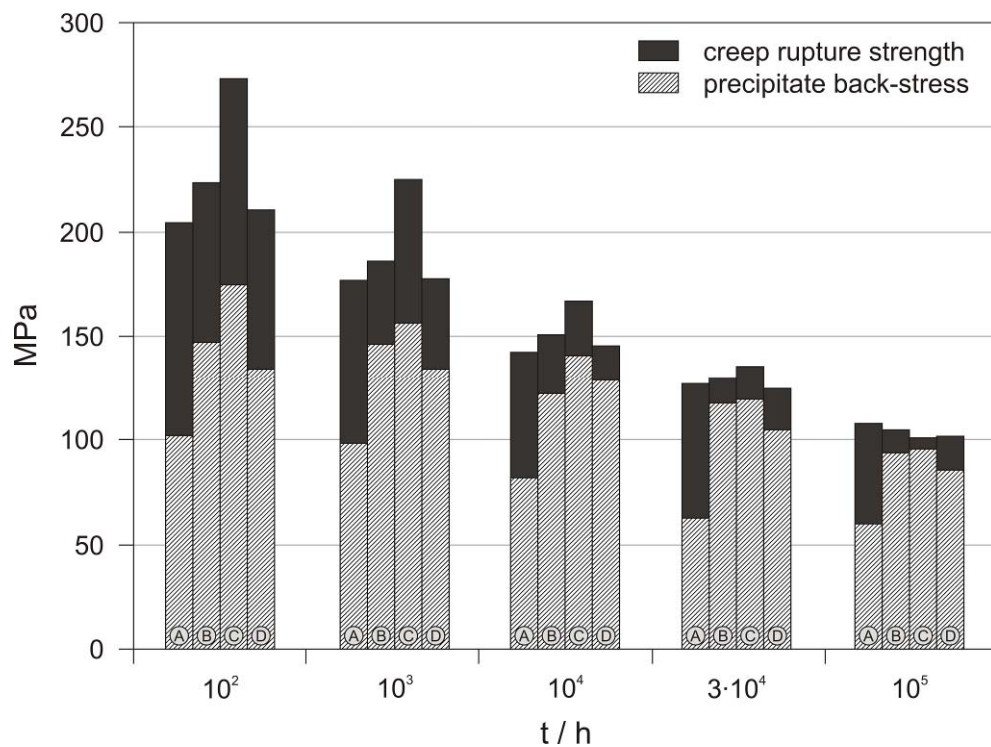
Figure 5.28. Creep rupture strength of COST alloy E2 for heat treatment variants A–D compared with the predicted precipitate back-stress evolution.

It is interesting to further compare the predicted precipitation strengthening effect with the experimental creep rupture strength. According to Figure 5.28, the tendencies in strength evolution are reasonably well reproduced by the simulations, particularly for treatments B to D. The prediction for variant A is less good and it can partially be attributed to the fact that the thermodynamic database predicts a significant amount of VN precipitates stable at the lowest austenitising temperature of 1020°C. The undissolved vanadium-nitrides are not available for re-precipitation and particle strengthening during quality heat treatment later, leading to a strongly reduced precipitation strengthening effect. Further reason for the less

good agreement between simulation and experiment for treatment A is unclear and shall be clarified in future work.

The simulations clearly emphasize the importance of precipitates in predicting the strength evolution of complex materials. The coarsening characteristics and competitive processes among different precipitates in these materials can be reasonably well described using the present computational technique. The combination of precipitate evolution data from simulation with the back-stress concept outlined in this study, moreover, provides an efficient methodology to predict the precipitation strengthening potential of complex structural materials from the researcher's desktop and can thus aid in reducing experimental costs in materials development.

5.3.5   Summary and Discussion

The results obtained in this study clearly demonstrate the potential of the present simulation approach to predict the strength evolution in complex high-performance materials. Comparison of the experimentally observed evolution of the creep rupture strength and the predicted precipitate back-stress for different heat treatment variants of the advanced 9–12 % Cr steel COST E2 show encouraging agreement.

The present simulations also confirm the important experimental observation that an optimization of the short-term creep strength by optimization of the austenitising and heat treatment parameters brings only a temporary benefit. After long-term service exposure, the initial strength differences can level out and, as demonstrated here, reach a relatively homogeneous level at the component design-lifetime of 100,000 hours.

Finally, it is noted that additional important strengthening mechanisms are not yet considered in the present back-stress simulation approach. This has to be a topic in further modeling and simulation activities. These are mainly the effects of solid solution strengthening and the strength contributions by disloactions and subgrain structure which are important factors when attempting a quantitative comparison of the creep rupture strengths of alloys. An approach to consider these effects on the base of determination of 0.2% proof stress of a 9-12% Cr steel is given in the following section.

5.4   Modelling of the 0.2% proof stress of a complex 11% Cr steel

A major quality characteristic in the processing of large scale power plant components is, apart from a minimum fracture ductility and absence of casting and forging defects, the strength of the material, commonly expressed by the 0.2% proof stress ($\sigma_{0.2}$) in the as-received condition. This material property is strongly affected by the applied heat treatment during the production process[218,221] due to the impact of heat treatment time and temperature on the resulting microstructure. The heat treatment of complex ferritic/martensitic high alloyed Cr steels involves a complex thermal history where the material experiences different holding times at varying temperatures with variable heating and cooling rates in between.

As shown by different researchers[84,163,164], the correlation between the mechanical properties and microstructures in steels is difficult because of the complex interaction of microstructural constituents in these materials. To describe the strength of these materials, the dominant strengthening mechanisms must be identified. Li[84] showed that, in ferritic/martensitic steel, the strength of the material can be reasonably well described if the following strength contributions are accounted for:

   (i)   inherent lattice strength of the matrix,

  (ii)   dislocation strengthening,

 (iii)   subgrain strengthening,

 (iv)   solid solution strengthening and

  (v)   precipitate strengthening.

In the following, the strengthening contribution of each mechanism is discussed, based on the example of the martensitic 11% Cr steel D1[221].

Austenitising and tempering for this material was carried out at 1020°C and 720°C respectively. The tempering time was varied between 2 and 24 hours, leading to different 0.2% proof stresses. According to these heat treatment variations the microstructural evolution was simulated with the software MatCalc and the 0.2% proof stress was calculated as a function of tempering time, based on the strengthening model introduced in chapter 4. Finally, the numerical result is compared with the experimentally determined 0.2% proof stress for 2, 8, 16 and 24 hours of tempering.

5.4.1   Heat treatment variations of the 11% Cr steel COST D1

The COST alloy D1 was developed in the framework of the European COST program 501. The chemical composition of the alloy D1 is characterized by the partial replacement of Mo by W. Prior experimental work in Japan indicated that this replacement leads to a significant increase in creep strength as reported by Berger et al.[217] and Mayr[2]. The chemical composition of the investigated steel is shown in Table 5.5.

Table 5.5. Chemical composition of steel D1 in wt.%[221] considered in the present simulations.

Al	C	Cr	Fe	Mn	Mo	N	Nb	Ni	Si	V	W
0.007	0.12	11.3	bal.	0.48	0.32	0.055	0.04	0.81	0.09	0.02	1.90

An overview of the heat treatment variations carried out together with the applied heating and cooling rates, is shown in Table 5.6. The heat treatments consist of austenitising at 1020°C and two tempering cycles, one at a relatively low temperature (570°C), typical for a forged material as investigated in the present case.

Table 5.6. Heat treatment parameters of steel D1[221].

Heat Treatment Variant	Solution treatment				Tempering								
					1				2				
	(°C)	(h)	HR	CR*	(°C)	(h)	HR	CR	(°C)	(h)	HR	CR
			(°C/h)				(°C/h)				(°C/h)	
A	1020	4	25	120/40	570	8	50	-10	720	2	50	-10
B	1020	4	25	120/40	570	8	50	-10	720	8	50	-10
C	1020	4	25	120/40	570	8	50	-10	720	16	50	-10
D	1020	4	25	120/40	570	8	50	-10	720	24	50	-10

HR … heating rate
CR … cooling rate
* … interrupted cooling from austenitising temperature wit 120°C/h down to 500°C and 40°C/h down to room temperature

Figure 5.29 shows the experimentally determined evolution of 0.2% proof stress as a function of tempering time. It can be seen that, with ongoing tempering time, the strength of the material decreases markedly. In the following, these data are the reference values for the subsequent numerical determination of the yield stress.
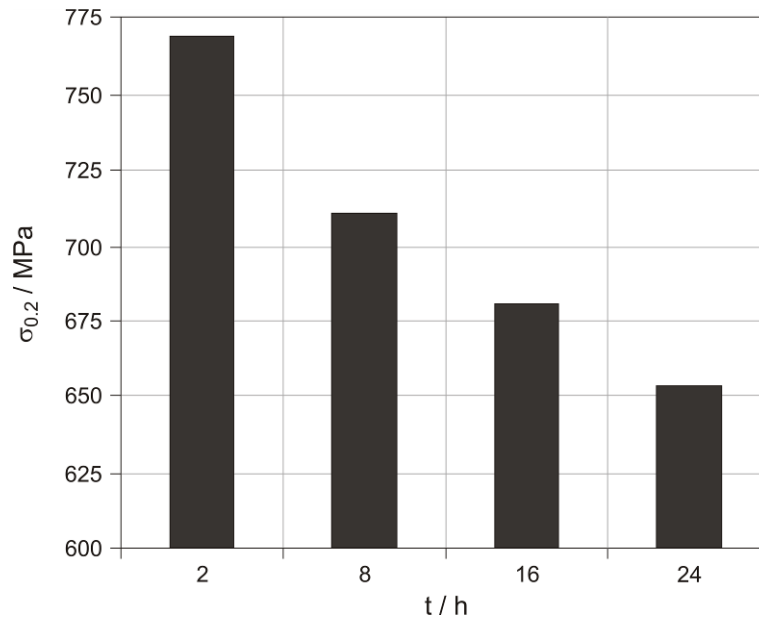
Figure 5.29. Development of experimentally determined 0.2% proof stress of alloy D1
as a function of tempering time t at tempering temperature T=720°C.

5.4.2   Modelling of the microstructure-property relationship

According to the work of Li[84] and Maropoulos et al.[164], the strength of a complex martensitic alloy can be determined by superposition of the inherent lattice strength σ_i, the dislocation strengthening σ_d, the subgrain strengthening σ_{sgb} the solid solution strengthening σ_{ss} and the precipitate strengthening σ_p. The latter strength contributions (σ_{ss} and σ_p) are determined on the basis of the data provided by the kinetic simulations with the software MatCalc, according to section 4.1.1 and section 4.2.1. For the present investigation, a Taylor factor M=3[57] was assumed. The strengthening coefficients for the evaluation of solid solution strengthening are adopted from Table 3.1. The mean particle distance λ was determined according to eq. (4.29). The other components necessary to determine the materials strength in the as-received condition are discussed individually as follows.

5.4.2.1 Inherent lattice strength σ_i

The inherent lattice strength of a matrix represents the exclusive strength of the matrix phase without the presence of any other strengthening component. Maropoulus et al.[164] used a value of 41 MPa for the inherent lattice strength. Li[84] used a value of 30 MPa for

his yield strength determination in a martensitic steel. For the present analysis, a value of 41 MPa, according to Maropoulus et al., was adopted.

5.4.2.2 Dislocation strengthening

The strength contribution of dislocations can be calculated according to Young and Bhadeshia[82] as

$$\sigma_\mathrm{d} = 0.38 G b \rho^{\frac{1}{2}}, \tag{5.8}$$

where, G (=83 GPa) is the shear modulus, b (=0.248 nm) the Burgers vector and ρ the dislocation density in the material. The mean dislocation density is assumed to be constant with $4.5 \cdot 10^{14}$ m/m^3 as typical value for forged materials in the as received condition[222]. With these input data, the strength increase by dislocation strengthening amounts to 166 MPa for the present 11% Cr steel.

5.4.2.3 Subgrain boundary strengthening

In a tempered martensite structure, different types of boundaries exist, i.e. former austenite grain boundaries, martensite packet boundaries and martensite lath boundaries. The latter types of boundaries are summarized in the following under the term subgrain boundary. As shown by experimental investigation[42,84], the prior austenite grain boundaries and the martensite packet boundaries represent only a small fraction of the total boundary surface, thus contributing insignificantly to the materials strength. In the following, it is assumed that the subgrain boundary strengthening is mainly influenced by the martensite lath boundaries. Smith and Hehemann[223] introduced an expression to evaluate the strength contribution according to

$$\sigma_\mathrm{sgb} = \frac{8.62 \cdot 10^{-2}}{w}, \tag{5.9}$$

where w is the mean martensite lath width in millimetres. For forged material, such as the current 11% Cr steel D1, typical values for the martensite lath width lie in the range of 0.3 μm to 0.4 μm[222]. In the present case a constant martensite lath width of 0.3 μm was

assumed. Thus, in the present case, a strength contribution by subgrain boundaries of 230 MPa can be determined.

5.4.2.4 Work hardening

If the 0.2% proof stress is experimentally determined, plastic deformation occurs during testing, denoted as work hardening in the present investigation. The effect of work hardening must be taken into account as contribution to $\sigma_{0.2}$. Maropoulos et al.[164] estimated a value of 65 MPa, which is used also in the present study and which is in the same order of magnitude compared to the applied value of Li[84] of 40 MPa.

To determine the 0.2% proof stress $\sigma_{0.2}$, the operative strengthening mechanisms are superimposed as described in section 4.3. In the present case, the *RMS* summation[84,163,164] is adopted. Thus, the variable α in eq. (4.36) is assumed with a value of $\alpha=2$. Finally, the 0.2% proof stress is calculated as

$$\sigma_{0.2} = \sqrt{\sigma_d^2 + (\sigma_{ss} + \sigma_p + \sigma_i + \sigma_{sgb} + \sigma_{wh})^2} \ . \tag{5.10}$$

5.4.3 Numerical simulation of the microstructural evolution

To simulate the microstructural evolution, i.e. evolution of precipitate parameters and chemical composition of the matrix phase, the precipitate phases AlN, $M_{23}C_6$, M_7C_3, M_3C, MX, M_2X and Laves phase are taken into account.

For the present simulations, the software MatCalc 5.32 version 1.003 was used. All simulations are carried out based on the thermodynamic database mc_steel.tdb[224] and the diffusion database mc_sample_fe.ddb[185]. It is pointed out that no fit parameters or correction factors are used in the present simulations. All thermodynamic and diffusion data are adopted unchanged from the databases. Figure 5.30 shows the calculated equilibrium phase fraction diagram of the 11% Cr steel D1.

For the heat treatment simulations, the time–temperature history summarized in Table 5.6 is applied. As explained in the previous section, the material undergoes several austenite/ferrite phase transformations during the production process, which are fully taken into account in the present simulations.
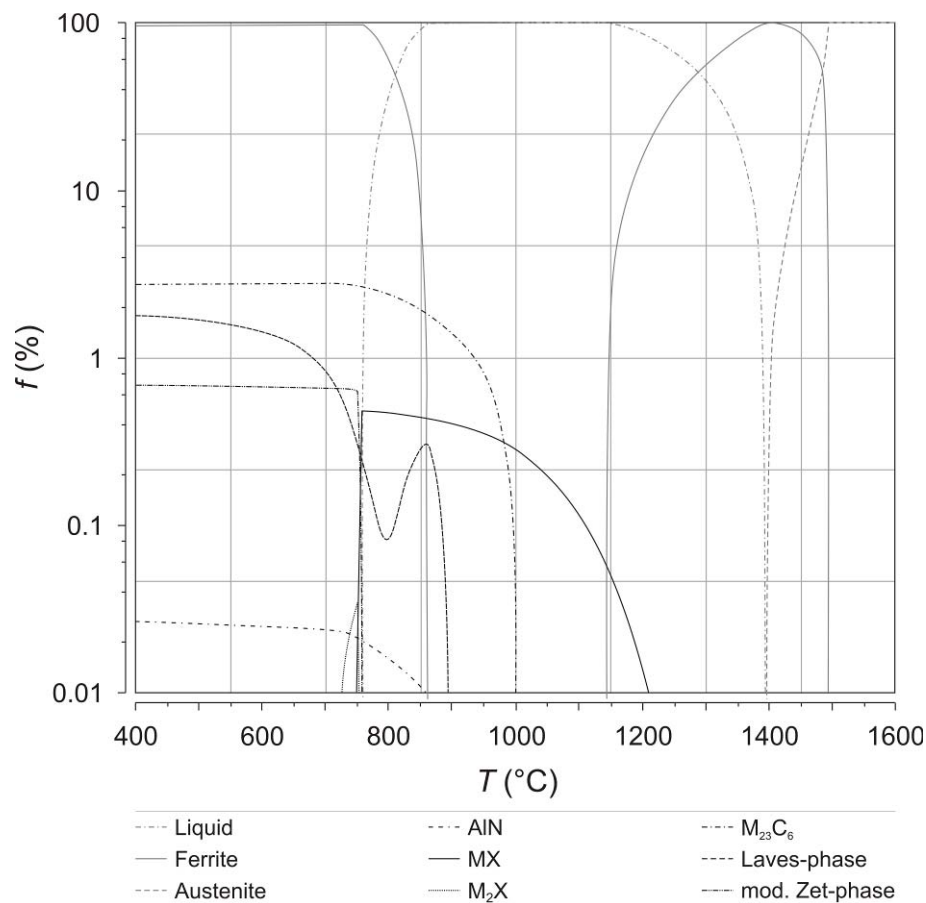
Figure 5.30. Calculated phase fraction diagram of COST alloy D1.

For all heat treatments, the numerical simulation starts at 1400°C with a cooling segment in an austenitic matrix. Cooling down to the calculated M_S temperature of 385°C is carried out with a cooling rate of -120°C/h down to 500°C and from 500°C to 385°C with a cooling rate of -40°C/h. At this temperature, the austenite matrix (thermodynamic phase FCC_A1) is assumed to fully transform into martensite. It is further assumed that no precipitation reactions occur below this temperature due to sluggish diffusion. In the next simulation step, the temperature is increased again. The simulation is now performed in a ferritic matrix (thermodynamic phase BCC_A2) up to the calculated transformation temperature of 811°C. Then, the matrix is switched to austenite again. Austenitising is simulated at 1020°C for 4 hours with subsequent cooling to M_S. The following tempering cycles at 570°C and 720°C take place in a ferritic matrix again.

The type of heterogeneous nucleation sites was defined according to experimental findings as reported in the earlier sections. Further assumptions and simulation settings are defined according to the explanations in the previous sections and refs.[3-5].

Figure 5.31 shows the result of the kinetic simulation of the COST alloy D1 for the evolution of precipitate phase fractions (Figure 5.31 (b)), mean precipitate radii (Figure 5.31 (c)) and number densities (Figure 5.31 (d)). It is interesting to note that the simulation shows that, during austenitising, the precipitates are not completely dissolved. This result corresponds to the previous observation in section 5.3. At 1020°C a certain amount of AlN, MX as well as $M_{23}C_6$ precipitates remains present in the matrix (Figure 5.31 (c)). During tempering at 570°C, re-precipitation of M_3C, M_7C_3, M_2X and Laves-phase is predicted by the simulation, followed by the dissolution of the M_3C and M_7C_3 phase during tempering at 720°C. Furthermore, a remarkable decrease of number density of the M_2X and Laves phase can be observed during this tempering cycle.
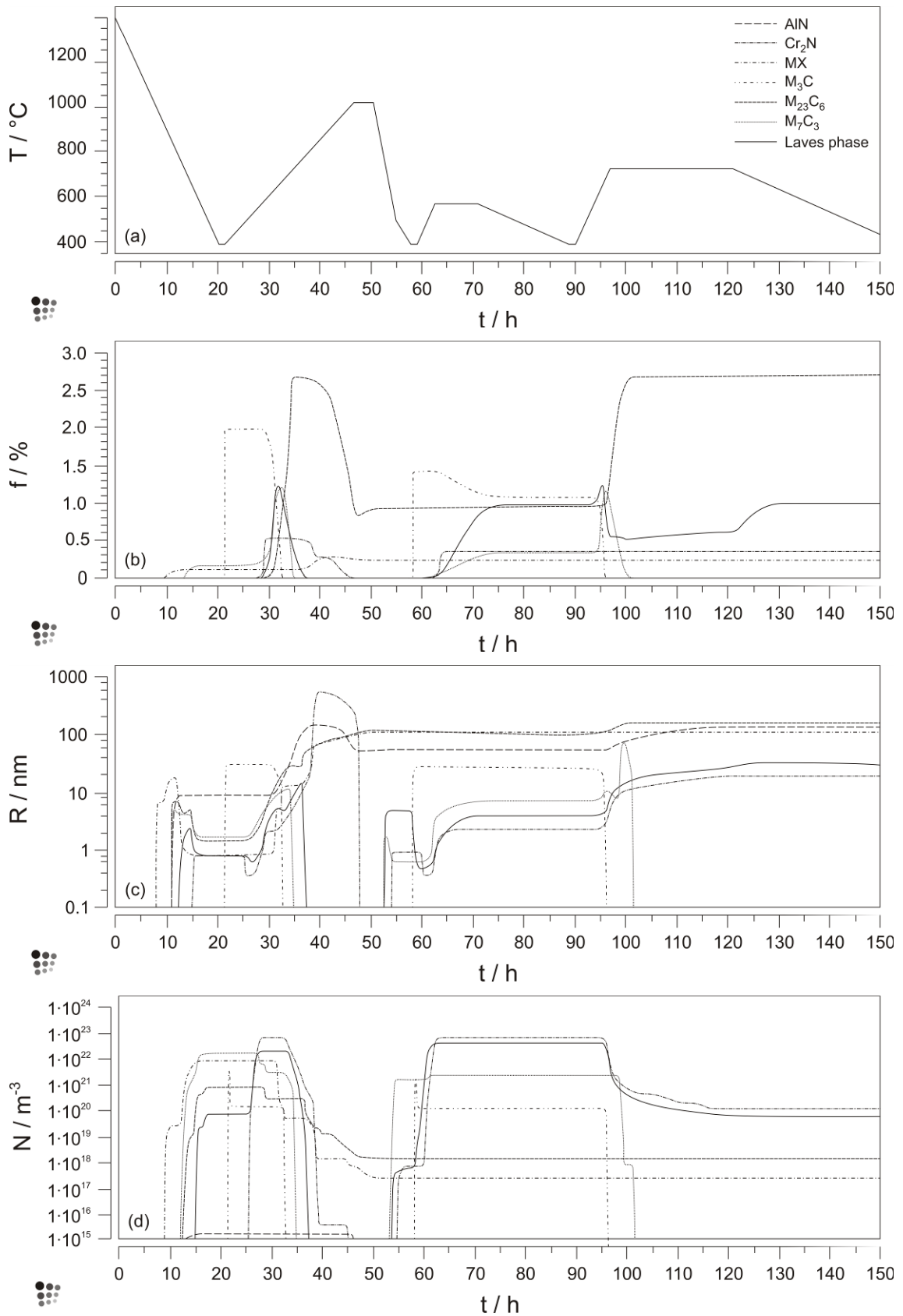
Figure 5.31. Kinetic simulation of the precipitate evolution in COST alloy D1 during (a) heat treatment; (b) *f*, phase fraction, (c) *R*, mean precipitation radius, (d) *N*, number density.

Figure 5.32 and Figure 5.33 show the evolution of the calculated precipitate back-stress and solid solution strengthening contributions during tempering at 720°C, respectively. After 2 hours, the precipitate back-stress amounts to 146 MPa and reduces to 80 MPa during 24 hours of tempering, which corresponds to a reduction of about 50%.
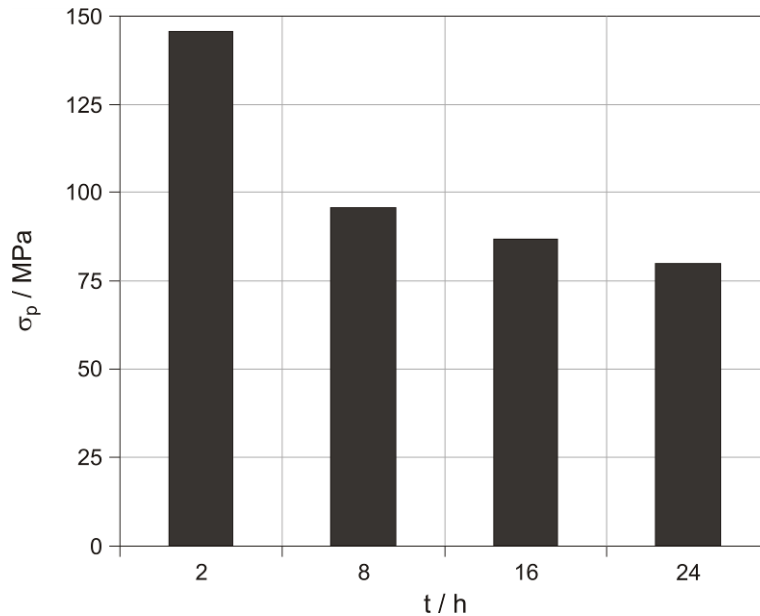
Figure 5.32. Calculated evolution of the precipitate back-stress of alloy D1 as a function of tempering time t and tempering temperature T=720°C.

In the simulation, only small changes in the chemical composition of the matrix phase BCC_A2 can be observed during tempering. Thus, the strength contribution by solid solution strengthening gives similar values in a range within 177 MPa (2h) to 163 MPa (24h). However, it is interesting to note that the chemical composition of the matrix during tempering at 720°C differs markedly from the calculated equilibrium composition at lower temperatures. This leads to a remarkable change in the solid solution strengthening contribution during long term service. This is indicated in Figure 5.33, where σ_{ss} is compared for the different tempering times as well as the equilibrium condition at 600°C. The latter condition is assumed to correspond to the matrix composition after long term service at 600°C. The equilibrium solid solution strength contribution is about 70% of the calculated values during the tempering cycle. This strength reduction can be mainly related to the precipitation of the Laves phase with ongoing service and the consequent depletion of the matrix of Mo and W.
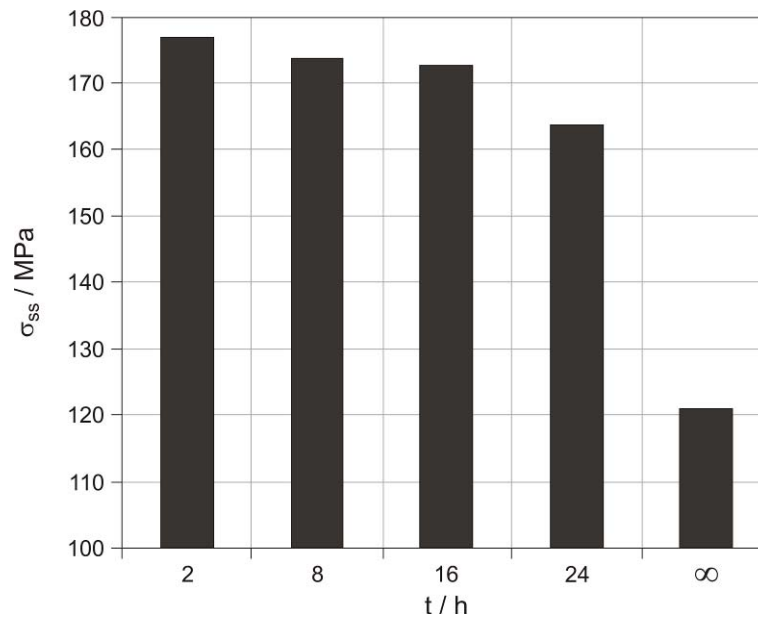
Figure 5.33. Calculated evolution of solid solution strengthening in alloy D1 as a function of tempering time t at T=720°C and in the equilibrium condition (t=∞) at 600°C.

These data are the basis for the determination of the 0.2% proof stress and comparison with the experimentally determined values outlined in the following.

5.4.4 Comparison of the calculated 0.2% proof stress with experimental results

To calculate the 0.2% proof stress of the investigated D1 alloy, the strength contributions in eq. (5.10) are adopted according to the sections 5.4.2.1 to 5.4.2.4 and 5.4.3. The result is shown in Figure 5.34. The calculated 0.2% proof stress agrees well with the experimentally determined values. The calculated deviation ($R_{p\ 0.2\ (calc)}$/$R_{p\ 0.2\ (exp)}$) varies between -4.1% and +1.0%.
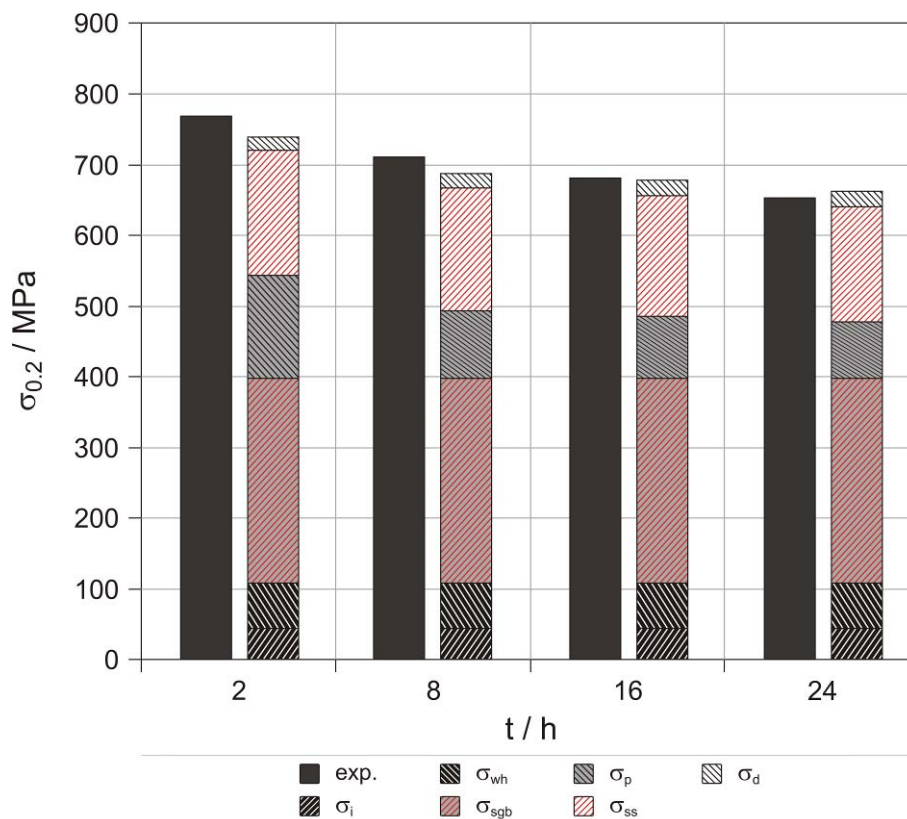
Figure 5.34. Comparison of experimentally determined and simulated 0.2% proof stress ($\sigma_{0.2}$) for 2, 8, 16 and 24 hours of tempering at 720°C. The calculated value for $\sigma_{0.2}$ is separated into the different strength contributions of Peierls stress (σ_i), work hardening (σ_{wh}), subgrain boundaries (σ_{sgb}), precipitates (σ_p), solid solution (σ_{ss}) and dislocations (σ_d).

It is interesting to note that, according to eq. (5.10), the strengthening effect by dislocations contributes only little to the overall strength of the material, although dislocation strengthening was determined with 166 MPa. The total fraction ($=\sigma_d/\sigma_{0.2}$) is less than 3.2% over the whole tempering cycle. Figure 5.34 also shows that strengthening by subgrain boundaries gives the largest contribution to the 0.2% proof stress for all stages. The result

further confirms that *RMS* summation is a good approximation over a large range of strengths and densities of obstacles as reported by other researchers[84,164].

5.4.5   Summary and Discussion

In the present investigation, the evolution of the 0.2% proof stress of a complex 11% Cr steel was simulated during tempering at 720°C. Numerical simulations of the microstructural evolution are carried out with the software package MatCalc. Based on these data, the strength contributions by precipitates and solid solution hardening are evaluated based on the strengthening model in section 4. The present investigation clearly demonstrates the applicability of the introduced model. It was possible to describe the strength evolution of the complex ferritic/martensitic 11% Cr steel D1 during the heat treatment in a reasonable manner.

The simulation shows that, applying the *RMS* summation method the strength contribution by dislocations is very small. It amounts to less than 3.2% of the overall strength of the alloy during the tempering cycle. The largest contribution to the 0.2% proof stress is given by subgrain boundary strengthening followed by solid solution and precipitation strengthening. This result is in agreement with the result reported by Maruyama et al.[23], who identified the dislocation substructure as strength determining microstructure parameter. From the present simulation results, it can be further concluded that the evolution of the 0.2% proof stress is mainly determined by the evolution of the precipitate structure. The precipitate back-stress reduces during tempering by about 50% from 146 MPa to 80 MPa, whereas the solid solution strengthening term remains almost constant (177 MPa – 163 MPa).

Generally, the comparison between experimentally determined and simulated values shows good agreement for all tempering times, although the strength contribution of dislocations and sub-boundaries is considered as a constant value, which might be a simplifying assumption. However, the determined deviation of experimental and calculated 0.2% proof stress is less than 4.1%.

6 Summary

In the present work, a new methodology to model strengthening in steel is outlined on the basis of a physical microstructure-property relationship in combination with numerical simulations carried out with the software MatCalc.

A model for precipitate and solid solution strengthening is introduced based on a modular structure, describing the different strengthening mechanisms as functions of microstructural parameters, e.g. precipitate radius r, number density N, as well as the chemical composition of the matrix phase. With this model, a continuous monitoring of the evolution of the considered strengthening mechanism is possible. Moreover, the present approach can be easily extended to additional strengthening mechanisms, e.g. dislocation or sub-boundary strengthening as shown in this work. The overall strength of a material is finally determined by a general superposition rule. The model developed within this work is implemented in the software MatCalc.

In combination with the results from the kinetic simulations, the introduced model is applied on a two component Fe-Cu alloy as well as on different complex 9-12% Cr steels, to study in detail the evolution of mechanical properties, i.e. materials strength, during different heat treatments and service conditions. It is shown that, with the present approach, the impact of different strengthening mechanism on the long term creep strength as well as on the lower yield stress can be described in a consistent manner for all investigated materials.

For a consistent treatment of the precipitation kinetics in the investigated Fe-Cu alloy, a new simulation methodology is introduced in the present work for simulation of the Cu precipitation kinetics in ferritic steel. The basic idea of the new approach is to take into account the variation of the chemical composition, i.e. the varying Fe to Cu ratio during the precipitation reaction of the initially coherent bcc Cu precipitates. The change of the chemical composition of these precipitates results in a notable change of interfacial energy and, thus, to a strong acceleration of the precipitation kinetics. The simulation clearly shows that, with the novel simulation methodology, it is possible to describe the evolution of the precipitation parameters phase fraction, particle radius and number density in a comprehensive and consistent manner. Furthermore, it is shown that other effects, e.g. impact of interface curvature on precipitate interfacial energy or quenched-in vacancies, must not be neglected when simulating Cu precipitation in ferritic steel.

Based on these data, precipitation strengthening in Fe-Cu alloys is critically discussed and the precipitation strengthening effect is assessed on the basis of different strengthening mechanisms. It is shown that precipitation strengthening by Cu precipitation can be well described, on one hand, by superposition of chemical hardening, coherency strengthening and modulus strengthening in the case of coherent bcc precipitates and, on the other hand, by the Orowan mechanism for the impenetrable fcc Cu precipitates.

To evaluate the impact of microstructural evolution on the overall creep strength and the degradation of complex 9-12% Cr steels, several kinetic simulations for a 10% (steel grade COST E2) and 11% (steel grade COST CB8) Cr steel are carried out. Based on these data and the so called back-stress concept, it is shown that the creep strength evolution during long term service can be reasonably well correlated with the precipitate back-stress in this type of steel. The detailed investigation of the precipitate strengthening effect revealed, according to previous experimental findings, that the MX and $M_{23}C_6$ precipitates strongly contribute to the strength of the material. Furthermore, it is shown on the example of the investigated CB8 alloy that Z-phase formation and dissolution of VN is the major reason for the observed drop in creep strength in several 9-12% Cr steels after several thousand hours of service. The present work also confirms the important experimental observation that an optimization of the short-term creep strength by optimization of the austenitising and heat treatment parameters brings about only a temporary benefit. After long-term service exposure, the initial strength differences can level out and reach a relatively homogeneous level at the component design-lifetime due to the microstructure approaching the equilibrium state.

Finally, the introduced strengthening model is applied to the 11% Cr steel COST D1 to determine the 0.2% proof stress for different tempering times at 720°C, varying between 2 and 24 hours. A detailed study of the solid solution and precipitate strengthening effect is carried out and the additional strength contributions are critically evaluated based on experimental data from literature. The investigation shows that experimental data and predicted proof stress are in good agreement.

References

[1] R. Blum, in: D. Kum, K.-T. Hong, J.T. Kim, C.Y. Kim, F. Abe, X. Xie (Eds.), Proceedings of Symposium on Heat Resistant Steels and Alloys for USC Power Plants 2007, Korea Institute of Science and Technology, Korea (2007) 1-15.

[2] P. Mayr PhD thesis, *Evolution of microstructure and mechanical properties of the heat affected zone in B-containing 9% chromium steels*, Graz University of Technology, 2007.

[3] H.-J. Rajek, PhD thesis, *Computer simulation of precipitation kinetics in solid metals and application to the complex power plant steel CB8*, Graz University of Technology, 2005.

[4] B. Sonderegger, E. Kozeschnik, H. Leitner, H. Clemens, J. Svoboda, F.D. Fischer, Int. J. Mat. Res. 99 (2008) 410-415.

[5] R. Radis, M. Schaffer, M. Albu, G. Kothleitner, P. Pölt, E. Kozeschnik, Acta Mater. 57 2009 5739-5747.

[6] *World energy, technology and climate policy outlook 2030 – WETO*, Directorate-General for Research, Belgium (2003).

[7] K. Riedle, in: P. Mayr, G. Posch, H. Cerjak (Eds.), *Safety and Reliability of Welded Components in Energy and Processing Industry, Proceedings of the IIW International Conference*, Graz University of Technology, Graz (2008), 389-399.

[8] F. Lin, S. Cheng, X. Xie, in: R. Viswanathan, D. Gandy, K. Coleman (Eds.), *Advances in Materials Technology for Fossil Power Plants – Proceedings from the Fifth International Conference*, ASM International, Ohio (2008), 46-58.

[9] T. Muraki, in: K. Yagi, G. Merckling, T.-U. Kern, H. Irie, H. Warlimont (Eds.), *Materials – Creep Properties of Heat Resistant Steels and Superalloys (Subvolume B)*, Springer Verlag, Berlin-Heidelberg (2004), 29-34.

[10] M. Yamada, in: K. Yagi, G. Merckling, T.-U. Kern, H. Irie, H. Warlimont (Eds.), *Materials – Creep Properties of Heat Resistant Steels and Superalloys (Subvolume B)*, Springer Verlag, Berlin-Heidelberg (2004), 62-66.

[11] M. Igarashi, M. Yoshizawa, H. Matsuo, O. Miyahara, A. Iseda, Mat. Sci. Eng. A 510-511 (2009) 104-109.

[12] P. von Hartrott, S. Holmström, S. Caminada, S. Pillot, Mater. Sci. Eng. A 510-511 (2009) 175-179.

[13] K.-H. Mayer, F. Masuyama, in: F. Abe, T.U. Kern, R. Viswanathan (Eds.), *Creep resistant steels*, Woodhead Publishing, Cambridge (2008), 15-77.

[14] M. Igarashi, in: K. Yagi, G. Merckling, T.-U. Kern, H. Irie, H. Warlimont (Eds.), *Materials – Creep Properties of Heat Resistant Steels and Superalloys (Subvolume B)*, Springer Verlag, Berlin-Heidelberg (2004), 74-83.

[15] R. Vanstone, in: A. Strang, W.M. Banks, R.D. Conroy, G.M. McColvin, J.C. Neal, S. Simpson (Eds.), *PARSONS 2000 Advanced Materials for 21st Century Turbines and Power Plant*, The University Press, Cambridge (2000), 91-97.

[16] R. Viswanathan, R. Purgert, S. Goodstine, J. Tanzosh, G. Stanko, J.P. Shingledecker, B. Vitalis, in: R. Viswanathan, D. Gandy, K. Coleman (Eds.), *Advances in Materials Technology for Fossil Power Plants – Proceedings from the Fifth International Conference*, ASM International, Ohio (2008), 1-15.

[17] R. Blum, R.W. Vanstone, C. Messelier-Gouze, in: R. Viswanathan, D. Gandy, K. Coleman (Eds.), *Advances in Materials Technology for Fossil Power Plants – Proceedings from the Fourth International Conference*, ASM International, Ohio (2005), 116-136.

[18] B. Scarlin, T.-U. Kern, M. Staubli, in: R. Viswanathan, D. Gandy, K. Coleman (Eds.), *Advances in Materials Technology for Fossil Power Plants – Proceedings from the Fourth International Conference*, ASM International, Ohio (2005), 80-99.

[19] T. Fujita, ISIJ Int. 32 (1992) 175-181.

[20] T. Fujita, Mater. Sci. Forum (2000) 55-58.

[21] E. Cerri, E. Evangelista, S. Spigarelli, P. Bianchi, Mater. Sci. Eng. A 245 (1998) 285-292.

[22] J. Hald, Steel Res. 67 (1996) 369-374.

[23] K. Maruyama, K. Sawada, J. Koike, ISIJ Int. 41 (2001) 641-653.

[24] R. Blum, in: D. Coutsouradis, J.H. Davidson, J. Ewald, P. Greenfield, T. Khan, M. Malik, D.B. Meadowcroft, V. Regis, R.B. Scarlin, F. Schubert, D.V. Thornton (Eds.), *Materials for Advanced Power Engineering 1994*, Kluwer Academic Publishers, Dordrecht (1994) 15-30.

[25] B. Wilshire, P.J. Scharnig, Scripta Mater. 56 (2007) 1023-1026.

[26] V. Foldyna, Z. Kubon, M. Filip, K.-H. Mayer, C. Berger, Steel Res. 67 (1996) 375-381.

[27] F. Masuyama, in: J. Lecomte-Beckers, F. Schubert, P.J. Ennis (Eds.), *Materials for Advanced Power Engineering 1998*, Forschungszentrum Jülich GmbH, Jülich (1998), 1807-1824.

[28] K. Spiradek, R. Bauer, G. Zeiler, in: D. Coutsouradis, J.H. Davidson, J. Ewald, P. Greenfield, T. Khan, M. Malik, D.B. Meadowcroft, V. Regis, R.B. Scarlin, F. Schubert, D.V. Thornton (Eds.), *Materials for Advanced Power Engineering 1994*, Kluwer Academic Publishers, Dordrecht (1994) 251-262.

[29] R.L. Klueh, A.T. Nelson, J. Nucl. Mater. 371 (2007) 37-52.

[30] R.L. Klueh, J. Nucl. Mater. 378 (2008) 159-166.

[31] T.-U. Kern, K. Wieghardt, H. Kirchner, in: R. Viswanathan, D. Gandy, K. Coleman (Eds.), *Advances in Materials Technology for Fossil Power Plants – Proceedings from the Fourth International Conference*, ASM International, Ohio (2005), 20-34.

[32] T.-U. Kern, in: F. Abe, T.U. Kern, R. Viswanathan (Eds.), *Creep resistant steels*, Woodhead Publishing, Cambridge (2008), 573-596.

[33] P. Hofer, M.K. Miller, S.S. Babu, S.A. David, H. Cerjak, ISIJ Int. 42 (2002) 62-66.

[34] K. Sakuraya, H. Okada, F. Abe, ISIJ Int. 46 (2006) 1712-1719.

[35] F. Abe, M. Taneike, K. Sawada, Int. J. Pres. Ves. Pip. 84 (2007) 3-12.

[36] J.A. Francis, W. Mazur, H.K.D.H. Bhadeshia, Mater. Sci. Tech. 22 (2006) 1387-1395.

[37] K. Sawada, M. Bauer, F. Kauffmann, P. Mayr, A. Klenk, Mater. Sci. Eng. A 527 (2010) 1417-1426.

[38] J. Hald, H. Danielsen, in: F. Abe, S. Muneki, X. Xie, K.T. Hong (Eds.), Tsukuba, *3rd Symposium on Heat Resistant Steels and Alloys for High Efficiency USC Power Plants 2009*, http://www.nims.go.jp /hrdg/USC /Proceeding/Proceeding013Hald.pdf, (23.03.2010).

[39] P. Hofer, PhD thesis, *Microstructural analysis as basis for the development of novel power plant materials on the example of G-X12 CrMoWVNbN 10-1-1*, Graz University of Technology, 1999 (in German).

[40] B. Schaffernak, PhD thesis, *Characterization of 9-12% Cr steels by thermodynamic model calculations*, Graz University of Technology, 2000 (in German).

[41] G. Krauss, Mater. Sci. Eng. A 273-275 (1999) 40-57.

[42] B. Sonderegger, PhD thesis, *Characterisation of the Substructure of Modern Power Plant Steels using the EBSD-Method*, Graz University of Technology, 2005 (in German).

[43] B. Sonderegger, Mater. Sci. Eng. A 481-482 (2008) 466-470.

[44] F. Abe, Sci. Technol. Adv. Mater. 9, 013002 (2008).

[45] T. Barkar, J. Ågren, Mater. Sci. Eng. A 395 (2005) 110-115.

[46] S.C. Bose, K. Singh, A.K. Ray, R.N. Gosh, Mater. Sci. Eng. A 476 (2008) 257-266.

[47] G. Dimmler, P. Weinert, H. Cerjak, Int. J. Pres. Ves. Pip. 85 (2008) 55-62.

[48] A. Kostka, K.-G. Tak, R.J. Hellmig, Y. Estrin, G. Eggeler, Acta Mater. 55 (2007) 539-550.

[49] J.S. Lee, H.G. Armaki, K. Maruyama, T. Muraki, H. Asahi, Mater. Sci. Eng. A 428 (2006) 270-275.

[50] K. Sawada, K. Kubo, F. Abe, Mater. Sci. Eng. A 319-321 (2001) 784-787.

[51] Y.Z. Shen, S.H. Kim, C.H. Han, H.D. Cho, W.S. Ryu, C.B. Lee, J. Nucl. Mater. 374 (2008) 403-412.

[52] Å. Gustafson, M. Hättestrand, Mater. Sci. Eng. A 333 (2002) 279-286.

[53] M. Hättestrand, H.-O. Andren, Mater. Sci. Eng. A 318 (2001) 94-101.

[54] F. Kager, N. Böck, K. Spiradek-Hahn, S. Höfinger, M. Brabetz, G. Zeiler, in: J. Lecomte-Beckers, M. Carton, F. Schubert, P.J. Ennis (Eds.), Materials for Advanced Power Engineering 2006, Forschungszentrum Jülich GmbH, Jülich (2006) 1031-1040.

[55] P.J. Ennis, A. Zielinska-Lipiec, O. Wachter, A. Czyrska-Filemonowicz, Acta Mater. 45 (1997) 4901-4907.

[56] K. Sawada, M. Takeda, K. Maruyama, R. Ishii, M. Yamada, Y. Nagae, R. Komine, Mater. Sci. Eng. A 267 (1999) 19-25.

[57] G. Dimmler, PhD thesis, *Quantification of creep resistance and creep fracture strength of 9-12%Cr steels on microstructural basis*, Graz University of Technology, 2003 (in German).

[58] G. Dimmler, P. Weinert, E. Kozeschnik, H. Cerjak, Mater. Charact. 51 (2003) 341-352.

[59] G. Dimmler, P. Weinert, H. Cerjak, Mater. Sci. Techn. 20 (2004) 1525-1530.

[60] H.K. Danielsen, PhD thesis, *Z-phase in 9-12% Cr Steels*, The Technical University of Denmark, 2007.

[61] A. Golpayegani, H.-O. Andren, H. Danielsen, J. Hald, Mater. Sci. Eng. A 489 (2008) 310-318.

[62] H.K. Danielsen, J. Hald, Mater. Sci. Eng. A 505 (2009) 169-177.

[63] K. Sawada, H. Kushima, K. Kimura, M. Tabuchi, in: F. Abe, S. Muneki, X. Xie, K.T. Hong (Eds.), Tsukuba, *3rd Symposium on Heat Resistant Steels and Alloys for High Efficiency USC Power Plants 2009*, http://www.nims.go.jp/hrdg/USC/Proceeding/Proceeding024Sawada.pdf, (06.04.2010).

[64] H.K. Danielsen, J. Hald, in: J. Lecomte-Beckers, M. Carton, F. Schubert, P.J. Ennis (Eds.), Materials for Advanced Power Engineering 2006, Forschungszentrum Jülich GmbH, Jülich (2006) 1275-1284.

[65] K. Sawada, K. Suzuki, H. Kushima, M. Tabuchi, K. Kimura, Mater. Sci. Eng. A 480 (2008) 558-563.

[66] T. Abe, C. Kocer, K. Sawada, Y. Toda, in: F. Abe, S. Muneki, X. Xie, K.T. Hong (Eds.), Tsukuba, *3rd Symposium on Heat Resistant Steels and Alloys for High Efficiency USC Power Plants 2009*, http://www.nims.go.jp/hrdg/USC/Proceeding/Proceeding031Abe.pdf, (06.04.2010).

[67] F. Kauffmann, G. Zies, D. Willer, C. Scheu, K. Maile, K.H. Mayer, S. Straub, in: 31. MPA-Seminar *Werkstoff- und Bauteilverhalten in der Energie- & Anlagentechnik*, Stuttgart, 13.-14. Oktober 2005.

[68] F. Mendez-Martin, PhD thesis, *Investigation of the effects and impacts of selective composition modifications on the precipitation kinetics and creep resistance of a12%Cr steel*, Graz University of Technology, 2010.

[69] F. Abe, in: F. Abe, T.U. Kern, R. Viswanathan (Eds.), *Creep resistant steels*, Woodhead Publishing, Cambridge (2008), 279-304.

[70] H. Mughrabi, *Zum Wechselspiel zwischen den mechanischen Eigenschaften und der Mikrostruktur metallischer Werkstoffe*, DGM-Fortbildungspraktikum, Erlangen (1988).

[71] L.A. Gypen, A. Deruyttere, Scripta Metall. Mater. 15 (1981) 815-820.

[72] E. Hornbogen, H. Warlimont, *Metallkunde – Aufbau und Eigenschaften von Metallen und Legierungen*, Springer Verlag, Berlin-Heidelberg (1991).

[73] P. Gomiero, Y. Brechet, F. Louchet, A. Tourabi, B. Wack, Acta Metall. Mater. 40 (1992) 857-861.

[74] M.Z. Butt, P. Feltham, Acta Metall. Mater. 26 (1978) 167-173.

[75] M.Z. Butt, P. Feltham, J. Mater. Sci. 28 (1993) 2557-2576.

[76] H. Traub, H. Neuhäuser, Ch. Schwink, Acta Metall. Mater. 25 (1977) 437-446.

[77] H. Sieurin, J. Zander, R. Sandström, Mater. Sci. Eng. A 415 (2006) 66-71.

[78] J. Zander, R. Sandström, L. Vitos, Comp. Mater. Sci. 41 (2007) 86-95.

[79] L.A. Gypen, A. Deruyttere, J. Mater. Sci. 12 (1977) 1028-1033.

[80] L.A. Gypen, A. Deruyttere, J. Mater. Sci. 12 (1977) 1034-1038.

[81] C.E. Lacy, M. Gensamer, Trans. Am. Soc. Met. 32 (1944) 88-110.

[82] C.H. Young, H.K.D.H. Bhadeshia, Mater. Sci. Technol. 10 (1994) 209-214.

[83] C.R. Hutchinson, M. Gouné, A. Redjaimia, Acta Mater. 55 (2007) 213-223.

[84] Q. Li, Mater. Sci. Eng. A361 (2003) 385-391.

[85] T. Gladman, *The Physical Metallurgy of Microalloyed Steels*, The Institute of Materials, London (1997).

[86] C.-M. Hsiao, T.-Y. Zhang, in: J.C.M. Li (Ed.), *Microstructure and Properties of Materials*, World Scientific, Singapore (2000), 179-333.

[87] P. Polcik, PhD thesis, *Modellierung des Verformungsverhaltens der warmfesten 9-12% Cr-Stähle im Temperaturbereich von 550-650°C*, Shaker Verlag, Aachen (1999) (in German).

[88] E. Arzt, M.F. Ashby, Scripta Metall. Mater. 16 (1982) 1285-1290.

[89] E. Orowan, Proc. of Symp. Internal Stresses in Metals and Alloys, The Institute of Metals (1948), 451-453.

[90] M. McLean, Acta Metall. 33 (1985) 545-556.

[91] B. Ilschner, *Hochtemperatur-Plastizität*, Springer-Verlag, Berlin/Heidelberg, (1973).

[92] J. Hald, S. Straub, in: J. Lecomte-Beckers, F. Schubert, P.J. Ennis (Eds.), Materials for Advanced Power Engineering 1998, Forschungszentrum Jülich GmbH, Jülich (1998) 155-170.

[93] H. Cerjak, P. Hofer, B. Schaffernak, K. Spiradek, G. Zeiler, in: J. Lecomte-Beckers, F. Schubert, P.J. Ennis (Eds.), Materials for Advanced Power Engineering 1998, Forschungszentrum Jülich GmbH, Jülich (1998) 287-296.

[94] P. Weinert, PhD thesis, *Modelling of creep of ferritic/martensitic 9-12%Cr steels on microstructural basis*, Graz University of Technology, 2001 (in German).

[95] C.S. Smith, Trans. AIME 175 (1948) 15-51.

[96] D. McLean, Trans. Metall. Soc. AIME 242 (1968) 1193-1203.

[97] R. Sandström, Acta Metall. Mater. 25 (1977) 905-911.

[98] R.J. McElroy, Z.C. Szkopiak, Int. Metall. Rev. 17 (1972) 175-202.

[99] G. Eggeler, N. Nilsvang, B. Ilschner, Steel Res. 58 (1987) 97-103.

[100] G. Eggeler, Acta Metall. Mater. 37 (1989) 3225-3234.

[101] P. Plocik, T. Sailer, W. Blum, S. Straub, J. Buršik, A. Orlová, Mater. Sci. eng. A 260 (1999) 252-259.

[102] R. Agamennone, W. Blum, C. Gupta, J.K. Chakravartty, Acta Mater. 54 (2006) 3003-3014.

[103] K. Kuchařová, J. Němec, A. Dlouhý, in: J.C. Earthman, F.A. Mohamed (Eds.), *Creep and Fracture of Engineering Materials and Structures*, The Minerals & Metals Society, Warrendale (1997), 79-88.

[104] J. Čadek, *Creep in metallic materials*, Elsevier, Amsterdam (1988).

[105] M. Ashby, *The theory of the critical shear stress and work hardening of dispersion-hardened crystals*, G.S. Ansell, T.D. Cooper and F.V. Lenel (Eds.), Metallurgical Society Conference, Vol. 47, Gordon and Breach, NewYork (1968), 143-205.

[106] B. Reppich, Z. Metallkde. 73 (1982) 697-705.

[107] E. Kozeschnik, in: K.G.F. Janssens, D. Raabe, E. Kozeschnik, M.A. Miodownik, B. Nestler (Eds.), *Computational Materials Engineering – An Introduction to Microstructure Evolution*, Elsevier Academic Press, Burlington (2007), 179-217.

[108] M. Perez, Scripta Mater. 52 (2005) 709-712.

[109] R. Bürgel, *Handbuch Hochtemperatur-Werkstofftechnik – Grundlagen, Werkstoffbeanspruchungen, Hochtemperaturlegierungen*, Vieweg & Sohn Verlagsgesellschaft, Braunschweig, (2001).

[110] J. Svoboda, F.D. Fischer, P. Fratzl, E. Kozeschnik, Mater. Sci. Eng. A 385 (2004) 166-174.

[111] E. Kozeschnik, J. Svoboda, P. Fratzl, F.D. Fischer, Mater. Sci. Eng. A 385 (2004) 157-165.

[112] E. Kozeschnik, J. Svoboda, F.D. Fischer, CALPHAD 28 (2005) 379-382.

[113] L. Onsager, Phys. Rev. 37 (1931) 405-426, 38 (1931) 2265-2279.

[114] J. Svoboda, I. Turek, F.D. Fischer, Phil. Mag. 85 (2005) 3699-3707.

[115] R. Kampmann, R. Wagner, Acta Scripta Metall. Ser. 91 (1984).

[116] E. Kozeschnik, J. Svoboda, F.D. Fischer, in: J.M. Howe (Ed.), *Proceedings International Conference Solid-Solid Phase Transformations in Inorganic Materials*, PTM 2005, Phoenix (2005), 301-310.

[117] B. Sonderegger, E. Kozeschnik, Metall. Mater. Trans. A 40 (2009) 499-510.

[118] W.L. Bragg, E.J. Williams, Proc. R. Soc. 145 (1934) 699-730.

[119] R. Becker, Ann. Phys. 32 (1938) 128-40.

[120] D. Turnbull, Impur. Imperf. (1955) 121-43.

[121] B. Sonderegger, E. Kozeschnik, Scripta Mater. 60 (2009) 635-638.

[122] Y.W. Lee, H.I. Aaronson, Acta Metall. 28 (1980) 539-548.

[123] T. Gladman, Mater. Sci. Tech. 15 (1999) 30-36.

[124] D. Hull, D.J. Bacon, *Introduction to dislocations – 3rd edition*, Pergamon Press, Oxford (1984).

[125] A. Deschamps, M. Militzer, W.J. Poole, ISIJ Int. 41 (2001) 196-205.

[126] U.F. Kocks, Can. J. Phys. 45 (1967) 737-755.

[127] A.J.E. Foreman, M.J. Makin, Philos. Mag. 14 (1966) 911-924.

[128] F. Vollertsen, S. Vogler, *Werkstoffeigenschaften und Mikrostruktur*, Carl Hanser Verlag, München (1989).

[129] G. E. Dieter, Mechanical Metallurgy – SI Metric Edition, McGraw-Hill Book Company, London (1988).

[130] A.J. Ardell, Metall. Trans. 16A (1985), 2131-2165.

[131] E. Arzt, Acta Mater. 46 (1998) 5611-5626.

[132] B. Sonderegger, Ultramicroscopy 106 (2006), 941-950.

[133] F. Fazeli, W.J. Poole, C.W. Sinclair, Acta Mater. 56 (2008) 1909-1918.

[134] L.M. Brown, R.K. Ham, *Dislocation-Particle Interactions*, in: *Strengthening methods in crystals*, A. Kelly, R.B. Nicholson (eds.), Applied Science Publishers, London (1965), 9-135.

[135] E. Nembach, *Particle Strengthening of Metals and Alloys*, John Wiley & Sons, New York (1996).

[136] V. Gerold, H. Haberkorn, Phys. Stat. Sol. 16 (1966) 675-684.

[137] K.C. Russell, L.M. Brown, Acta Metall. Mater. 20 (1972) 969-974.

[138] U.F. Kocks, Acta Metall. Mater. 14 (1966) 1629-1631.

[139] S. Torquato, B. Lu, J. Rubinstein, J. Phys A-Math. Gen. 23 (1990) L103-L107.

[140] G. Cao, X. Chen, J.W: Kysar, D. Lee, Y.X. Gan, Mech. Res. Commun. 34 (2007) 275-282.

[141] U.F. Edgal, J. Math. Chem. 42 (2007) 1101-1134.

[142] J.W. Leggoe, Scripta Mater. 53 (2005) 1263-1268.

[143] J.W. Leggoe, J.B. Riggs, Mater. Sci. Eng. A 426 (2006) 289-297.

[144] A. Tewari, A.M. Gokhale, Mater. Sci. Eng. A 396 (2005) 22-27.

[145] A. Tewari, A.M. Gokhale, Mater. Sci. Eng. A 385 (2004) 332-341.

[146] B. Sonderegger, *Herleitung von nearest neighbour distances: punktförmige und globulare Teilchen in 3D und 2D*, Graz University of Technology (2008).

[147] E.E. Underwood, *Quantitative Stereology*, Addison Wesley, Massachusetts (1970).

[148] R. Schnitzer, R. Radis, M. Nöhrer, M. Schober, R. Hochfellner, S. Zinner, E. Povoden-Karadeniz, E. Kozeschnik, H. Leitner, J. Alloy Compd., *in press.*

[149] R. Radis, E. Kozeschnik, *technical report* (CD-Labor Bericht).

[150] R. Schnitzer, *private communication.*

[151] U.F. Kocks, Phil. Mag. 13 (1966) 541.

[152] U.F. Kocks, Acta. Met., Letter to the Editor, (1966).

[153] R. Labusch, Acta Metall. Mater. 20 (1972) 917-927.

[154] P. Haasen, R. Labusch, Mater. Sci. Eng. 12 (1973) 216.

[155] F.R.N. Nabarro, Philos. Mag. 35 (1977), 613-622.

[156] P. Feltham, Mater. Sci. Eng. 11 (1973) 118-119.

[157] A.W. Zhu, A. Cosontos, E.A. Starke jr., Acta Mater. 47 (1999) 1713-1721.

[158] H. Saage, M. Heilmaier, J. Eckert, Z. Metallkd. 96 (2005) 799-804.

[159] J.A. del Valle, A.C. Picasso, R. Romero, 51 (2003) 6443-6452.

[160] U. Lagerpusch, V. Mohles, E. Nembach, Mater. Sci. Eng. A 319-321 (2001) 176-178.

[161] U. Lagerpusch, E. Nembach, Scripta. Mater. 42 (2000) 615-619.

[162] U. Lagerpusch, V. Mohles, D. Baither, B. Anczykowski, E. Nembach, Acta. Mater. 48 (2000) 3647-3656.

[163] J. Irvine, T.N. Baker, Mater. Sci. Eng. 64 (1984) 123-134.

[164] S. Maropoulos, J.D.H. Paul, N. Ridley, Mater. Sci. Tech. 9 (1993) 1014-1019.

[165] T.J. Koopenaal, D. Kuhlmann-Wilsdorf, Appl. Phys. Lett. 4 (1964), 59-61.

[166] I. Holzer, E. Kozeschnik, Mater. Sci. Eng. A 527 (2010) 3546-3551.

[167] E. Kozeschnik, I. Holzer, in: F. Abe, T.U. Kern, R. Viswanathan (Eds.), *Creep resistant steels*, Woodhead Publishing, Cambridge (2008), 305-328.

[168] I. Holzer, E. Kozeschnik, Int. J. Mat. Res. 99 (2008) 416-421.

[169] I. Holzer, E. Kozeschnik, H. Cerjak, T. Indian I. Metals, *in press.*

[170] E. Kozeschnik, B. Buchmayr, in: H. Cerjak, H.K.D.H. Bhaddeshia (Eds.), *Mathematical Modelling of Weld Phenomena*, IOM Communications Ltd., London (2001), 349-361.

[171] S.R. Goodman, S.S. Brenner, J.R. Low jr., Metall. Trans. 4 (1973) 2363-2369.

[172] S.R. Goodman, S.S. Brenner, J.R. Low jr., Metall. Trans. 4 (1973) 2371-2378.

[173] K. Osamura, H. Okuda, S. Ochiai, M. Takashima, K. Asano, M. Furusaka, K. Kishida, F. Kurosawa, ISIJ Int. 34 (1994) 359-365.

[174] R. Monzen, K. Takada, K. Matsuda, Z. Metallkd. 94 (2003) 1241-1246.

[175] D. Isheim, R. Prakash Kolli, M.E. Fine, D.N. Seidman, Scr. Mater. 55 (2006) 35-40.

[176] M.E. Fine, J.Z. Liu, M.D. Asta, Mater. Sci. Eng. A 463 (2007) 271-274.

[177] F. Soisson, A. Barbu, G. Martin, Acta Mater. 44 (1996) 3789-3800.

[178] T. Nagano, M. Enomoto, Scr. Mater. 55 (2006) 223-226.

[179] E. Kozeschnik, Scr. Mater. 59 (2008) 1018-1021.

[180] J Yang, M. Enomoto, ISIJ Int. 45 (2005) 1335-1344.

[181] M. Perez, M. Dumont, D. Acevedo-Reyes, Acta. Mater. 56 (2008) 2119-2132.

[182] M.A. Turchanin, P.G. Agraval, I.V. Nikolaenko, J. Phase Equilib. 24 (2003) 307-319.

[183] J. Fridberg, L.-E. Törndahl and M. Hillert, Jernkontorets Ann., 153 (1969) 263-276.

[184] Thermodynamic Database 'mc_steel', version 1.63, Institute of Materials Science and Technology, Vienna University of Technology.

[185] Mobility Database 'mc_sample_fe', version 1.03, Institute of Materials Science and Technology, Vienna University of Technology.

[186] A. Van der Ven, L. Delaey, Prog. Mater. Sci. 40 (1996) 181-264.

[187] O.R. Myhr, Ø. Grong, S. Klokkehaug, H.G. Fjær, in: Mathematical Modelling of Weld Phenomena vol. 6, Bhadeshia H.K.D.H. (ed.), Maney Publishing, London, 2002.

[188] O.R. Myhr, Ø. Grong, H.G. Fjær, C.D. Marioara, Acta Mater. 52 (2004) 4997-5008.

[189] M. Nicolas, A. Deschamps, Acta Mater. 51 (2003) 6077-6094.

[190] H. Ogi, H. Ledbetter, S. Kim, J. Alloy. Compd. 310 (2000) 432-435.

[191] R. Rana, W. Bleck, S.B. Singh, O.N. Mohanty, Mater. Lett. 61 (2007) 2919-2922.

[192] M.J. Konstantinovic, A. Almazouzi, M. Scibetta, E. van Walle, J. Nucl. Mater. 362 (2007) 283-286.

[193] R. Prakash Kolli, D.N. Seidman, Acta Mater. 56 (2008) 2073-2088.

[194] C.S. Pande, M.A. Imam, Mater. Sci. Eng. A 457 (2007) 69-76.

[195] M.F. Fine, D. Isheim, Scripta Mater. 53 (2005), 115-118.

[196] J.Z. Liu, A. van de Walle, G. Gosh, M. Asta, Phys. Rev. B 72 (2005) 144109 1-16.

[197] A. Deschamps, M. Militzer, W.J. Poole, ISIJ Int. 41 (2001) 196-205.

[198] T. Harry, D.J. Bacon, Acta Mater. 50 (2002) 195-208.

[199] T. Harry, D.J. Bacon, Acta Mater. 50 (2002) 209-222.

[200] J. Eliasson, A. Gustafson, R. Sandström, Key Eng. Mater. 171-174 (2000) 277-284.

[201] R. Lagneborg, *Effect of grain size and precipitation of carbides on creep properties in Fe-20%Cr-35%Ni alloys*, J. of Iron and Steel Institute, (1969) 1503-1506.

[202] F.R.N. Nabarro, Physics of the Solid State 42 (2000) 1456-1459.

[203] K.E. Amin, J.E. Dorn, Acta Metall. 7 (1969) 1429-1434.

[204] W. Blum, in: F. Abe, T.U. Kern, R. Viswanathan (Eds.), *Creep resistant steels*, Woodhead Publishing, Cambridge (2008), 365-402.

[205] S.W. Plimon, Master thesis, *Simulation of an industrial heat treatment and accompanying microstructural investigation of a modern 9-12% chromium steel*, Graz University of Technology, 2004 (in German).

[206] H.K. Danielsen, J. Hald, CALPHAD 31 (2007) 505-514.

[207] H.K. Danielsen and J. Hald, *Z-phase in 9-12% Cr Steels*, internal report 863, Värmeforsk AB, (2004).

[208] H.K. Danielsen, J. Hald, F. G. Grumsen and M.A.J. Somers, Metall. Mater. Trans. 37A (2006) 2633-2640.

[209] M. McLean, Acta metal. 33 (1985) 545-556.

[210] R.B. Nicholson, in: *Effect of second-phase particles on the mechanical properties of steel*, the Iron and Steel Institute, London (1971) 1-8.

[211] R. Lagneborg, Scripta Metallurgica 7 (1973) 605-614.

[212] J.D. Verhoeven, *Fundamentals of Physical Metallurgy*, John Wiley & Sons, New York, (1975).

[213] P.A. Manohar, M. Ferry, T. Chandra, ISIJ International 38 (1998) 913-924.

[214] O. Kosik, D.J. Abson, J.J. Jonas, J. of Iron and Steel Inst., Vol. 209:88 (1971) 624-629.

[215] G. Guntz, M. Julien, G. Kottmann, F. Pellicani, A. Pouilly and J.C. Vaillant, *The T 91 Book – Ferritic tubes and pipe for high temperature use in boilers*, Vallourec Industries – France, 1991.

[216] H. Cerjak, P. Hofer, B. Schaffernak, K. Spiradek, G. Zeiler: VGB Kraftwerkstechnik 77 (1997) 691.

[217] C. Berger, R.B. Scarlin, K.H. Mayer, D.V. Thornton, S.M. Beech, in:D. Coutsouradis, J.H. Davidson, J. Ewald, P. Greenfield, T. Khan, M. Malik, D.B. Meadowcroft, V. Regis, R.B. Scarlin, F. Schubert, D.V. Thornton (Eds.), Kluwer Academic Publishers, Dordrecht (1994) 47-72.

[218] R.W. Vanstone, COST 501/3 WP11 Metallography and alloy design group - Analysis of quantitative data, internal report, GEC Alsthom Turbine Generators Limited, Rugby UK, 1994.

[219] V. Vodarek, A. Strang, in: J. Lecomte-Beckers, M. Carton, F. Schubert, P.J. Ennis (Eds.), Materials for Advanced Power Engineering 2002, Forschungszentrum Jülich GmbH, Jülich (2002) 1223.

[220] TCFE3 thermodynamic database, Thermo-Calc Software AB, Stockholm, Sweden, 1992-2004.

[221] K.H. Mayer, *private communication*, 03.04.2007.

[222] F. Kager, *private communication*, 06.05.2008.

[223] D.W. Smith, R.F. Hehemann, J. Iron Steel I. 209 (1971) 467-481.

[224] Thermodynamic Database 'mc_steel', version 1.102, Institute of Materials Science and Technology, Vienna University of Technology.

Appendix

A   Calculation of lower yield stress in a 1.4 at.% Cu alloy

The present part of the appendix is related to the application section 5.1. In this section the calculation of the lower yield stress (LYS) evolution is critically assessed on the basis of the strengthening mechanism operative in an Fe-1.4at.% Cu alloy aged isothermally at 500°C. In the following, detailed information are given how to simulate Fe-Cu precipitation kinetics taking into account a coherent bcc as well as an incoherent fcc precipitate phase. Further, the correct application of the strength module implemented in MatCalc is determined and the LYS evolution is calculated taking into account all relevant strength contributions.

On the basis of the MatCalc Tutorial *T14: Introduction to precipitation kinetics*, the most important simulation steps are discussed in sequence. Thus, the interested reader is also referred to the MatCalc homepage (http://www.matcalc.at), where additional information about the software and simulation settings are given.

For the present calculation MatCalc 5.32 (rel 1.003) is used. The utilized databases are the thermodynamic database mc_steel.tdb and the diffusion database mc_sample_fe.ddb.

A.1   Thermodynamic setup

The first step in the present calculation is to set up the thermodynamics of the considered system. Thus, create a new workspace (press Ctrl+N), and open the dialog window 'MatCalc setup – Thermodynamics' (press F5). Open the database mc_steel.tdb and select the elements FE and CU. Further, select the phases BCC_A2 (ferrite phase) and CU_S (copper phase). When the thermodynamic data have been read in, close the dialog window and press F7 to open the 'Nominal composition ...' window. Enter a copper content of 0.014. Be careful that the unit 'mole fraction' is selected and press OK.

As mentioned previously, in the present calculation two types of Cu-precipitates are considered. These are on one hand incoherent, almost pure fcc copper precipitates (described by the CU_S phase) and coherent bcc precipitates. The latter precipitate phase is taken into account by creating an additional BCC_A2 phase. Thus, open the 'Phase status ...' dialog window (F8) and mark the BCC_A2 phase. Go on 'Create ...' and select the equilibrium phase type. A new phase BCC_A2#01 is created. Change the major

constituents of this phase from ':FE:VA:' to ':CU:VA:' and confirm the change by pressing 'Set now'. This phase will represent the bcc Cu-precipitate phase.

A.2 Experimental data and nucleus composition

To simulate the precipitation kinetics of the investigated Fe-Cu alloy in a comprehensive and consistent manner, different effects have to be considered as pointed out in section 5.2.1. To take the effect of variable nucleus composition of the coherent bcc Cu-precipitates into account, a table with information about Cu-content of the matrix (Cu_M) and corresponding equilibrium Cu-content of the precipitates (Cu_P) at 500°C is created. In the following this table is denoted by 'table_1'. The pairs of values are shown in Table A.1. How to create a Table in MatCalc is described in detail in Tutorial *T10: T_0-temperature in Fe-Cr-C* on the MatCalc homepage.

Table A.1. Equilibrium Cu-content of the critical nucleus (Cu_P) as function of nominal Cu-content of the matrix (Cu_M) at 500°C.

Cu_M, at.%	Cu_P, at.%	Cu_M, at.%	Cu_P, at.%	Cu_M, at.%	Cu_P, at.%
		(table_1)			
0,0005	0,98	0,011	0,80	0,021	0,47
0,002	0,98	0,012	0,77	0,022	0,44
0,003	0,98	0,013	0,73	0,023	0,42
0,004	0,97	0,014	0,69	0,024	0,40
0,005	0,96	0,015	0,65	0,025	0,38
0,006	0,94	0,016	0,61	0,026	0,37
0,007	0,92	0,017	0,58	0,027	0,35
0,008	0,90	0,018	0,55	0,028	0,34
0,009	0,87	0,019	0,52	0,029	0,33
0,01	0,84	0,020	0,49	0,030	0,32

To compare the simulation results with the experimental data referred in section 5.1, four further tables are created (table_2 to table_5). The content of the tables for the phase fraction *f*, mean particle radius *R*, number density *N* and lower yield stress (LYS) is shown in the following.

Table A.2. Experimentally determined evolution of precipitate parameters and lower yield stress (LYS) at room temperature during isothermal ageing at 500°C.

t, s (table_2)	f, %	t, s (table_3)	R, nm	t, s (table_4)	N, m^{-3}	t, s (table_5)	LYS, MPa
1012	0,071	3453	0.8	3666	$9.4 \cdot 10^{23}$	0	247
3556	0,218	10572	1.2	10777	$1.0 \cdot 10^{24}$	0	254
10666	0,727	31677	2.8	32261	$1.08 \cdot 10^{23}$	359	302
31996	1,040	141003	4.8	32261	$4.5 \cdot 10^{21}$	363	311
122264	1,278	427554	7.2	124734	$2.7 \cdot 10^{22}$	1205	471
429657	1,298	141003	5.1	124734	$6.9 \cdot 10^{21}$	3628	570
		427554	8.2	436150	$8.3 \cdot 10^{21}$	3629	560
				436150	$7.3 \cdot 10^{21}$	10680	572
						10681	567
						32236	549
						32243	538
						144295	458
						144314	451
						436048	379
						436115	372

A.3 Precipitation domain

To carry out the kinetic simulation a precipitation domain must be defined. Therefore, open the 'Precipitation domains …' window (Ctrl+F8) and create a precipitation domain with the BCC_A2 phase as matrix phase (ferritic domain). Leave all other settings, for now, as default.

A.4 Precipitate phases

To create the bcc and fcc precipitate phases open the 'Phase status …' window (F8). Select the BCC_A2#01 phase in the list at the left hand side and go on 'Create …'. Select the precipitate phase type and press OK. Do the same for the CU_S phase. Now, two new phases appear in the list. The BCC_A2#01_p0 and the CU_S_p0 phase. Select the flag 'Precipitate' and define for both precipitate types 500 size classes and add the precipitate phases to the precipitation domain.

As pointed out in section 5.1.2, several effects have to be considered when calculating the interfacial energy of the precipitates. Thus, make sure that for both precipitate phases the interfacial energy size correction is used in the simulation. Further, reduce the calculated interfacial energy of the BCC_A2#01_p0 phase by 10%. Thus, unmark the 'auto' check for the interfacial energy and insert the expression 'cie$bcc_a2#01*0,9'. This correction factor takes into account the atomic mixing effect at the precipitate/matrix interface, as already pointed out in the application section. Finally, for a better representation of the experimental results, especially the number density of precipitates, reduce the interfacial energy of the CU_S_p0 phase by 2% ('cie$cu_s*0,98').

Then select the flag 'Nucleation' and define for both precipitate phases 'bulk (homogeneous)' as nucleation sites. For the nucleus composition of the CU_S_p0 phase select 'ortho-equilibrium' and for the BCC_A2#01_p0 phase select 'fixed molar site fractions'. The latter setting is defined to take into account the variable nucleus composition of the bcc precipitate phase during ageing. Therefore, go on 'Set …' and insert in the column 'x_CU(0)' the expression table_1(xbcc_a2cu). In the column 'x_FE(0)' type (1-table_1(xbcc_a2cu)). With this setting the nucleus composition is always adapted to the current matrix supersaturation. Press OK and switch to the 'Special' flag.

Unmark the 'Nucleation site saturation …' check for both precipitate phases and change for the BCC_A2#01_p0 phase in the 'Diffusion in precipitate …' field the ratios for the diffusivity in the precipitate from 10^{-2} to 10^{-5}. To finish the precipitate phase setup the quenched-in vacancy factor for both precipitate phases has to be considered. For this, enter in the 'Special precipitate options …' field a value of 150 in the 'Substitutional matrix diffusion enhancement' field.

With this setting the setup for the kinetic simulation is completed. However, to get an executable simulation file, a mobility database must be read in. Again, press F5 to open the 'MatCalc setup' window. Select in the left column of the window 'Diffusion data' and press 'Read' to open the diffusion database mc_sample_fe.ddb.

A.5 MatCalc strength module

To determine the evolution of the lower yield stress (LYS) with MatCalc, the strength module outlined in section 4 is applied. In the following the simulation settings are listed. For further information about the implemented strength module and the theory about strengthening mechanism the interested reader is referred to section 4.

A.5.1 Calculation of LYS

As discussed in section 5.1, the strength contributions by inherent lattice strength, the grain size strengthening, solid solution strengthening and precipitation strengthening are considered for the investigated 1.4 at.% Cu alloy. The inherent lattice strength and the grain size strengthening effect are assumed to be constant. If both effects are superimposed the strength contribution amounts to 180 MPa (for details see section 5.1.3.1).

The solid solution strengthening effect ($\sigma_{\text{solid-sol.}}$) is evaluated as function of the Cu concentration in the matrix according to eq. (4.30) with a concentration exponent $n= 2/3$ and a strengthening factor k_{Cu}=40 MPa/(wt.% Cu).

The precipitation hardening effect is considered according to eq. (5.2). The respective precipitation strengthening contributions are directly determined by the strength module in MatCalc. Thereto, open the 'Precipitation domains ...' window and select the 'Structure' flag. Define the Taylor factor as 2.5 and the strength superposition exponent as 1. Close the window and open the 'Phase status ...' window. Go to the 'Structure' flag and select the BCC_A2#01_p0 phase in the list at the left side. Define the values in the dialog window as follows (leave all other settings as default)[*]:

- elastic modulus: $129 \cdot 10^9$ Pa (elastic modulus of copper)
- volumetric misfit: 0.0171 (=$3 \cdot \varepsilon_{\text{coh}}$, to convert the linear in a volumetric misfit)
- C (Ashby-Orowan): 0.06
- C' (dislocation line tension): 0.09
- C'' (modulus strengthening): 0.07
- modulus strengthening m: 0.75
- alpha (α): 1.0 (superposition exponent for weak and strong obstacles)

---

[*] The terms C, C', C'', m, α and β are identical to the constants used in section 4.

■ beta (β): 2.0 (superposition exponent for weak obstacles only)

For the CU_S_p0 phase only the constants C=0.06 and C'=0.09 have to changed, based on the assumption that for this phase only the Orowan mechanism is operative. α and β again are defined as 1.0 and 2.0, respectively. Leave all other settings as default.

A.6 Simulation results

If all settings are correctly made, the simulation can be started. Press Ctrl+K and insert a simulation end time of 10^{10} seconds. Select in the 'Temperature control ...' field the option 'isothermal' and define an ageing temperature of 500°C. Press 'Go' to start the simulation.
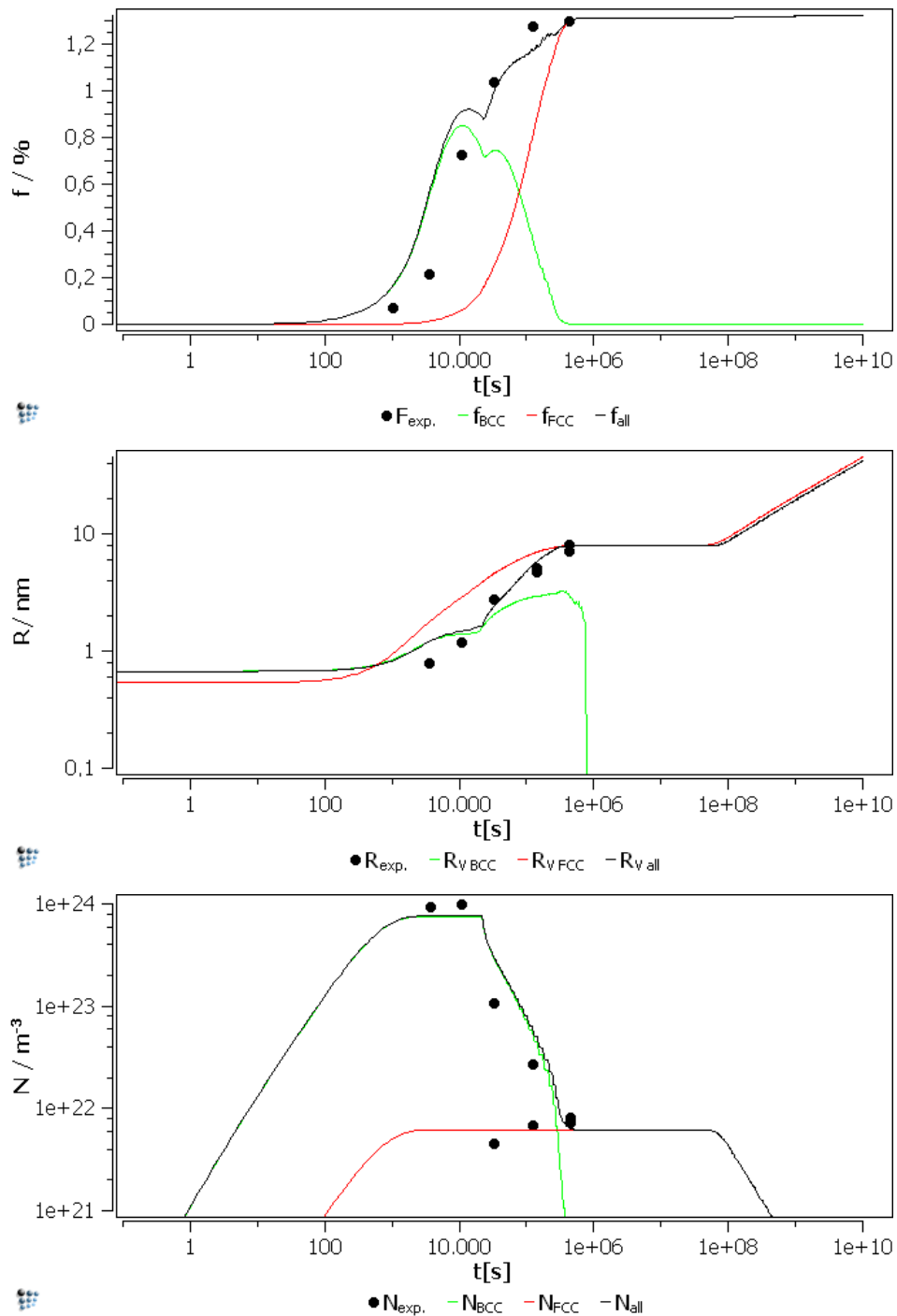

Figure A.1. Calculated evolution of phase fraction *f*, mean precipitate radius *R* and number density *N* compared to the experimental data reported in section 5.1.

Figure A.1 shows the results of the kinetic simulation for the evolution of phase fraction *f*, mean particle radius *R* and number density *N* compared to the experimental data. It has to be pointed out that MatCalc displays all values in SI units and thus, several changes have been made for a better presentation of the simulation results. For further information on the graphical presentation of results in MatCalc, the reader is referred to Tutorial *T4: Graphical presentation and export of results (1)* and *T5: MatCalc built-in variables; graphical output (2)*.

Figure A.2 shows the evolution of LYS as well as the different strength contributions by precipitates and the solid solution hardening effect. Again, the results are compared to the experimental data. The several series in the present plot are defined as following:

- $LYS_{exp.}$: table_5
- σ_{Orowan}: TAO_OROWAN\$CU_S_P0*1e-6
- $\sigma_{chem.}$: TAO_CHEM\$BCC_A2#01_P0*1e-6
- $\sigma_{coh.}$: TAO_COHER\$BCC_A2#01_P0*1e-6
- $\sigma_{mod.}$: TAO_MOD\$BCC_A2#01_P0*1e-6
- $\sigma_{solid-sol.}$: 40*(x\$bcc_a2\$cu\$wp^(2/3))
- $LYS_{calc.}$: TTAO_ALL\$ferrite*1e-6+(40*(x\$bcc_a2\$cu\$wp^(2/3)))+180
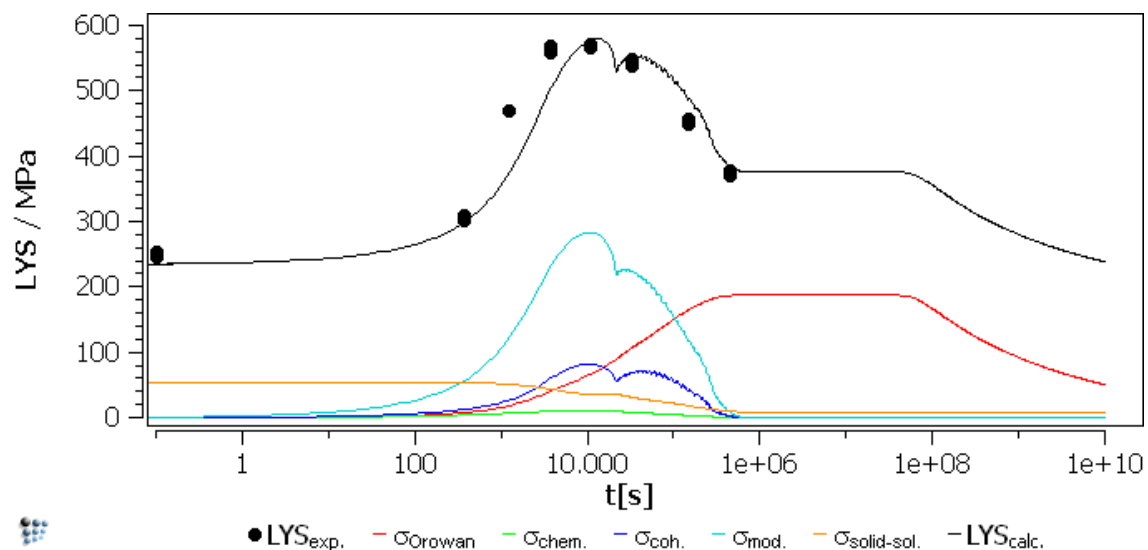
Figure A.2. Calculated and experimental evolution of the lower yield stress (LYS) as a function of inherent lattice strength, grain size strength contribution, chemical strengthening($\sigma_{chem.}$), coherency strengthening ($\sigma_{coh.}$) modulus mismatch hardening ($\sigma_{mod.}$) and solid solution hardening ($\sigma_{solid-sol.}$).
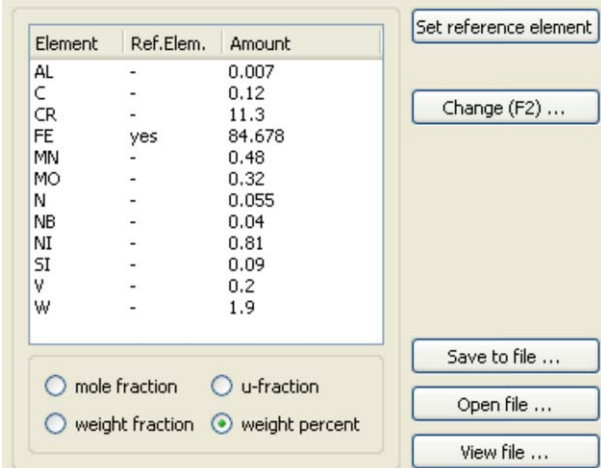
B Calculation of the 0.2% proof stress in the 11% Cr steel COST D1

In this section detailed information is given on how to determine the 0.2% proof stress evolution of a martensitic 11% Cr steel during tempering using the strength module implemented in the software MatCalc. All simulation steps discussed in the following are based on the application section 5.4. The layout of this section is strongly related to Appendix A. Thus, the repetition of some points is possible. However, the author wants to list as clear as possible all crucial simulation settings to give the interested reader a comprehensible support.

Also for this calculation MatCalc 5.32 (rel 1.003) is used. The utilized databases are the thermodynamic database mc_steel.tdb and the diffusion database mc_steel.ddb.

B.1 Thermodynamic setup

To set up the thermodynamics of the considered system create a new workspace (press Ctrl+N), and open the dialog window 'MatCalc setup – Thermodynamics' (press F5). Open the database mc_steel.tdb and select the elements AL, C, CR, FE, MN, MO, N, NB, NI, SI, V and W. Then, select the phases ALN_COST, BCC_A2, CEMENTITE, CR2N, FCC_A1, LAVES_PHASE, M23C6 and M7C3. When the thermodynamic data have been read in, close the dialog window and press F7 to open the 'Nominal composition ...' window.

Figure B.1. Considered chemical composition in the present calculation of COST alloy D1.

Enter the chemical composition of the alloy according to Figure B.1 and press OK.

B.2 Precipitation domain

As already pointed out in section A.3, a precipitation domain must be defined for an executable simulation setup. Therefore, open the 'Precipitation domains ...' window (Ctrl+F8) and create two precipitation domains with the FCC_A1 phase (Austenite) and BCC_A2 phase (Martensite) as matrix phase, respectively. Insert the following parameters in the respective precipitation domains listed in Table B.1. Leave all other settings as default.

Table B.1. Microstructure parameters of precipitation domains.

	Austenite	Martensite
Grain diameter, (m)	$50 \cdot 10^{-6}$	$50 \cdot 10^{-6}$
Grain size elongation factor, -	1	1
Subgrain diameter, (m)	-	$0.5 \cdot 10^{-6}$
Subgrain size elongation factor, -	1	100
Equilibrium dislocation density, (m^{-2})	$1 \cdot 10^{-11}$	$1 \cdot 10^{-14}$

B.3 Precipitate phases

To create the precipitate phases open the 'Phase status ...' window (F8). Select e.g. the FCC_A1#01 equilibrium phase in the list at the left hand side and go on 'Create ...'. Select the precipitate phase type and press OK. Do the same for the other phases until you have created the other precipitate phases (labelled by the appendix '_p0') shown in Figure B.2.

Figure B.2. Considered precipitate phases in
the present calculation.

Select the flag 'Precipitate' and define for all precipitate types 10 size classes and add the precipitate phases to the precipitation domain 'Austenite'. Leave all other settings as default to calculate the interfacial energy of the precipitates.

Then select the flag 'Nucleation' and define for all precipitate phases the initial nucleation site 'grain boundaries'.

B.4 Heat treatment definition

In the present calculation a heat treatment according to the parameters shown in Table B.2 is considered. To define this heat treatment simulated in the present section, open the 'Edit heat treatments …' window (press Alt+F8) and define the heat treatment segments as shown in Figure B.3. For details about the definition of a multi-stage heat treatment the reader is referred at this point to Tutorial *T17: Complex multi-stage heat treatments* on the MatCalc homepage.

Table B.2. Heat treatment parameters of steel D1.

Heat Treatment Variant	Solution treatment				Tempering								
					1				2				
	(°C)	(h)	HR	CR*	(°C)	(h)	HR	CR	(°C)	(h)	HR	CR
			(°C/h)				(°C/h)				(°C/h)	
A	1020	4	25	120/40	570	8	50	-10	720	2	50	-10
B	1020	4	25	120/40	570	8	50	-10	720	8	50	-10
C	1020	4	25	120/40	570	8	50	-10	720	16	50	-10
D	1020	4	25	120/40	570	8	50	-10	720	24	50	-10

HR … heating rate
CR … cooling rate
* … interrupted cooling from austenitising temperature wit 120°C/h down to 500°C and 40°C/h down to room temperature

As it can be seen for heat treatment segment 1, 3 and 7 MatCalc '*Pre-Segment scripts*' are defined and the precipitation domain is changed to account for the transformation from austenite to martensite and back. The content of the pre-segment scripts is shown in Figure B.4 and Figure B.5. The command lines define the nucleation sites of the different precipitate phases in the austenitic and martensitic matrix phases respectively.
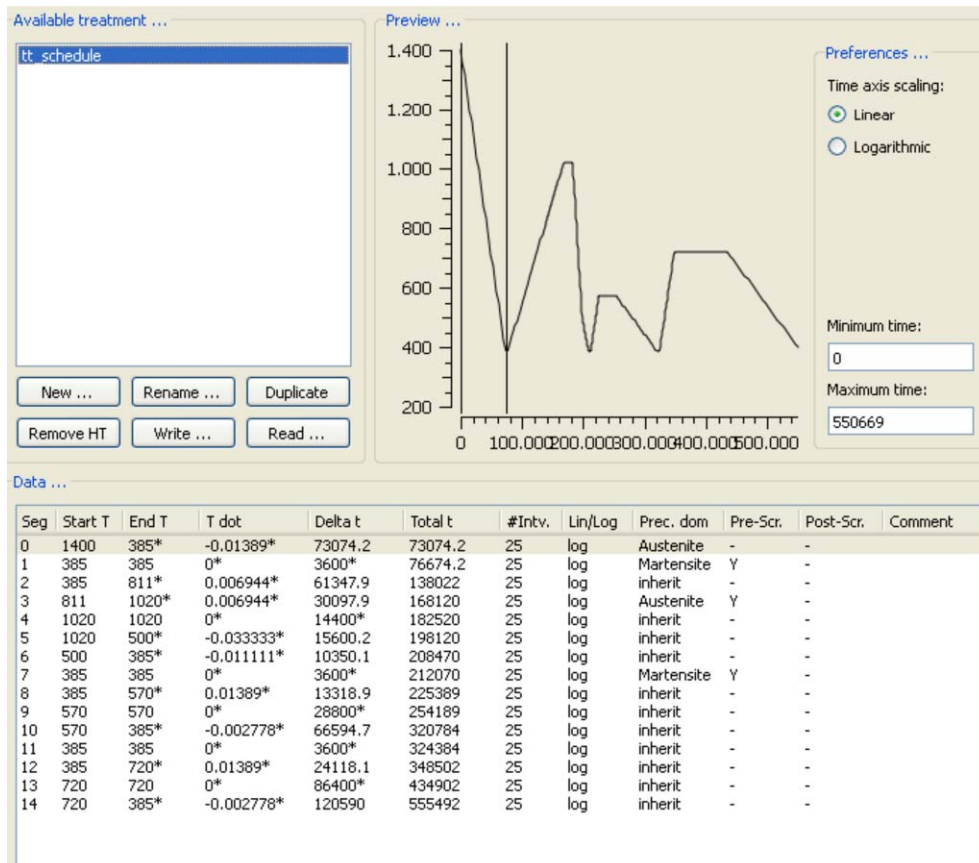
Figure B.3. Overview of heat treatment segments of the simulated
heat treatment named '*tt_schedule*'.

With this setting the setup for the kinetic simulation is completed. However, to get an executable simulation file, a mobility database must be read in. Again, press F5 to open the 'MatCalc setup' window. Select in the left column of the window 'Diffusion data' and press 'Read' to open the diffusion database mc_steel.ddb.
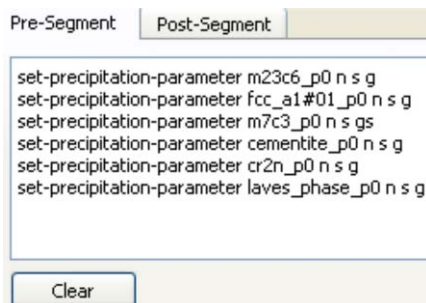
Figure B.4. Pre-segment script to define the nucleation sites in the austenitic matrix.
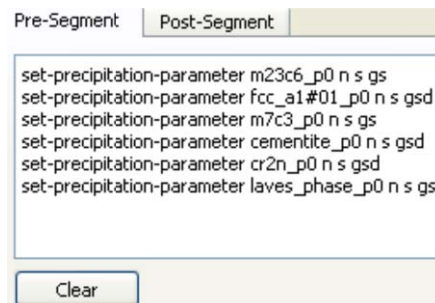
Figure B.5. Pre-segment script to define the nucleation sites in the ferritic/martensitic matrix.

B.5 MatCalc strength module

To determine the evolution of the 0.2% proof stress with MatCalc, the strength module outlined in section 4 is applied. In the following section the simulation settings are listed. For further information about the implemented strength module and the theory about strengthening mechanism, the interested reader is referred to section 4.

B.5.1 Calculation of the 0.2% proof stress

As already discussed in section 5.4, the 0.2% proof stress can be calculated taking into account the contributions of the following:

(i)   inherent lattice strength of the matrix,

(ii)   dislocation strengthening,

(iii)   subgrain strengthening,

(iv)   solid solution strengthening and

(v)   precipitate strengthening.

The inherent lattice strength σ_i (=41 MPa), dislocation strengthening σ_d (=166 MPa), the subgrain strengthening effect σ_{sgb} (=290 MPa) and the work hardening term σ_{wh} (=65 MPa) are assumed to be constant. For details see section 5.4.2.

The solid solution strengthening effect (σ_{ss}) is evaluated as function of the chemical composition of the matrix (BCC_A2 phase) according to eq. (4.34) and eq. (4.35) with the concentration exponents n_i and strengthening factors k_i according to Table B.3.

Table B.3. Overview of parameters to determine the solid solution strengthening in the COST alloy D1.

	Al	Cr	Mn	Mo	Nb	Ni	Si	V	W	C	N
k_i, MPa/wt.%	4000	1400	7000	9600	4000*	6100	11000	4000	11000	1722.5	1722.5
n_i, -	0.75	0.75	0.75	0.75	0.75	0.75	0.75	0.75	0.75	0.5	0.5

*... due to lack of data for the solid solution strength contribution of Nb, a value equal to the value of V is assumed due to similar atomic sizes.

The precipitation hardening effect is considered according to eq. (4.6). The respective precipitation strengthening contributions are directly determined by the strength module in MatCalc. Thereto, open the 'Precipitation domains ...' window and select for the Martensite

precipitation domain the 'Structure' flag. Define the Taylor factor as 3.0, close the window and open the 'Phase status ...' window. Go to the 'Structure' flag for all precipitate phases in the list on the left side. Define the constant *C* (Ashby-Orowan) as 0.06 (leave all other settings as default).

B.6 Simulation results

If all settings are correctly made, the simulation can be started. Press Ctrl+K and insert a simulation end time of 550669 seconds. Select in the 'Temperature control ...' field the option 'from heat treatment' and select the defined heat treatment schedule (Figure B.6). Press 'Go' to start the simulation.
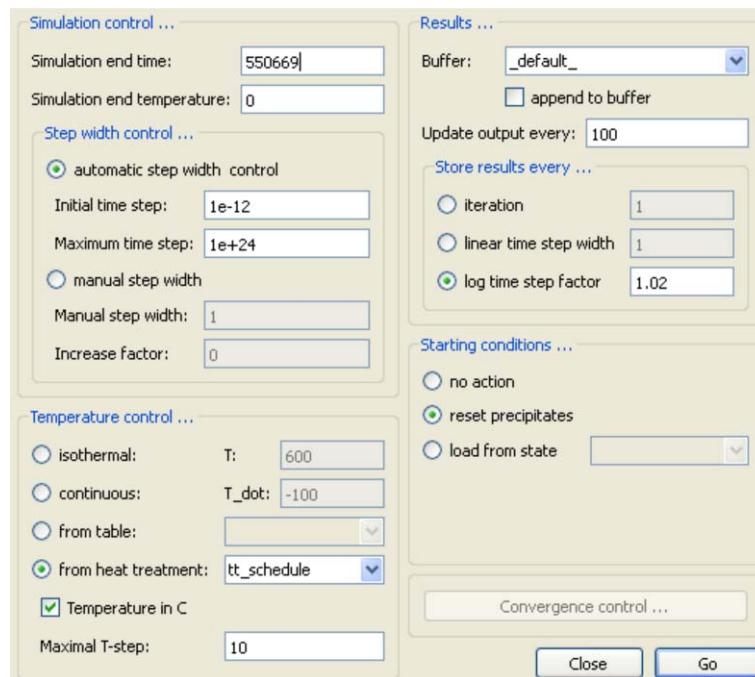
Figure B.6. Precipitation simulation setup.

Table B.4 and Table B.5 show the results of the kinetic simulation for the chemical composition of the matrix after 2, 8, 16 and 24 hours of tempering as well as the calculated resulting solid solution and precipitate strengthening contributions. These data are further utilized to determine the 0.2% proof stress evolution discussed in section 5.4.

Table B.4. Calculated chemical composition of the ferritic/martensitic matrix (BCC_A2 phase)
and resulting solid solution strength contribution.

time	Al, wt.%	Cr, wt.%	Mn, wt.%	Mo, wt.%	Nb, wt.%	Ni, wt.%
2h	$7.26 \cdot 10^{-3}$	10.113	0.497	0.235	$3.63 \cdot 10^{-3}$	0.839
8h	$7.26 \cdot 10^{-3}$	10.043	0.498	0.224	$3.00 \cdot 10^{-3}$	0.841
16h	$7.27 \cdot 10^{-3}$	10.032	0.498	0.216	$2.54 \cdot 10^{-3}$	0.841
24h	$7.29 \cdot 10^{-3}$	10.038	0.499	0.196	$2.19 \cdot 10^{-3}$	0.844
time	Si, wt.%	V, wt.%	W, wt.%	C, wt.%	N, wt.%	σ_{ss}, MPa
2h	0.0933	0.0537	1.215	$8.08 \cdot 10^{-4}$	$5.92 \cdot 10^{-5}$	177
8h	0.0934	0.0522	1.178	$7.45 \cdot 10^{-4}$	$4.62 \cdot 10^{-5}$	174
16h	0.0934	0.0520	1.167	$7.38 \cdot 10^{-4}$	$4.55 \cdot 10^{-5}$	173
24h	0.0937	0.0507	1.007	$6.34 \cdot 10^{-4}$	$2.62 \cdot 10^{-5}$	164

Table B.5. Calculated precipitate strength contribution
of all precipitate phases.

time	σ_p, MPa (variable: TTAO_ALL$ferrite)
2h	146
8h	96
16h	87
24h	80

C Additional scientific investigations carried out from 2005 to 2010

In addition to the modelling and simulation of strengthening in steels, the author of the present thesis was involved in further scientific investigations during his time as PhD student at the Institute for Materials Science and Welding.

In the following, an excerpt of selected papers is given which were published from 2008 to 2010. The present papers were not covered in the previous application section. However, the author considered the publications as worthwhile to add them to the present work. A complete list of publications which were published within the framework of the present PhD project is given at the beginning of the thesis.

Content

C.1 Computer simulation of the time-temperature-precipitation diagram of 1.4 wt.% Cu ferritic steel

Ivan Holzer[1], Ernst Kozeschnik[2]

[1] *Institute for Materials Science and Welding, Graz University of Technology Graz, A-8010, Austria.*
[2] *Christian Doppler Laboratory for Early Stages of Precipitation, Institute of Materials Science and Technology, Vienna University of Technology Vienna, A-1040, Austria.*

Abstract. In the present work, the computer simulation of Cu-precipitation in an Fe-1.4wt.% Cu alloy is described over a wide range of temperatures. A comprehensive simulation approach is developed taking into account (i) variations of the nucleus composition of the coherent bcc Cu precipitates in the nucleation stage, (ii) size corrections to the interfacial energy due to interfacial curvature, (iii) the temperature-dependent effect of atomic mixing at the precipitate / matrix interface on the interfacial energy, (iv) the influence of quenched-in vacancies on the diffusion kinetics, which is otherwise often neglected in precipitation simulations in steel, and (v) the structural change of the Cu precipitates from bcc to fcc during precipitation. With this approach, the time-temperature-precipitation diagram for the investigated alloy is calculated and compared to experimental data between 400°C and 750°C.

Keywords: Numerical simulation, Copper precipitates, Precipitation kinetics, ttp-diagram

1. Introduction

Characterization of Cu precipitation kinetics in ferritic steel was object of many experimental as well as numerical studies[1-7]. It is generally accepted that, in the early stages of ageing, Cu precipitates undergo a multi-stage transformation from coherent body centred cubic (bcc) to incoherent face centred cubic (fcc) structure. Precipitates with a radius below 2.5 nm[1,2] to 4 nm[8] are assumed to be fully coherent. Larger precipitates gradually lose coherency and finally transform into fcc. This loss of coherency is accompanied by a change in the chemical composition of the Cu precipitates from Fe-rich nuclei in the early stages to almost pure Cu after reaching diameters around 2-3 nm[6].

The computer simulation of this complex precipitation reaction turns out to be a challenging task. Several physical mechanisms have to be accounted for in order to consistently reproduce the experimentally observed kinetics in all relevant precipitation parameters (compare also ref.[9] for details on simulations at 500°C). These effects are implemented on a physical basis in the present simulation methodology. Alternative approaches have been developed earlier by, e.g., Hutchinson et al.[10] and Perez et al.[11], however, these authors did not attempt to utilize their models in calculations of the entire ttp-diagram.

The method proposed in this paper is applied to an Fe-1.4 wt.% Cu alloy investigated experimentally by Perez et al.[12]. The time-temperature-precipitation plot is calculated in the temperature range between 400°C and 750°C, and compared to the experimentally determined phase fraction curves for 10, 50 and 90 percent precipitation. The simulation results consistently reproduce the experimental values over the whole temperature range.

2. Simulation of Cu-precipitation in ferritic steel

The numerical simulations in the present work are carried out with the software MatCalc[13-16], version 5.32.0006. For the simulations, the thermodynamic data of Turchanin[17] and the diffusion data of Fridberg et al.[18] are used.

2.1 The numerical model

The numerical model utilized in the present work is, on one hand, based on Classical Nucleation Theory (CNT)[19]. Accordingly, the time dependent nucleation rate J is evaluated from

$$J = N_0 Z \beta^* \cdot \exp\left(\frac{-G^*}{k \cdot T}\right) \cdot \exp\left(\frac{-\tau}{t}\right). \tag{1}$$

In this equation, N_0 represents the total number of potential nucleation sites, Z is the Zeldovich factor, β^* is the atomic attachment rate, k is the Boltzmann constant, T is the temperature, τ is the incubation time and t is time. G^* is the critical nucleation energy and is calculated with

$$G^* = \frac{16\pi}{3} \frac{\gamma^3}{\Delta G_{vol}^2}, \tag{2}$$

where G_{vol} is the volume free energy change and γ is the effective energy of the precipitate/matrix interface.

On the other hand, once a precipitate is nucleated, its further growth is evaluated from the evolution equations for multi-component multi-phase precipitation derived in ref.[14] and based on the numerical integration scheme described in ref.[15]. This approach has already been successfully applied earlier to various complex precipitation reactions, see e.g.[20-23]. For precipitation simulations in the Fe-Cu system, however, the methodology must be advanced and several additional effects must be taken into account, which are relevant and specific to this particular system.

In addition to the conventional treatment, the following effects are considered in the present treatment:

(i)   the varying nucleus composition of the coherent bcc Cu precipitates in the nucleation stage,
(ii)   size corrections for the interfacial energy due to curvature effects as recently proposed by Sonderegger and Kozeschnik[24],
(iii)   the temperature-dependent impact of entropic effects on the interfacial energy,
(iv)   the influence of quenched-in vacancies and
(v)   the structural transformation from bcc to fcc, indirectly, by considering separate bcc and fcc precipitate populations.

In the following, these effects are discussed in detail in the context of the present simulations.

(i) Nucleus composition: On investigating eq. (1) in detail, it is found that almost all quantities entering the nucleation rate are uniquely determined. Details on the corresponding equations are summarized, for instance, in refs.[25,26]. The only unknown in eq. (1) is the chemical composition of the precipitate nucleus, which represents an undefined degree of freedom and must be fixed by some assumption or hypothesis. In conventional precipitation kinetics simulations, the nucleus composition is often assumed to be identical to the particular composition yielding the maximum chemical driving force. In the present case, this would correspond to almost pure Cu-nuclei with a small solubility range for Fe.

However, when investigating eq. (2), we observe that the critical nucleation energy depends inversely quadratically on the driving force, and on the cube of the interfacial energy. The latter quantity is approximately a quadratic function of the composition difference between precipitate and matrix[27], thus itself strongly affected by the nucleus composition. As recently discussed for the Fe-Cu system[7], the highest probability for a nucleation event to occur is observed at the minimum nucleation energy G^*, and the 'most likely' nucleus composition can be obtained from a minimization of this quantity.

In the present simulations, the time-dependent nucleation rate J given in eq. (1) is calculated according to the concept of the 'most likely' nucleus composition[7] or minimum nucleation barrier[2], where the Cu to Fe ratio in the critical nucleus is calculated as a function of matrix-supersaturation and temperature. The results of this preliminary analysis are shown in Fig. 1. Accordingly, with increasing Cu content in the matrix and decreasing temperature, the Cu nuclei incorporate increasing amounts of Fe.

It should be emphasized that, apart from the huge impact of the compositional variations on the interfacial energy and, thus, the nucleation rate J, these variations also heavily influence the further stages of precipitation, as shown in the next sections.
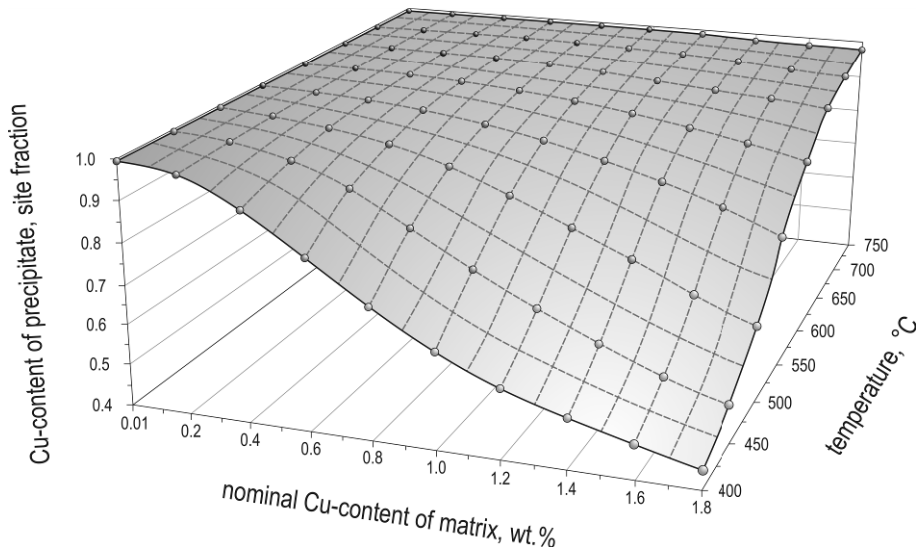
Figure 1. Calculated equilibrium Cu-content of the critical nucleus as function of
nominal Cu-content and temperature according to ref.[7].

<u>(ii)-(iii) Interfacial energy corrections:</u> The energy of the bcc and fcc precipitate/matrix interface (γ_0) is a most essential input parameter in precipitation kinetics simulations. In the present study, it is calculated from the generalized broken-bond (GBB) model[28] for planar, sharp interfaces (Fig. 2). As shown in the figure, the interfacial energy γ_0 increases for both phases with increasing temperature, mainly as a consequence of the ferromagnetic contribution of the matrix. The increasing difference between fcc and bcc interfacial energy at lower temperature is due to the effect of the variable nucleus composition for the bcc precipitates (Fig. 1).

It is important to note that the sharp, planar interfacial energy γ_0 cannot be used directly in the simulation but must be further processed into the *effective* interfacial energy γ by considering two effects. These are the size of the precipitate, having an effect on the interfacial curvature, and atomic mixing across the precipitate / matrix interface. The latter is assumed to be relevant mainly for the interfacial energy of the coherent bcc Cu precipitates. Atomic mixing across the incoherent phase boundary of the fcc-precipitate is assumed to be negligible.

The size effect on the interfacial energy is taken into account by a radius-dependent correction factor as derived in ref.[24]. The atomic mixing process (see, e.g., Lee and Aaronson[27]) is considered only approximately by a temperature-dependent correction factor. The value of this contribution, as used in the present simulations, is displayed in Fig. 3.
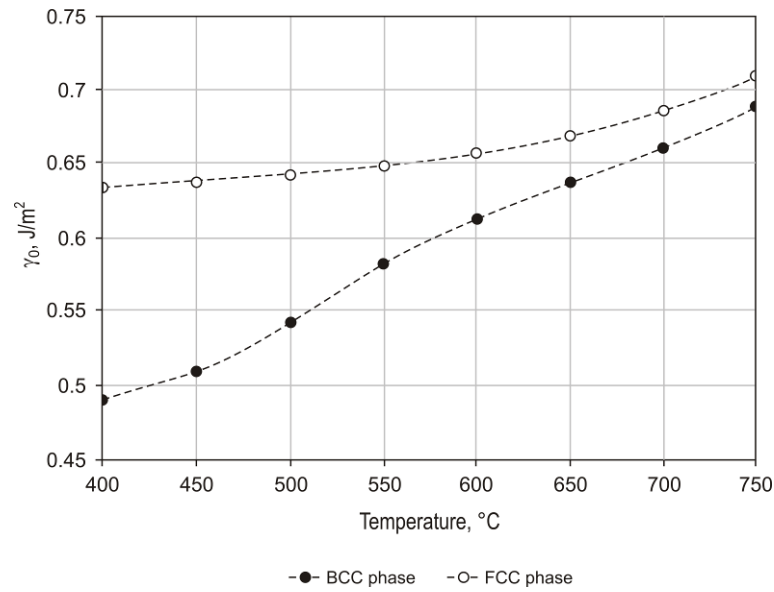
Figure 2. Planar, sharp interface energy γ_0 between ferrite and equilibrium bcc and fcc Cu precipitates calculated from the GBB model[28]. For the bcc-phase, the variation of chemical composition with temperature is taken into account (see text).
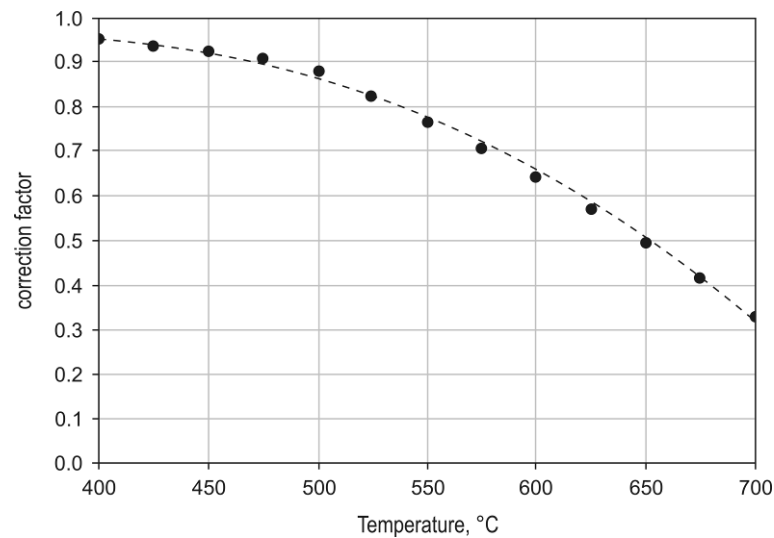
Figure 3. Effective corrections to the planar, sharp interfacial energy γ_0 to obtain the effective interfacial energy γ utilized in the numerical simulation.

(iv) Quenched-in vacancies: In the experiments by Perez et al.[12], the samples were subjected to a heat treatment consisting of a solution treatment at 850°C, quenching to room temperature and reheating to test temperature. In the course of this procedure, the material always remained in the ferrite phase region. During solution treatment, we assume

that the fraction of structural lattice vacancies X_{Va}^{equ} reached a value close to thermodynamic equilibrium given with

$$X_{Va}^{equ} = \exp(-\frac{\Delta H_{Va}}{RT}),$$ (3)

where ΔH_{Va} = 154 kJ/mol[29] is the enthalpy of vacancy formation in α-Fe, R is the Universal Gas Constant and T is temperature. In the course of water-quenching from 850°C to room temperature and reheating to test temperature, time will not be sufficient for the structural vacancies to diffuse to sources and sinks in order to establish the equilibrium fraction at the new temperature. Hence, a considerable fraction of these structural vacancies becomes effectively frozen in the lattice during quenching, leading to an acceleration of all following diffusion-driven processes.

To consider this effect on the effective diffusion rate in the present simulations, in a first approximation, a temperature-dependent correction factor C is introduced according to

$$C = \alpha_i \cdot \beta_i \cdot \frac{X_{Va,850°C}^{equ}}{X_{Va,T*}^{equ}} .$$ (4)

$X_{Va,850°C}^{equ}$ and $X_{Va,T*}^{equ}$ are the equilibrium mole fractions of lattice vacancies at 850°C and at the respective ageing temperature T^*. α_i is a time-independent average value accounting for the continuous excess vacancy annihilation at T^* by diffusion to vacancy sinks at dislocations, grain boundaries or incoherent phase boundaries. The values of α_i are varied between 0.04% and 75%, depending on the evaluated precipitate fraction line (10%, 50% or 90%). β_i is a temperature-dependent factor between 0 and 1, which takes into account the additional annihilation of excess vacancies by nucleation of dislocation loops[30,31] or vacancy condensation into micro pores. This effect is expected to be more pronounced at lower temperatures and high vacancy supersaturation. The values of C as used in the present simulations are shown in Table 1.

Table 1. Mean correction factor *C* for the accelerating effect of quenched-in vacancies on the diffusional mobilities as a function of ageing temperature for 10%, 50% and 90% precipitate fraction.

Temperature (°C)	$C_{10\%}$	$C_{50\%}$	$C_{90\%}$
750	4	2	1
725	6	2	2
700	10	4	3
675	17	7	4
650	30	12	5
625	53	21	6
600	98	39	6
575	185	74	6
550	362	145	6
525	740	296	6
500	1579	632	6
475	1948	779	6
450	2684	1074	6
425	4853	1941	6
400	11356	4543	6

(v) Incoherent Cu-precipitation: Finally, the experimentally observed loss of coherency of the Cu-precipitates when transforming from bcc to fcc crystal structure[1,3,8] is taken into account indirectly by considering an additional population of precipitates in the simulations with equilibrium fcc structure. When both precipitate types (bcc and fcc) are treated simultaneously and in competition, faster precipitation of the coherent metastable bcc phase with lower Cu content and, thus, lower interfacial energy is observed. With increasing annealing time, the incoherent fcc precipitates become dominant due to their higher thermodynamic stability. Thus, the bcc precipitates finally disappear, leading to a single population of fcc precipitates at the end of the precipitation process, consistent with experimental observations.

3. Results and Discussion

In this section, the present simulation method is utilized to determine the 10%, 50% and 90% precipitation lines for the Fe-1.4 wt.% Cu alloy investigated in ref.[12]. A series of ttp-plots are presented, taking into account a bcc and fcc precipitate population and incorporating stepwise the previously discussed effects (i)-(iv). All ttp-plots are compared to the experimental data reported in ref.[12].

To generate the ttp-plots, the relative precipitate fractions of the bcc and fcc precipitates are evaluated from isothermal kinetic simulations carried out with MatCalc in 25K steps between 400°C and 750°C. The numerical simulation reveals that the structural transformation from bcc to fcc is not relevant when calculating the ttp-plots, because the transformation occurs only after reaching the 90% precipitation line. Figure 4 shows the phase fraction evolution of the bcc (f_{BCC}) and fcc (f_{FCC}) precipitates as well as the evolution of the total phase fraction (f_{Total}) at 500°C for the different simulations carried out, starting with ortho-equilibrium bcc and fcc nuclei (Fig. 4 (a)). Stepwise, the impact of the variable nucleus composition together with the effects of precipitate size and atomic mixing across the interface (Fig. 4 (b)), as well as the accelerating effect of excess vacancies (Fig. 4 (c)-(e)) are taken into account. The simulations show that the early stages of the precipitation process are mainly determined by the coherent bcc precipitates, until the stable fcc precipitates become dominant. In the evaluation of the times for 10%, 50% and 90% precipitate phase fraction in Fig. 4, the first plateau when reaching the maximum precipitate phase fraction was used as reference ($f_{Ref.}$).
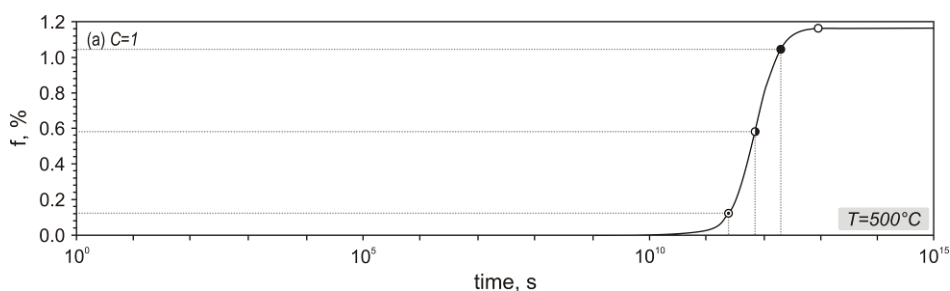

Figure 4 (a)-(e). Exemplary result of the kinetic simulation for an assumed ortho-equilibrium nucleus composition (a), In (b), the variable nucleus composition together with interfacial energy corrections is taken into account. In (c)-(e), different factors for the quenched-in vacancies effect (C>1) are applied to determine the time for 10%, 50% and 90% precipitation.
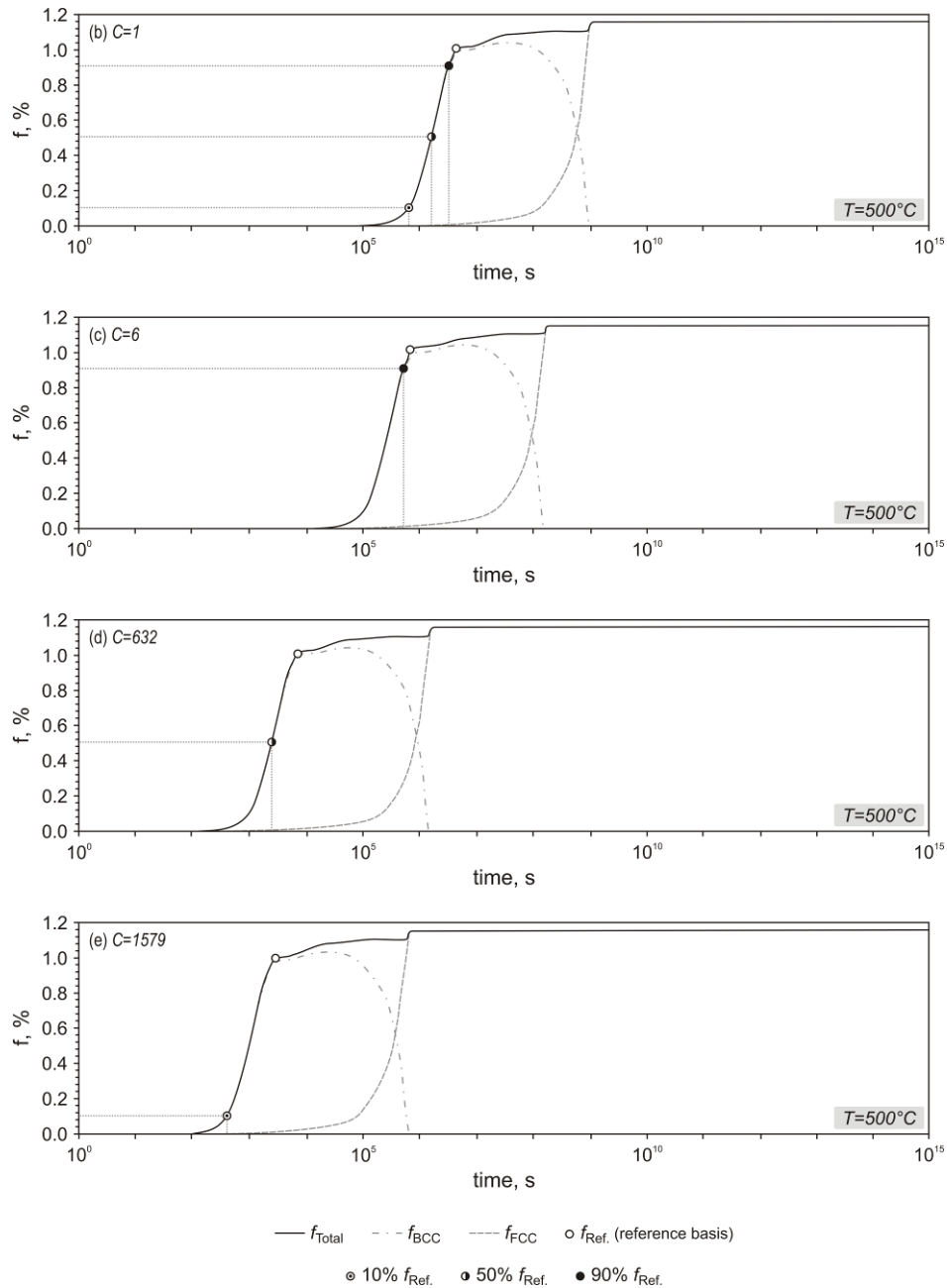
Figure 4 (a)-(e). *(continued)* Exemplary result of the kinetic simulation for an assumed ortho-equilibrium nucleus composition (a), In (b), the variable nucleus composition together with interfacial energy corrections is taken into account. In (c)-(e), different factors for the quenched-in vacancies effect (C>1) are applied to determine the time for 10%, 50% and 90% precipitation.

Figure 5 illustrates the impact of these changes directly on the calculated ttp-plot. In analogy to the simulations in Fig. 4, in plot (a), the precipitate fractions are evaluated numerically using the assumption of a maximum nucleation driving force, which corresponds to the assumption of ortho-equilibrium composition for the precipitate nucleus[25,26]. No further assumptions are made and the evaluation routines in MatCalc are

utilized as developed originally in refs.[14-16]. According to Fig. 5 (a), the agreement of simulation and experiment in this case is poor. The precipitation start times are orders of magnitude too late and the maximum precipitation temperature is evaluated too low by values of 150 to 200 K.
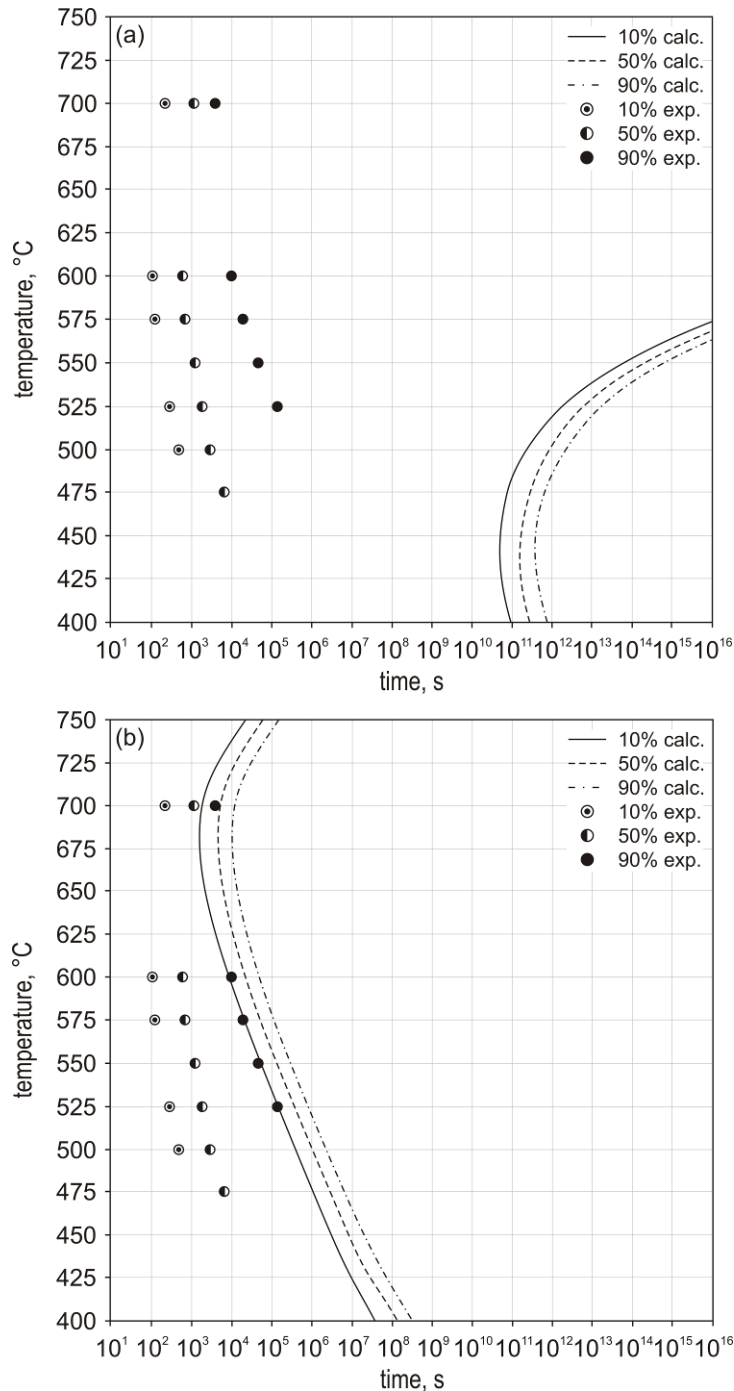
Figure 5 (a)-(c). Calculated ttp-plots for 10%, 50% and 90% Cu-precipitation compared with the experimental data referred in[12], with (a) ortho-equilibrium nucleus composition, (b) taking into account the different effects (i)-(iv) on the interfacial energy and (c) the effect of quenched-in vacancies on the overall diffusional processes.
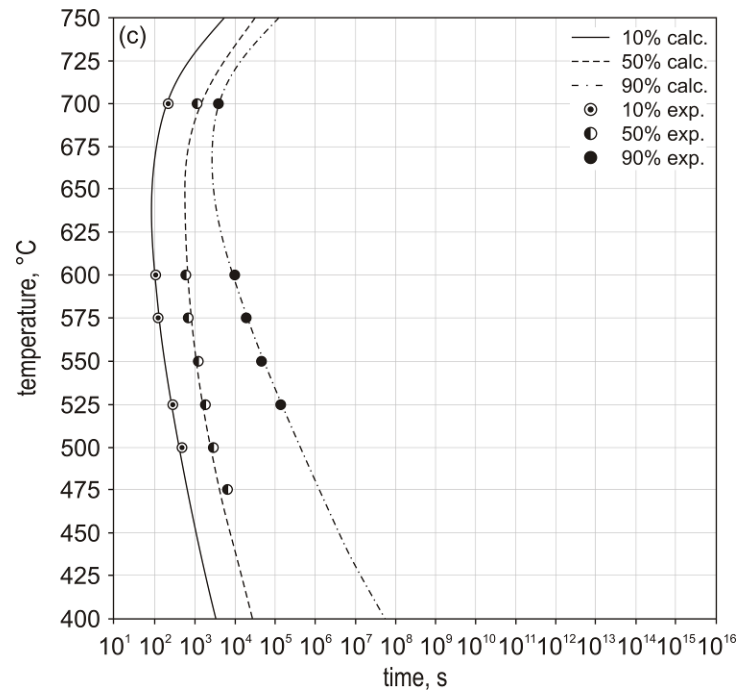
Figure 5 (a)-(c). *(continued)* Calculated ttp-plots for 10%, 50% and 90% Cu-precipitation compared with the experimental data referred in[12], with (a) ortho-equilibrium nucleus composition, (b) taking into account the different effects (i)-(iv) on the interfacial energy and (c) the effect of quenched-in vacancies on the overall diffusional processes.

In a next step, in Fig. 5 (b), the simulation is adapted such as to take into account (i) the compositional variations of the Cu nuclei, (ii) the precipitate size effect and (iii) entropic effects, simultaneously. Compared to Fig. 5 (a), the precipitation start times are considerably shorter, and the entire curve is in better qualitative agreement with experimental evidence. However, with decreasing temperature, the predicted 10% and 50% precipitation times are still several orders of magnitude too late compared to the experimental data. In Fig. 5 (c), the quenched-in vacancy effect is also taken into account, finally leading to an excellent agreement between simulation and experiment in the entire temperature range. The 10%, 50% and 90% Cu-precipitate fraction lines can be well reproduced. The figure clearly shows wide spreading between the 10%, 50% and 90% curves at lower temperatures. This effect is caused by the dynamics of the excess vacancies, which affect the diffusional processes particularly in the early stages of precipitation. With ongoing excess vacancy annihilation, the accelerating effect decreases proportionally. These trends are also observable in the tabulated values for the quenched-in vacancy acceleration factor *C* (Table 1).

4. Summary

An advanced simulation approach has been developed for the numerical simulation of Cu-precipitation in ferritic steel, taking into account the major mechanisms affecting the precipitation kinetics in Cu alloyed ferritic steels. These are the varying nucleus composition and the temperature-dependent reduction of the interfacial energy of the coherent bcc Cu precipitates as well as the influence of quenched-in vacancies on the diffusional mobilities of Cu and Fe. With these model ingredients, the experimental ttp-data of Perez et al.[12] for Fe-1.4wt.% Cu can be reproduced consistently.

From the present results, it is important to recognize the large influence of quenched-in vacancies on the Cu-precipitation kinetics. Although this effect is well-known and heavily utilized, for instance, in Al-alloy processing, it is commonly considered as negligible in steel. In this work, we show that quenched-in vacancies play a major role also in steel, at least, if solution annealing temperatures below the allotropic phase boundary are employed.

Acknowledgement

References

[1]   S.R. Goodman, S.S. Brenner and J.R. Low jr., Metall. Trans. 4 (1973) 2363.

[2]   S.R. Goodman, S.S. Brenner and J.R. Low jr., Metall. Trans. 4 (1973) 2371.

[3]   K. Osamura, H. Okuda, S. Ochiai, M. Takashima, K. Asano, M. Furusaka, K. Kishida and F. Kurosawa, ISIJ Int. 34 (1994) 359.

[4]   R. Monzen, K. Takada and K. Matsuda, Z. Metallkd. 94 (2003) 1241.

[5]   D. Isheim, R. Prakash Kolli, M.E. Fine and D.N. Seidman, Scr. Mater. 55 (2006) 35.

[6]   M.E. Fine, J.Z. Liu and M.D. Asta, Mater. Sci. Eng. A 463 (2007) 271.

[7]   E. Kozeschnik, Scr. Mater. 59 (2008) 1018.

[8]   Y. Le Buoar, Acta Mater. 49 (2001) 2661.

[9]   I. Holzer and E. Kozeschnik, Mater. Sci. Eng. A 527 (2010) 3546.

[10]   C.R. Hutchinson, M. Gouné and A. Redjaimia, Acta Mater. 55 (2007) 213.

[11]   M. Perez, M. Dumont and D. Acevedo-Reyes, Acta. Mater. 56 (2008) 2119.

[12]   M. Perez, F. Perrard, V. Massardier, X. Kleber, V. Schmitt and A. Deschamps, Mater. Sci. Forum 500-501 (2005) 631.

[13] E. Kozeschnik and B. Buchmayr, *MATCALC – A Simulation Tool for Multicomponent Thermodynamics, Diffusion and Phase Transformations*, H. Cerjak, H.K.D.H. Bhadeshia, eds., IOM Communications Ltd, London, 2001, 349.

[14] J. Svoboda, F.D. Fischer, P. Fratzl and E. Kozeschnik, Mater. Sci. Eng. A 385 (2004) 166.

[15] E. Kozeschnik, J. Svoboda, P. Fratzl and F.D. Fischer, Mater. Sci. Eng. A 385 (2004) 157.

[16] E. Kozeschnik, J. Svoboda and F.D. Fischer, CALPHAD 28 (2004) 379.

[17] M.A. Turchanin, P.G. Agraval and I.V. Nikolaenko, J. Phase Equilib. 24 (2003) 307.

[18] J. Fridberg, L.E. Törndahl and M. Hillert, Jernkontorets Ann. 153 (1969) 263.

[19] K. Russell, Adv. Coll. Interf. Sci. 13 (1980) 205.

[20] B. Sonderegger, E. Kozeschnik, H. Leitner, H. Clemens, J. Svoboda and F.D. Fischer, Int. J. Mat. Res. 99 (2008) 410.

[21] B. Sonderegger, E. Kozeschnik, H. Leitner, H. Clemens, J. Svoboda, F.D. Fischer and P. Staron, Steel Res. Int. 81 (2010) 64.

[22] E. Kozeschnik, J. Svoboda, R. Radis and F.D. Fischer, Model. Simul. Mater. Sci. Eng. 18 (2010) 015011 (19pp).

[23] R. Radis and E. Kozeschnik, Model. Simul. Mater. Sci. Eng. 18 (2010) 055003 (16pp).

[24] B. Sonderegger and E. Kozeschnik, Scr. Mater. 60 (2009) 635.

[25] E. Kozeschnik, J. Svoboda and F.D. Fischer, in Proc. Int. Conference Solid-Solid Phase Transformations in Inorganic Materials, PTM 2005, Phoenix, AZ, USA, 2005, 301.

[26] K.G. F. Janssens, D. Raabe, E. Kozeschnik, M.A. Miodownik and B. Nestler, *Computational Materials Engineering - An Introduction to Computational Microstructure Evolution of Polycrystalline Materials*, Elsevier Publishing, London, 2007.

[27] Y.W. Lee and H.J. Aaronson, Acta Metall. Mater. 28 (1980) 539.

[28] B. Sonderegger and E. Kozeschnik, Met. Trans. 40A (2009) 499.

[29] M. E. Glicksman, Diffusion in Solids, John Wiley & Sons, New York, 2000.

[30] F.C. Duckworth and J. Burke, Brit. J. Appl. Phys. 18 (1967) 1071.

[31] A. Seeger, Phys. Stat. Sol. 167 (1998) 289.

C.2 Modelling of Microstructure Evolution in Hot Work Tool Steels during Service

F. Krumphals[1], T. Wlanis[1], Ch. Sommitsch[1], I. Holzer[2], B. Sonderegger[2], V. Wieser[3]

[1] *Christian Doppler Laboratory for Materials Modelling and Simulation, Chair of Metal Forming, University of Leoben, Franz-Josef-Strasse 18, 8700 Leoben, Austria*
[2] *Institute for Materials Science and Welding, University of Technology, Kopernikusgasse 24, 8010 Graz, Austria.*
[3] *Böhler Edelstahl GmbH & Co KG, Mariazellerstrasse 25, 8605 Kapfenberg, Austria.*

Abstract. To establish a reliable lifetime prediction of hot work tool steels during service, it is necessary to characterize the initial microstructure as well as its evolution during application since the material properties depend on the microstructural configuration. The microstructure evolution during heat treatment is simulated with the software MatCalc, where the precipitation kinetics is of particular interest. The investigated X38CrMoV5-1 hot work tool steel, which has a bcc lattice structure, forms a distinct dislocation cell and subgrain structure, respectively, which is described by a dislocation density model for thermal creep using the rate theory with particular consideration of the subgrain boundary behaviour. The precipitation calculations with MatCalc are compared with microstructural investigations.

MODELLING OF MICROSTRUCTURE EVOLUTION IN HOT WORK TOOL STEELS DURING SERVICE

FRIEDRICH KRUMPHALS[1], THOMAS WLANIS[1], CHRISTOF SOMMITSCH[1], IVAN HOLZER[2],
BERNHARD SONDEREGGER[2], VOLKER WIESER[3]

[1] *Christian Doppler Laboratory for Materials Modelling and Simulation, Chair of Metal Forming,
University of Leoben, Franz-Josef-Strasse 18, 8700 Leoben, Austria*
[2] *Institute for Materials Science and Welding, University of Technology,
Kopernikusgasse 24, 8010 Graz, Austria*
[3] *Böhler Edelstahl GmbH & Co KG, Mariazellerstrasse 25, 8605 Kapfenberg, Austria*
Corresponding Author: Corresponding Autor: friedrich.krumphals@mu-leoben.at (F. Krumphals)

Abstract

To establish a reliable lifetime prediction of hot work tool steels during service, it is necessary to characterize the initial microstructure as well as its evolution during application since the material properties depend on the microstructural configuration. The microstructure evolution during heat treatment is simulated with the software MatCalc, where the precipitation kinetics is of particular interest. The investigated X38CrMoV5-1 hot work tool steel, which has a bcc lattice structure, forms a distinct dislocation cell and subgrain structure, respectively, which is described by a dislocation density model for thermal creep using the rate theory with particular consideration of the subgrain boundary behaviour. The precipitation calculations with MatCalc are compared with microstructural investigations.

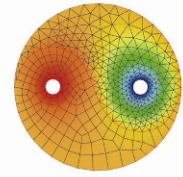**Key words**: hot work tool steels, extrusion, microstructure modelling, dislocation density evolution

1. INTRODUCTION

Hot work tool steels are commonly in use as tools for manufacturing processes of metallic materials at elevated temperatures. Since the loading of the tools during hot metal working, e.g. extrusion, is often near the elastic limit, the lifetime is much shorter in comparison to the Cr-steels for energy applications [2]. Here, the microstructure evolution of the hot work tool steel X38CrMoV5-1 is investigated during heat treatment as well as in thermo-mechanical loading conditions, which occur during service. Therefore, the precipitation kinetics during heat treatment is calculated, using the scientific program MatCalc [3] in order to get initial conditions for a subsequent dislocation density simulation of creep loading using the rate theory with particular

consideration of the subgrain boundary behaviour [1]. Subgrains as well as precipitations limit the dislocation movement and their diameter is a key parameter in determining the creep rate under varying conditions. Two different load cases, representing die loading during both, aluminium and copper extrusion [8], and the resulting microstructure evolution are demonstrated in this work.

2. HEAT TREATMENT SIMULATION AND COMPARISON WITH EXPERIMENTAL INVESTIGATIONS

The chemical composition of the hot work tool steel X38CrMoV5-1 is shown in table 1 and a standard heat treatment condition to achieve a hardness of about 48-50 HRC is depicted in figure 1. The

hardening temperature is 1020°C, with a holding time of one hour and following annealing at 550°C and 580°C for two hours.

**Table 1.** *Chemical composition of BÖHLER W400 hot work tool steel.*

Grade \ weight %	C	Si	Mn	Cr	Mo	V	Fe
X38CrMoV5-1	0.38	0.20	0.25	5.00	1.30	0.45	bal.
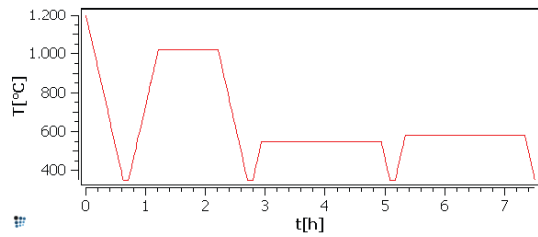
Fig. 1. *Temperature-time profile for the considered hot work tool steel X38CrMoV5-1 during heat treatment after hot working.*
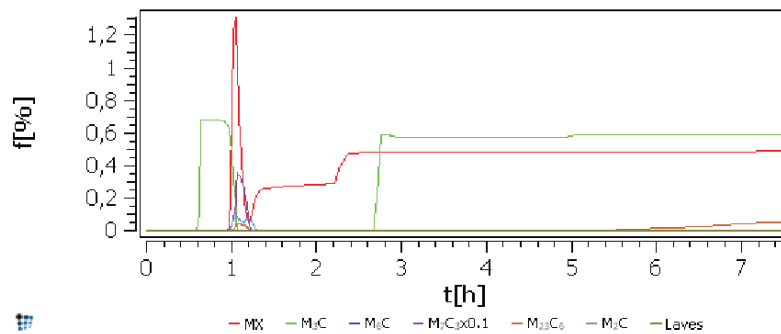
Fig. 2. *Evolution of the phase fraction of the precipitates during the heat treatment. To get a more reasonable delineation, the amount of M_7C_3 is divided by 10.*
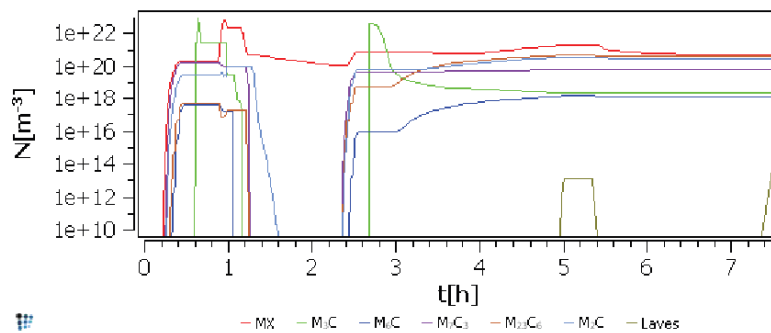
Fig. 3. *Evolution of the number of particles per volume during heat treatment.*

The temperature decrease from 1200°C at the beginning simulates the cooling from the prior hot working process. The heating up to austenitization temperature in industrial processes is performed stepwise with three hold points to assure a homogeneous temperature distribution in the billet. How-

ever, for the MatCalc simulation the exact time-temperature history of the heating up is not that important. The controlled cooling rate from austenitizing temperature is $\lambda = 8$, and after each annealing step the material is cooled by air.

The precipitation kinetics are simulated with the software MatCalc, the phase fractions f of the precipitates, namely MX (V(C,N)), M_3C (Fe$_3$C), M_6C (Cr$_6$C), M_7C_3 (Cr$_7$C$_3$), $M_{23}C_6$ (Cr$_{23}$C$_6$), M_2C (Mo$_2$C) and Laves phase are shown in figure 2, the particle number N per volume is depicted in figure 3 and the related mean radius Rv_{mean} is displayed in figure 4. Primary MX phase was not considered so far, because the phase amount was not determined quantitatively and additionally, the formation of primary phases in the liquid metal cannot be simulated in MatCalc. However, with the known primary phase fraction, the amount of dissolved carbon content in the matrix could be reduced by the amount of carbon, which has been used for the formation of the primary carbides and thus the influence of primary carbides on the precipitation kinetics of secondary carbides could be considered. Secondary phases MX, M_3C and M_7C_3 form during heating up and dissolve again during the austenitization at 1020°C. During the second annealing step, the fraction of $M_{23}C_6$ increases significantly in comparison to M_6C, M_7C_3, M_2C and Laves phase as depicted in figure 2. After the heat treatment is finished, the main existing phase fractions are M_3C, MX and $M_{23}C_6$ (M_3C: green line, MX: red line, $M_{23}C_6$ brown line in figures 2-4).

The number of particles N per volume reaches a quasi-stable condition at the end of the heat treatment, except for Laves phase (figure 3). Dislocation reactions (dipole forming, cutting, immobilizing) and precipitations have a strong influence onto dislocation structure evolution. The smaller and numerous a particle population the more it will affect dislocation glide.

– **229** –

M₃C precipitations are far the largest secondary particles that form during the heat treatment, which is depicted in figure 4. The significantly higher growth rate of the other secondary phases during the 30°C higher second annealing period is remarkable.

Microstructure investigations after heat treatment mainly indicated bainitic structure as well as fractions of tempered martensite. So far, only the size of M₃C carbides has been analyzed quantitatively, see figure 5. The mean radius is 75 ± 20 nm, which is in the same range as in the calculations (≈ 100 nm).
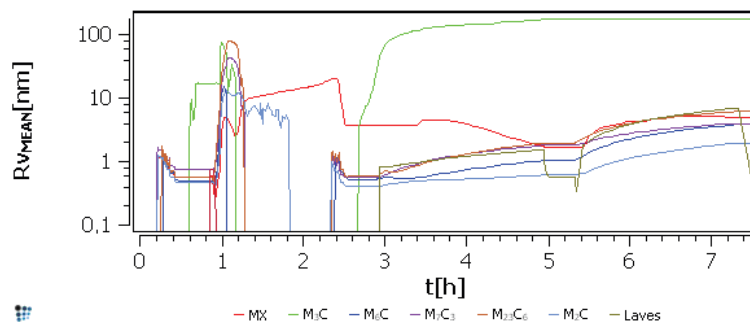

Fig. 4. Evolution of the mean radius of the precipitates during heat treatment.

sidered thermal loads are lower than the last annealing step in the heat treatment, a constant precipitation state as initial condition is assumed and the following focus lies on the investigation of the dislocation structure.

3.1. Concept of the model

The basis of the model is to describe the dislocation structure evolution by:
- the generation and immobilization of dislocations at subgrain boundaries, i.e. multiplication as well as annihilation of dislocations due to interaction processes,
- the recovery of the static dislocations at the boundaries as well as the absorption of mobile dislocations in the cell wall,
- the generation of dislocations by emission from the cell wall,
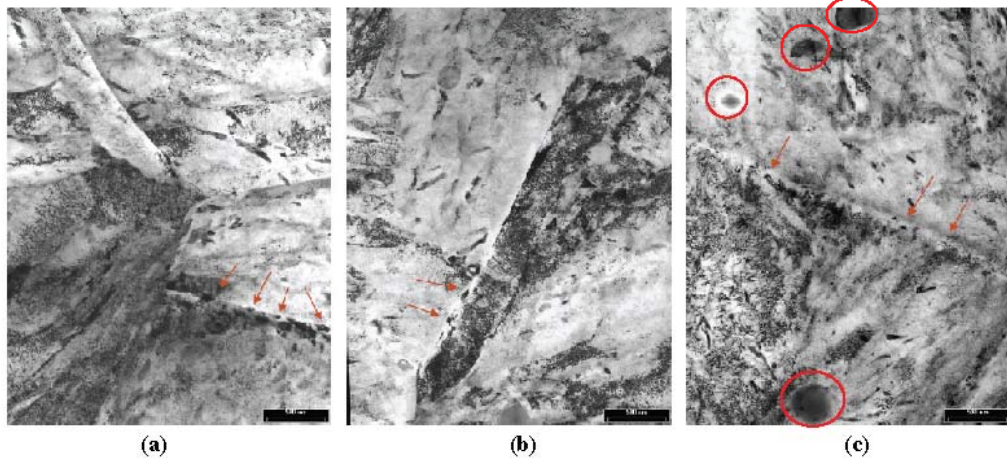- the dynamics of nucleation and growth of subgrains from dislocations within the cells as well as

Fig. 5. TEM-investigations of the bainitic microstructure show secondary precipitations at grain boundaries (M₃C, MX, marked with arrows), large primary MX carbides (marked with circles in (c)) and generally a high dislocation density. All images are 4 μm in width.

3. MODELLING OF THE DISLOCATION STRUCTURE EVOLUTION DURING SERVICE

The precipitation state after the heat treatment, the thermal and mechanical loading conditions, the initial dislocation density as well as subgrain size are key parameters in the used physically based dislocation model according to Ghoniem et al. [1]. Since the con-

- the subgrain growth due to coalescence driven by the subboundary energy.

Hence the total dislocation density ρ_{ges}, is separated into three categories of dislocations, namely mobile ρ_m, static ρ_s, and boundary dislocations ρ_b to consider all the specific dislocation dynamics mentioned above.

The temporal evolution of the mobile dislocation density ρ_m is given in equation 1 with v_g as the glide

– 230 –

velocity of the dislocations, β as a parameter for the dislocation emission, R_{sub} is the subgrain radius, h_{sg} the distance between two dislocations in the subgrain boundary, v_c^m the creep velocity of mobile dislocations and δ determines the dynamic annihilation distance: Read Frank sources Immobilization

$$\frac{d\rho_m}{dt} = \underbrace{v_g\rho_m^{0.5}}_{Frank-Read-sources} + \underbrace{\frac{\beta R_{sub}}{h_{sg}^2}v_g}_{Emission\ from\ cell\ walls} -$$

$$- \underbrace{8v_c^m\rho_m^{3/2}}_{Static\ recovery} - \underbrace{\delta(\rho_m+\rho_s)v_g}_{Dynamic\ recovery} \qquad (1)$$

The evolution equation for describing the static dislocation density is given in equation (2), where v_c^s denotes the creep velocity of static dislocations:

$$\frac{d\rho_s}{dt} = \underbrace{\frac{\rho_m}{2R_{sub}}v_g}_{Immobilization} + \underbrace{8\frac{\rho_s}{h_{sg}}v_c^s}_{Static\ recovery} - \underbrace{\delta\cdot\rho_s\rho_m v_g}_{Dynamic\ recovery}$$

$$(2)$$

The principle, which is valid for all three dislocation categories are dislocation generation by:
- Frank-Read sources and emission of dislocations at cell walls (ρ_m),
- immobilization (ρ_s),
- absorption and static recovery (ρ_b)

as well as the decrease of dislocation density due to:
- static and dynamic recovery (ρ_m, ρ_s),
- coalescence and growth (ρ_b).

A further important parameter, which is included in the formula of the glide velocity v_g, is the space length λ between forest dislocations. When the static dislocation density decreases, λ increases, which means easier gliding and following faster annihilation of mobile dislocations.

The effects of solutes and precipitations, which strengthen the material, are considered in the evolution of the boundary dislocation density, which can be seen in equation (3). The input parameters from the precipitation calculations $Rv_{mean,i}$ and N_i, for seven different types (i=1..7) of precipitations, which are depicted in figures 3 and 4, are introduced into the model:

$$\frac{d\rho_b}{dt} = \underbrace{8(1-2\zeta)\frac{\rho_s}{h_{sg}}v_c^s}_{Absorption\ of\ dislocation\ and\ static\ recovery} -$$

$$\underbrace{\frac{\rho_b}{R_{sub}}M_{sg}\left[p_{sg} - 2\pi\cdot\left(\sum_{i=1}^{7}Rv_{mean,i}^2\cdot N_i\right)\cdot\gamma_{sg}\right]}_{Coalescence\ and\ growth\ of\ subgrains} \quad (3)$$

with the parameter ζ describing the annihilation at the subgrain boundary, v_c^s the creep velocity of static dislocations, M_{sg} the mobility of subgrains, p_{sg} the driving force of the subgrain boundary, $Rv_{mean,i}$ the radius of precipitation class i, N_i the related number of particles per volume and γ_{sg} the surface energy of the subgrain boundary.

The microstructure calculations can be compared with FE-Simulations and experiments [6,8] via the resulting true inelastic strain rate $d\varepsilon/dt$, which is an additional output of the model:

$$\frac{d\varepsilon}{dt} = \frac{1}{M}\rho_m v_g b \qquad (4)$$

where $M = 3$ is the Taylor factor for the bcc lattice structure [7] and b is the burgers vector.

3.2. Calculation of the dislocation density evolution during thermo-mechanical loads

During austenitization at 1020°C for one hour, the total dislocation density decreases, but during quenching bainite and martensite form, this causes high stresses and strains in the lattice structure, generating dislocations. The total dislocation density after austenitization and quenching, to produce mainly bainitic structure in our case, can be assumed to be $\rho_{ges}=10^{12}$ m^{-2}, i.e. $\rho_m = 8\cdot10^{11}$ m^{-2}, $\rho_s=1\cdot10^{11}$m^{-2} and $\rho_b=1\cdot10^{11}$ m^{-2} [10] and $R_{sub}= 7\cdot10^{-7}$ m.

The dislocation density calculations in this paper are executed for constant mechanical loads of 370MPa at 500°C (figure 6a), which should represent a heavily loaded point in the liner for aluminium extrusion application [8,9] and 750MPa at 570°C (figure 6b), which is a realistic case for copper extrusion [4, 5] and that is near the elastic limit at these conditions.

Calculations were performed with MathCad™ with the initial conditions as mentioned before and the loading time was set to 40 hours (1.44·10^5 seconds), which equals to 500 – 2000 press cycles in typical extrusion processes, however the cyclicality of loading has been neglected so far.

The total dislocation density at a load of 370MPa and 500°C increases very slowly (figure 6a), the main mechanism is the formation of a stable subgrain structure, i.e. the dislocation density in the cell walls increases significantly whereas the mobile as well as the static dislocation density finally decreases and the subgrain size almost remains constant. The macroscopic strain after 40 hours of loading is small in comparison to the strain occurring at

– 231 –

the considered higher thermo-mechanical load case (figure 6b), where the dislocation structure immediately begins to change and a distinctive subgrain structure is formed. Remarkable is the resulting higher dislocation density of $\rho_{ges}= 2\cdot10^{14}\,\mathrm{m^{-2}}$ in comparison to $1.5\cdot10^{12}\,\mathrm{m^{-2}}$ for the lower load case. The diagrams also show that a constant total dislocation density production rate (slope of blue curve in figures 6a,b) develops with progress in time.
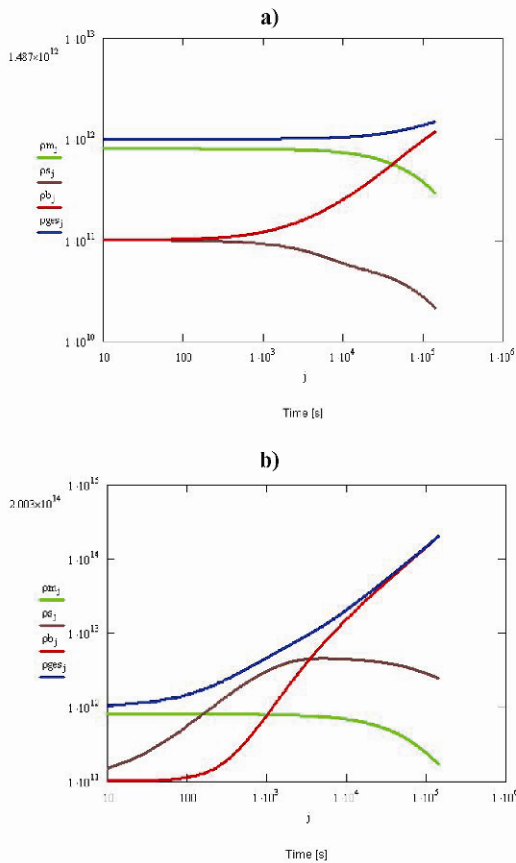

Fig. 6. Evolution of the mobile (ρ_m, green line), static (ρ_s, brown line), boundary (ρ_b, red line) and total (ρ_{ges}, blue line) dislocation density $[m^{-2}]$ at 500°C and 370MPa (a) and 570°C and 750MPa (b) in double logarithmic scale.

To validate the dislocation density model, the resulting inelastic strain is compared (figure 7) with ABAQUS calculations including an elastic-viscoplastic Chaboche type constitutive model that has been validated by a comprehensive experimental program [8].

The ABAQUS simulation output for the accumulated viscoplastic strain for 370MPa at 500°C after 40 hours amounts to $2.5\cdot10^{-5}$, whereas the result from the microstructure model is $1.0\cdot10^{-4}$, which is

fairly comparable, while the results for the second considered thermo-mechanical load case agree better. Remarkable is that the dislocation density model exhibits a constant slope (d log ε / d log t), contrary to the ABAQUS model results.
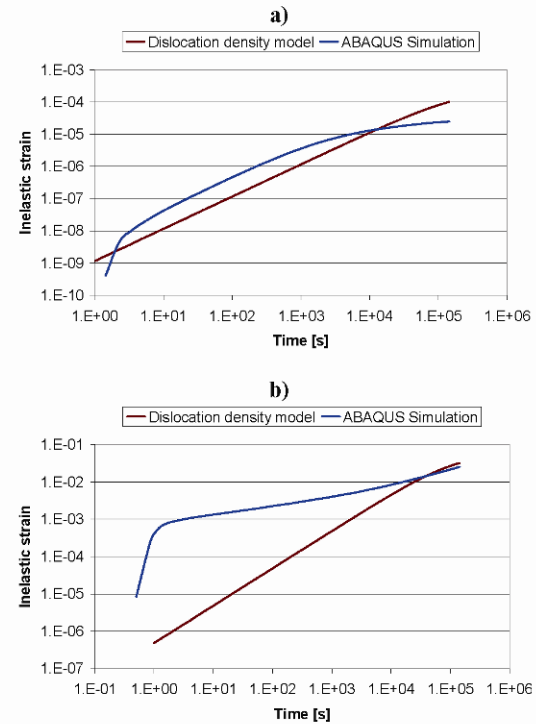

Fig. 7. Comparison of the calculated (this work, brown curve) as well as FE-simulated ([8], blue curve) inelastic strains for 370MPa at 500°C (a) and 750MPa at 570°C (b).

4. CONCLUSIONS AND OUTLOOK

In this work it was shown, that by applying physical based models, the microstructure evolution of hot work tool steels during both heat treatment and industrial service can be described. Precipitation of secondary phases during annealing was modelled in order to consider the significant influence of the precipitation state on the mobility of dislocations. However, possible further precipitation reactions during service, which was related to short time dislocation creep, were neglected. On the basis of two chosen examples, i.e. aluminium extrusion and copper extrusion, representative loads were applied to calculate the evolution of mobile, static and boundary dislocation densities as well as of the subgrain structure. Resulting inelastic accumulated strains were compared with the outcome of a constitutive formerly validated model.

– **232** –

To further validate the microstructure calculations, the secondary hardening carbides in the material will be analysed after the heat treatment as well as during service in more detail. The model for the calculation of the dislocation density and subgrain size evolution will be verified by dislocation density measurements as well as via the resulting inelastic strain, which can be compared to both macroscopically measured and viscoplastically simulated values. Additionally, damage evolution as well as lifetime estimation of hot work tool steels shall be modelled in order to make progress in both materials development and process optimization.

REFERENCES

1. Ghoniem, N., Matthews, J., Amodeo, R., A dislocation model for creep in engineering materials, Res Mechanica, 29, 1990, 197-219.
2. Holzer, I., Rajek, J., Kozeschnik, E., Cerjak, H.-H., Simulation of the precipitation kinetics during heat treatment and service of creep resistant martensitic 9-12% Cr Steel, Proc. Materials for Advanced Power Engineering, Liege, 2006, 1191-1198.
3. Kozeschnik, E., Sonderegger, B., Holzer, I., Rajek, J., Cerjak, H., Computer simulation of the precipitate evolution during industrial heat treatment of complex alloys, Materials Science Forum, 539-543, 2007, 2431-2436.
4. Krumphals, F., Wlanis, T., Sommitsch, C., Buchner, B., Huber, D., Redl, C., Wieser, V., Creep fatigue in hot work tool steels during copper extrusion, Proc. Sixth International Conference on Low Cycle Fatigue, Berlin, eds, Portella, P.D. et al., DVM Berlin, 2008, 721-726.
5. Krumphals, F., Wlanis, T., Sommitsch, C., Redl, C., Creep fatigue of multi-part container during hot extrusion of copper – Simulation and experimental comparison, Computer Methods in Materials Science, 7, 2007,47-53.
6. Mitter, W., Haberfellner, K., Danzer, R., Stickler, C., Lifetime prediction of hot work tool steels, Lab. Report, Journal of Heat Treatment and Materials Science (HTM), 52, 1997, 253-258.
7. Orlova, A., Miclicka, K., Dobes, F., Choice of evolution equation for internal stress in creep, Materials Science and Engineering, A194, 1995, 9-16.
8. Sommitsch, C., Sievert, R., Wlanis, T., Günther, B., Wieser, V., Modelling of creep-fatigue in containers during aluminium and copper extrusion, Computational Materials Science, 39, 2007, 55-64.
9. Sommitsch, C., Krumphals, F., Stotter, C., Dendl, D., Wlanis, T., Huber, D., Wieser, V., Lifetime comparison of different hot work tool steels for extrusion tools in aluminium extrusion, Proc. ET'08-Ninth International Aluminium Extrusion Technology Seminar and Exposition, Orlando, 2, 2008, 425-436.
10. Weinert, P., Modellierung des Kriechens von ferritisch/martensitischen 9-12% Cr-Stählen auf mikrostruktureller Basis, PhD thesis, University of Technology, Graz, 2001 (in German).

MODELOWANIE ROZWOJU MIKROSTRUKTURY STALI NARZĘDZIOWYCH PODCZAS OBRÓBKI CIEPLNEJ I PRACY W WARUNKACH EKSPLOATACYJNYCH

Streszczenie

Tematem pracy jest przewidywanie czasu pracy narzędzi w warunkach eksploatacyjnych. Końcowe własności wyrobu zależą od jego początkowej mikrostruktury oraz zmian tej mikrostruktury podczas wytwarzania. Dlatego za główny cel pracy postawiono sobie modelowanie rozwoju mikrostruktury podczas procesu obróbki cieplnej oraz pracy narzędzi w warunkach eksploatacyjnych. Modelowanie ewolucji mikrostruktury ze szczególnym uwzględnieniem kinetyki wydzieleń wykonano z wykorzystaniem pakietu MatCalc. W pracy analizie poddano stal narzędziową X38CrMoV5-1 o strukturze bcc, która tworzy wyraźną strukturę dyslokacyjną oraz podziarnową. Wykonane obliczenia numeryczne poddano również weryfikacji doświadczalnej.

C.3 Experience with 9Cr3W3CoVNbBN Base Material and Crosswelds at 650°C for Implementation in USC Power Plants

P. Mayr[1], F. Mendez Martin[1], I. Holzer[1], A. Agüero[2], V. González[2], S. Baumgartner[3] and H.H. Cerjak[1]

[1] Institute for Materials Science and Welding, Graz University of Technology, Kopernikusgasse 24, 8010 Graz, Austria.
[2] Instituto Nacional de Técnica Aeroespacial, Ctra. de Ajalvir Km 4, 28850 Torrejón de Ardoz, Spain.
[3] Böhler Schweißtechnik Austria GmbH, Böhler-Welding-Str. 1, 8605 Kapfenberg, Austria.

Abstract

This manuscript gives an overview on recent developments of a martensitic steel grade based on 9Cr3W3CoVNb with controlled additions of boron and nitrogen. Alloy design by thermodynamic equilibrium calculations and calculation of boron-nitrogen solubility is discussed.

Two melts of a 9Cr3W3CoVNb steel were produced. The oxidation resistance was examined at 650°C in steam atmosphere. The alloy exhibited high resistance to steam oxidation at 650°C for at least 5.000 hours of exposure.

Microstructural evolution during welding within the heat-affected zone was investigated by physical weld simulation, thermo-dilatometry and in situ X-ray diffraction using high energy synchrotron radiation. The heat-affected zone microstructure is characterized by optical microscopy. Two multilayer welds, one with a nickel based filler and one with a newly developed flux cored filler of matching chemical composition, were fabricated. All weldability experiments showed that within the heat-affected zone the initial base material microstructure is retained to a large extent. The formation of a uniform fine-grained heataffected zone region is suppressed.

Uniaxial creep tests of base material, weld metal and crossweld specimens were started at different levels of stress at 650°C. Up to the established maximum testing time of 20.000 hours, the base material shows significant improvement compared to standard 9 wt. % Cr grades P91 and P92. Crossweld specimens show an improved strength level, higher than that of grade P92 base material.

Preliminary results of an extensive testing program on a 9Cr3W3CoVNbBN steel show significant improvement compared to the state-of-the-art 9 wt. % Cr martensitic steel grades.

Experience with 9Cr3W3CoVNbBN Base Material and Crosswelds at 650°C for Implementation in USC Power Plants

Peter Mayr[1], **Ivan Holzer**[1], **Francisca Mendez-Martin**[1], **Alina Agüero**[2], **Vanessa González**[2], **Susanne Baumgartner**[3] and **Horst Cerjak**[1]

[1] **Institute for Materials Science and Welding, Graz University of Technology, Kopernikusgasse 24, 8010 Graz, Austria, peter.mayr@tugraz.at**

[2] **Instituto Nacional de Técnica Aeroespacial, Ctra. de Ajalvir Km 4, 28850 Torrejón de Ardoz, Spain**

[3] **Böhler Schweißtechnik Austria GmbH, Böhler-Welding-Str. 1, 8605 Kapfenberg, Austria**

ABSTRACT

This manuscript gives an overview on recent developments of a martensitic steel grade based on 9Cr3W3CoVNb with controlled additions of boron and nitrogen. Alloy design by thermodynamic equilibrium calculations and calculation of boron-nitrogen solubility is discussed.

Two melts of a 9Cr3W3CoVNb steel were produced. The oxidation resistance was examined at 650°C in steam atmosphere. The alloy exhibited high resistance to steam oxidation at 650°C for at least 5.000 hours of exposure.

Microstructural evolution during welding within the heat-affected zone was investigated by physical weld simulation, thermo-dilatometry and in situ X-ray diffraction using high energy synchrotron radiation. The heat-affected zone microstructure is characterized by optical microscopy. Two multilayer welds, one with a nickel based filler and one with a newly developed flux cored filler of matching chemical composition, were fabricated. All weldability experiments showed that within the heat-affected zone the initial base material microstructure is retained to a large extent. The formation of a uniform fine-grained heat-affected zone region is suppressed.

Uniaxial creep tests of base material, weld metal and crossweld specimens were started at different levels of stress at 650°C. Up to the established maximum testing time of 20.000 hours, the base material shows significant improvement compared to standard 9 wt. % Cr grades P91 and P92. Crossweld specimens show an improved strength level, higher than that of grade P92 base material.

Preliminary results of an extensive testing program on a 9Cr3W3CoVNbBN steel show significant improvement compared to the state-of-the-art 9 wt. % Cr martensitic steel grades.

1. Introduction

In Japan and Europe, research and development works in the field of advanced martensitic creep resistant steels has a long history [1-3]. The fields of application for such materials are especially large diameter and thick section boiler components, such as main steam pipes and headers of ultra-supercritically (USC) operated plants. The target of steel development is defined by a creep rupture strength of 100 MPa after 100.000 hours at 650°C. Beside high creep rupture strength, also high steam oxidation resistance at service temperature, acceptable thermal cycling capabilities, i.e. fatigue strength, and also good formability and weldability are mandatory for new martensitic creep resistant steel grades.

Within the last years, the alloy design philosophy for martensitic steels strongly targets the long-term stability of microstructure [4]. Migration of lath and block boundaries, causing the coarsening of martensite laths and blocks by annihilation of excess dislocations, closely correlates with the onset of accelerated creep. A fine dispersion of $M_{23}C_6$ and MX particles, which exert a pinning force on migrating boundaries and dislocations, has been identified as main contributor in suppressing recovery of the martensitic microstructure.

The work presented in this manuscript is following an extensive research program started at the National Institute for Materials Science (NIMS), Japan [4]. In detail, the NIMS alloy design concept follows stabilization of $M_{23}C_6$ carbides and grain boundaries by the addition of boron in combination with finely dispersed MX particles as a possible solution to stabilize the martensitic substructure. As basis for the systematically study of the influence of boron and nitrogen on long term creep behavior, a Fe-0.08C-9Cr-3W-3Co-0.2V-0.05Nb (wt. %) steel with different concentrations of boron and nitrogen was investigated [5,6].

The influence of boron on 9Cr3W3CoVNb steel was studied in the range of 0 to 140 ppm (parts per million) while nitrogen level was kept constant at a minimum between 10 to 30 ppm [5]. The influence of boron on creep properties was studied by uniaxial-creep testing at 650°C at different stress levels. At stress levels higher than 100 MPa, no big difference in creep strength between 0B, 0.0048B and 0.0092B steel was found. Only 0.0139B steel showed improved creep strength. While at lower stress levels, creep strength of the lower boron steels decreased significantly, 0.0139B steel showed a stable creep behavior. It was concluded that controlled addition of boron can delay the decrease of long-term creep strength in 9Cr3W3CoVNb steel. As a result of the boron series creep tests, a boron content of 140 ppm was identified as optimum for improved creep behavior.

The combined effect of boron plus additional MX precipitation was studied by 9Cr3W3CoVNb test melts with a fixed boron content of 140 ppm and varying nitrogen levels of 15, 79 and 650 ppm [6]. Increasing the nitrogen level to 79 ppm resulted in further improvement of the creep strength of the base 9Cr3W3CoVNb-0.0140B steel. However, further increase of nitrogen to 650 ppm showed no beneficial effects and in turn reduced creep strength of the alloy.

The main idea behind the NIMS alloying concept is to combine boron-strengthening with nitride-strengthening. However, excess addition of nitrogen in combination with boron causes the formation of boron nitrides (BN) during forming and heat treatments at elevated temperatures. Precipitation of boron nitrides offsets the beneficial effect of boron and nitrogen addition. Sakuraya et. al [7] showed in their work on BN formation in high Cr heat resistant steels that, a particular relationship between boron and nitrogen has to be kept to avoid

formation of coarse BN particles. From experimental observations the authors derived a formulation for the solubility product of BN.

Also weldability of 9Cr3W3CoVNb steel was investigated by several researchers [8,9]. Creep rupture data at 650°C for crosswelds of 9Cr3W3CoVNb steel with addition of 130 ppm boron and low nitrogen content of 15 ppm, standard P92 and P91-type steel was compared to creep rupture data of their base metals. There was basically no degradation of creep rupture strength in the 9Cr3W3CoVNbB-low N steel welded joints, while degradation of creep strength of P92 welded joints became more significant with increasing test duration. This behavior was attributed to the suppression of a grain refined region in the heat-affected zone (HAZ) of the 9Cr3W3CoVNbB-low N steel. The responsible mechanism discussed are austenite memory effect and martensitic reverse transformation [9].

Within the present work, the NIMS alloy design regarding the optimum boron-nitrogen relationship was slightly modified based on thermodynamic studies. On the following pages the alloy design for a boron and nitrogen strengthened 9Cr3W3CoVNb steel is described in detail and first results of creep tests, oxidation test and welding trials are presented.

2. Experimental

Alloy Design. Thermodynamic equilibrium calculations were performed using the software Matcalc [10-13] utilizing the thermodynamic database Fe-data6 [14]. The description of BN in the database was slightly modified, based on the work of Fountain et al. [15].

Materials. A 20 kg heat (Heat 1) of 9Cr3W3CoVNb steel with controlled additions of 120 ppm boron and 130 ppm nitrogen was produced by vacuum induction melting. The addition of boron and nitrogen was set to avoid the formation of large boron nitrides but still allow the precipitation of strengthening MX particles. For homogenization of Heat 1, the ingot (110 mm square) was forged to final dimensions of 50 mm square. A second heat (Heat 2) of a 9Cr3W3CoVNb steel with slightly reduced boron (110 ppm) and nitrogen (110 ppm) content was produced and rolled to 20 mm thick plates. The exact chemical composition in weight % (wt. %) of Heat 1 and Heat 2 is given in Table 1. The final quality heat treatment for both heats consisted of normalizing at 1150 °C for 1 hour followed by tempering at 770 °C for 4 hours.

Table 1: Chemical composition of 9Cr3W3CoVNbBN test melts in wt. % (balanced Fe).

Analysis	C	Si	Mn	Cr	W	Co	V	Nb	B	N
Heat 1	0.074	0.29	0.44	9.26	2.84	2.95	0.21	0.056	0.012	0.013
Heat 2	0.090	0.30	0.51	9.26	2.92	2.88	0.20	0.050	0.011	0.010

Within this manuscript, data on Heat 2 is exclusively limited to welding trials using a newly developed chemically matching martensitic weld metal. All data reported on microstructural characterization, oxidation and creep testing is related to Heat 1.

Welding Trials. To investigate the weldability of the newly developed steel and the creep behavior of crossweld specimens, two plates of Heat 1 were welded by gas tungsten arc welding (GTAW) process using a nickel based filler metal (Nibas 70/2-IG). A nickel based

filler metal was chosen, as at that time, no martensitic filler material with sufficient creep strength was available and fracture would always have occurred in the weld metal. Details regarding the welding procedure can be found in [16].

A second weld was produced of Heat 2 material using a flux-cored wire with chemically matching composition, which was developed within the current project. Postweld heat treatment for both welds was carried out at 740°C for 4 hours.

Steam Oxidation Laboratory Testing. The schematics of the closed loop laboratory rig employed at INTA are shown elsewhere [17]. Prior to testing, laboratory air is displaced from the chamber by means of N_2 which is kept flowing while heating up to the test temperature (approximately at 600°C/h). Once the test temperature is reached, the N_2 flow is closed and pure steam is introduced at a linear velocity of 8 cm/s. To carry out weight measurements or to remove samples, the furnace is cooled to about 300°C under N_2 atmosphere and the specimens are subsequently removed. The reheat cycle is also carried out under N_2 atmosphere.

Characterization. Base material microstructure was characterized by light optical microscopy, scanning electron microscopy (SEM) and analytical transmission electron microscopy (TEM). Details are reported in [18]. The oxidized specimens were characterized by optical and field emission scanning electron microscopy (FESEM) employing a JEOL JSM 840 system equipped with an energy dispersive X-ray spectrometer (EDS) KEVEX MICROANALYST 8000 with a RÖNTEC signal processor.

3. Modified Alloy Design Concept

To take advantage of boron and nitrogen addition the formation of large boron nitrides (BN) has to be avoided. Therefore, in the present work the allowable boron and nitrogen limits for high chromium martensitic steels were determined by thermodynamic equilibrium calculations. Within this study, the BN solubility product for a 9Cr3W3CoVNbBN steel, based on the chemical composition of Heat 1, was calculated for various B/N ratios and different temperatures (representative for normalizing), considering also possible formation of boride (M_2B).

The result is shown in Figure 1. The solubility products (solid lines) are shown for different temperatures ranging from 900°C to 1250°C. The dashed grey lines show the solubility product for the M_2B phase. Furthermore, the BN solubility line reported by Fountain et al. [15] at 1150°C and Sakuraya et al. [19] are included in the figure.

The grey areas in Figure 1 indicate the critical B/N ratios where BN formation is predicted. No formation of BN is expected below the respective BN solubility line. Figure 1 clearly shows that the experimental findings reported by Sakuraya et al. [19] are well described by the thermodynamic equilibrium considerations in the temperature range between 900°C and 1250°C. For the B/N ratios reported by Sakuraya et al. [7] no BN formation is predicted for temperatures higher than 1250°C, consistent with the experimental findings.

Due to the temperature dependence of the BN solubility product it can be assumed that coarse BN (>1μm) exist for high boron and nitrogen contents and low normalizing temperatures. This leads to the conclusion that in Heat 1 only small and in Heat 2 no BN should form.
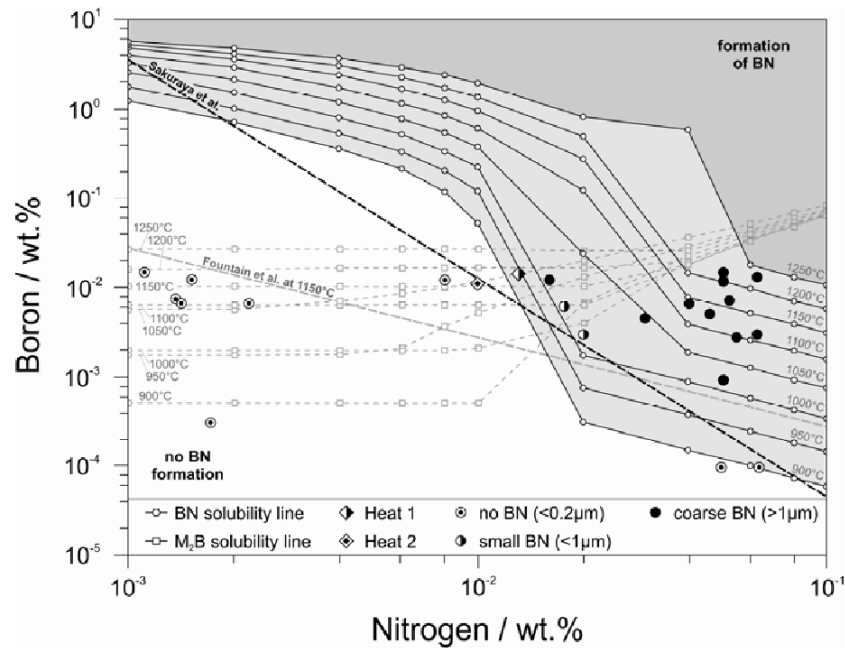
Figure 1: BN solubility product for a 9Cr3W3CoVNbBN steel as a function of temperature in the range between 900°C and 1250°C. The grey areas indicate the range of BN formation at high temperatures. The calculation is compared to the solubility products reported by Sakuraya et al. [19] and Fountain et al. [15].

4. Microstructure of 9Cr3W3CoVNbBN steel

Optical micrographs of 9Cr3W3CoVNbBN base material (Heat 1) show a tempered martensitic microstructure (see Figure 2). The average prior austenite grain size is 250 μm in diameter and precipitates are finely distributed mainly along prior austenite grain and martensite lath boundaries.

Via electron microscopy, MX (V,Nb)(N,C) carbonitrides and $M_{23}C_6$ $(Cr,Fe,Mo,W)_{23}C_6$ carbides have been identified at grain and lath boundaries and/or in the matrix of the base material. MX (V,Nb)(N,C) particles have a representative diameter smaller than 100 nm and Cr-rich carbides have a diameter between 150 and 250 nm. By SEM and EDS only very few and small (<1μm) BN particles for Heat 1 and no BN particles for Heat 2 have been detected. A detailed description of the method of detecting BN particles is given in [19]. These experimental findings support the results of the thermodynamic equilibrium calculations in the alloy design stage.
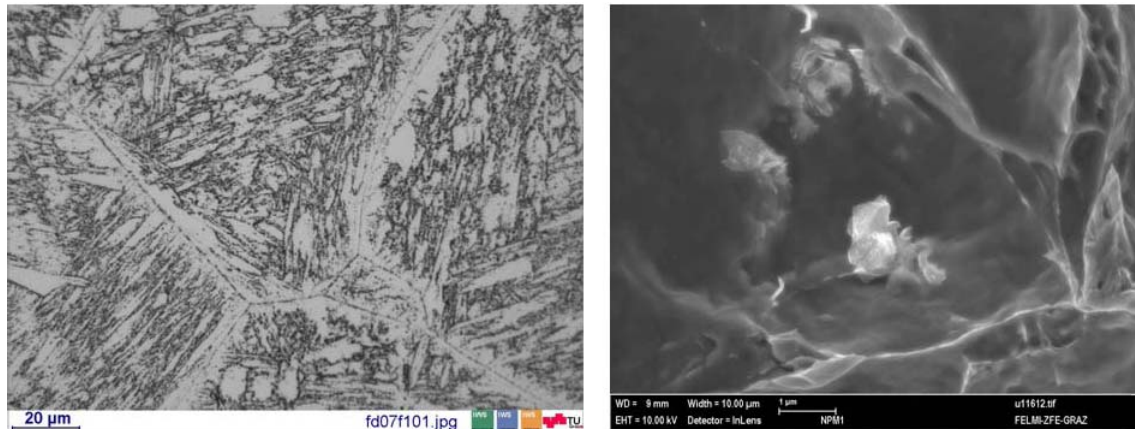
Figure 2: Optical micrograph of normalized and tempered 9Cr3W3CoVNbBN base material (left) and small BN particle (right) identified by EDS - both images for Heat 1.

After creep exposure for 8.971 hours at 650 °C and 130 MPa light-optical and electron microscopical investigations have been performed. The prior austenite grain and martensite lath structure, after almost 10.000 h of creep, show no significant changes. The precipitate size and number density of carbonitrides and carbides remain almost the same as in the base material. The electron microscopy investigation reveals the precipitation of two new phases: laves phase (intermetallic phase A_2B, $(Fe,Cr)_2(W,Mo)$ with approximately 38 atom % of tungsten and more than 45 atom % of iron, distributed mainly at the grain boundaries and modified Z-phase (complex nitride $[(Cr,V,Nb)N]$) with a very low phase fraction. Details on the microstructural evolution of 9Cr3W3CoVNbBN steel during creep exposure can be found in [20].

5.   Oxidation behavior

Specimens of 9Cr3W3CoVNbBN (Heat 1) were exposed to pure, flowing steam at 650°C for 4.908 h. Figure 3 shows the mass variation of the new steel as function of time as well as that of 9 wt.% ferritic steels P91 and P92 for comparison purposes. 9Cr3W3CoVNbBN exhibits a mass gain considerably lower than that of the other two 9 wt. % Cr steels. This behavior is surprising, as work done by several research groups have indicated the steam oxidation resistance of steels correlates strongly with the Cr contents, and results so far have indicated that 9 wt. % Cr steels oxidized very fast when exposed to steam at T > 600°C [21-24]. For instance, Quadakkers and collaborators have concluded that a Cr wt.% of 11 or more is required to form a protective scale [21].
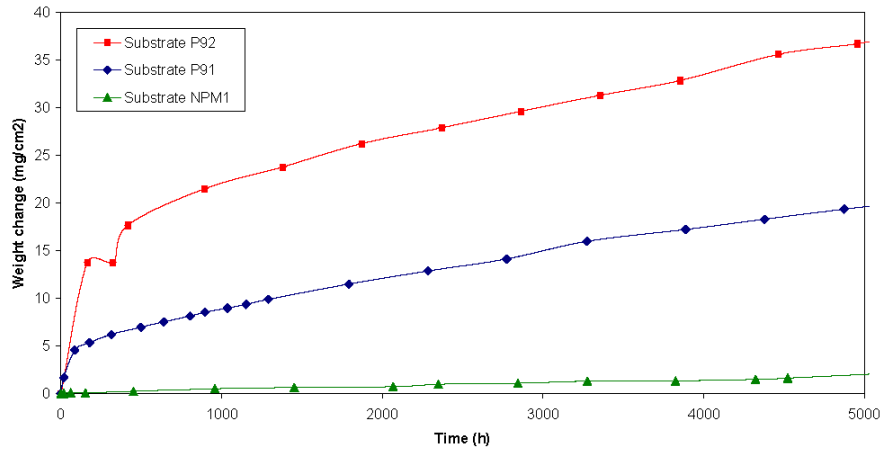
Figure 3: Mass variation of substrates exposed to flowing steam (1 bar) at 650º C

Figure 4 shows an image of a specimen exposed 4.908 h. Nodular features can be observed, especially at the samples edges but most of the surface appears smooth. On the cross section of the exposed surface a very thin (< 100 nm) Cr and O rich layer, most likely Cr_2O_3 can be observed with difficulty.
This type of oxide is typical of steels containing 11 wt. % of Cr. Quadakkers found that Co tends to increase the oxidation resistance of 9-12 Cr wt. % ferritic steels [21], but not to the extent observed for 9Cr3W3CoVNbBN. On the other hand, other groups have observed that the higher the W content the lower the oxidation resistance of this type of steels [22,25,26]. It is therefore not clear yet why this 9 wt. % steel exhibits such high steam oxidation resistance and further studies are required.
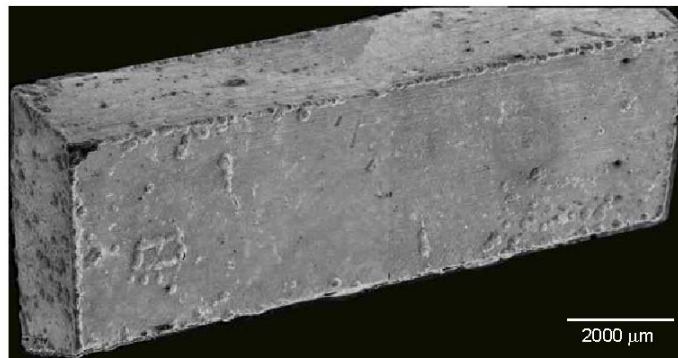

Figure 4: SEM image of a 9Cr3W3CoVNbBN specimen exposed to steam at 650ºC for 4.908 h
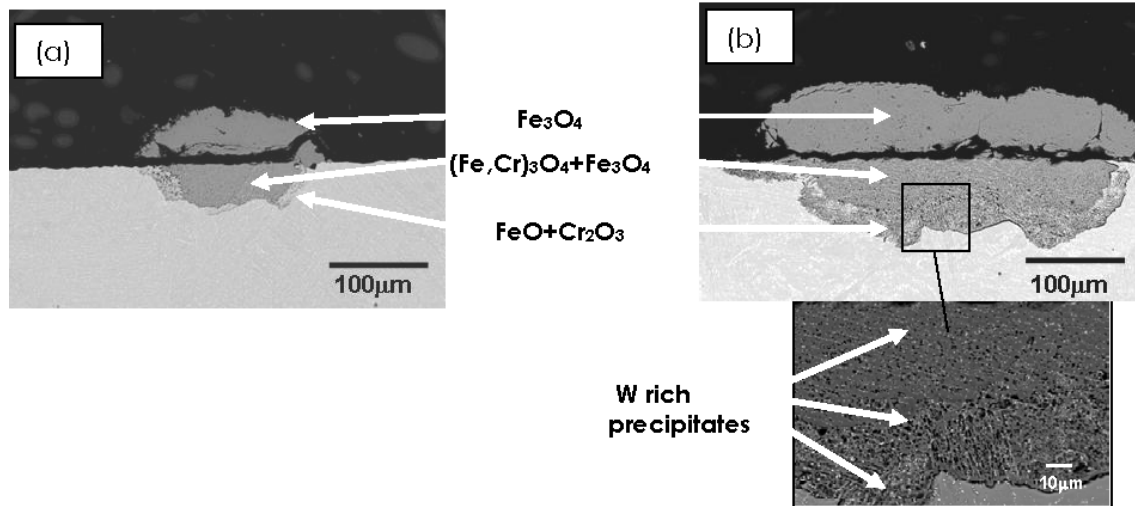
Figure 5: FESEM image of the cross section of 9Cr3W3CoVNbBN exposed to steam at 650°C at a nodule site: (a) for 1.260 h, (b) for 4.908 h

The cross section of representative nodules formed after 1.260 and 4.908 h are shown in Figure 5a and b respectively. The microstructure corresponds to a dual oxide layer similar to that observed on ferritic steels containing 9 wt.% in Cr, with a top outwards growth Fe_3O_4 layer and an inner growing mixed oxide layer containing $(Fe, Cr)_3O_4$, FeO and Cr_2O_3 [27] which also contains W, Co and V. Interestingly, W rich nanoscale precipitates which are also present in the substrate can be observed in this inner oxide layer. The nodules in the 1.260 h specimen exhibit lower thickness and width than those observed in the specimen exposed for 4.908 h, indicating that these oxides are growing fast and therefore are not protective, and moreover, the number of nodules on the 4.908 h is higher than that observed on the 1.260 h specimen.
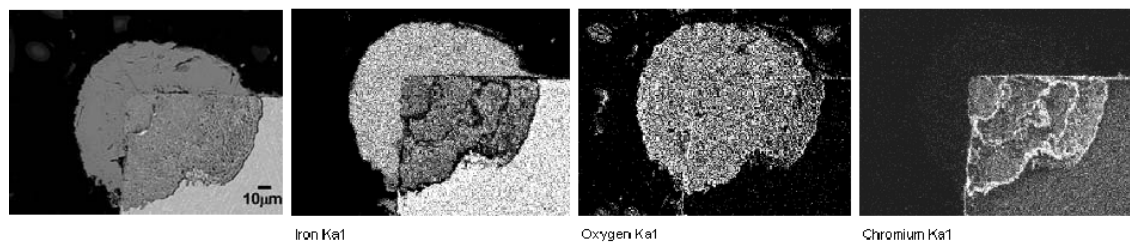

Figure 6: Cross section of the edge of a 9Cr3W3CoVNbBN specimen exposed to steam oxidation at 650° C for 4.908 h

At the specimen's edge (Figure 6) the corresponding EDS composition map reveals Cr rich layers within the inner oxide and the original specimen surfaces can be clearly observed. The average Cr content (19 wt. %) in this inner oxide zone is significantly higher than that of the

substrate, but because it is not uniformly distributed as shown, it is not protective. According to Quaddakers and coworkers, this pattern results from the repetition of cycles in which Cr rich spinels form due to rapid Cr diffusion from the bulk alloy until the spinel cannot be sustained due to continuous Cr depletion, resulting in the formation of Fe rich oxides [21]. Formation of oxidation nodules has been observed on oxidation resistant 12 wt. % steels and has been attributed to compositional inhomogeneities [21,28]. For this 9Cr steel the presence of nodules can be rather attributed to local cracks, imperfections and/or rupture of the protective scale on a Cr depleted substrate. The fact that the samples edges are fully covered with nodules support this hypothesis as due the higher residual stresses, corners and edges are more prone to develop cracks.

6. Weldability

The transformation behavior and weldability of 9Cr3W3CoVNbBN steel was investigated by thermo-dilatometry, in-situ X-ray diffraction using synchrotron radiation [29] and physical heat-affected zone (HAZ) simulation using a Gleeble thermo-mechanical simulator. Additionally, two welded joints were produced, one with a Ni-based filler (Heat 1) and one with compositional matching flux-cored wire (Heat 2).
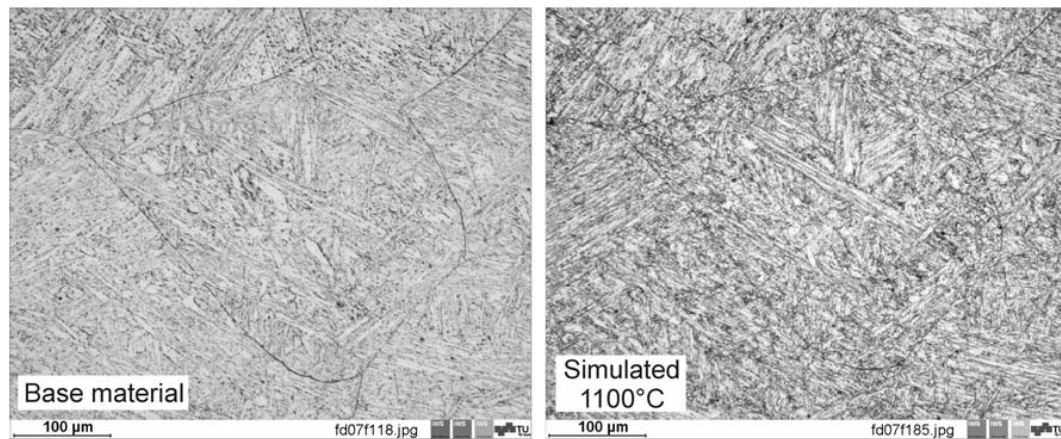

Figure 7: Comparison of the NPM1 microstructure at the same location before and after HAZ simulation applying a peak temperature of 1100°C revealing no grain refinement during the weld thermal cycle.

Applying a heating rate of 100°C/s resulted in an A_{c1} temperature of 909°C and a A_{c3} of 1028°C. Therefore, heating a sample to a peak temperature of 1100°C results in complete austenitisation and martensitic transformation on subsequent cooling (cooling rate 100°C/s). The onset of martensite formation (M_s) was measured at 488°C. Although, the steel undergoes two phase transformations during such thermal cycle, the initial grain structure is almost retained completely. Identical prior austenite grain boundaries and martensitic lath structure can be observed before (Figure 7 left) and after thermal HAZ simulation (Figure 7 right). 9Cr3W3CoVNbBN steel does not form a uniform fine-grained HAZ region.

Within this work, a matching flux cored wire of matching chemical composition for a 9Cr3W3CoVNbBN steel was developed. Flux cored wires in general combine the beneficial effects of covered stick electrodes like slag metallurgy, protection of the weld pool by a slag and improved out of position weldability with the advantage of solid wires to be used in automatic and robotic welding applications. To assure good welding behavior and out of position weldability a rutile (TiO_2) slag system has been designed. This slag concept has already been applied successfully to other creep resistant flux cored wires. Special focus for the 9Cr3W3CoVNbBN filler has been put on the adjustment of the boron and nitrogen content. The welding procedure resulted in a sound and defect free weld (Figure 8).
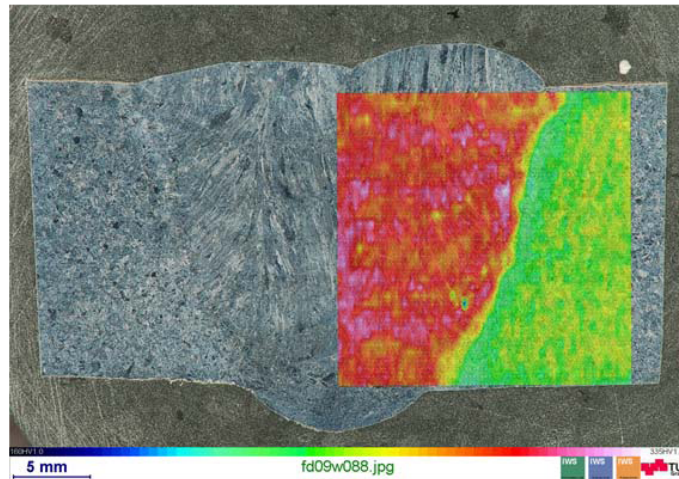

Figure 8: 9Cr3W3CoVNbBN steel (Heat 2) welded with filler metal of matching composition and corresponding hardness mapping (blue corresponds to 160HV1 and white to 335 HV1) after PWHT of 740°C for 4 hours.

7. Creep Strength

Uniaxial creep tests of 9Cr3W3CoVNbBN base material, weld metal and crossweld specimens have been carried out at 650°C. At present, the longest running creep test of base material has reached 21.000 hours at 100 MPa, as shown in Figure 9. The base material tested at a higher stress level of 130 MPa fractured after 8.971 h. This results in an improvement of rupture stress at approximately 9.000 hours of +60 MPa and +40 MPa compared to grades P91 and P92 respectively.

Pure weld metal specimens of type 9Cr3W3CoVNbBN were tested at 650°C and 150 MPa solely for creep strength screening purpose. The pure weld metal specimens exhibit similar short term creep rupture strength as the base material.

Results of creep tests of crossweld specimens are only available for the weld produced with Ni-base filler metal. Tests have reached a maximum duration of more than 11.000 hours. Three crossweld samples have fractured so far. Crossweld creep rupture data shows a

significant improvement compared to the mean creep strength of base material P91 and P92. Specimens tested at stresses lower than 100 MPa are still running.
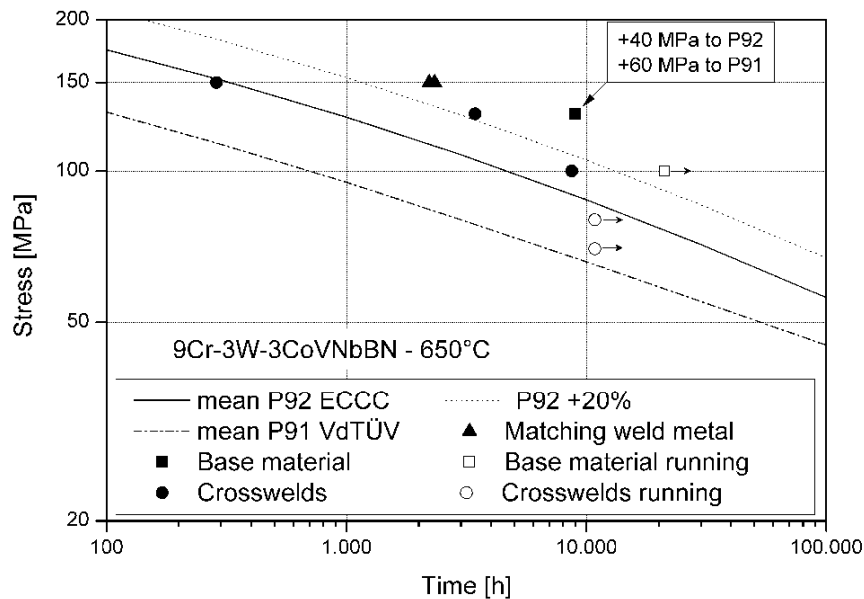

Figure 9: Creep testing data of 9Cr3W3CoVNbBN base material, weld metal and crosswelds at 650°C compared to well-established grades P91 and P92.

8. Summary and Conclusions

Alloy design for a 9 wt. % Cr steel has been successfully improved by thermodynamic calculation of phase fraction diagrams and calculation of the boron-nitrogen solubility product The boron and nitrogen content of a 9Cr3W3CoVNbBN steel was adjusted to have either only very small boron nitrides (Heat 1) or no precipitation of BN (Heat 2).

9Cr3W3CoVNbBN exhibits an unexpected high steam oxidation resistance at 650°C despite its low Cr content. It develops a thin Cr rich protective oxide scale despite its relatively low Cr content. However, oxidation nodules form, very likely due to protective oxide imperfections, growing in thickness, width and number as a function of steam exposure time.

Two welded joints have been successfully produced, one with a Ni-base filler wire and one with a newly developed chemically matching flux-cored filler wire.

Creep tests performed at 650°C of base material, martensitic weld metal and crosswelds show improved creep strength. The increased creep rupture strength of the welded joint can be attributed to the suppressed formation of a fully refined heat-affected zone microstructure.

As a whole, the boron and nitrogen alloyed martensitic 9Cr3W3CoVNbBN steel and its welded joints show very promising creep properties at 650°C and also unexpected high oxidation resistance in steam. The underlying mechanism are currently studied.

9. Acknowledgements

10. References

[1] Kern T U, Wieghardt K and Kirchner H, in 4th int conf Advances in Materials Technology for Fossil Power Plants, Hilton Head Island, ASM International, 2005.

[2] Masuyama F, in 4th int conf Advances in Materials Technology for Fossil Power Plants, Hilton Head Island, ASM International, 2005.

[3] Cerjak, H.-H.; Dimmler, G.; Holzer, I.; Kozeschnik, E.; Mayr, P.; Pein, C.; Sonderegger, B.: Materials science forum 539-543 (2007) , S. 2954 - 2959

[4] Abe F, in 4th int conf Advances in Materials Technology for Fossil Power Plants, Hilton Head Island, SC, EPRI, 2004.

[5] Abe F, Horiuchi T and Sawada K, Materials Science Forum, 2003, 426-432, 1393-1398.

[6] Semba H and Abe F, "in 4th int conf Advances in Materials Technology for Fossil Power Plants, Hilton Head Island, SC, EPRI, 2004.

[7] Sakuraya K., Okada H., Abe F., ISIJ Int., vol. 46 (2006), 1712.

[8] Kondo M, Tabuchi M, Tsukamoto S, Yin F and Abe F, in 4th int conf Advances in Materials Technology for Fossil Power Plants, Hilton Head Island, SC, EPRI, 2004.

[9] Kondo M, Tabuchi M, Tsukamoto S, Yin F and Abe F, STWJ, 2006 11(2) 216-223

[10] Kozeschnik E., Buchmayr B., Mathematical Modelling of Weld Phenomena 5, Institute of Materials, London, 2001, 349.

[11] Svoboda J., Fischer F. D., Fratzl P., Kozeschnik E., Mater. Sci. Eng. A, vol 385 (2004) 166.

[12] Kozeschnik E., Svoboda J., Fratzl P., Fischer F. D., Mater. Sci. Eng. A, vol 385 (2004) 157.

[13] Kozeschnik E., Svoboda J., Fischer F. D., CALPHAD, vol 28 (2005) 379.

[14] Saunders M., Fe-data6.tdb.

[15] R.W. Fountain, Chipman J., Transactions of the Metallurgical Society of AIME, vol. 224 (1962) 599.

[16] Mayr P, Cerjak H, Jochum C and Pasternak J: in 8th International Conference on Creep and Fatigue at Elevated Temperatures 2007, San Antonio, 2007

[17] Agüero A., Muelas R., Scarlin B., and Knödler R., Materials for Advanced Power Engineering 2002, Part III (2002), p. 1143

[18] Mayr P., PhD-Thesis, Graz University of Technology, 2007

[19] Sakuraya K., Okada H., Abe F., in: Advances in Materials Technology for Fossil Power Plants: Proceedings of the Fourth International Conference, (2004) 1270.

[20] Mayr, P.; Mendez Martin, F.; Albu, M.; Cerjak, H.-H.: in: Creep and Fracture in High Temperature Components - Design & Life Assessment Issues (2009), S. 1029 - 1037

[21] Quadakkers W.J. and Ennis P.J., Materials for Advanced Power Engineering 1998, Part I (1998) p. 123

[22] Nava-Paz J.C. and Knödler R., Materials for Advanced Power Engineering 1998, Part I (1998) p. 451

[23] Fukuda Y., Tamura K. and Sato T., Materials for Advanced Power Engineering 1998, Part I (1998) p. 461

[24] Ennis P.J. and Quadakkers W.J., Materials for Advanced Power Engineering 2002, Part II (2002) p. 1131

[25] Knödler R. and Scarlin B., Materials for Advanced Power Engineering 2002, Part III (2002) p. 1601

[26] Agüero A. and Muelas R., Materials Science Forum, 461-464 (2004) p. 957

[27] Zurek J., Nieto-Hierro L., Piron-Abellan J., Niewolak L., Singheiser L. and Quadakkers W.J., Materials Sceince Forum, 461-464 (2004) p. 791

[28] Lepingle V., Louis G., Petelot D., Lefevre B. and Vandenberghe B., Materials Science Forum, 461-464 (2004) p. 1039

[29] Mayr, P.; Palmer, T. A.; Elmer, J. W.; Specht, E. D.: International journal of materials research 99 (2008) 4, p. 381 - 387

C.4 Simulation and Validation of the Evolution of precipitates during production and fabrication of a complex martensitic 9 wt.% Cr steel

I. Holzer[1], P. Mayr[1], B. Sonderegger[1], E. Kozeschnik[1], H.H. Cerjak[1]

[1] Institute for Materials Science and Welding, Graz University of Technology, Kopernikusgasse 24, 8010 Graz, Austria.

Abstract

Martensitic 9-12 wt.% Cr steels are favoured grades for high temperature components in thermal power generation industry. Welding is the major joining and repair technology of such components. The creep strength of 9-12 wt.% Cr steels is mainly based on the fine distribution and long-term stability of different populations of precipitates. After the quality heat treatment, i.e. in normalised and tempered condition, the steels show a tempered martensitic microstructure with finely dispersed precipitates. Due to thermal influence by the welding processes the initial optimized microstructure is significantly altered. Most of the precipitates are dissolved during heating and virgin martensite is formed on cooling. The heat-affected zone (HAZ) of martensitic steels is often afflicted with inferior mechanical properties. A post weld heat treatment (PWHT) is mandatory and can recover the base material microstructure and properties of the 'as-received' condition

to a certain extent. Although especially during long-term service, the HAZ of martensitic steels is prone to premature failures.

The present work is divided into three parts. In the first part, a defined time-temperature sequence representing a welding process and subsequent PWHT is simulated in the laboratory. At defined time-steps, specimens are taken out of the furnaces for microstructural investigations using optical as well as electron microscopic methods. In the second part of the work, the evolution of the precipitates in this martensitic steel is simulated, based on the software package MatCalc, resembling the time-temperature sequence of the simulated heat treatment. In the third part, results obtained from the kinetic simulations are linked with those of the microstructural investigations. Comparison of the experimental and simulated results shows very good agreement. Optimisation of the heat treatment procedure and further application of microstructure modelling are discussed.

SIMULATION AND VALIDATION OF THE EVOLUTION OF PRECIPITATES DURING PRODUCTION AND FABRICATION OF A COMPLEX MARTENSITIC 9 WT.% CR STEEL

I. Holzer, P. Mayr, B. Sonderegger, E. Kozeschnik, H. Cerjak

Martensitic 9-12 wt.% Cr steels are favoured grades for high temperature components in thermal power generation industry. Welding is the major joining and repair technology of such components. The creep strength of 9-12 wt.% Cr steels is mainly based on the fine distribution and long-term stability of different populations of precipitates. After the quality heat treatment, i.e. in normalised and tempered condition, the steels show a tempered martensitic microstructure with finely dispersed precipitates. Due to thermal influence by the welding processes the initial optimized microstructure is significantly altered. Most of the precipitates are dissolved during heating and virgin martensite is formed on cooling. The heat-affected zone (HAZ) of martensitic steels is often afflicted with inferior mechanical properties. A post-weld heat treatment (PWHT) is mandatory and can recover the base material microstructure and properties of the 'as-received' condition to a certain extent. Although especially during long-term service, the HAZ of martensitic steels is prone to premature failures.

The present work is divided into three parts. In the first part, a defined time-temperature sequence representing a welding process and subsequent PWHT is simulated in the laboratory. At defined time-steps, specimens are taken out of the furnaces for microstructural investigations using optical as well as electron microscopic methods. In the second part of the work, the evolution of the precipitates in this martensitic steel is simulated, based on the software package MatCalc, resembling the time-temperature sequence of the simulated heat treatment. In the third part, results obtained from the kinetic simulations are linked with those of the microstructural investigations. Comparison of the experimental and simulated results shows very good agreement. Optimisation of the heat treatment procedure and further application of microstructure modelling are discussed.

INTRODUCTION

In the past, in the field of material development for thermal power plant applications, great efforts were undertaken to increase the efficiency of power plant components [1]. The increase in efficiency is mainly driven by the use of ultra-supercritical steam conditions (USC). Within research programs in the USA, Japan and Europe, several types of creep resistant ferritic/martensitic 9-12%Cr steels have been developed for application under such harsh conditions. These steels are characterized by a microstructure with a dense distribution of precipitates, tight subgrain structure and high dislocation density within the subgrains produced by complex heat treatment procedures during production process. This quality heat treatment consists of austenitisation and several tempering treatments [2]. The resulting microstructure exhibits superior resistance against plastic deformation at high temperatures and long service times. This behaviour is achieved by strong pinning forces of precipitates on dislocations as well as on grain- and subgrain boundaries. Therefore, optimisation of the precipitation state in the as-received condition by optimisation of the quality heat treatment is an important issue for steel producers. Nevertheless, these optimised conditions are altered by fabrication processes such as welding due to the thermal influence of the welding process as well as the pre- and post-weld heat treatments. This can lead to inferior mechanical properties of the weldments compared to the base material and, therefore, to premature failure in the regions of weldments. Research and in-service experience have shown that the heat-affected zone (HAZ) of weldments is often the weakest part in welded constructions [3].

The following sections focus on the evolution of precipitates during production and welding process. Therefore, a defined time-temperature sequence was simulated on specimens of a modified 9Cr-1Mo steel in the laboratory of the Institute for Materials Science and Welding (IWS). These specimens were investigated using optical as well as electron microscopic methods. Finally, the results were compared to the results from numerical simulation, based on the software MatCalc.

EXPERIMENTAL

Material

The experimental investigations were performed on a modified 9Cr-1Mo cast steel. A 100kg trial melt was cast at voestalpine foundry Linz, Austria. The chemical composition of the investigated material is shown in Table 1. The quality heat treatment of the as-cast material consisted of austenitisation at 1100°C for 8h, double tempering (730°C/10h, 730°C/24h).

Thermal simulation

Thermal simulation of the production process consisted of a single thermal weld cycle with peak temperature of 1300°C and a characteristic cooling time of 80 seconds (T_P=1300°C/$t_{8/5}$=80s). The post-weld heat treatment was carried out at 730°C for 12 hours. To simulate the time-temperature sequence of the welding process a thermo-mechanical testing machine, Gleeble 1500, was used. The complete time-temperature sequence with labelled sampling points for microstructural investigations is shown in Fig. 1. The calculated equilibrium and the measured transformation temperatures (A_1, A_3 and M_S temperature) of the investigated material is summarised in Table 2. In the next section, the results of the microstructural investigation of the simulated specimens are presented. Particular attention is paid to the precipitate evolution during the welding cycle and PWHT.
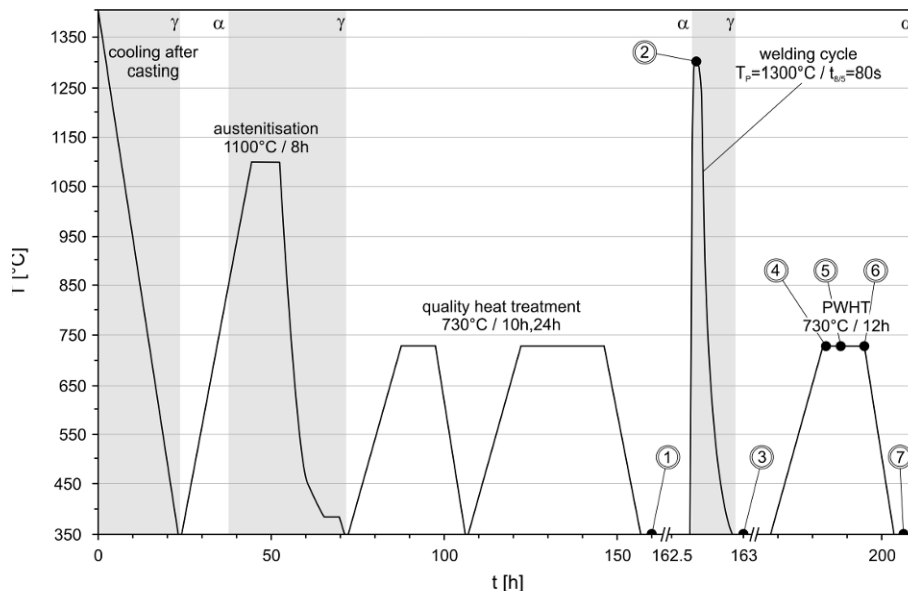
Figure 1: Time temperature sequence of production and fabrication process in the range from 350°C - 1400°C. Sampling points are numbered from 1 to 7. Prevailing matrix phase distinguished by different background colours (grey for austenitic and white for ferritic-martensitic matrix respectively).

Table 1: Chemical composition of the modified 9Cr-1Mo steel in wt.%.

C	Si	Mn	Cr	Mo	Ni	V	Nb	B	N
0.168	0.23	0.22	8.85	1.54	0.18	0.29	0.057	0.0092	0.016

Table 2: Transformation temperatures of the modified 9Cr-1Mo steel in °C. Labelled values (*) are calculated values from thermodynamic equilibrium considerations [3].

	heat treatment		welding cycle	
	heating	cooling	heating	cooling
A_1	835*		903	
A_3	887*		1001	
M_s		390		390

MICROSTRUCTURAL CHARACTERISATION

The microstructural investigations were carried out at the Institute for Materials Science and Welding and the Institute for Electron Microscopy of Graz University of Technology. In the following the results of microstructural investigations are reported. Thereby, a comprehensive picture of precipitate evolution during the welding cycle and PWHT can be drawn.

Light microscopy

The base material of the 9Cr steel shows a tempered martensitic microstructure in "as-received" (spec. 1) condition (Figure 2). The prior austenite grain size differs strongly because of the cast microstructure and ranges from several hundred micrometers to millimetres. Prior austenite grain boundaries and martensite lath boundaries are densely decorated with precipitates. No delta ferrite is detected after the quality heat treatment.
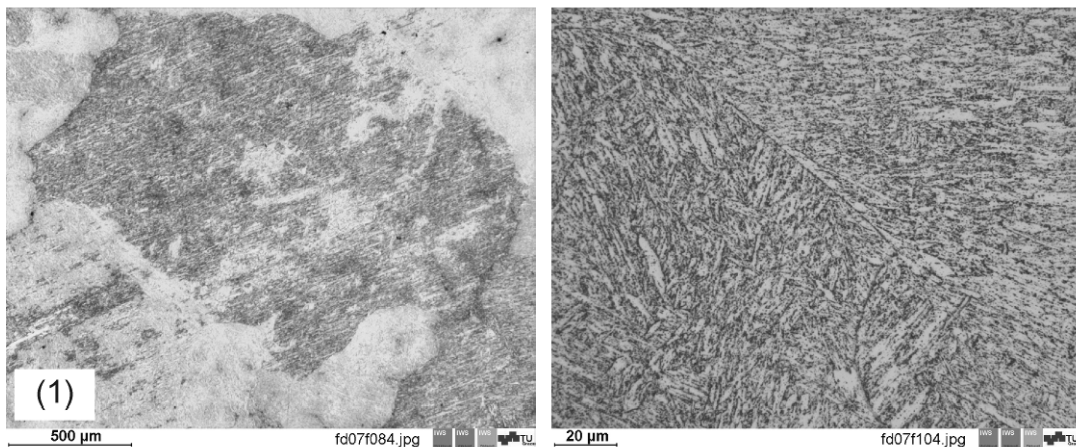
Figure 2: Optical micrograph of the base material in "as-received" condition showing large prior austenite grains (left) and tempered martensitic microstructure with densely distributed precipitates (right).

Light microscopy of the specimen after the welding simulation in "as-welded" (spec. 3) condition showed a certain amount of retained delta ferrite (Figure 3). No precipitates could be detected by light microscopy in the as-welded condition.
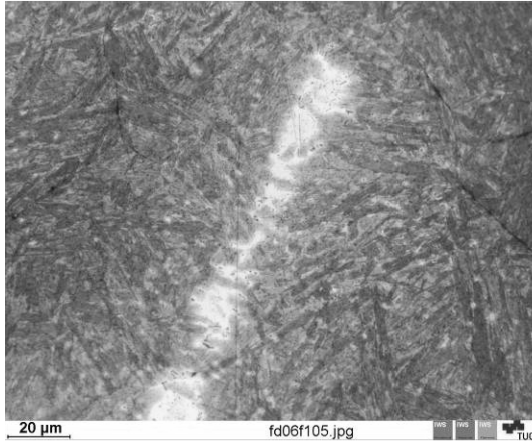
Figure 3: Optical micrograph of 9Cr steel in "as-welded" (spec. 3) condition showing retained delta ferrite (bright appearance) surrounded by newly formed virgin martensite.

After the PWHT, the steel shows again a tempered martensitic microstructure with finely dispersed precipitates along prior austenite grain, sub-grain and martensite lath boundaries.

Electron microscopy

Electron microscopy was carried out at the Institute for Electron Microscopy of Graz University of Technology using a Philips CM20 with 200keV. Figure 4 gives an overview of the precipitate evolution during welding and PWHT starting from the as-received condition. In the as-received condition, TEM observations show that precipitates present in the microstructure are, above all, $M_{23}C_6$ and MX precipitates (Fig. 4-1). During welding, the $M_{23}C_6$ and MX precipitates dissolve completely (Fig. 4-2). After the welding process, small rod shaped precipitates were present in the microstructure (Fig. 4-3). Further investigations showed that these precipitates are carbides with increased chromium content. Nevertheless, because of the small size of the precipitates, it was not possible to further specify these precipitates. During PWHT, these carbides dissolve in the first stages of the heat treatment and re-precipitation of $M_{23}C_6$ and MX precipitates takes place. Figure 4-4 to 4-7 show the precipitate evolution for the PWHT process quenched after 15 min., 2h and 12h at 730°C and after cooling to room temperature. An overview of the measured precipitate radii for the $M_{23}C_6$ and MX precipitates is given in Fig. 5. The evaluation of the precipitate radii from the TEM images was performed according to Sonderegger [4].
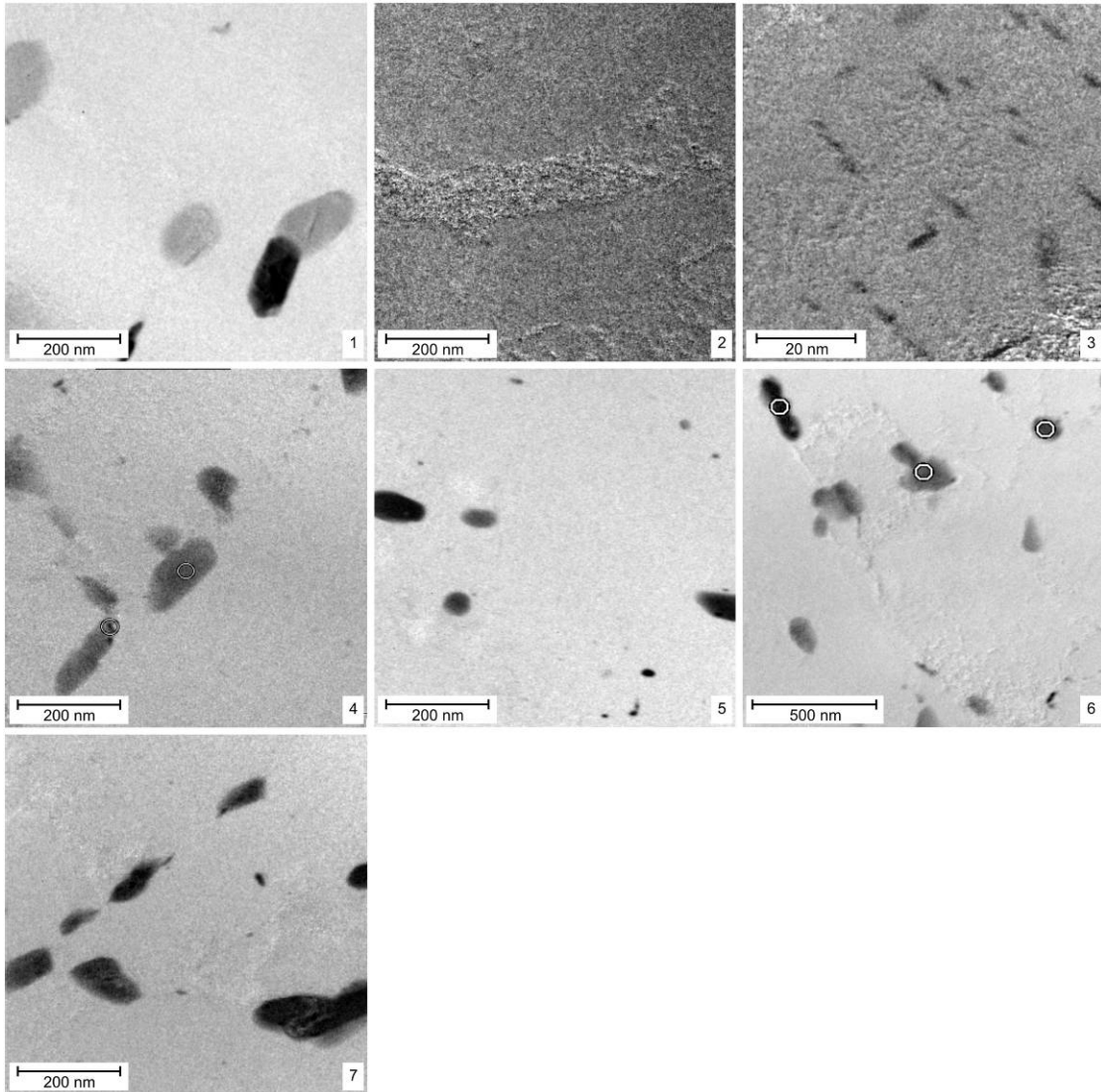
Figure 4: Characteristic TEM iron mappings of the investigated samples 1 to 7 according to the sampling points in Fig. 1.
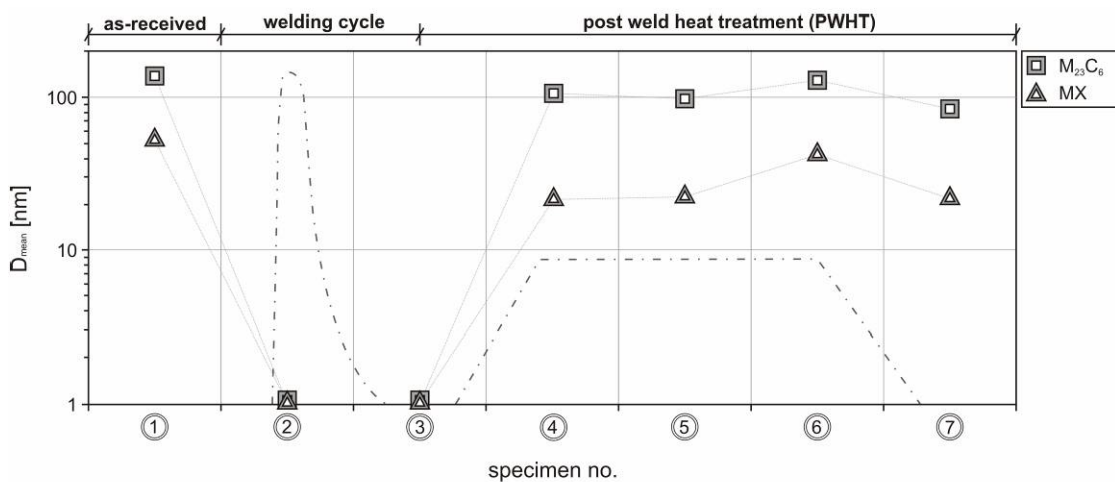
Figure 5: Measured particle size evolution of $M_{23}C_6$ and MX precipitates. Dash dotted line resembles (schematically) the simulated time-temperature sequence of the welding process and PWHT. The investigated specimens are numbered from 1 to 7 (according to Fig. 1)

NUMERICAL SIMULATION

For the numerical simulation of the precipitate evolution the software package MatCalc is used [5]. Details of the simulation procedure have been reported elsewhere [6-8].

Simulation settings

For the following heat treatment simulation, the time temperature sequence was defined according to Fig. 1. It is important to emphasize that, during the course of the production process the material undergoes several austenite/ferrite phase transformations (see also Fig. 1) - these are fully taken into account in the present simulation.

The numerical calculation starts closely below the solidus temperature of the steel at 1400°C in an austenitic matrix. Cooling down slowly to the M_S temperature of 390°C is carried out within 20 hours. At this temperature, the austenite transforms into martensite. It is assumed that no precipitation reactions occur below this temperature due to the sluggish diffusion. In the next simulation step, the austenitisation, temperature is increased. The simulation is performed in a ferritic matrix up to the calculated A_1 temperature of this steel at 835°C. Then, the matrix is switched to austenite and austenitisation is completed at 1100°C with subsequent cooling to 390°C. The two quality heat treatment cycles take place in a ferritic matrix at temperatures of 730°C. For the simulation of the subsequent welding cycle, the temperature is increased again. Because of the very high heating rate during the welding process the transformation temperatures A_1 and A_3 of the present alloy are shifted to higher temperatures. Therefore, altering from ferrite to austenite during heating takes place at 903°C (see also Table 2). After reaching the peak temperature T_P at 1300°C and subsequent cooling the matrix is switched to ferrite again at 390°C. Simulation of the PWHT at 730°C for 12h again is carried out again in a ferritic matrix.

For the present simulation, the precipitate phases $M_{23}C_6$, M_7C_3, M_3C and MX were considered in accordance with experimental findings in these type of steels [9]. During the simulation, all precipitates interact with each other by exchanging atoms with the matrix phase. The kinetics of this process is controlled by the multi-component diffusivities of all elements, which are available through kinetic databases, such as the mobility database of the software package DICTRA [10]. The thermodynamic parameters for calculation of the chemical potentials are taken from the TCFE3 database [11] with some modifications specific to these type of steels [12].

Apart from accurate thermodynamic and kinetic data, a very important input parameter for the simulation is the type of heterogeneous nucleation site for each of the precipitate phases, such as grain boundaries, subgrain boundaries, dislocations, grain boundary edges and/or grain boundary corners. For the present simulation, the nucleation site for each precipitate phase was defined according to experimental observations. The number of nucleation sites, which are actually available at each instant of the simulation, is defined by the microstructural quantities grain size, subgrain size and dislocation density as well as the grain or subgrain elongation factor. The latter takes into account the geometrical elongation, for instance, of a martensite lath. All relevant parameters for the entire heat treatment simulation are shown in tables 3 and 4 and described in detail in ref. [9,12].

Table 3: Microstructural parameters of the matrix phases

	Austenite	Ferrite
Grain size [m]	$700 \cdot 10^{-6}$	$700 \cdot 10^{-6}$
Subgrain size [m]	-	$0.7 \cdot 10^{-6}$
Subgrain size elongation factor [-]	1	100
Dislocation density [m^{-2}]	$1 \cdot 10^{11}$	$1 \cdot 10^{14}$

Table 4: Nucleation sites for the precipitate phases

	Matrix phase	Precipitate phases			
		$M_{23}C_6$	M_7C_3	M_3C	MX
Casting (1400°C - 390°C)	Austenite	GB	GB	GB	GB
Austenitising (390°C - 835°C)	Ferrite	GB, SGB	GB, SGB	GB, D, SGB	GB, D, SGB
Austenitising (835°C - 1100°C - 390°C)	Austenite	GB	GB	GB	GB
Heat treatment (3 cycles) (390°C - 730°C - 390°C)	Ferrite	GB, SGB	GB, SGB	GB, D, SGB	GB, D, SGB
Welding cycle (390°C - 903°C)	Ferrite	GB, SGB	GB, SGB	GB, D, SGB	GB, D, SGB
Welding cycle (903°C - 1300°C - 390°C)	Austenite	GB	GB	GB	GB
PWHT (390°C - 730°C - 390°C)	Ferrite	GB, SGB	GB, SGB	GB, D, SGB	GB, D, SGB

GB... Grain boundary, SGB... Subgrain boundary, D... Dislocations

In the simulations, it is assumed that the transformation from austenite to martensite and back occurs instantaneously and that the parent and product phase have the same chemical composition. The precipitate population does not change during this transformation. When the simulation starts at 1400°C, all elements are initially assumed to be in solid solution.

COMPARISON OF NUMERICAL RESULTS WITH EXPERIMENTAL DATA

Figure 6 shows the results of the numerical simulation. The upper graph (a) shows the simulated time-temperature sequence consisting of cooling after casting, austenitisation, double tempering, welding cycle and PWHT. The middle graph (b) shows the evolution of the phase fraction of different precipitate phases. It has to be pointed out that the phase fraction of $M_{23}C_6$, and M_3C is multiplied by a value of 1/10 for better illustration. In the lower graph (c) in Fig. 6 the development of the mean particle radius of the precipitate phases is shown. The various symbols in this graph resemble the experimental findings resulting from microstructural characterisation.

As-received condition
After the numerical simulation of the production process in the so called as-received condition, only $M_{23}C_6$ and MX precipitates are present in the matrix. Also in the investigated specimen (spec. 1) only these precipitate phases can be observed. The precipitates are observed with a size of 70nm for the $M_{23}C_6$ and 27nm for the MX phase compared to 60nm ($M_{23}C_6$) and 17.5nm (MX) in the numerical simulation.

Welding cycle
Experimental findings show that all precipitate phases dissolve during the welding cycle. The specimen quenched at peak temperature T_P=1300°C (spec. 2) shows no precipitate phases in the TEM images. Also the simulation doesn't show any precipitate phases after reaching peak temperature T_P. During cooling appearance of rod shaped precipitates was observed in the

TEM specimens, shown in Fig. 2-3. Characterisation of these precipitates showed that the present precipitates were carbides with high chromium content. Nevertheless, it was not possible to further specify these precipitates due to their small size. Simulation does not show the appearance of such phases.

PWHT

After dissolving all precipitates during the welding process, re-precipitation takes place during the PWHT at 730°C. Experiment shows that during PWHT, similar to the quality heat treatment, above all, $M_{23}C_6$ as well as MX precipitates are present. As it can be seen in Fig. 6-c, agreement between experiments and simulation can be designated as very good for $M_{23}C_6$ as well as for MX precipitates. The measured particle size after PWHT for $M_{23}C_6$ and MX precipitates are 42nm and 11nm respectively, whereas, numerical simulation results in 44.5nm for $M_{23}C_6$ and 14nm for MX precipitates.
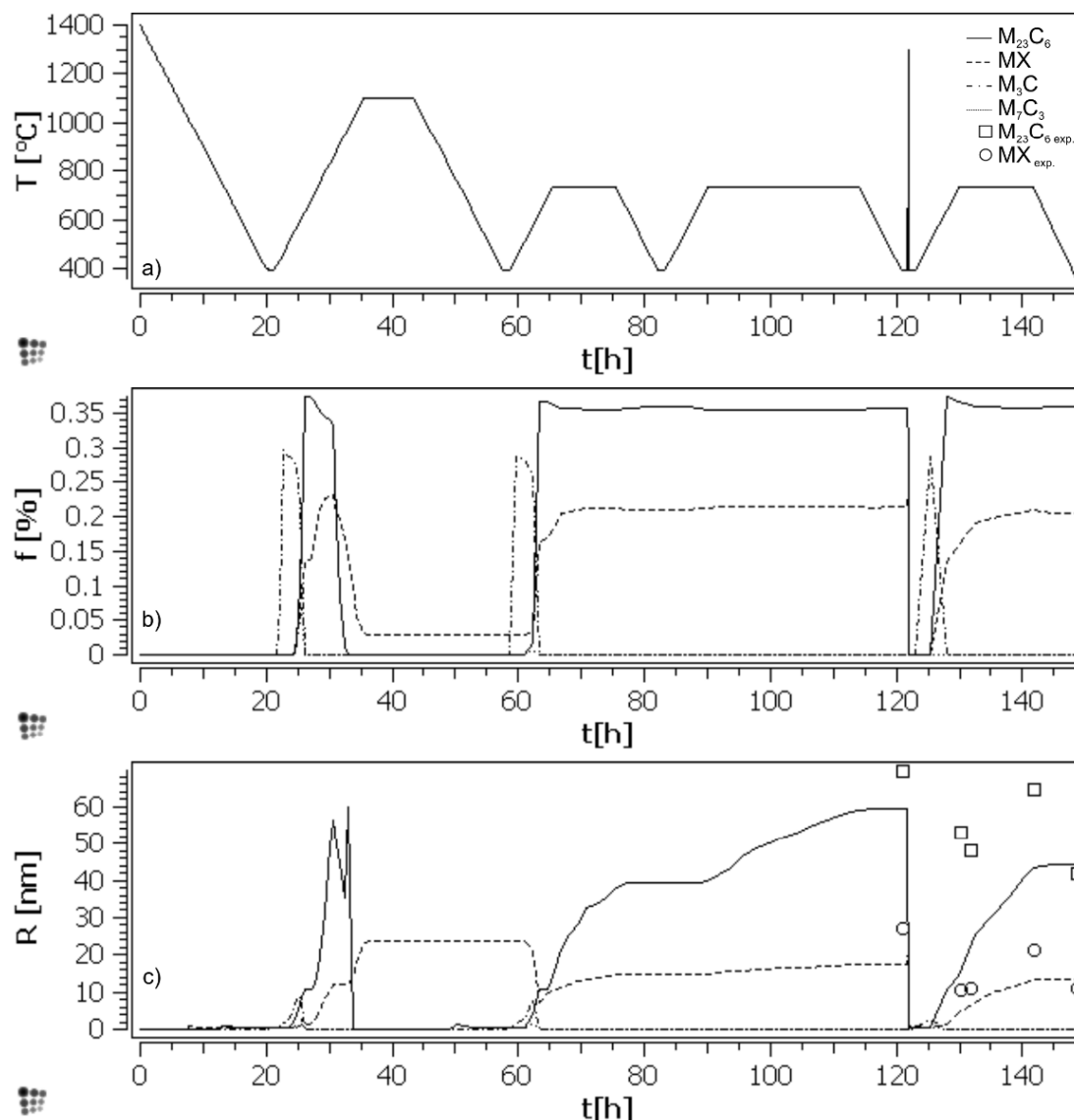
Figure 6: Result of the kinetic simulation of the precipitate evolution during production and fabrication process (f…phase fraction and R…mean precipitation radius). The phase fractions of $M_{23}C_6$ and M_3C are multiplied by a factor of 1/10 to give a better visual representation of the results. Squares and circles represent the experimental findings for evolution of the mean particle radius of $M_{23}C_6$ and MX particles respectively.

SUMMARY AND OUTLOOK

The possibility to simulate precipitation kinetics during the whole production and fabrication process of materials used for power plant applications is of particular importance, especially for the development of modern 9-12% Cr steels with advanced creep strength at enhanced service temperature and pressure. The results of the simulation presented in this paper show very good agreement with measured experimental data characterising the precipitate microstructure in the production and fabrication stages, i.e. in the as-received condition, during welding and post weld heat treatment. The results clearly demonstrate the potential of the present simulation approach to save time as well as costs for further efforts in material development and optimisation of production and fabrication procedures.

ACKNOWLEDGEMENT

REFERENCES

1 Scarlin B, Kern T U, Staubli M, The European efforts in material development for 650°C USC power plants – COST 522, in Proc. Int. Conf. on: 4th International Conference on Advances in Materials Technology for Fossil Power Plants, EPRI, 2004.
2 Cerjak H, Hofer P, Schaffernak B, Spiradek K, Zeiler G, Haupteinflussgrößen auf die Kriechbeständigkeit von 9- bis 12%igen Cr-Stählen für Kraftwerke mit erhöhten Dampfparametern, VGB Kraftwerkstechnik 77, 1997, Heft 9, 762-769.
3 Mayr P, Evolution of microstructure and mechanical properties of the heat affected zone in B-containing 9% chromium steels, Graz, Graz University of Technology, 2007.
4 Sonderegger B, Modifications of stereological correction methods for precipitate parameters using transmission microscopy, Ultramicroscopy, 2006, 106, 941-950.
5 Kozeschnik E, Buchmayr B, Mathematical Modelling of Weld Phenomena 5, London, Institute of Materials, 2001, 349-361.
6 Svoboda J, Fischer F D, Fratzl P, Kozeschnik E, Modelling of kinetics in multi-component multi-phase systems with spherical precipitates I. – Theory, Mater. Sci. Eng. A, Vol 385 (No. 1-2), 2004, 166-174.
7 Kozeschnik E, Svoboda J, Fratzl P, Fischer F D, Modelling of kinetics in multi-component multi-phase systems with spherical precipitates II. – Numerical solution and application, Mater. Sci. Eng. A, Vol 385 (No. 1-2), 2004, 157-165.
8 Kozeschnik E, Svoboda J, Fischer F D, Modified evolution equations for the precipitation kinetics of complex phases in multi-component systems, CALPHAD, Vol 28 (No. 4), 2005, 379-382.
9 Sonderegger B, Characterisation of the Substructure of Modern Power Plant Steels using the EBSD-Method, Graz, Graz University of Technology, 2005 (in German).
10 Andersson J O, Höglund L, Jönsson B, Ågren J, Computer simulations of multicomponent diffusional transformations in steel, in: Fundamentals and Applications of Ternary Diffusion, G.R. Purdy (ed.), New York, Pergamon Press, 1990, 153-163.
11 TCFE3 thermodynamic database, Thermo-Calc Software AB, Stockholm, Sweden, 1992-2004.

12 Rajek J, Computer simulation of precipitation kinetics in solid metals and application to the complex power plant steel CB8, Graz, Graz University of Technology, 2005.